

---

# Short-Range Ultra-Wideband Imaging with Multiple-Input Multiple-Output Arrays

---

*The pictures on the cover are the experiment setup of MIMO-SAR based UWB imaging system and the resulting 3-D image of the mannequin. (See also figure 5.2 and figure 5.6 of this thesis)*

# Short-Range Ultra-Wideband Imaging with Multiple-Input Multiple-Output Arrays

Proefschrift

ter verkrijging van de graad van doctor  
aan de Technische Universiteit Delft,  
op gezag van de Rector Magnificus prof. ir. K. C. A. M. Luyben,  
voorzitter van het College voor Promoties,  
in het openbaar te verdedigen op maandag 8 november 2010 om 10:00 uur

door

Xiaodong ZHUGE

elektrotechnisch ingenieur  
geboren te Beijing, China

Dit proefschrift is goedgekeurd door de promotor:

Prof. DSc. O. G. Yarovyi

Samenstelling promotiecommissie:

Rector Magnificus

voorzitter

Prof. DSc. O. G. Yarovyi

Technische Universiteit Delft, promotor

Prof. dr. ir. L. P. Ligthart

Technische Universiteit Delft

Prof. ir. P. Hoogeboom

Technische Universiteit Delft

Prof. ir. F. le Chevalier

Technische Universiteit Delft

Prof. dr. C. Pichot

Université de Nice-Sophia Antipolis

Prof. dr.-ing. habil. R. S. Thomä

Technische Universität Ilmenau

This research was partly supported by PASR project PROBANT (Grant Agreement no. SEC5-PR-104000), by FP6 project Radiotect (COOP-CT-2006-032744), and by FP7 project ATOM (FP7-AAT-2008-RTD-1-234014)

ISBN/EAN 978-94-6113-026-6

Short-Range Ultra-Wideband Imaging with Multiple-Input Multiple-Output  
Arrays.

Dissertation at Delft University of Technology.

Copyright © 2010 by Xiaodong Zhuge.

*All rights reserved. No parts of this publication may be reproduced or transmitted in any form or by any means, electronic or mechanical, including photocopy, recording, or any information storage and retrieval system, without permission in writing from the author.*

*To my family*



# Contents

<b>1</b>	<b>Introduction</b>	<b>1</b>
1.1	Overview of array-based UWB imaging systems .....	3
1.2	State-of-the-art in microwave imaging.....	5
1.3	Research objectives .....	9
1.4	Challenges and chosen approach.....	10
1.5	Novelties and main results.....	12
1.6	Research framework.....	15
1.7	Outline of the thesis.....	16
	References.....	19
<b>2</b>	<b>Ultra-wideband focusing</b>	<b>25</b>
2.1	Review of existing theories.....	26
2.2	Formulation of electromagnetic focused beam.....	27
2.2.1	Ultra-wideband electromagnetic missile.....	27
2.2.2	Imaging with synthetic aperture radar.....	31
2.3	Interference region in the near-field and beyond .....	35
2.4	Spatial sampling criteria .....	38
2.5	Sidelobe level of UWB aperture .....	40
2.6	Resolution and beam pattern.....	42
2.7	Characteristics of sparse aperture array .....	44
2.7.1	Effect of center frequency .....	45
2.7.2	Effect of fractional bandwidth .....	46
2.7.3	Effect of aperture size .....	47
2.7.4	Effect of number of elements within the aperture.....	48
2.8	Summary .....	49
	References.....	50

<b>3</b>	<b>Multiple-input multiple-output arrays for real-aperture imaging</b>	<b>51</b>
3.1	Review of existing theories.....	52
3.2	Near-field wideband beam pattern formulation .....	53
3.3	Unified theory with narrowband far-field beam pattern .....	57
3.4	Effective aperture and synthetic aperture.....	61
3.5	Factorization approach.....	63
3.6	Design procedure .....	65
3.7	Near-field and bandwidth effects.....	70
3.8	Experimental results.....	72
3.9	Summary .....	76
	References.....	78
<b>4</b>	<b>Two-dimensional planar MIMO arrays</b>	<b>81</b>
4.1	Review of existing theories.....	82
4.2	Array redundancy and element shadowing.....	83
4.3	Two-dimensional design methodologies .....	87
4.3.1	Equivalent uniform rectilinear array .....	87
4.3.2	Curvilinear composed array .....	91
4.3.3	Mills Cross array .....	93
4.4	Experimental verification.....	95
4.4.1	Tx/Rx coupling within 2-D MIMO array.....	97
4.4.2	Beam pattern .....	98
4.4.3	3-D volumetric imaging of distributed target.....	102
4.5	Summary .....	104
	References.....	104
<b>5</b>	<b>Comparison between real-aperture array and synthetic aperture</b>	<b>107</b>
5.1	Theoretical comparison.....	108
5.2	Experimental comparison .....	111
5.3	Summary .....	117
	References.....	117
<b>6</b>	<b>Advanced imaging algorithms for UWB MIMO array</b>	<b>119</b>
6.1	Modified Kirchhoff migration .....	120
6.1.1	Formulation.....	121
6.1.1.1	Formulation for MIMO array.....	123
6.1.1.2	Compensation of limited aperture effects .....	125

6.1.1.3	Extending Kirchhoff integral to subsurface .....	127
6.1.1.4	Efficient calculation of travel time.....	129
6.1.2	Results in free-space .....	131
6.1.3	Results in subsurface.....	135
6.2	MIMO range migration.....	140
6.2.1	Range migration for SAR configuration .....	141
6.2.2	Formulation for MIMO array.....	142
6.2.3	Algorithm implementation.....	145
6.2.4	Sampling constrains .....	147
6.2.5	Imaging results.....	149
6.3	Summary .....	154
	References.....	154
<b>7</b>	<b>Utilization in different applications</b>	<b>159</b>
7.1	Concealed weapon detection.....	160
7.1.1	Prototype of the system.....	161
7.1.2	Test results .....	164
7.2	Through-wall radar .....	167
7.2.1	Propagation loss .....	167
7.2.2	Dynamic range .....	170
7.2.3	Choice of UWB technologies.....	172
7.2.4	Prototype of through-wall imaging radar .....	173
7.2.5	Test results .....	175
7.3	Ground penetrating radar in a multi-sensor fusion system .....	177
7.3.1	Array-based UWB GPR Sensor .....	178
7.3.2	GRP embedding in multi-sensor suit .....	179
7.3.3	Test results .....	182
7.4	Summary .....	184
	References.....	184
<b>8</b>	<b>Conclusions</b>	<b>187</b>
8.1	Results and novelties of this research .....	188
8.2	Recommendations.....	189
<b>A</b>	<b>Design of low profile UWB antenna for near-field imaging</b>	<b>191</b>
A.1	Introduction.....	191

A.2	Antenna element design.....	193
A.3	Performances of the antenna .....	196
A.4	Summary .....	199
	References.....	199
	 <b>List of acronyms</b>	 201
	 <b>Summary</b>	 203
	 <b>Samenvatting</b>	 207
	 <b>Author's publications</b>	 211
	 <b>Acknowledgements</b>	 215
	 <b>About the author</b>	 217

# CHAPTER 1

## INTRODUCTION

The development of safe, reliable and cost-efficient imaging technologies has been a constant and yet growing demand from modern societies. Imaging science has enabled mankind to look inside the Earth, inside our bodies, and out to the Universe of which we live in. It has helped us to resolve our fears caused by the unseen and the unknown. It gives us addition to our ability to probe, to solve and to cure.

Imaging can be done by means of different probing substances: acoustic field, electromagnetic field (from radio wave to gamma ray), neutrons, etc. The majority regions of the electromagnetic (EM) spectrum can be used for imaging with different operating frequencies which can provide variant information about the object under test. In order to see through optically opaque materials, frequencies above the ultraviolet (UV) region ( $>3 \times 10^{17}$  Hz) or below the infrared absorption region ( $<10^{12}$  Hz) have to be considered. These can be referred as the X-ray and radiofrequency (RF) methods, respectively. Although the imaging physics behind these two are distinct from each other, they are both competitive in many applications. In this thesis, non-intrusive imaging technologies are developed using microwave frequencies between 300 MHz and 300 GHz.

Microwave imaging system is a picture-taking device with long-wavelength microwave energy. The utilized microwave spectrum is able to pass through barriers without being a health hazard. The target or scene is illuminated by microwave transmitters and the reflected or scattered field is intercepted and collected by receiving antennas. The system processes the received echoes in the beamforming process transforming the observed wave field into a map of the electromagnetic scattering coefficient of the scene. This beamforming process is, in certain extent, analogous to the function of lens in a camera. The microwave transmitter serves as the role that the sun does in optical photography, therefore, avoiding limitation in possible indoor or night-time scenarios.

Like the optical photograph, the image obtained by a narrowband microwave imaging system is an angle-angle image, within which the distance dimension has been collapsed onto the image plane. By employing an emitted signal with bandwidth exceeding the lesser of 500 MHz or 20% of the center frequency, an ultra-wideband (UWB) imaging system allows resolving capability not only in the cross-range (angular domain) but also in the down-range (depth). An additional range dimension is added to the angular dimensions of the image providing the capability of three-dimensional (3-D) volumetric imaging. By combining the advantage of UWB, real-aperture array, and digital beamforming, the whole imaging process can be performed instantly providing possibilities of real-time 3-D observation and operation.

Array-based UWB microwave imaging system has strong potentials in various short-range applications. In the field of healthcare, microwave imaging equipments are less physically intrusive on patients and apply safe level of radiation. This technology could assist traditional X-ray systems which have high doses of ionizing radiation thus having limited usage per patient. There are reasons to be optimistic that in the next decade a viable microwave diagnostic system will be available, and one day to be used to detect cancer in local health centers. Developing such system is not mean to replace existing medical screening devices such as computed tomography (CT) or magnetic resonance imaging (MRI), but to assist, improve detection, and to reduce risks for early-stage patients. For security application, constant threats from terrorism and crime require specialized surveillance tools for concealed weapons detection (CWD) and observation of people inside building or behind walls. Scanning and surveillance of people do not allow the use of ionizing radiation for safety concerns. The current inductive magnetic field (metal detector) solution is limited as it lacks of classification. A microwave imaging system is more reliable and less disruptive to passengers at airport and railways, or to people passing security checkpoints.

From 1999 the International Research Centre for Telecommunications and Radar (IRCTR) at Delft University of Technology has been participating in several national and European projects in the effort to develop high performance UWB imaging systems. These projects include “Advanced relocatable multi-sensor system for landmine detection” (STW-sponsored project), “UWB mini-array” (MoD-sponsored project), “Cadmium – multi-sensor system for landmine detection” (joint project with TNO), “PROBANT - People Real-time Observation in Buildings: Assessment of New Technologies in support of surveillance and intervention operations” (Supported by European Commission via PASR program), “RADIOTECT - Ultra Wideband Radio application for localization of hidden people and detection of unauthorized objects” (Supported by European Commission via FP6), and “ATOM – Airport detection and Tracking Of dangerous Materials by passive and active sensor arrays” (Supported by European Commission via FP7). Close cooperation between different governmental and industrial organizations in Europe has provided substantial support to the projects, and also to the present dissertation. The developed

researches in this thesis have been achieved with the support from the projects from 2006 to 2010.

## 1.1 Overview of array-based UWB imaging systems

UWB signal, which provides advantage in propagating in cluttered and opaque media compared to narrowband signals, enable the exploration and imaging of hidden inhomogeneities, through the use of UWB radar techniques by acquisition and processing of backscattered signal [1]. UWB radar technology is of special interest due to its high down-range resolution and capability of detection and classification. It has been implemented for various systems in different applications, such as ground penetrating radar (GPR) [2-5], indoor/outdoor probing and positioning [6-8], and sensing/imaging in medical studies etc [9-11]. Nowadays, the State of the art UWB radar systems are based on Synthetic aperture radar technology (SAR) or array with sequential operation of identical transmit/receive antenna pairs [2, 4, 5, 12-14]. Although such system exhibits high cross-range resolution capability and relative fast scanning speed, it can hardly fulfill the demand of real-time data acquisition and operation due to practical limitations. The next technological step is to develop UWB array-based real-aperture systems with multiple-input multiple-output (MIMO) arrays which would provide high cross-range (angular) resolution, reduced element density, and lower costs.

UWB impulse combined with real-aperture array and digital beamforming yields very attractive features for achieving improved performance in terms of high three-dimensional (3-D) resolution, focusing, and electronic-beam-steering capabilities. Angular resolution can be enhanced by increasing the size of array aperture relative to the wavelength. Ultra-wideband sparse arrays can be constructed to achieve high angular resolution without encountering the grating lobe problem which is associated with narrowband array beamforming. By using spatially distributed transmit/receive array with well-designed array topologies, low grating/sidelobe level is possible with less number of antenna elements in comparison with the number of measurement positions needed in SAR. This in turn reduces the data-acquisition time and computational costs for focusing and imaging. Moreover, UWB technology is cost effective which allows for design and construction of antenna arrays with required number of elements [15].

Figure 1.1 illustrates the block diagram of a generic UWB MIMO array-based imaging system. The system consists of transmit/receive array of wideband transducers and supporting electronics. The microwave transducers convert electrical signals to electromagnetic waves and also convert electromagnetic waves back to radio frequency electrical signals. The transducer array topology is that of a highly sparse multiple transmit multiple receive array. The transmit array elements are sequential excited by the UWB signal generator through the transmit switch circuit,

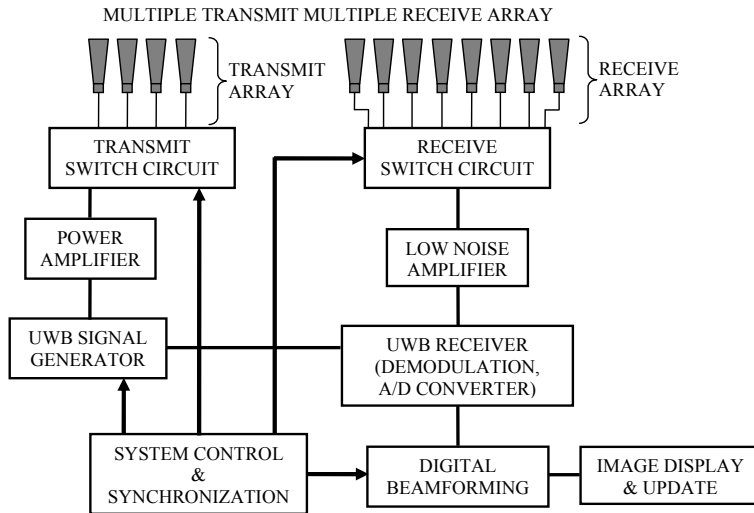


Figure 1.1 Block diagram of a generic UWB MIMO array-based imaging system

which connects each antenna element under synchronization from the system control unit. When the scattered electromagnetic field arrives at the receive array, the receive switch circuit passes the corresponding receive element's signal to the UWB receiver through a low noise amplifier (LNA). The receiver converts the radio frequency analog signal to baseband and further digitalizes it to discrete digital signals. The digitized signals sequentially received from each transmit/receive pair are fed into the digital beamforming unit, which processes the signal contribution from individual element pair to each sampled pixel within the current image. The resulting image is fed into the display unit which continuously refreshes in real-time.

For an array-based UWB imaging system, multiple aspects must be considered in order to reach the optimal performance. It is a complex problem that requires cross-discipline research in electrical engineering. Fundamentally, it can be divided into two related sub-problems, signal processing, radar design on one hand and antennas and electromagnetics on the other. Array design can be seen as an interface between both aspects. Arising from the demands of applications (ex. see through wall), size and allocation of frequency band must be decided first based on the electromagnetic and end-user requirements. Antenna elements operating in the proposed frequency then be designed considering together with the required performance. Next, antenna array will be designed which includes selection of data acquisition type (MIMO/SAR), and design of array topology. Coupling between array elements must be considered at both antenna element and array design stage. Then signal processor needs to be formulated to provide mainstream signal processing for detection and initial parameter estimation. Imaging algorithms must be specified for the proposed array in order to give required performance and processing speed. A data manager, as

a part of signal processor, follows to support the data and information processing functionality of the system and work together with a display sub-system through which the system operator can interact with and make the most effective use of the resources at his/her command in real-time.

## 1.2 State-of-the-art in microwave imaging

Before and during the research studies presented herein, research institutions and industries has been heavily involved in the field of microwave imaging. In this section, the approach and performances of existing microwave imaging systems are highlighted under different applications. The review of the current research and development gives motivation for the research of this thesis.

### *Concealed weapon detection (CWD)*

Many recent events show that the current security system is not sufficient to deal with the increasing threads from terrorism and crime. Numerous imaging systems have been proposed to detect both metallic and non-metallic materials hidden under clothes or inside baggage. Some technologies have already been developed into products and applied in screening and surveillance applications.

Majority of microwave imaging systems oriented for CWD applications are based millimeter-wave (MMW) technology. The history of millimeter-wave started in the 1890s [16]. In recent years, various applications have been developed as a result of the rapid progress in monolithic microwave integrated circuit (MMIC) technology. One of its main applications is imaging for security surveillance. A MMW is an electromagnetic wave with wavelength ranging from 10 mm to 1 mm (30 to 300 GHz). In this region, the transmission of MMW is attenuated by atmospheric absorption caused by water vapor and oxygen. Some regions of low attenuation, named “atmospheric windows”, exist around 35, 94, 140, and 220 GHz. MMW based imaging system are basically of two types: passive and active. Passive millimeter-wave systems observe and form an image through passive detection of naturally occurring millimeter wave scene radiation. Passive sensors have the advantage of producing image without emitting any EM radiation. Representative examples of such system can be found in [17-23]. Imaging of concealed weapons in a passive manner has been demonstrated and the performance can be drastically different when applied in variant environment, especially between indoor and outdoor (or between daytime and nighttime). By contrast, active millimeter wave sensors illuminate the environment with electromagnetic waves using single or distributed transmitters. Because the transmitted signals have known properties, such system is capable to extract weak target responses from competing sources of noise. Examples of developed active MMW systems can be found in [23-31]. Specially, the

Pacific Northwest National Laboratory (PNNL) in WA, USA, has developed a variety of active millimeter-wave imaging systems and technologies including the cylindrical imaging technique that has been successfully commercialized with L3-Communications/Safeview [32]. The developed ProVision body scanning checkpoint system has been deployed at the security checkpoints in some of the US and Europe's major airports. The device operates in the Ka frequency band and is capable of providing quasi-3D images by scanning cylindrically around the body using two vertically arranged linear arrays with sequential operation of identical transceiver pairs. Although it claims a high checkpoint throughput (200-400 people per hour), this kind of data acquisition approach in certain extent reduces the speed of passenger flow if compared with an ideal standoff system. Both passive and active MMW imaging systems are being pursued by several groups around the world. It has been realized that due to the very large number of spatial samples required at high frequencies, a practical active MMW weapon detection system is expected to operate at W-band or lower. The relative high cost of MMW components makes such system more suitable for high security checkpoints as a centralized system, and prevents it from widely deployed at various level of public transportation nodes.

### *Through-wall imaging (TWI)*

'Seeing' through obstacles such as walls, doors, and other visually opaque materials, using microwave signals offers powerful tools for a variety of applications. Through-wall imaging is highly desirable for police, fire and rescue, and military applications. The ultimate desire of such system is to provide detailed information to determine the layout of buildings, where occupants may be, and even identify objects within buildings. Through wall sensing grew from ground penetrating radar systems applied to walls, and specific applications have been increasingly documented in the literature since the late 1990s showing abilities to sense beyond a single wall from near-range [14, 33- 37].

The majority of the existing TWI systems are based on UWB technology. One of the most well-known and widespread radars for detection of human beings behind a wall on the market, is an UWB impulse radar called RadarVision2, developed by Time Domain Corporation [38], located in Huntsville, AL, USA. The radar enhances situation awareness by showing the location of room occupants before a forced entry. The device uses ultra-wideband pulses (2.1 – 5.6 GHz) to penetrate most common building materials, and utilizes an array of 22 circular polarized antennas arranged to provide resolving capabilities mainly in the horizontal direction. RadarVision2 only provides a 2-D (angle-range) image of targets with motions and can not classify the detected targets (e.g., between human and animal, object with movement and human). Georgia Tech Research Institute researchers have developed a prototype called Radar flashlight that allows the user to detect a stationary individual located behind a solid wooden door, or standing four feet behind an eight-inch block wall [39]. It uses a radar beam of 15 to 20 degrees and a specialized signal processor to discern

---

respiration from up to three meters away. Its signal penetrates clothing, and the "flashlight" requires a body movement of only a few millimeters to detect human presence. The laboratory prototype unit operates on a frequency near 10.525 GHz. The current laboratory prototype is a homodyne radar configuration, although a frequency modulated continuous wave (FM-CW) system could be used for applications where information is required to determine the range to the target. Cambridge Consultants worked in the Security and Defence market for over 40 years and have over 20 years' experience in designing and developing radar systems. They are specialised in the development of through-wall radar systems and components for government and commercial clients [40]. The developed systems include PRISM100 and PRISM200. Based on the first-generation PRISM100 radar, the 2<sup>nd</sup> generation PRISM200 can be used by military and emergency service personnel in situations such as hostage taking, search and rescue. A unique feature of the PRISM200 RADAR core is an array of antennas which gives it a large field of vision - at least 140 degrees in both vertical and horizontal planes - combined with 3-D object location and motion tracking. Operators can use the system to decide whether people are standing, sitting or lying, or whether the object detected is human or an animal. Held against a wall or mounted on a tripod up to 2 meters away, PRISM200 transmits low frequency ultra-wideband (UWB) radar pulses that pass through building materials over 40 cm thick, to detect activity over a range of up to 15 meters. A company in Israel, Camero Inc, is also involved in development of radars for security applications [41]. The developed Xaver™ real-time 3-D 'Through-Wall Vision' system allows observation of multiple stationary and moving objects concealed by walls. The main feature of this system is its true 3-D imaging function, which provides the capability to observe in real-time motion of moving targets behind walls and to distinguish among different types of target. The system operates in a wide frequency band from 3 to 10 GHz and provides a maximum operational distance of 20 m. It utilizes a 2-D array which provides 3-D imaging capability up to 8 m with less than 0.2 m resolution. The technical details of this system are not published and therefore not available to the public. As we can see, real-time imaging capability is the frontier of through-wall radar systems and is a crucial technology desired by the potential end-users.

### *Ground penetrating radar (GPR)*

Ground penetrating radar is a geophysical equipment that uses electromagnetic wave in the microwave frequency band to image the subsurface. It has been demonstrated that GPR is a useful tool for landmine detection and geophysics applications. In the Earth sciences it is used to study bedrock, soils, groundwater, and ice. Engineering applications include nondestructive testing (NDT) of structures and pavements, locating buried structures and utility lines. In archaeology, it is used for mapping archaeological features and cemeteries. GPR is also extensively applied in military applications to detect mines, unexploded ordnance, and tunnels.

Conventional GPR system uses a single pair of transmitting and receiving antennas or only one containing both functions. The system scans over the area of survey to collect the reflected waves from the subsurface. Several systems based on such principle have been developed by industry and are available in the market [42-45]. In order to avoid 2-D mechanical scanning over the surface and to speed up the ground survey, a number of array-based GPRs have been developed [4, 5, 12, 46]. In these existing systems, the array is formed by a number of parallel transceivers. The mechanical scanning in the direction of the array is replaced by sequential operation of identical transmit/receive pairs. Despite the substantial increase of the survey speed comparing with conventional 2-D mechanical scan, this approach still limits the scanning speed up to a few kilometers per hour. A more advanced approach to the array-based GPR has been realized in the EFGPR system developed by Geo-Centers from USA, where controlled time delays are introduced to individual transmitter and receivers to actively focus and image the subsurface [47]. It is foreseen that further development of multistatic array combined with multi-channel receiver and digital beamforming is the next technological step to further increase the scanning speed [2].

### *Medical diagnosis*

Microwave imaging of human body for cancer detection has been of interest to the scientific society for quite long time. The main attractions of using microwave systems in the field of diagnostic medicine are the harmless nature of microwave at low radiation level, the relatively lower cost of even complex microwave systems comparing to computer-assisted tomography (CAT) and magnetic resonance imaging (MRI), and the different permittivity of malignant tissue (tumor) compared with normal tissue. Among cancer detection systems, breast cancer detection has its unique features. The size, physical accessibility, and large contrast between lesion and healthy tissue are definite advantages to explore. The desire for complimentary diagnostic tool for breast cancer detection is also high due to the limitations associated with the standard mammography, which is an X-ray imaging procedure that involves uncomfortable breast compression and exposure of body to harmful ionizing radiation. This prevents patients from frequent early-stage examination, which is the best and most effective phase for medical treatment. Therefore, in recent years, various researches and prototypes based on microwave imaging have been proposed and developed.

Several research groups in Europe and US have been performing theoretical and experimental studies for breast cancer detection over the last decade [9, 10, 48-55]. The research group at Dartmouth College has developed a clinical system reported in [48]. It is a microwave tomography system operating in frequency-domain, where 2-D images are obtained by a set of 32 antennas. Over the years, the group at University of Wisconsin, Madison, USA, lead by Dr. Hagness has introduced several UWB microwave imaging techniques for breast cancer detection [9, 49, 50]. Their

initial methods are based on linear approximation similar to those of CAT in order to avoid complex and computation intensive nonlinear inverse scattering problem. The limitations to this kind of approach to complicated human body anatomy are apparent. In recent years, progress has been made in development of more complex approach that uses numerical methods to solve nonlinear inverse problems [56-58]. Because of the difficulties of solutions to inverse scattering problem at RF and microwave frequencies and complications posed by human anatomy, the challenges of developing a microwave diagnostic tool has not yet been fully resolved. Nevertheless, recent progresses in numerical methods and increasing power of parallel computers have made such attempt feasible.

### **1.3 Research objectives**

The main research question of this thesis refers to the development of array-based ultra-wideband imaging system for short-range applications. The primary focus lies on the investigation of capabilities of ultra-wideband multiple-input multiple-output (MIMO) array, and development of advanced algorithms for UWB array imaging.

A sparse multistatic array is required in order to achieve high angular resolution with only small number of antennas. The combination of ultra-wideband signal and MIMO array offers three major advantages: sparse aperture array with low element density, absence of grating lobes despite the large element spacing, and high resolution in both down-range and cross-range (angular) directions. Meanwhile, with the front-end of the UWB sparse array simplified, higher requirements are shifted to the imaging algorithms. Development of advanced algorithms which exhibit high imaging performance, high tolerance toward aperture sparsity, and low computation cost is another main focus of this thesis. Specifically, we can state the main research objectives of this thesis as the following:

1. To obtain a comprehensive understanding and develop the fundamental theory of ultra-wideband focusing within the near-field of the array aperture and beyond. This will serve as the basis for developing both sparse aperture array and imaging algorithms.
2. To develop the theory of MIMO array topologies and investigate their performance in narrowband/wideband, near-field/far-field conditions.
3. To develop a design concept of UWB MIMO array for short-range imaging. The procedure should be able to translate requirements from the application into specific array specifications, such as operation frequency band, number of element, array dimension, array topology, etc.

4. To develop design strategies for two-dimensional MIMO array which would be able to provide three-dimensional imaging capabilities with low grating/side lobe level over the entire imaging space.
5. To verify the performance and potential of real-aperture MIMO array imaging against synthetic aperture radar (SAR) technique, and to obtain a systematic comparison which helps to push the array-based UWB imaging concept forward into practice.
6. To develop advanced imaging algorithms for UWB array imaging. Investigate the performance of the algorithms in terms of resolution, grating/side lobe level, and computational costs. To provide a practical guideline for choosing suitable imaging algorithms for specific applications.
7. To utilize the developed array theory and imaging algorithms in different applications. Test and verify the theories and designs developed in this thesis in practical conditions.

#### **1.4 Challenges and chosen approach**

From the system level, there are many challenges facing UWB array-based imaging system, namely, the system should be reliable, portable, and has both short data acquisition time and processing time. The system performance should be robust against different target scenarios, ambiguity and inaccuracy of subsurface parameters and should properly function under complex scene, multiple target dynamics, non-uniform subsurface and target motion. Ultimately, the system should have high range and cross-range resolution and low side/grating lobe level, which could be application specific. Finally, the imaging system must be able to detect and classify different targets and motions in a populated scenario and in the presence of heavy clutter, which may include strong scatters, interior back and side walls in through-wall application, metal bars, pipes, electrical cords, and various types of non-target items.

Figure 1.2 provides a graphical illustration of the research scheme of this thesis. The main goal of research is to investigate the properties of wideband imaging arrays and propose design concepts for developing high-performance array-based UWB imaging system. Since experimental demonstrators are aimed at to access the proposed concept and design approaches, attention has been given to the properties and designs of both ultra-wideband MIMO array and advanced imaging algorithms.

For many who design microwave imaging arrays, the ultimate goal is to obtain sharp images that can closely resemble the picture from an optical device. The main challenge is to generate high-resolution imaging capability with limited number of

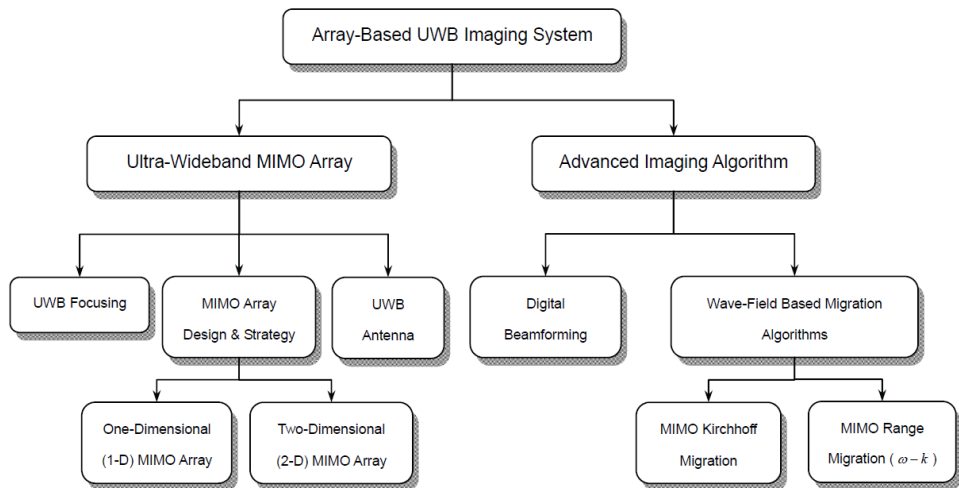


Figure 1.2 Research scheme

antenna elements within the array. Our approach for this problem is to combine the merit of both ultra-wideband focusing, MIMO array configuration, and low-profile UWB antenna elements. Conventionally, the design of imaging arrays is mostly experimental and empirical. The bandwidth of the system is specified based on availability of wideband antenna element or requirement of down-range resolution. The design of array starts from a uniform configuration or topology and optimization follows to find a moderate solution. Since the dimension of the problem is tremendous, such search optimization is certain to fall into local optimums and engineers are not certain whether their design have reached the full potential of the system. In order to propose a design theory and systematic design strategy, the problem of designing ultra-wideband multistatic array were devided into three connected research blocks: UWB focusing, MIMO array (topology design and strategy), and UWB antenna element. Based on the investigated properties of UWB focusing, MIMO array topologies can be proposed to enhance and complement the performance of the complete imaging system. Bandwidth of the system is derived systematically and antenna element design follows to reach the requirement for high-quality imaging.

Regarding the imaging algorithm, two research directions were identified as relevant for realizing and improving the imaging potential of the ultra-wideband multistatic array. Conventional digital beamforming algorithms are normally developed for narrowband uniformly spatial sampling data set. They need to be adapted to deal with wideband non-periodic sparse array configuration in order to fully focus the scattered wave-field from a near-field target. Meanwhile, theoretical and experimental investigations have shown improvements of wave extrapolation algorithm, such as Kirchhoff migration, in terms of both beamwidth and sidelobe

rejection ratio when compared with back-projection algorithm (also known as diffraction stack). However, in practice the measured aperture will enclose the target scene only partially and therefore the validity region of wave field extrapolation will in practice be limited. Typically, one calculates the field assuming that the backscattered fields vanish outside the measurement aperture. This means that the further we back propagate the backscattered field, the higher will be the truncation errors in the estimation of the fields. The mitigation of these truncation errors is an important and challenging subject which needs to be dealt with individually. Furthermore, another type of wave-field based algorithm, namely range migration, is developed for MIMO array configurations. This further offers an image reconstruction solution with significantly improved computational efficiency. The developed imaging algorithms, including digital beamforming, Kirchhoff migration and range migration algorithm (RMA) are based on the linearization of the electromagnetic wave scattering problem. Such assumption simplifies the computational procedure and makes it robust against noise and clutters. This approximation is widely applied in the field of radar and ultrasonic imaging.

## 1.5 Novelties and main results

The researches addressed in this thesis have resulted in several scientific contributions that are resolved in an original manner. The major novelties presented in this thesis are listed as follows:

- A new theory regarding the impact of bandwidth on wideband focusing has been proposed. The theory corrects the previous widely-accepted misunderstanding in the field of both ultrasound and radar engineering. Previous theory believes that wideband sparse array will not suffer from grating lobe problems. Specifically, it was a general misunderstanding that grating lobes are not formed when the spatial sampling of the aperture is greater than the length of the radiated impulse. Our study shows that this condition only ensures the existence of a non-interference region (or grating lobe free region) within the image space outside the focal point or main beam but does not guarantee absence of grating lobes. Instead, the bandwidth relative to the center frequency (or fractional bandwidth) places deterministic impact on the formation of grating lobes. The importance of this proposition is that the dilemma of sparse array faced by radar engineers between angular resolution and grating lobe level can be resolved. Instead of trading one with the other, image resolution can be improved with low grating/side lobes from an ultra-sparse aperture/array under the condition that fractional bandwidth is greater than 100%.
- Effective strategies for designing one-dimensional and two-dimensional multiple-input multiple-out array topologies have been proposed. The proposed

---

topologies significantly improve the performance of UWB imaging array. They change the design principle and are novel to the field of array imaging systems in general. Based on this research a patent application has been prepared and filed.

- A deterministic design process for UWB MIMO array for short-range imaging has been developed. The procedure does not need any search optimization process to reach the theoretical optimum performances, and can translate requirements from the application into specific array specifications, such as operation frequency band, number of element, array dimension, array topology, etc.
- A novel combination of ultra-wideband and MIMO array is introduced for microwave imaging systems. The MIMO array-based UWB imaging system is able to provide high down- and cross- range resolution, low side/grating lobe level, simplified RF scheme and significantly increased data acquisition and processing speed. Prototypes of MIMO array-based UWB imaging systems are designed and implemented for through-wall imaging, ground penetrating radar, and concealed weapon detection showing satisfactory performances in different short-range applications.
- A systematic and experimental comparison between synthetic aperture radar (SAR) and real-aperture MIMO array has been performed. Clear advantage of the real-aperture system is concluded which pushes the new system concept further into practical design and application.
- Modified Kirchhoff migration has been developed for both free-space and subsurface UWB multistatic array imaging. The algorithm combines the high quality imaging performance with high flexibility to array configurations and can be applied to demanding applications in practice.
- Modified range migration has been developed for UWB multistatic array imaging in the frequency-wavenumber domain. As a result, the implementation of the algorithm on a massively parallel computer is fairly straightforward. The algorithm offers both the high quality imaging performance with extremely fast processing speed and is an ideal imaging algorithm for real-time applications.
- Prototypes of MIMO array-based UWB imaging systems are designed and implemented for through-wall imaging, ground penetrating radar, and concealed weapon detection showing satisfactory performances in different short-range applications.

The following results are listed as the main achievements of this thesis:

- We have theoretically derived and experimentally proved the deterministic influence of the fractional bandwidth of a sparse aperture/array on the performance of ultra-wideband focusing in both near-field and beyond. Our theory and results illustrate that the bandwidth of an imaging system must exceed its central frequency in order to benefit from the merit of wideband impulse properties, allowing high-resolution imaging with significantly reduced number of antenna elements.
- We have formulated the derivation of point spread function (PSF) or beam pattern for UWB MIMO array in both near-field and far-field. The formulation is able to include previous narrowband far-field expression as a special case. The formulation leads to design approach for designing MIMO arrays for high resolution imaging.
- We have investigated the design and optimization of non-uniform linear array for subsurface imaging. The impact of the electromagnetic wave refraction on the air-ground interface is taken into consideration in order to compensate the refraction effects and improve imaging quality. Experimental results verified the improvements of the proposed new array in terms of sidelobe level and sidelobe size comparing with the uniform linear array with same number of array elements.
- We have developed design concept for one-dimensional and two-dimensional MIMO arrays and proposed several effective strategies for forming high-performance array configurations. The design approach is straight forward and does not require optimization. The designed MIMO arrays are able to provide three-dimensional imaging capabilities and low grating/side lobe level with large element spacing and reduced number of antenna elements.
- We have compared the performances of real aperture MIMO array with synthetic aperture radar (SAR). Specifically, 1-D MIMO array combined with SAR is compared with 2-D planar SAR for short-range imaging. The results show the advantage of the real aperture system and illustrate the potential of the MIMO UWB imaging system for multiple applications.
- We have developed advanced imaging algorithms for UWB-MIMO array imaging. Thesis algorithms include MIMO Kirchhoff migration, MIMO range migration. Investigation of the algorithms in terms of resolution, grating/side

lobe level, and computational costs has been performed and provide different choices of imaging algorithms for specific applications.

- We have developed artifact reduction procedure to reduce the level of side/grating lobes in the initial image of a sparse array. Numerical simulation of both isolated and distributed target scenarios show significant reduction of sidelobe level and target break-up. Measurement further verified the potential of the proposed technique in practice.
- We have utilized the design and theory of UWB MIMO array in different applications including concealed weapon detection, through-wall imaging, ground penetrating radar, and medical imaging. The resulting demonstrators and experimental results confirm the proposed theory and designs and illustrate the strong potential of the UWB MIMO imaging system in short-range applications.

## 1.6 Research framework

The research presented herein was conducted with the support from the following projects

### 1. PROBANT - People Real-time Observation in Buildings: Assessment of New Technologies in support of surveillance and intervention operations

The project was supported by European Commission (EC) via PASR program, and aimed at the realization of breakthrough in security technology: visualization and tracking in real time of people located inside buildings. The development and validation of an integrated set of new technologies permit future industrialization of powerful investigative tools enabling to guide security forces in surveillance and crisis interventions. The team guarantees an optimum match between user requirements and technological excellence, being composed of an innovative French industrial company, a European Research Centre, a Dutch University and two national police agencies for specialist criminal investigations. The developed technologies were validated by demonstrator during tests in realistic environment.

### 2. Radiotect - Ultra Wideband Radio application for localization of hidden people and detection of unauthorized objects

The Radiotect project is an EC-funded PF6 project completed in 2009. The aim of the project was to support innovative SMEs to adapt their technologies, to develop transnational cooperation and to extend their cooperative relations. This was achieved in the specific area of wideband radio for the detection of hidden

people and objects. Three application scenarios were concentrated: sensor network for building monitoring, handheld sensor for local building inspection, and body scanning. The support to the SMEs in the project helped ensure that Europe continues to capitalize on the knowledge and expertise which it has for ultra-wideband technology which is proving to be more and more suitable for varying applications.

### 3. Cadmium

This is a joint project with TNO from 2007 with the goal to verify the real-time performance of ground penetrating radar (GPR) for landmine detection, and to compare GPR with other sensors, namely metal detector array and polarization camera. TNO's responsibility was assembling the system, hardware and software integration of the sensors while IRCTR prepared the GPR hardware/software module. This model produces a confidence map of subsurface targets with a resolution of 2.5 cm. Series of test has been conducted in the facilities of TNO-DSS. The multisensor vehicle-based demonstrator was able to provide real-time confidence maps of the subsurface under 36-km/h scanning speed. The goal of the project to verify the real-time operation of the novel array-based GPR has been achieved.

### 4. ATOM - Airport detection and Tracking Of dangerous Materials by passive and active sensor arrays

ATOM project is an EC-funded PF7 project. The objective of the project is to study, design and develop the functional prototype of an innovative multi-sensor based system integrating active and passive radar sensors, improving the security level also in the terminal area of the airport. ATOM system will be a non-intrusive but pervasive security system, which require no ad-hoc check points for passengers and will reduce interference with normal passenger flow. Within the frame of the project, TU Delft is responsible for the development of ultra-wideband imaging sensor system. We aim for a medium cost and complexity concept to enable the deployment of large number of systems to form sensor network, which would help to achieve a global monitoring of passengers from the moment of their arrival to the airport.

## 1.7 Outline of the thesis

This dissertation is organized in 4 major parts, covering the main aspects associated with the development and design of array-based UWB imaging systems. In the first part, the theoretical formulation of UWB focusing will be presented. Spatial sampling, resolution, point spread function, and characteristic of sparse aperture/array are theoretically studied and numerically investigated. The second part

of the thesis will be dedicated to the analysis and design of wideband MIMO arrays. Comparison between real-aperture multistatic array and synthetic aperture radar technique will be discussed from both technological and design aspects. The third part covers the development related to advanced imaging algorithms. Features and advantages of different algorithms are given special attention in particular for wideband multistatic array configurations. The last part will focus on the utilization of the developed imaging technology for different short-range applications. Demonstrators developed in various research projects give clear demonstration of the proposed theory and designs in practical applications.

Hereafter, a description of the chapters to follow is provided:

- **Chapter 2 – *UWB focusing*.** This chapter investigates the ultra-wideband focusing behavior with special focus on the characteristics in the near-field. Reviews of existing theories regarding aperture focusing are first presented. Followed by formulations of electromagnetic focused beam. The focusing characteristics of a wideband aperture is discussed for near-field operation and further extended to far-field conditions. The spatial sampling of aperture for monochromatic and non-monochromatic signals is explored. The characteristics of wideband aperture during aperture thinning are investigated as the confirmation to the proposed wideband aperture theories and provide further implications for sparse array design.
- **Chapter 3 – *Multiple-input multiple-output arrays for real-aperture imaging*.** This chapter aims to study the capabilities of UWB-MIMO array and present a generic design approach for sparse MIMO array topology. Existing theories regarding MIMO arrays are first reviewed. Beam pattern of MIMO array in the near-field of aperture with UWB excitations is formulated and provides a unified theory with existing narrowband far-field beam pattern formulations. The equivalence between MIMO and conventional arrays is demonstrated, and the concept of an equivalent array is introduced. Factorization approach from a desired equivalent aperture into transmit/receive topologies is proposed, and the design procedure for UWB-MIMO array is described together with a few design examples. The near-field and bandwidth effects on the imaging performances of the MIMO array are studied. Finally, the performance of the above-mentioned MIMO arrays is experimentally studied using Vivaldi antenna arrays.
- **Chapter 4 – *Two-dimensional planar MIMO arrays*.** This chapter aims to further extend the MIMO-UWB array design approach to full 2-D dimensions. Reviews of existing theories regarding 2-D transducer arrays are presented. Influences of array redundancy and element shadowing are discussed. Various types of 2-D design strategies for two-way MIMO array design are introduced and analyzed. Experimental results of sparse 2-D arrays designed following the introduced approaches are presented and compared.

- **Chapter 5 – Comparison between real-aperture array and synthetic aperture.** This chapter aims to further compare the designed real-aperture MIMO arrays against conventional SAR technique. The theoretical influence of replacing synthetic aperture with real-aperture array is discussed and summarized. The experimental comparison between MIMO-SAR and 2-D SAR are presented.
- **Chapter 6 – Advanced imaging algorithms for UWB MIMO array.** The aim of this chapter is to develop high performance and efficient 3-D imaging technique for the identification and characterization of radar reflectivity components of complex objects appearing within the near-field of a 2-D MIMO array aperture. The extension of Kirchhoff migration for MIMO array imaging in both free-space and subsurface scenarios are presented. In the second part, the implementation of MIMO array imaging is further formulated and developed in the frequency-wavenumber domain in order to achieve higher computational efficiency.
- **Chapter 7 – Utilization in different applications.** This chapter presents the utilization of the developed theories and techniques within the framework of EU projects in various imaging applications, including concealed weapon detection for enhancing security at public settings, through-wall imaging for anti-terrorism and rescue operations, and ground penetrating radar for humanitarian demining.
- **Chapter 8 – Conclusions.** This chapter summarizes the main results of the study and provides recommendations for future research.

## References

- [1] J. D. Taylor, *Ultra-Wideband Radar Technology*, Ed, CRC Press, 2001.
- [2] A.G. Yarovoy, T.G. Savylyev, P.J. Aubry, P.E. Lys, and L.P. Lighthart, “UWB Array-Based Sensor for Near-Field Imaging”, *IEEE Trans. Microw. Theory Tech.*, vol. 55, no. 6, pp. 1288-1295, Jun. 2007.
- [3] X. Zhuge, T. G. Savylyev, A .G. Yarovoy, L. P. Lighthart, “Subsurface Imaging with UWB Linear Array: Evaluation of Antenna Step and Array Aperture,” in *Proc. IEEE International Conference on Ultra-Wideband (ICUWB)*, Sep. 2007, pp. 66-70.
- [4] J. E. McFee, V. C. Aitken, R. Chesney, Y. Das, and K. L. Russell, “Multisensor vehicle-mounted teleoperated mine detector with data fusion,” in *Proc. SPIE Detection and Remediation Technologies for Mines and Minelike Targets III*, 1998, vol. 3392, pp. 1082-1093.
- [5] R.B. Cosgrove, P. Milanfar, and J. Kositsky, “Trained detection of buried mines in SAR images via the deflection-optimal criterion”, *IEEE Trans. Geosci. Remote Sens.*, vol. 42, no. 11, pp. 2569-2575, Nov. 2004.
- [6] Y. Yunqiang, and A.E. Fathy, “See-through-wall imaging using ultra wideband short-pulse radar system,” in *Proc. IEEE Antenna Propag. International Symposium*, Jul. 2005, Volume 3B, pp. 334 – 337.
- [7] A. Beeri, and R. Daisy, “High-resolution through-wall imaging,” in *Proc. SPIE*, vol. 6201, 62010J, 2006.
- [8] X. Zhuge, T. G. Savylyev, A .G. Yarovoy, “Assessment of Electromagnetic Requirements for UWB Through-Wall Radar,” in *Proc. International Conference on Electromagnetics in Advanced Applications (ICEAA)*, Sep. 2007, pp. 923-926.
- [9] X. Li, E. J. Bond, B. D. Van Veen, and S. C. Hagness, “An overview of ultrawideband microwave imaging via space-time beamforming for early-stage breast cancer detection,” *IEEE Antennas and Propagation Magazine*, vol. 47, no. 1, pp. 19-34, Feb. 2005.
- [10] R. Benjamin, I.J. Craddock, J. Leendertz, R. Nilavalan, A. Preece, “Experimental investigation of real aperture synthetically organised radar for breast cancer detection,” in *Proc. IEEE Antennas and Propagation Society International Symposium*, 2005, vol. 1B, pp.179 - 182.

- [11] X. Zhuge, M. Hajian, A. G. Yarovoy, L. P. Ligthart, "Ultra-wideband Imaging for Detection of Early-Stage Breast Cancer," in *Proc. European Radar Conference (EuRAD)*, Oct. 2007, pp. 38-42.
- [12] R.J. Chignell, and M. Hatef, "LOTUS – a Real Time Integrated Sensor Suite for Anti-Personnel Mine Detection, Incorporating the MINEREC GPR," in *Proc. Xth Int. Conf. Ground Penetrating Radar*, Delft, the Netherlands, June 21-24, 2004, pp. 665-668.
- [13] I.J. Craddock, A. Preece, J. Leendertz, M. Klemm, R. Nilavalan, R. Benjamin, "Development of a Hemi-spherical Wideband Antenna Array for Breast Cancer Imaging," in *Proc. EuCAP* (ESA SP-626), Nov. 6-10, 2006, pp. 1-5.
- [14] S. Nag, M. A. Barnes, T. Payment., and G. Holladay, "An ultra-wideband through-the-wall radar for detecting the motion of people in real time", in *Proc. SPIE: Radar Sensor Technology and Data Visualization*, Jul. 2002, vol. 4744, pp. 48-57.
- [15] J. D. Taylor, *Introduction to Ultra-Wideband Radar Systems*, CRC Press, 1994.
- [16] J. C. Wiltse, "History of millimeter and submillimeter waves," *IEEE Trans. Microw. Theory Tech.*, vol. 32, no. 9, pp. 1118-1127, 1984.
- [17] L. Yujiri, M. Shoucri, and P. Moffa, "Passive Millimeter-Wave Imaging," *IEEE microwave magazine*, Sep. 2003, pp. 39-50.
- [18] R. Appleby, "Passive millimetre-wave imaging and how it differs from terahertz imaging," The Royal Society, 10.1098/rsta.2003.1323, 2003, pp. 379-394.
- [19] S. E. Clark, J. A. Lovberg, C. A. Martin, and V. Kolinko, "Passive millimetre-wave imaging for airborne and security applications," in *Proc. SPIE*, Aug. 2003, vol. 5077, pp. 16-21.
- [20] N. A. Salmon, "A W-band real-time passive millimetre-wave imager for helicopter collision avoidance," in *Proc. SPIE on Passive Milli.-Wave Imaging Tech. III*, Orlando, Florida, Apr. 1999, USA, vol. 3703, pp. 28-32.
- [21] R. Appleby, R. N. Anderton, S. Price, N. A. Salmon, G. N. Sinclair, J. R. Borrill, P. R. Coward, P. Papakosta, and A. H. Lettington, "Compact real-time (video rate) passive millimeter-wave imager," in *Proc. SPIE on Passive Milli.-Wave Imaging Tech. III*, Orlando, Florida, USA, Apr. 1999, vol. 3703, pp. 13-19.

- 
- [22] K. Mizuno, Y. Wagatsuma, H. Warashina, K. Sawaya, H. Sato, S. Miyanaga, Y. Yamanaka, "Millimeter-Wave Imaging Technologies and Their Applications," in *Proc. IEEE Vacuum Electronics Conference (IVEC 07)*, May 2007, pp. 1-2.
  - [23] Stanko, S., Klöppel, F., Huck, J., Nötel, D., Hägelen, M., Briese, G., Gregor, A., Erukulla, S., Fuchs, H.-H., Essen, H., Pagels, "A. Remote concealed weapon detection in the millimeterwave region: Active and passive," in *Proc. SPIE*, 2006, vol. 6396, pp. 639–606.
  - [24] P. F. Goldsmith, C.-T. Hsieh, G. R. Huguenin, J. Kapitzky, and E. L. Moore, "Focal plane imaging systems for millimeter-wavelengths," *IEEE Trans. Microw. Theory Tech.*, vol. 41, pp. 1664–1675, Oct. 1993.
  - [25] Appleby, R. and R. N. Anderton, "Millimeter-wave and submillimeter-wave imaging for security and surveillance," in *Proc. IEEE*, vol. 95, no. 8, pp. 1683–1690, Aug. 2007.
  - [26] F. Gumbmann, H. P. Tran, J. Weinzierl, L-P. Schmidt, "Optimization of a Fast Scanning Millimeter-Wave Short Range SAR Imaging System," in *Proc. European Microwave Conference (EuMC)*, 2007, pp. 24-27.
  - [27] A. Schiessl, S.S. Ahmed, "W-band imaging of explosive substances," in *Proc. European Microwave Conference (EuMC)*, 2009, pp. 1888-1891.
  - [28] F. Sakai, H. Suzuki, H. Sato, K. Sawaya, K. Mizuno, "High resolution millimeter-wave imaging using inline Tx/Rx antennas," in *Proc. European Radar Conference (EuRAD)*, 2008, pp. 156-159.
  - [29] S. Kharkovsky, J. T. Case, M. A. Abou-Khousa, R. Zoughi, F. L. Hepburn, "Millimeter-wave detection of localized anomalies in the space shuttle external fuel tank insulating foam," *IEEE Trans. Instrum. Meas.*, vol. 55, no. 4, pp. 1250-1257, Aug. 2006.
  - [30] D. L. McMakin, D. M. Sheen, and H. D. Collins, "Remote Concealed Weapons and Explosive Detection on People Using Millimeter-wave Holography," in *Proc. Security Technology, 30<sup>th</sup> Annual International Carnahan Conference*, Oct 1996, pp. 19-25.
  - [31] D. M. Sheen, D. L. McMakin, and T. E. Hall, "Three-Dimensional Millimeter-Wave Imaging for Concealed Weapon Detection," *IEEE Trans. Microw. Theory Tech.*, vol. 49, no. 9, pp. 1581-1592, Sep. 2001.
  - [32] L3-Communications/Safeview, ProVision System, Available online: <http://www.sds.l-3com.com>

- [33] D. D. Ferris, Jr. and N. C. Currie, “A survey of current technologies for through-the-wall surveillance (TWS),” in *Proc. SPIE Conference on Sensors, C31 Information, and Training Technologies for Law Enforcement*, Boston, MA, Nov. 1998, vol. 3577, pp 62-72.
- [34] L. M. Frazier, “Surveillance through walls and other opaque materials,” in *Proc. IEEE National Radar Conference Electronic Systems*, May 1996, pp. 27-31.
- [35] E. F. Greneker III, “RADAR flashlight for through-the-wall detection of humans,” in *Proc. SPIE Targets and Backgrounds: Characterization and Representation IV*, Jul. 1998, Vol. 3375, pp. 280-285.
- [36] Lin-Ping Song, Chun Yu, Qing Huo Liu, “Through-wall imaging (TWI) by radar: 2-D tomographic results and analyses,” *IEEE Trans. Geosci. Remote Sens.*, vol. 43, no. 12, pp. 2793- 2798, Dec. 2005.
- [37] A. R. Hunt, “Image formation through walls using a distributed radar sensor network,” in *Proc. SPIE: Laser Physics and Photonics, Spectroscopy, and Molecular Modeling V*, 2005, vol. 5778, pp. 169-174.
- [38] Time Domain Corporation. <http://www.radarvision.com>
- [39] Georgia Tech Research Institute.  
[http://gtresearchnews.gatech.edu/newsrelease/FLASH\\_SP.html](http://gtresearchnews.gatech.edu/newsrelease/FLASH_SP.html)
- [40] Cambridge Consultants.  
[http://www.cambridgeconsultants.com/def\\_index.shtml](http://www.cambridgeconsultants.com/def_index.shtml)
- [41] Camero Inc. <http://www.camero-tech.com>
- [42] Seeker SPR system. <http://www.usradar.com>
- [43] IDS. <http://www.idscompany.it>
- [44] SATIMO. <http://www.satimo.com>
- [45] TRIM. <http://www.trimcom.ru>
- [46] Humanitarian Demining R&D Program. <http://www.humanitarian-demining.org>
- [47] GeoCenters EFGPR. <http://www.geo-centers.com>
- [48] P. M. Meaney, M. W. Fanning, S. P. Poplack, and K. D. Paulsen, “A clinical prototype for active microwave imaging of the breast,” *IEEE Trans. Microw. Theory Tech.*, vol. 48, pp. 1841–1853, Nov. 2000.

- 
- [49] D. W. Winters, J. D. Shea, P. Kosmas, B. D. Van Veen, and S. C. Hagness, "Three-dimensional microwave breast imaging: Dispersive dielectric properties estimation using patient-specific basis functions," *IEEE Trans. Med. Imag.*, vol. 28, no. 7, pp. 969–981, Jul. 2009.
  - [50] X. Li, S. K. Davis, S. C. Hagness, D. van der Weide, and B. D. Van Veen, "Microwave imaging via space-time beamforming: Experimental investigation of tumor detection in multi-layer breast phantoms," *IEEE Trans. Microw. Theory Tech.*, vol. 52, no. 8, pp. 1856–1865, Aug. 2004.
  - [51] M. Klemm, I. J. Craddock, J. A. Leendertz, A. Preece, and R. Benjamin, "Radar-based breast cancer detection using a hemi-spherical antenna array—experimental results," *IEEE Trans. Antennas Propag.*, vol. 57, no. 6, pp. 1692–1704, Jun. 2009.
  - [52] M. Klemm, J. A. Leendertz, D. Gibbins, I. J. Craddock, A. Preece, R. Benjamin, "Microwave Radar-Based Breast Cancer Detection: Imaging in Inhomogeneous Breast Phantoms," *IEEE Antennas AND Wireless Propagation Letters*, vol. 8, pp. 1349–1352, 2009.
  - [53] E. C. Fear, X. Li, S. G. Hagness, and M. A. Stuchly, "Confocal microwave imaging for breast tumor detection: Localization of tumors in three dimensions," *IEEE Trans. Biomed. Eng.*, vol. 49, pp. 812–822, Aug. 2002.
  - [54] E. C. Fear and M. A. Stuchly, "Microwave detection of breast cancer," *IEEE Trans. Microw. Theory Tech.*, vol. 48, pp. 1854–1863, Nov. 2000.
  - [55] S. M. Salvador, G. Vecchi, "Experimental Tests of Microwave Breast Cancer Detection on Phantoms," *IEEE Trans. Antennas Propag.*, vol. 57, no. 6, pp. 1705–1712, Jun. 2009.
  - [56] N. Joachimowicz, C. Pichot, and J. P. Hugonin, "Inverse scattering: An iterative numerical method for electromagnetic imaging," *IEEE Trans. Antennas Propag.*, vol. 39, pp. 1742–1751, 1991.
  - [57] T. Rubk, P. M. Meaney, P. Meincke, K. D. Paulsen, "Nonlinear Microwave Imaging for Breast-Cancer Screening Using Gauss-Newton's Method and the CGLS Inversion Algorithm," *IEEE Trans. Antennas Propag.*, vol. 55, pp. 2320–2331, 2007.
  - [58] D. W. Winters, B. D. Van Veen, and S. C. Hagness, "A Sparsity Regularization Approach to the Electromagnetic Inverse Scattering Problem," *IEEE Trans. Antennas Propag.*, vol. 58, no. 1, pp. 145–154, Jan. 2010.



## CHAPTER 2

# ULTRA-WIDEBAND FOCUSING

A UWB imaging system, specifically impulse-based, transmits very short pulses of electromagnetic energy, typically only a few cycles or less. A very short pulse is a rapidly changing signal, and thus occupies a wide bandwidth. This allows far more accurate measurement of distance, and thus resolution. Two-dimensional (2-D) focused aperture/array based on UWB impulse waveforms is able to generate localized radiation and energy at specified focal point with high-resolution in three-dimensions. These properties are attractive for numerous applications in radar, communications, medical imaging and diagnosis, automotive industry and security systems.

The focusing characteristics of an UWB aperture/array is the cornerstone for the development of wideband array antenna and imaging system. This chapter aims to investigate the properties of ultra-wideband focusing in the near-field and far-field. It serves as references for the designs of wideband real-aperture array discussed in Chapters 3 and 4.

The chapter is organized as follows. Reviews of existing theories regarding aperture focusing are presented in section 2.1. Formulations of electromagnetic focused beam are presented in section 2.2. In section 2.3, the focusing characteristics of a wideband aperture is discussed for near-field operation and further extended to far-field conditions. The spatial sampling of aperture for monochromatic and non-monochromatic signals is explored in section 2.4. The sidelobe level of wideband aperture is discussed in section 2.5. In section 2.6, the effects of bandwidth on the resolution and focusing performances are studied. The characteristics of wideband aperture during aperture thinning are investigated in section 2.7 as the confirmation to the proposed wideband aperture theories and provide further implications for sparse array design. The chapter is summarized in the last section.

## 2.1 Review of existing theories

In the past, two types of theory exist for aperture/array focusing, the monochromatic theory and the impulse theory. Among them, the most classical formulation is based on narrowband far-field assumptions. It states that the elements of a uniform array must be placed closely with less than half of the wavelength ( $\lambda/2$ ) spacing to satisfy the Nyquist criterion and avoid grating lobes [1]. This posts a practical limit in the size of the aperture, and hence the resolution. Since the mathematical formulation under such approximation can be greatly simplified, it leads to an easier and more straightforward understanding of the physical phenomenon behind. Therefore, researchers commonly use such narrowband far-field approximation as a starting point to design array for different applications and treat the wideband near-field behavior as asymptotic phenomenon.

By contrast, the other type of theory is based on the ultra-wideband impulse theory. Such theory describes the array behavior in terms of interception of pulses and claims that the shorter the pulses, the sparser the array, the smaller the interference without even incurring grating lobe problems. Von Ramm and Smith pointed out in [2] that the level of grating lobes can be somewhat reduced for pulse echo phased array imaging systems which transmit acoustic pulses a few cycles in duration. They explained the amplitude lowering by arguing that signals from far fewer elements form the grating lobe than the mainlobe in a pulsed transducer array. Anderson further expressed the idea that the resolution of a wideband array may be increased by simply moving the elements apart without incurring grating lobe problems [3]. A quasi-closed form beam pattern definition for beamforming with rectangular pulse was presented in [4] placing special emphasis on the invariance of grating lobe level to the inter-element spacing. The principle of UWB focused array for the generation of electromagnetic missiles was described in [5] for impulse radiators. A sparsity analysis for UWB planar square focused array is further presented in [6]. Schwartz and Steinberg thoroughly described the wideband array behavior in terms of interception of pulses, and defined sparse array as the condition where the average inter-element spacing is much greater than the pulse length [7]. They also claimed that the minimum side/grating lobe level is to approach  $N^{-4}$  where  $N$  is the number of elements in the transmit/receive arrays.

In practice, imaging/array engineers often experience grating lobe problems despite the absolute bandwidth of their system is not small. Actually, most of these systems have emitted signal bandwidth exceeding the lesser of 500 MHz or 20% of the center frequency, which is recognized as UWB. Moreover, experiences indicate that increasing the element spacing only makes the aperture/array performance worse, which is contrary to the impulse theory [7]. For this reason, the UWB array properties are not widely applied in applications. In the following sections, we further developed the impulse theory to explain the contradictions and define the true criteria of UWB aperture/array focusing. To put everything in a simple way, a

tipping point exist, exceeding which the wideband properties begin to place significant impact on the aperture focusing characteristics, and both narrowband and wideband theories need to be considered to interpret the complete ultra-wideband focusing phenomena.

## 2.2 Formulation of electromagnetic focused beam

In this section, formulations of focused electromagnetic beam and synthetic aperture radar imaging (or array with sequential operation of identical transceiver pairs) are presented. The resulting derivation shows the similarities between them despite their different natures. The formulations serve as reference for further analysis of the characteristics of UWB focusing.

### 2.2.1 Ultra-wideband electromagnetic missile

Conventional phase array applied for electronic beamsteering with sinusoidal waves forms a radiation beam pattern defined in terms of azimuth and elevation. A focused wideband antenna array provides a concentrated energy pattern in the case of radiated impulse signals, which exhibits a decaying behavior of energy of the propagating wave in terms of travelled distance from the aperture. The planar array illustrated in Figure 2.1 can generate a focused electromagnetic wave by setting proper delay time at each of the radiating elements. The delay time is configured so that the radiated signals will arrive simultaneously and sum coherently at the focusing point of the array. At positions other than the focal point, the interaction of the propagated signals will result in out-of-focus, or a distorted wave field whose time variation differs completely from that of the radiated impulses.

A two-dimensional planar array of  $N$  elements is shown in Figure 2.1. The array elements are located within the  $xz$ -plane with variant separation between two adjacent antennas. Each array element is an UWB impulse radiator, such as the large-current radiator described in [8], and its position vector is denoted by  $\mathbf{r}$ . The distribution of the elements within the aperture is described by  $w(\mathbf{r})$ . For a focusing distance  $R$  from the center of the array aperture in Figure 2.1 to an arbitrary focusing point located at  $\mathbf{r}_F$ , the relative focusing delay time  $\tau$  for each array element must be set according to the expression

$$\tau(\mathbf{r}, \mathbf{r}_F) = R/c - |\mathbf{r}_F - \mathbf{r}|/c \quad (2.1)$$

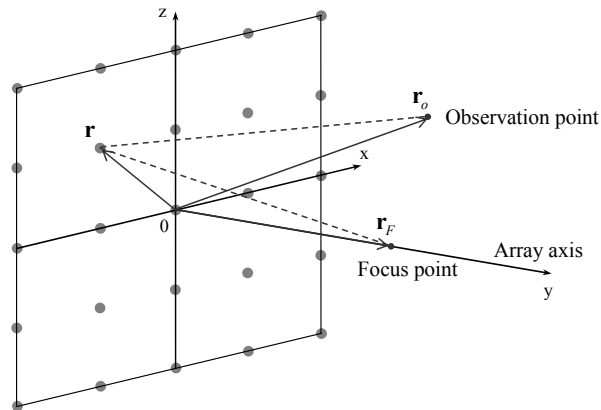


Figure 2.1 Geometry of two-dimensional planar aperture array antenna composed of  $N$  impulse radiators  $\mathbf{r}$  distributed in the transverse  $xz$ -plane with distribution function  $w(\mathbf{r})$ .

where  $c$  is the speed of propagation in the medium. According to (2.1), the focusing delay time for the reference element located at the aperture center is the largest since the impulse radiated by this element will experience the shortest propagation delay to arrive at the focusing point. Accordingly, the array element  $\mathbf{r}$  other than the reference point will be excited prior to the reference element and radiate their EM pulse earlier in time.

The elementary Green's function  $G_E$  for each array element to propagation from  $\mathbf{r}$  to the observation point  $\mathbf{r}_o$  with adjusted focusing delay time can be obtained by the convolution between focused and propagated waves as

$$G_E(\mathbf{r}_o, \mathbf{r}_F, \mathbf{r}, t) = G_F(\mathbf{r}_F, \mathbf{r}, t) * G_p(\mathbf{r}_o, \mathbf{r}, t) \quad (2.2)$$

where

$$\begin{aligned} G_F(\mathbf{r}_F, \mathbf{r}, t) &= \delta(t - \tau(\mathbf{r}, \mathbf{r}_F)) \\ G_p(\mathbf{r}_o, \mathbf{r}, t) &= (4\pi |\mathbf{r}_o - \mathbf{r}|)^{-1} \delta(t - |\mathbf{r}_o - \mathbf{r}|/c) \end{aligned} \quad (2.3)$$

therefore

$$G_E(\mathbf{r}_o, \mathbf{r}_F, \mathbf{r}, t) = (4\pi |\mathbf{r}_o - \mathbf{r}|)^{-1} \delta(t - (|\mathbf{r}_o - \mathbf{r}| - |\mathbf{r}_F - \mathbf{r}|)/c - R/c) \quad (2.4)$$

Let the UWB impulse defined by  $p(t)$  be radiated by the focused planar array. The wave  $s(\mathbf{r}_o, \mathbf{r}_F, t)$  arriving at the observation point  $\mathbf{r}_o$  is the integral of the UWB pulses radiated by the elements of the focused planar array,

$$\begin{aligned} s(\mathbf{r}_o, \mathbf{r}_F, t) &= \int_{\mathbf{r}} w(\mathbf{r}) \cdot G_E(\mathbf{r}_o, \mathbf{r}_F, \mathbf{r}, t) * p(t) d\mathbf{r} \\ &= \int_{\mathbf{r}} w(\mathbf{r}) \cdot (4\pi |\mathbf{r}_o - \mathbf{r}|)^{-1} \cdot p(t - (|\mathbf{r}_o - \mathbf{r}| - |\mathbf{r}_F - \mathbf{r}|)/c - R/c) d\mathbf{r} \end{aligned} \quad (2.5)$$

By (2.5), the focused waveform at arbitrary observation point over the entire space and time can be estimated. Here we assume a generalized Gaussian pulse (GGP) to be radiated by the focused square array [9]

$$p(t) = E_0 \sum_{k=0}^1 I_k \exp\{-a_k [(t - t_0)/\Delta T]^2\} \quad (2.6)$$

where coefficients  $I_k$  and  $a_k$  are defined as follows

$$I_0 = 1/(1 - \alpha), \quad I_1 = -\alpha/(1 - \alpha), \quad \alpha \neq 1 \quad (2.7)$$

$$a_0 = 4\pi, \quad a_1 = 4\pi\alpha^2 \quad (2.8)$$

Within (2.6),  $E_0$  is the peak amplitude at the time  $t = t_0$ ,  $\Delta T$  is a nominal duration, and  $\alpha$  represents a scaling parameter that controls the shape of the power spectrum density of the pulse. The GGP signal is a convenient signal model to represent a physical realizable UWB electromagnetic impulse whose spectrum is free from dc component.

The radiated energy contained in the wave field at observation point  $\mathbf{r}_o$  is estimated by the time-domain integrals,

$$E(\mathbf{r}_o, \mathbf{r}_F) = \int_0^{+\infty} [s(\mathbf{r}_o, \mathbf{r}_F, t)]^2 dt \quad (2.9)$$

and the energy pattern of the focused array is defined by the ratio

$$Er(\mathbf{r}_o, \mathbf{r}_F) = \frac{E(\mathbf{r}_o, \mathbf{r}_F)}{E(\mathbf{r}_F, \mathbf{r}_F)} \quad (2.10)$$

where  $E(\mathbf{r}_F, \mathbf{r}_F)$  represents the maximum wave field energy concentrated at the focal point by the array aperture.

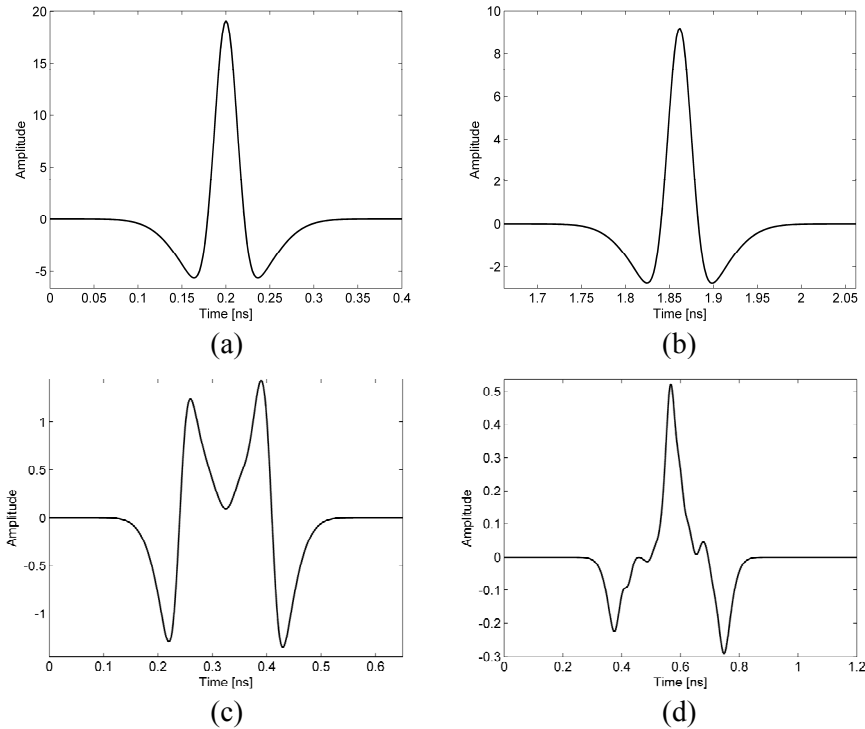


Figure 2.2 Time variation of the wave field  $s(\mathbf{r}_o, \mathbf{r}_F, t)$  at different observation points. (a) Waveform at the focal point  $(0, 20\lambda_c, 0)$ , (b) waveform along the range axis behind the focal point  $(0, 40\lambda_c, 0)$ , (c) waveform at  $(8\lambda_c, 20\lambda_c, 0)$ , (d) waveform at  $(10\lambda_c, 20\lambda_c, 10\lambda_c)$ .

The example of waveform  $s(\mathbf{r}_o, \mathbf{r}_F, t)$  given in (2.5) is illustrated in Figure 2.2. Signals for observation points on the array axis and off the array axis are plotted. The figures are calculated for a focused uniform aperture array with  $11 \times 11$  elements,  $\lambda_c/2$  element spacing, and focusing distance of  $20\lambda_c$ . The radiated UWB impulse from each array element is the GGP signal given in (2.6) with normalized duration  $\Delta T = 0.2\text{ns}$  and scaling factor  $\alpha = 3$ . As observed in Figure 2.2, a focused wave field having the exact shape as that of the radiated impulse but with larger peak amplitude is generated at the focal point on the array axis. Almost identical waveform is also generated at position behind the focal point along the array axis with decreased amplitude. At any other observation point off the axis, the generated wave field is out-of-focus and distorted with small amplitude of response.

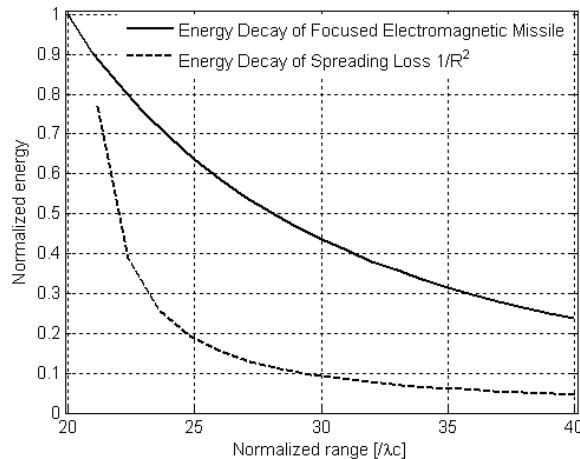


Figure 2.3 Comparison of energy decay between focused aperture array with  $11 \times 11$  elements, radiating GGP impulse with  $\Delta T = 0.2\text{ns}$ , and scaling factor  $\alpha = 3$ , and spreading loss ( $1/R^2$ ). The plot is computed for focal point at  $(0, 20\lambda_c, 0)$ , and element spacing of  $\lambda_c/2$  with  $f_c = 12\text{GHz}$ .

The energy pattern of the same focused aperture array calculated by (2.10) is further illustrated in Figure 2.3. On the array axis, the focused wave  $s(\mathbf{r}_o, \mathbf{r}_F, t)$  has the characteristics of an UWB electromagnetic missile [10-12] whose energy is maximum at the focal point  $(0, 20\lambda_c, 0)$  and decays in a fashion much slower than  $1/R^2$  as the wave field propagates away from the focal point of the focused ultra-wideband aperture array.

## 2.2.2 Imaging with synthetic aperture radar

In the sense of imaging with synthetic aperture radar (SAR) or array with sequential operation of identical transceiver pairs, a process of illumination, scattering, reception, and focusing is followed in order to form a map of the electromagnetic scattering coefficient of an unknown target. Instead of generating focused beam in space and time, each transceiver pair (or one antenna operating in monostatic mode) transmits an electromagnetic impulse and receives the reflected or scattered waves from the target. The collected data set is processed by introducing time-delays in each received signal. Such focusing is performed throughout the entire image space adaptively. A focused signal and high energy response appears when the target position coincides with the focal point. By contrast, the signals would interact destructively at positions outside the target space, and result in a low energy response.

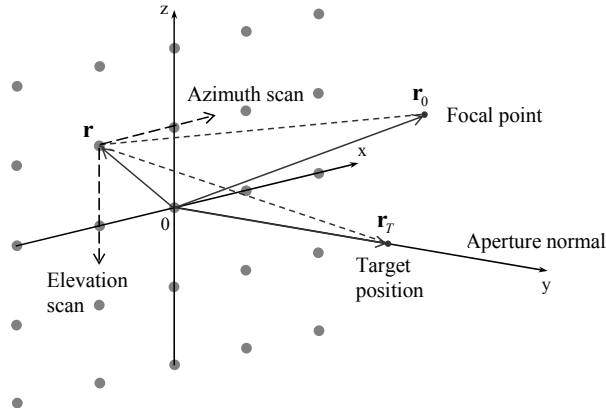


Figure 2.4 Geometry of two-dimensional synthetic aperture radar imaging with  $N$  scanning position or transceivers  $\mathbf{r}$  distributed in the transverse  $xz$ -plane with distribution function  $w(\mathbf{r})$ .

The SAR imaging geometry is illustrated in Figure 2.4. We start with the elementary Green's function  $G_E(\mathbf{r}_T, \mathbf{r}, t)$  of each transceiver pair that can be expressed by the two-way propagation between the target  $\mathbf{r}_T$  and transceiver  $\mathbf{r}$

$$\begin{aligned} G_E(\mathbf{r}_T, \mathbf{r}, t) &= (4\pi|\mathbf{r}_T - \mathbf{r}|)^{-1} \delta(t - |\mathbf{r}_T - \mathbf{r}|/c) * (4\pi|\mathbf{r}_T - \mathbf{r}|)^{-1} \delta(t - |\mathbf{r}_T - \mathbf{r}|/c) \\ &= (16\pi^2|\mathbf{r}_T - \mathbf{r}|^2)^{-1} \delta(t - 2|\mathbf{r}_T - \mathbf{r}|/c) \end{aligned} \quad (2.11)$$

The signal received at the transceiver  $\mathbf{r}$  due to the presence of a distributed target space  $o(\mathbf{r}_T)$  can be expressed as

$$u(\mathbf{r}, t) = \int_{\mathbf{r}_T} G_E(\mathbf{r}_T, \mathbf{r}, t) \cdot o(\mathbf{r}_T) * p(t) d\mathbf{r}_T \quad (2.12)$$

where  $p(t)$  denotes the radiated impulse signal from the transceiver. After collecting the signal over the entire aperture, the time-domain output or image at focused point  $\mathbf{r}_0$  is formulated by combining the signals  $u(\mathbf{r}, t)$  collected at each point within the aperture  $\{\mathbf{r}\}$  according to the defined focusing rule  $\Gamma$

$$I(\mathbf{r}_0, t) = \int_{\mathbf{r}} w(\mathbf{r}) \cdot u(\mathbf{r}, \Gamma(\mathbf{r}_0, \mathbf{r}, t)) d\mathbf{r} \quad (2.13)$$

The image  $I(\mathbf{r}_0, t)$  represents the summation of spherical projections of the object space. The focusing rule  $\Gamma$  defines the beamforming system with focal points scanning through the space  $\mathbf{r}_0$

$$\Gamma(\mathbf{r}_0, \mathbf{r}, t) = t + \frac{2|\mathbf{r}_0 - \mathbf{r}|}{c} \quad (2.14)$$

Substitute (2.12) into (2.13), we can express the image explicitly in terms of the target object

$$\begin{aligned} I(\mathbf{r}_0, t) &= \int_{\mathbf{r}_T} \int_{\mathbf{r}} w(\mathbf{r}) \cdot G_E(\mathbf{r}_T, \mathbf{r}, \Gamma(\mathbf{r}_0, \mathbf{r}, t)) \cdot o(\mathbf{r}_T) * p(t) d\mathbf{r} d\mathbf{r}_T \\ &= \int_{\mathbf{r}_T} PSF(\mathbf{r}_0, \mathbf{r}_T, t) \cdot o(\mathbf{r}_T) d\mathbf{r}_T \end{aligned} \quad (2.15)$$

where the point spread function (PSF) over the space and time of the aperture can be formulated as

$$\begin{aligned} PSF(\mathbf{r}_0, \mathbf{r}_T, t) &= \int_{\mathbf{r}} w(\mathbf{r}) \cdot G_E(\mathbf{r}_T, \mathbf{r}, \Gamma(\mathbf{r}_0, \mathbf{r}, t)) * p(t) d\mathbf{r} \\ &= \int_{\mathbf{r}} w(\mathbf{r}) \cdot (16\pi^2 |\mathbf{r} - \mathbf{r}_T|^2)^{-1} p(t - 2(|\mathbf{r}_T - \mathbf{r}| - |\mathbf{r}_0 - \mathbf{r}|)/c) d\mathbf{r} \end{aligned} \quad (2.16)$$

It is obvious that the PSF is a spatial variant function of both target location  $\mathbf{r}_T$  and scanning position  $\mathbf{r}_0$ . We can also foresee from the expression (2.15) that PSF alone does not determine the imaging quality. The object distribution  $o(\mathbf{r}_T)$  also has influence on the resulting image and can degrade the dynamic range of the imaging system if the quality of PSF is less than adequate. Despite the differences of spreading loss factor, comparison of the formulations in (2.5) and (2.16) shows strong correlation between the electromagnetic field of a focused aperture array and the PSF of synthetic aperture radar. The relation between one-way aperture array and SAR can be explained by the concept of exploding reflector model (ERM), under which the wave field is assumed to start expanding from the target at time zero with half of the actual propagation speed  $v = c/2$ . Within the frame of ERM, the two-way synthetic aperture with co-located transceiver pairs can be seen as one-way array with aperture size twice as large relative to the corresponding halved wavelength  $\lambda_{ERM} = v/f = \lambda/2$ .

Although the space-time formulation of PSF of synthetic aperture for imaging is equivalent to the electromagnetic missile generated by a one-way focused aperture

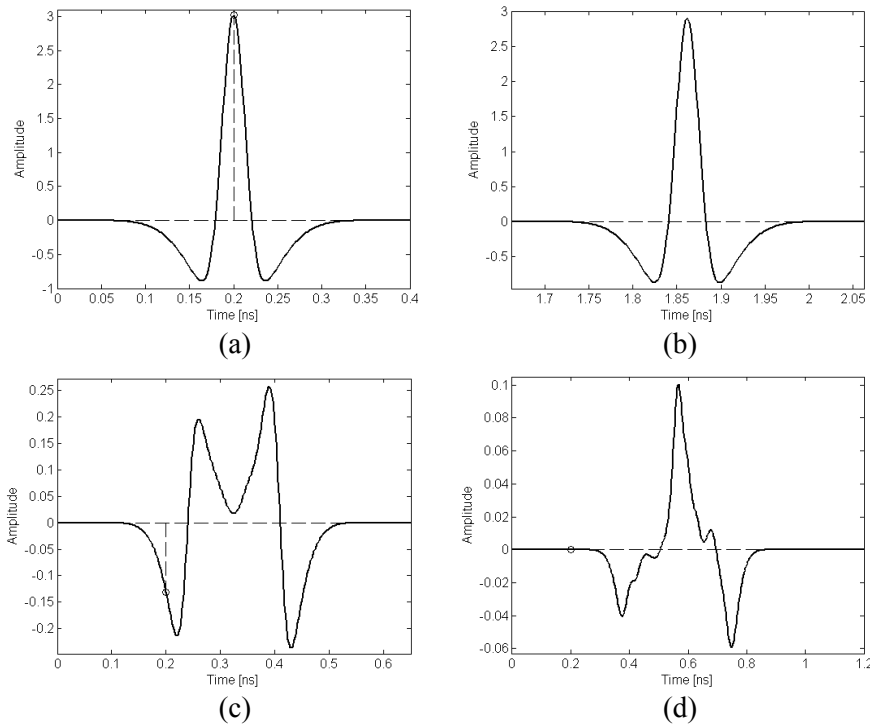


Figure 2.5 Time variation of the wave field  $PSF(\mathbf{r}_0, \mathbf{r}_T, t)$  at different focal points and scattering coefficient taken at reference time  $t_{ref}$ . (a) Waveform at the target location  $(0, 20\lambda_c, 0)$ , (b) waveform along the range axis behind the target  $(0, 40\lambda_c, 0)$ , (c) waveform at  $(8\lambda_c, 20\lambda_c, 0)$ , (d) waveform at  $(10\lambda_c, 20\lambda_c, 10\lambda_c)$ .

array, its dependence on time is eliminated in order to obtain the scattering coefficient which is only a spatial variant function

$$PSF(\mathbf{r}_0, \mathbf{r}_T) = \int_{\mathbf{r}} w(\mathbf{r}) \cdot (16\pi^2 |\mathbf{r} - \mathbf{r}_T|^2)^{-1} p(t - 2(|\mathbf{r}_T - \mathbf{r}| - |\mathbf{r}_0 - \mathbf{r}|)/c) d\mathbf{r} |_{t=t_{ref}} \quad (2.17)$$

where PSF is taken as the value at the chosen reference time  $t_{ref}$ . In the case of GGP signal in (2.6), the reference time corresponds with the time when the impulse reaches its peak value at  $t_0$ . The example of waveform  $PSF(\mathbf{r}_0, \mathbf{r}_T, t)$  given in (2.16) is illustrated in Figure 2.5 under the same GGP signal and aperture function used in Figure 2.2. We can observe almost identical change of waveforms as the focused aperture except the amplitudes. The range profile of PSF of the same SAR aperture along the aperture axis is shown in Figure 2.6. Comparing with Figure 2.3, the PSF

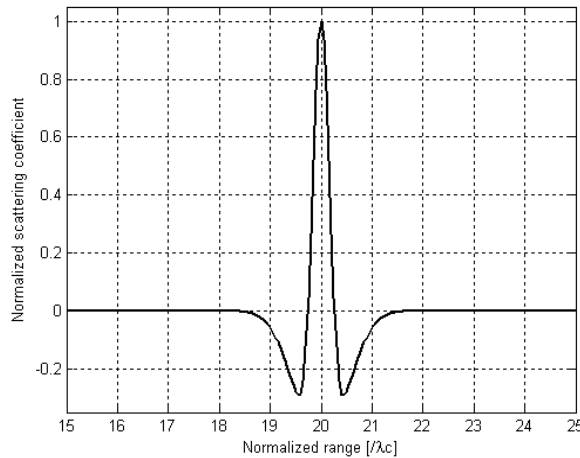


Figure 2.6 range profile of PSF from SAR aperture with  $11 \times 11$  elements, illuminating a single scatter at  $(0, 20\lambda_c, 0)$  using GGP impulse with  $\Delta T = 0.2\text{ns}$ , and scaling factor of  $\alpha = 3$ . The plot is computed for element spacing of  $\lambda_c/2$  with  $f_c = 12\text{GHz}$ .

shows much faster delay before and after the target location indicating a single scatterer at its correct location.

## 2.3 Interference region in the near-field and beyond

Conventional narrowband array analysis is based on constant spatial interference of monochromatic waves. By contrast, the short duration of the UWB pulse does not allow for such interfering condition in a complete space. During the beamforming process, the pulses from all array elements interfere only around the focusing location. Therefore, narrowband theory applies only in this region. It is referred as interference region (IR) [7]. Outside this region, both grating lobe and sidelobe of an UWB array are not formed due to the absence of interference.

Let us first determine the maximal interference region of an UWB array in near-field. Figure 2.7 illustrates the interference of pulses transmitted from a transmitting aperture. One-way linear array is considered here for simplicity. The focal point is assumed to be located at boreside at range  $R$ . The pulse duration is  $T$ , and the wave field propagates within free-space at the speed of light  $c$ . Among all array elements the maximal interference region is created by pulses radiated from the closest element and its nearest element with assumed spacing  $\bar{d}$ . Such interference region is

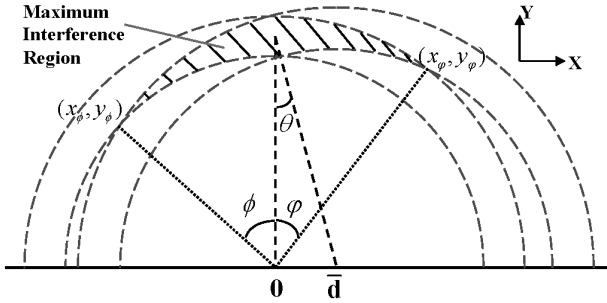


Figure 2.7 Illustration of the maximum interference region (IR) of a one-way ultra-wideband aperture/array

marked by two interception points,  $(x_\phi, y_\phi)$  and  $(x_\psi, y_\psi)$ , located at both sides of the focus point or mainlobe. These two points can be estimated as the interceptions between the inner and outer rims of the radiated pulses

$$\begin{cases} x_\phi = -\frac{cT}{2\bar{d}} \left[ R + \sqrt{\bar{d}^2 + R^2} \right] = -\frac{cT}{2} \left[ \frac{R}{\bar{d}} + \sqrt{1 + (\frac{R}{\bar{d}})^2} \right] \\ y_\phi = \left[ (R - cT/2)^2 - x_\phi^2 \right]^{\frac{1}{2}} \end{cases} \quad (2.18)$$

$$\begin{cases} x_\psi = \frac{cT}{2\bar{d}} \left[ R + \sqrt{\bar{d}^2 + R^2} \right] = \frac{cT}{2} \left[ \frac{R}{\bar{d}} + \sqrt{1 + (\frac{R}{\bar{d}})^2} \right] \\ y_\psi = \left[ (R + cT/2)^2 - x_\psi^2 \right]^{\frac{1}{2}} \end{cases} \quad (2.19)$$

The locations of these two points mark the maximal interference region of the array in the near-field. Outside this region, the pulses radiated from different array elements avoid interference with each other, preventing grating lobes at higher angle. It's also obvious from equations (2.18), (2.19) that the larger the spacing  $\bar{d}$ , the shorter the impulse  $T$ , the closer the target  $R$ , the smaller the interference region will be. To make a straight forward impression, assuming an impulse with duration of 250 ps, for a target located at 0.5 m from the aperture, the minimum spacing  $\bar{d}$  has to be 0.25 m in order to have an interference region of about 0.4 m wide. This reminds us that although the wide bandwidth provides another dimension where the array's leakage energy can be redirected, the size of its interference region is still not

as small as we would like it to be. In the near-field of a UWB array, both impulse and narrowband analysis has to be considered.

In far-field, we are able to apply the Fraunhofer approximation. Under the assumptions that the range between the focal plane and the aperture is much greater than the size of the aperture  $R \gg \bar{d}$ , then the relation  $\sqrt{\bar{d}^2 + R^2} \approx R + \bar{d} \cdot \sin \theta$  applies. By further assuming that the range distance is also much greater than the pulse length,  $R \gg cT$ , the expression for the interference region can be simplified to

$$\begin{aligned}\sin \phi &= \frac{|x_\phi|}{R - cT/2} = \frac{cT}{\bar{d}} \cdot \frac{R + \bar{d} \sin \theta/2}{R - cT/2} \approx \frac{cT}{\bar{d}} \\ \sin \varphi &= \frac{|x_\varphi|}{R + cT/2} = \frac{cT}{\bar{d}} \cdot \frac{R + \bar{d} \sin \theta/2}{R + cT/2} \approx \frac{cT}{\bar{d}}\end{aligned}\quad (2.20)$$

Equation (2.20) indicates that the maximum interference angle at far-field is determined only by the pulse duration and minimum element spacing. If the average spacing is smaller than the pulse length, the wave field from the elements could interfere across the entire visible image space. On the other hand, it also gives an indication that if the array spacing is much greater than the impulse  $\bar{d} \gg cT$ , the interference region can be minimized enabling the possibility of an ultra-sparse array without incurring grating lobe problems. However, one must realize that both the level and location of grating lobes are simultaneously influenced by the sparsity and spatial sampling of the aperture/array.

Before discussing the spatial sampling criteria, we intend to first explore whether it is possible to constrain the IR as small as possible while still satisfying the narrowband requirement. In order to avoid grating lobes, the average antenna spacing  $\bar{d}$  must be no further than the half wavelength  $\lambda_{\min}/2$  of the maximum frequency  $f_{\max}$ . Assuming the spacing  $\bar{d}$  equals to  $\alpha$  times of the pulse length  $cT$  at the same time

$$\bar{d} = \alpha \cdot cT = \alpha \cdot \frac{c}{B} \leq \frac{\lambda_{\min}}{2} = \frac{c}{2f_{\max}} \quad (2.21)$$

where  $B$  represents the absolute bandwidth, and  $\lambda_{\min}$  is the wavelength at the maximum frequency  $f_{\max}$ . It leads to the fact that

$$\alpha \leq \frac{B}{2f_{\max}} = \frac{f_{\max} - f_{\min}}{2f_{\max}} \leq 0.5 \quad (2.22)$$

which leads to  $\bar{d} \leq cT$ . As indicated by equation (2.20), under such condition the elements will interfere across the visible space, therefore creating no spaces without interference among the array elements. Same story holds if the array is ultra-sparse and the average spacing exceeds the pulse length. In this case, the element spacing will be inevitably larger than the half wavelength of the maximum frequency. Therefore, the ideal narrowband and wideband spatial sampling requirements can not be satisfied at the same time. To reduce costs while maintaining its beam steering capabilities, we must find the point exceeding which wide-band properties can have the major impact on the aperture focusing performance. This threshold is not the relative relation between element spacing and pulse length.

## 2.4 Spatial sampling criteria

The spatial sampling of the aperture influences its beam steering capability in a large extent. Under monochromatic condition, Nyquist criteria must be satisfied in order to obtain a successful discretization. Specifically, the phase shift from one spatial sampling point to the next must be less than  $\pi$  rad. For a distributed target located very close to the aperture, the largest phase shift occurs at the farthest opposite edge of the target and aperture sampling points as indicated in Figure 2.8.

Therefore, the relation has to be satisfied as

$$2k|r_1 - r_2| \leq \pi \quad (2.23)$$

where  $k = 2\pi/\lambda$  denotes the wavenumber in free-space, and the difference of propagation distance is approximated as

$$|r_1 - r_2| \approx \bar{d} \cdot \frac{(L + D)/2}{\sqrt{(L + D)^2/4 + R^2}} \quad (2.24)$$

where  $L$  is the size of the aperture,  $D$  denotes the width of the target, and  $R$  is the range distance of the target. Substituting (2.24) in (2.23), the spatial separation  $\bar{d}$  at the edge of aperture must satisfy

$$\bar{d} \leq \frac{\lambda}{2} \frac{\sqrt{(L + D)^2/4 + R^2}}{L + D} \quad (2.25)$$

It is worth noting that (2.25) is derived based on the model of two-way SAR configuration. Such criterion must be reached for the smallest wavelength over the entire frequency band of the system. The extreme case happens when the target is extremely close to the aperture. In this situation, the propagation distance between

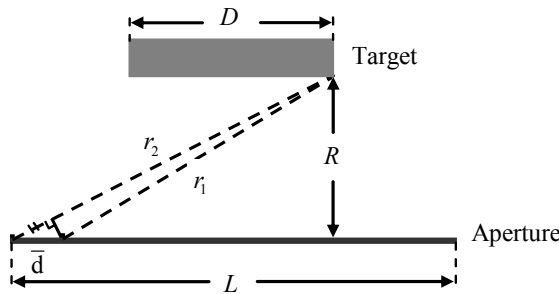


Figure 2.8 Illustration of Nyquist criteria for aperture spatial sampling

the two spatial sampling points approaches the separation between them, which leads to the most restrictive requirement of  $\bar{d} \leq \lambda/4$ . This is more than what is usually required because the target is often located at a moderate distance from the aperture and the antenna beamwidth is commonly less than  $180^\circ$ . Therefore, practical short-range imaging system can apply sampling intervals on the order of  $\lambda/2$ .

The Nyquist criterion poses a very demanding requirement for imaging system design. For example, to achieve centimeter resolution at 0.5 meter distance, the effective aperture must be at least 50 times of a wavelength along both azimuth and elevation. In order to reach the monochromatic sampling requirement, the 2-D aperture needs to be filled with at least  $101 \times 101$  (10201) elements. Unfortunately, fabrication of such dense array and its beamforming electronics is almost prohibitive using current microwave technology. The measurement time needed to scan the aperture also makes it unrealistic for real-time operation.

Utilization of ultra-wideband transmission is an effective approach to ease the requirement for spatial sampling. The extremely short duration of the emitted UWB impulse means that spatial interference of component monochromatic waves can be limited within a region around the focusing location. It is named interference region (IR) while the area outside is referred as NIR. In the NIR, grating lobes caused by sparsity of the aperture can not be formed due to the absence of interference.

Assuming a wideband array/aperture with a pulse duration of  $T$ , the maximum interference region can be approximated by the angle  $\phi$  expressed as

$$\phi = \arcsin \frac{cT}{\bar{d}} \quad (2.26)$$

where  $\bar{d}$  represents the average spacing within the aperture. Meanwhile, based on the narrowband theory [1], for a continuous wave 2-D aperture with a uniform spacing  $\bar{d}$ , replications of the mainlobe, known as grating lobes appear at directions

$$\begin{aligned} u &= u_0 \pm m\lambda/\bar{d} \\ v &= v_0 \pm n\lambda/\bar{d} \quad m, n = 1, 2, \dots \end{aligned} \quad (2.27)$$

where  $u = \sin \theta \cos \phi$  and  $v = \sin \theta \sin \phi$  are the directions along the cross-range with  $(\theta, \phi)$  as the steering angle. It is indicated by (2.27) that the closest grating lobe of a 2-D aperture with uniform spacing  $\bar{d}$ , appears along the two principle planes at the angle  $\psi$  to the mainlobe

$$\psi = \arcsin \frac{\lambda}{\bar{d}} \quad (2.28)$$

and grating lobes can avoided if  $\lambda/\bar{d} \geq 2$ . The finite width of IR allows to suppress the closest grating lobe to the main beam if  $\psi \geq \phi$ , therefore

$$\frac{\lambda}{\bar{d}} \geq \frac{cT}{\bar{d}} \Rightarrow \frac{c}{f} \geq \frac{c}{B} \Rightarrow \frac{B}{f} \geq 1 \quad (2.29)$$

As we can see, the influence of spatial sampling vanishes during the derivation. Instead, bandwidth takes control of the aperture property when the absolute bandwidth is greater than certain frequency component within the spectrum. With more than 100% fractional bandwidth, where  $B \geq f_c$ , majority of grating lobes raised by the spectrum lower than the center frequency can be isolated outside the interference region. To ensure the elimination of the entire grating plateau, one must go beyond the condition where the bandwidth is greater than the highest frequency  $B \geq f_{\max}$  with 200% fractional bandwidth. The importance of this result is that the cross-range resolution of an UWB array can be improved by increasing the array/aperture size without jeopardizing the array pattern. This provides a valid tool to solve the dilemma between the cross-range resolution and array patterns (more precisely, the grating lobe level). Because of such wideband property, very high cross-resolution can be achieved by a rather coarse spatial sampling and/or much fewer antenna elements, which can significantly reduce data acquisition time, complexity of the front-end, mutual coupling between antennas, and computation load for imaging.

## 2.5 Sidelobe level of UWB aperture

Under the ideal condition where all grating plateau have been eliminated, the mainlobe to sidelobe ratio can be simply estimated by the ideal sidelobe level (ISL) defined as

$$ISL = -20 \log_{10} N \quad (2.30)$$

where  $N$  is the total number of sampling points or array elements within the aperture. It indicates the maximum sidelobe level in the resulting image of a one-dimensional (1-D) sparse aperture. For a two-dimensional aperture, the calculation of  $N$  depends on the aperture sampling, specifically redundancy and shadowing along each rotating cutting plane. This problem will be addressed in Chapter 4. The ISL can be used as the starting point to determine the minimum number of elements needed in sparse wideband array for the oriented applications.

Due to both spreading loss and limited beamwidth of the antenna, the achievable ISL in the near field is generally worse than the ideal value. By taking into considering the near-field spreading loss between the aperture and focal point, the ideal near-field sidelobe level (INSL) is estimated as

$$INSL = -20 \log_{10} R \sum_{i=1}^N \frac{1}{\sqrt{L_i^2 + R^2}} = -20 \log_{10} \sum_{i=1}^N \left( \sqrt{1 + (L_i / R)^2} \right)^{-1} \quad (2.31)$$

where  $L_i$  represent the position of the  $i^{th}$  sampling point or array element within the aperture. Note that expression (2.31) is purely for one-way transmitting or receiving aperture. For a two-way transmit/receive array/aperture, the expression is changed to

$$INSL_{TR} = -20 \log_{10} \sum_{i=1}^N \left( 1 + (L_i / R)^2 \right)^{-1} \quad (2.32)$$

As we can see from the formulations in (2.31) and (2.32), the ratio between aperture size and focal distance,  $L/R$ , largely influences the sidelobe level of a near-field aperture/array. The INSL approaches the ISL when the focal range is greater than the size of aperture.

Without the influence of grating lobes, the estimation of sidelobe level is the most important factor to determine the minimum number of elements or samples needed along the two principle planes of the aperture/array based on the required dynamic range from specific application. For example, considering concealed weapon detection with a standing person as the target with 0.5 m width and 1.8 m height at 0.5 m range distance, the Nyquist criteria calculated by (2.25) indicate the sampling steps of  $0.3 \lambda_{min}$  and  $0.25 \lambda_{min}$  along the azimuth and elevation directions for a narrowband system in order to avoid grating lobes. By contrast, with ultra-wideband, only necessary number of samples or elements shall be considered for the required dynamic range. We require 30 dB ISL for the azimuth direction, and a higher 40 dB ISL for elevation due to the larger dimension of the body in the direction. This leads to 32 and 100 samples or elements along the two principle planes. The required

sampling rate from an UWB system is considerably lower than the one required by Nyquist criteria.

## 2.6 Resolution and beam pattern

For detection, reconstruction, and classification, imaging system must be able to resolve objects in both down-range and cross-range directions. The down-range resolution is determined by the bandwidth of the system and is expressed as

$$\delta_r = \frac{c}{2B} \quad (2.33)$$

where  $B$  is the frequency bandwidth at -10 dB level. With the bandwidth of 10 GHz, a range resolution 1.5 cm is obtained. The down-range resolution is independent of the range to the target.

Traditionally, cross-range resolution is achieved by illuminating the scene from different angles. This requires the use of high-gain directional antenna, which will become too bulky for low frequencies. Furthermore, the need of slow mechanical scan makes it impractical. Another option is to use synthetic aperture radar (SAR). By moving the antenna over a large distance, the cross-range resolution can be obtained by the synthesized large aperture. This method asks for accurate positioning of sensor traces as well as relatively long data acquisition time. It will become a problem for tracing motions in real-time. Then we come to the choice of using antenna array with multiple transmitters and receivers, which provides acceptable data acquisition time for demanding applications.

The cross-range resolution can be determined by the dimension and sampling of the aperture/array, the potential range distance of the target, and the operational frequency band. The definition of cross-range resolution  $\delta_{cr}$  based on narrowband analysis is commonly used to determine the size  $L$  and center frequency of the array

$$\delta_{cr} = \frac{\lambda_c \cdot R}{L} \quad (2.34)$$

The effect of bandwidth is commonly ignored because the influence of available bandwidth in long range imaging is very limited. Here we will discuss under what condition the bandwidth start to influence the cross-range resolution. Figure 2.9 illustrates the interfering cell of the IR of a one-way wideband aperture. The width of IR for an aperture of size  $L$  can be estimated as the interception of pulses and be expressed as

$$\eta = cT \frac{\sqrt{(L/2)^2 + R^2}}{L/2} = \frac{cT}{\sin \theta} \quad (2.35)$$

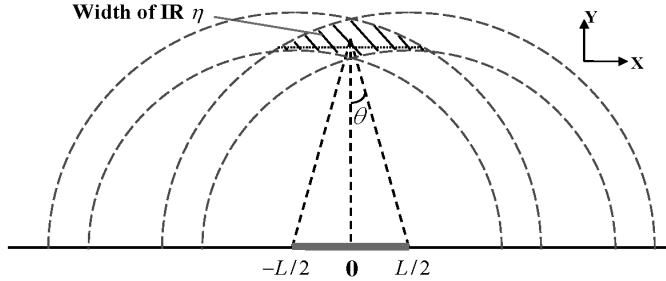


Figure 2.9 Illustration of the width of interference region of a one-way ultra-wideband aperture

The minimal width of IR is determined by the pulse length and the angle of view by the aperture. Within the interference region, narrowband analysis dominates the properties of aperture, including the cross-range resolution. However, if the width of IR starts to approach or even becomes smaller than the resolution cell defined by the narrowband properties, the pulse duration shall begin to play a role in the image resolution. Since the narrowband cross-range resolution definition is based on far-field assumptions, we make the assumption for the impulse formation by assuming that  $R \gg L$ . Hence

$$\eta = cT \frac{\sqrt{(L/2)^2 + R^2}}{L/2} \approx cT \left( \frac{R}{L/2} + \sin \theta \right) \approx cT \frac{2R}{L} \quad (2.36)$$

which suggests the width is inverse proportional to the size of aperture. Therefore, we are able to define the 3 dB resolution of a wideband aperture as

$$\delta_{cr}^{UWB} = \min \left[ \frac{c}{0.7079 \cdot B}, \lambda_c \right] \cdot \frac{R}{L} \quad (2.37)$$

Equation (2.37) indicates that the bandwidth has to be the order of the center frequencies in order to start its influence on the cross-range resolution. Therefore, the rule of thumb for design is that the size of aperture must be similar to the distance of the potential target in order to obtain a level of angular resolution comparable to the utilized electromagnetic wavelength.

In contrast to its effect on cross-range resolution, bandwidth plays an important role in controlling the array pattern. The array aperture is electrically scaled over the spectrum of frequencies. This causes side and grating lobes to appear at different

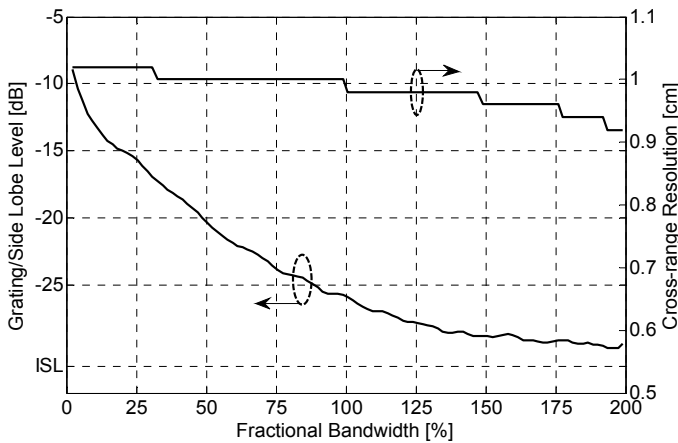


Figure 2.10 Influence of fractional bandwidth on the grating/side lobe level and cross-range resolution under the same center frequency. The aperture size is  $100 \lambda_c$  with  $2.5 \lambda_c$  element spacing. Results are obtained by full-wave numerical simulation.

directions while mainlobe always remains at the same focal point. Therefore, after wide-bandwidth pattern synthesis the level of side and grating lobes relative to the mainlobe becomes smeared off, improving the array pattern in comparison to sparse narrowband array. Figure 2.10 illustrates the change of cross-range resolution and grating /side lobe level over increasing bandwidth with center frequency and aperture size fixed while the focal point is within the near-field of the aperture. The results are obtained by numerical simulation using frequency-domain synthesize and standard impulse beam steering procedure. The result indicates that bandwidth improves the cross-range resolution in a very limited extent. On the other hand, the level of grating lobe decreases significantly with increasing fractional bandwidth. The speed of descending gradually reduces when approaching the maximum limit. About 80% of grating lobe level reduction is performed at the 100% fractional bandwidth mark. After achieving the level of 150%, the fractional bandwidth has less impact on the beam pattern. The minimal grating/side lobe level approaches the ISL level for corresponding array elements ( $N=41$ ).

## 2.7 Characteristics of sparse aperture array

The behaviors of wideband array pattern are investigated to demonstrate the influence of fractional bandwidth in terms of limiting the degradation of array focusing performance. Full-wave electromagnetic simulations are utilized. Numerical

models are implemented by the applied electromagnetic simulation tool FEKO which utilizes the method of moment (MoM) to solve the integral equations. In the models, Hertzian dipoles are used as transmit and receive antennas. The antennas are arranged in co-polar directions. The modeled data is focused within the near-field of the array aperture by digital beamforming, which is described in Chapter 6. Two-dimensional images are calculated and the maximum value along the range direction is taken to represent the beam pattern in the near-field. Therefore, the PSF defined in (2.17) is reduced to one-dimensional function of the cross-range as

$$PSF(x) = \max_y [PSF(x, y)] \quad (2.38)$$

In the following sections, several typical conditions of aperture array are discussed and analyzed.

### 2.7.1 Effect of center frequency

With same absolute bandwidth  $B$ , the sizes of both IR and NIR region controlled by the wideband properties remain the same while the central frequency  $f_c$  changes. Down-range resolution keeps the same along temporal domain. Within the interference region around the target, narrowband properties dominate the array performance. This means, as the wavelength  $\lambda_c$  decreases, the same physical size array aperture becomes electrically larger, also sparser. The cross-range resolution improves along with larger aperture size. After the array element spacing gradually exceeds the half wavelength, artifact appears and rises further with increasing grating plateau. The energy leakages also tend to stand closer to the mainlobe as the array becomes thinner. Outside the IR, no interference happens within the aperture, leading to the array pattern unchanged.

Figure 2.11(a) shows the change of array pattern with increasing center frequency under the condition that the average antenna spacing is less than the pulse length  $\bar{d} < cT$ . In this situation, we shall expect the narrowband properties to dominate the entire visible image space. As can be clearly seen, the simulation shows the exact same pattern behavior. For the  $0 \sim 10$  GHz band, the element spacing is close to the half wavelength, therefore exhibiting no grating lobes. After exceeding the tipping point, grating lobe starts to appear at high angle with acceptable level and gradually close in to the mainlobe with rising amplitude. Figure 2.11(b) shows the change of array pattern with increasing center frequency under the condition that the average antenna spacing is greater than the pulse length  $\bar{d} \gg cT$ . We can clearly observe the existence of both IR and NIR properties. The IR pattern behaves similar way as the previous situation. By contrast, the pattern remains unchanged with increasing frequency within the NIR region. It is important to note that the array pattern within

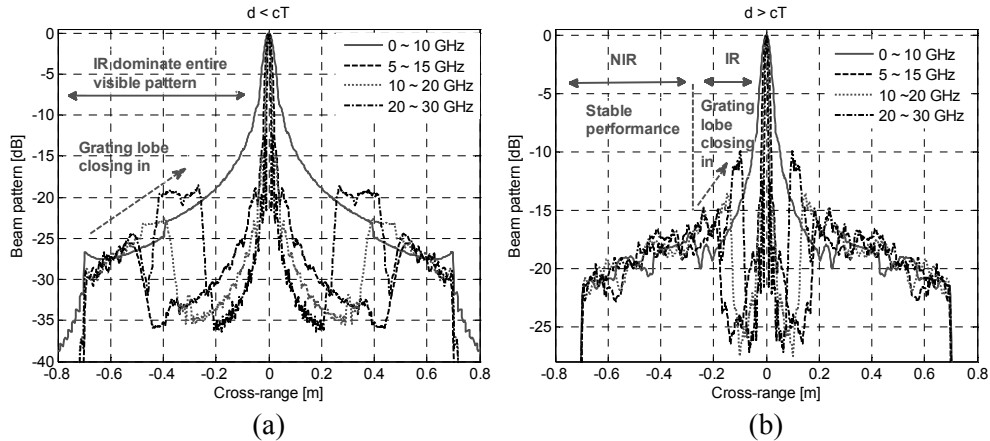


Figure 2.11 Change of array pattern with center frequency under the same bandwidth. Results are obtained assuming target at 0.5 m range, linear SAR aperture array with 0.6 m aperture and 10 GHz bandwidth. (a) Array with 2 cm antenna spacing where  $\bar{d} < cT$ , and (b) array with 6 cm antenna spacing where  $\bar{d} \gg cT$ .

NIR in Figure 2.11(b) is higher than Figure 2.11(a) due to the reduced number of array elements since the aperture size is kept unchanged.

### 2.7.2 Effect of fractional bandwidth

Following previous discussion, we analyze the influence of changing bandwidth under the same center frequency. We separate the analysis into conditions where the antenna spacing is larger or smaller than the half wavelength of center frequency. As the bandwidth increases, down-range resolution improves while cross-range resolution remains approximately unchanged for a planar aperture array. As we stated previously, enlarging bandwidth helps to reduce the interference within the IR, hence reducing any sidelobe or grating plateau. Under the condition that  $\bar{d} \leq \lambda_c / 2$ , the whole image space is within the IR region, therefore, the pattern improvement by bandwidth change is limited. In fact, we only observe a decrease of pattern level at the initial stage when the bandwidth increases from narrowband to wideband as shown in Figure 2.12(a). After certain level of bandwidth, the changes caused by bandwidth are negligible. For a super-sparse array when  $\bar{d} \gg \lambda_c / 2$ , the bandwidth places a much more significant impact on grating/side lobe reduction as shown in Figure 2.12(b). The grating/side lobe level of the array decreases over 15 dB after a 20 GHz increase of bandwidth, literally making the aperture array from useless to applicable.

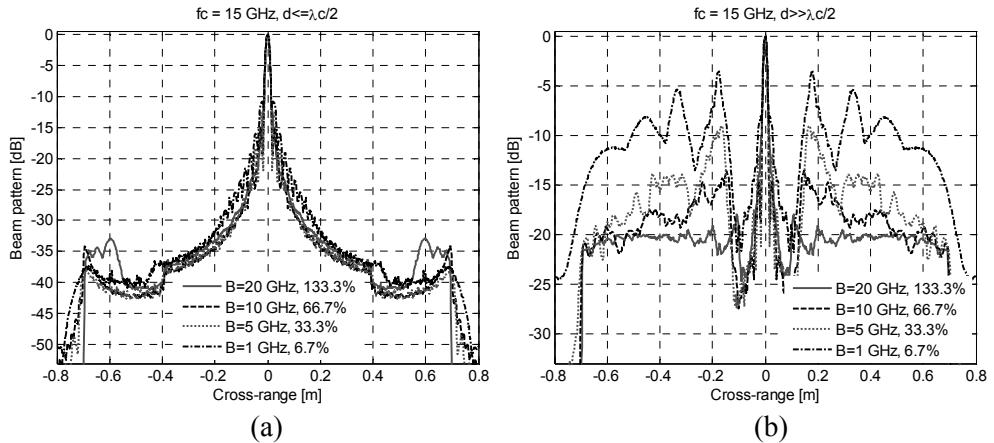


Figure 2.12 Change of array pattern with bandwidth under the same center frequency. Results are obtained assuming target at 0.5 m range, linear array with 0.6 m aperture and 15 GHz center frequency. (a) Array with 1 cm antenna spacing, and (b) array with 6 cm antenna spacing.

### 2.7.3 Effect of aperture size

Under the same circumstances, when the array expands, it becomes both physical and electrical larger and thinner. This improves the cross-range resolution as we can see in Figure 2.13. According to the narrowband analysis, the array pattern would degrade within the interference region. Meanwhile due to the increase of NIR region indicated by (2.20), the sidelobe level within NIR will approach the ideal sidelobe level (ISL) of a sparse UWB array as formulated in (2.30).

Figure 2.13(a) shows the array pattern under the condition where the fractional bandwidth is less than 100%. Because the bandwidth is not large enough, the pattern behaves mostly according to the narrowband properties within the visible image space. As the antenna spacing increases to four times of  $\lambda_e$ , the sidelobe level at high angle equals to the value we expect,  $ISL \approx -32.3$  dB.

Figure 2.13(b) demonstrates the array performances when it has a fractional bandwidth more than 100%. We can see that the array handles pattern degradation much better than its narrower bandwidth rival. The maximum sidelobe level only increases by 4 dB while the array grows to 8 times larger and sparser. The slight degrade of sidelobe level is caused by the near-field effect from the change of spreading loss over the aperture, and can be anticipated by the INSL defined in (2.31). The pattern is flat over the entire visible space outside the mainlobe. It is clear that the larger bandwidth improves the performances of sparse aperture array, and a

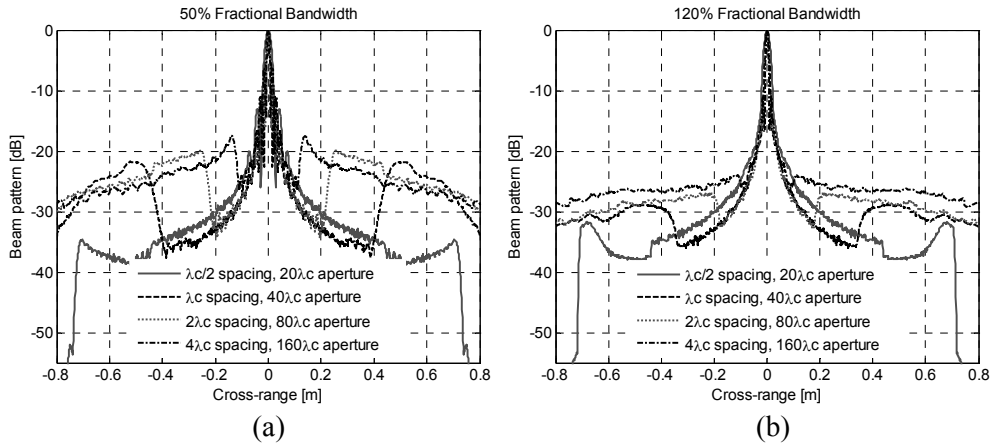


Figure 2.13 Effect of enlarging aperture on the beam pattern. (a) Array patterns obtained with 50% fractional bandwidth, and (b) Array patterns obtained with 120% fractional bandwidth. Results are obtained with focal point at  $20\lambda_c$  range distance at boreside with the same number of array elements ( $N=41$ ). Results are obtained by full-wave numerical simulation.

fractional bandwidth greater than 100% is necessary to really benefit from such unique UWB properties.

#### 2.7.4 Effect of number of elements within the aperture

With decreasing number of array elements within the frame of the same aperture size, two major factors are influencing the array performance. The first is the ideal sidelobe level, which defines the basic level of the array pattern in the NIR region. The ISL inevitably degrades along with decreasing element number. Therefore, we expect an increased sidelobe level along with such thinning procedure. The second important factor is the sparsity relative to the half wavelength. It is a narrowband property mainly influence in the IR region, causing the rise of grating plateau when the number of array elements decreases. While the ISL is rising without doubt, the degradation by the rising grating plateau can be regulated or minimized by larger fractional bandwidth.

This is what we attempt to demonstrate in Figure 2.14. In the first aperture array, the system fractional bandwidth is less than 100%. When the number of array elements reduces 10 times from 101 to 11, the grating plateau becomes higher and spatially closer to the mainlobe due to the deteriorating narrowband properties. By contrast, the grating lobe is much better managed in Figure 2.14(b) with much larger fractional bandwidth. Although the array pattern still rises as expected, the pattern

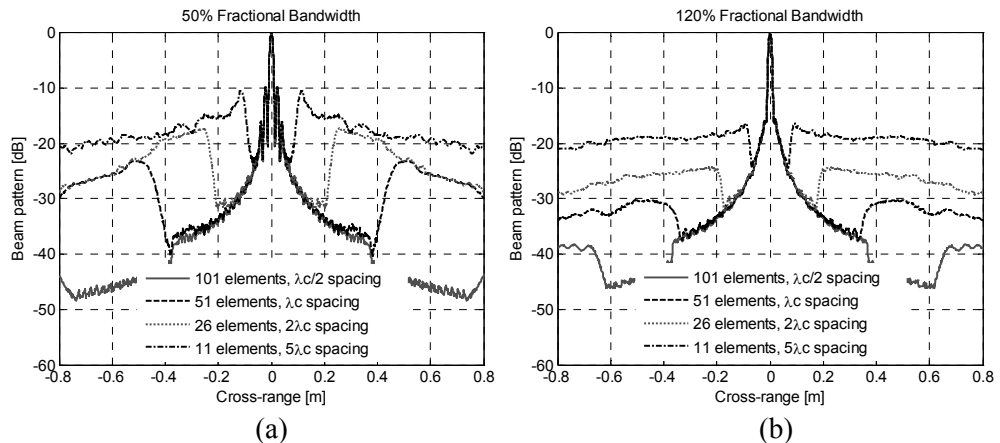


Figure 2.14 Effect of aperture thinning on the beam pattern. (a) Array patterns obtained with 50% fractional bandwidth, and (b) Array patterns obtained with 120% fractional bandwidth. Results are obtained with the same  $50\lambda_c$  aperture and focal point at  $20\lambda_c$  range distance at boreside. Results are obtained by full-wave numerical simulation.

appears to be much flatter than the previous case. If we compare Figure 2.14 (a) and (b) in parallel, we can clearly see that the mainlobes of the array with the same elements but different bandwidth are almost identical. What is different is the grating lobe which is regulated by the reduced interference outside the IR area by the greater fractional bandwidth in the second case.

## 2.8 Summary

This chapter has described and discussed the ultra-wideband focusing behavior with special focus on the characteristics in the near-field. The introduced analysis unifies the existing narrowband and impulse theories regarding sparse array and aperture thinning. Large bandwidth brings two sets of benefits to an imaging system. The first is the down-range resolution which provides the depth of view to the target image and revolving capability along the range direction. Certain level of absolute bandwidth is necessary in order to achieve the same level of resolution as the angular directions. The second benefit is directly related to sparse aperture array which is commonly preferred in order to reduce cost and complexity of the imaging system. A high fractional bandwidth ensures the isolation of grating lobe and the reduction of artifacts caused by the sparsity of aperture, therefore, achieving the same level of performance using simplified array aperture and electronics.

## References

- [1] B. D. Steinberg, *Principles of Aperture and Array Systems Design*, New York: Wiley, 1976.
- [2] O. T. Von Ramm, and S. W. Smith, "Beam steering with linear arrays," *IEEE Trans. Biomed. Eng.*, vol. BME-30, pp. 438-452, 1983.
- [3] F. Anderson, W. Christensen, L. Fullerton, B. Kortegaard, "Ultra-wideband beamforming in sparse arrays," *IEE Proceedings-H.*, vol. 138, pp. 342-346, Aug. 1991.
- [4] Vittorio Murino, Andrea Trucco , Alessandra Tesei, "Beam pattern formulation and analysis for wide-band beamforming systems using sparse arrays," *Signal Processing*, vol. 56, pp. 177–183, 1997.
- [5] M. G. M. Hussain, "Characteristics of ultra-wideband electromagnetic missiles generated by focused two-dimensional array," *Progr. Electromagn. Res., PIER* 49, pp. 143–159, 2004.
- [6] M. G. M. Hussain, and A. S. Al-Zayed, "Aperture-sparsity analysis of ultrawideband two-dimensional focused array," *IEEE Trans. Antennas Propagat.*, vol. 56, pp. 1908-1918, 2008.
- [7] J. L. Schwartz, B.D. Steinberg, "Ultrasparse, Ultrawideband Arrays," *IEEE Trans. Ultrason., Ferroelectr. Freq. Control*, vol. 45, pp. 376-393, Mar. 1998.
- [8] H. F. Harmuth, R. N. Boules, M. G. M. Hussain, *Electromagnetic Signals: Reflection, Focusing, Distortion, and Their Practical Applications*, Kluwer Academic/Plenum, New York, 1999.
- [9] M. G. M. Hussain, "Signal design for ultra-wideband radar and wireless communications," *Recent Advances in Simulation, Computational Methods and Soft Computing*, N. E. Mastorakis (ed.), WSEAS Press, 2002.
- [10] J. N. Brittingham, "Focus waves modes in homogeneous Maxwell's equations: Transverse electric mode," *J. Appl. Phys.*, vol. 54 (3), pp. 1179-1189, 1983.
- [11] T. T. Wu, "Electromagnetic missiles," *J. Appl. Phys.*, vol. 57 (7), pp. 2370-2373, 1985.
- [12] R. W. Ziolkowski, "Localized transmission of electromagnetic energy," *Phys. Rev. A*, vol. 39 (4), pp. 2005-2033, 1989.

## CHAPTER 3

# MULTIPLE-INPUT MULTIPLE-OUTPUT ARRAYS FOR REAL-APERTURE IMAGING

Multiple-input multiple-output (MIMO) array has generated significant attention and widespread interest in academia, industry, and government laboratories. MIMO array antenna is characterized by using multiple transmit antennas to emit probing fields (electromagnetic, ultrasound, etc) and by applying multiple antennas to receive the scattered or reflected wave field from the target. Like its role in wireless communications, MIMO array offers a new research paradigm for imaging applications. Comparing with a standard phase array, which transmits and receives with the same set of antenna elements, a MIMO array can apply different antennas and/or waveforms for simultaneous transmission and reception. This diversity and design freedom enable superior capabilities for imaging. Exploiting the potentials of such concept can result in enhanced resolution, clutter suppression, reduced date acquisition time, and improved target shape reconstruction.

Advantages of MIMO technology can be combined with large operational bandwidth to develop sparse arrays for short-range imaging. Adoption of both approaches allows for reaching the required imaging performances with significantly fewer number of array elements in comparison with classical (narrowband and monostatic) approach. This chapter aims to present a generic design approach for

sparse UWB-MIMO array topology. It serves as basis for exploiting the design approaches for two-dimensional MIMO arrays presented in Chapters 4.

The chapter is organized as follows. Reviews of existing theories regarding MIMO arrays are presented in section 3.1. Formulation of MIMO array in the near-field of aperture with UWB excitations is presented and discussed in section 3.2. In section 3.3, a unified theory with existing narrowband far-field beam pattern formulations is presented. The equivalence between MIMO and conventional arrays is demonstrated, and the concept of an equivalent array is introduced in section 3.4. Factorization approach from a desired equivalent aperture into transmit/receive topologies is proposed in section 3.5. The design procedure for UWB-MIMO array is described together with a few design examples in section 3.6. In section 3.7, the near-field and bandwidth effects on the imaging performances of the MIMO array are studied. The performance of the above-mentioned MIMO arrays is experimentally studied using Vivaldi antenna arrays. The measurement results are presented in section 3.8. The chapter is summarized in the last section.

### **3.1 Review of existing theories**

Typical approach for radar imaging is based on the use of monostatic scattering from a target and is implemented by sequential operation of a number of collocated transmit-receive antenna pairs (which in the array terminology means the use of the identical sub-arrays for transmit and receive modes). By contrast, the multistatic approach to imaging which is realized via sequential or simultaneous operation of spatially diverse transmit-receive pairs (or multiple-input multiple-output array approach) attracts more and more attention in recent years [1]. The term MIMO array refers to an array topology that employs multiple, spatially distributed transmitters and receivers.

This concept has been first proposed and practiced in ultrasonic imaging. In 1975, Von Ramm et al. have suggested to use different element spacings for transmit and receive arrays so that grating lobes raised from transmit and receive arrays can be moved to different spatial locations in the complete two-way radiation pattern [2]. Synthetic focusing using partial datasets from the complete two-way transducer array was suggested by Cooley and Robinson in [3]. Hoctor and Kassam invented a synthetic aperture approach to the two-way sparse array design, known as co-array [4]. Lockwood et al. proposed a framework for optimizing sparse transmit/receive aperture functions [5].

For radar engineering, MIMO is an emerging technology that is attracting the attention from researchers and practitioners. In [6] [7], the diversity offered by widely separately transmit/receive antenna elements are exploited. The merits of a MIMO radar system with collocated antennas have been considered in [8-12]. A summary of advantages of MIMO radar system with both collocated and widely

separated antenna elements are provided in [13]. For collocated transmit and receive antennas, the MIMO radar scheme has been shown to offer higher resolution [10], higher sensitivity to detect slow moving targets [11], and better parameter identification [14]. Flexible transmit beam pattern design can be achieved with waveform optimization [8, 15, 16]. The degrees of freedom and resolution improvement of MIMO radar are summarized in [10].

In this chapter, we aim to investigate the capabilities of MIMO array for near-field wideband imaging. Based on the properties of one-way UWB array, our goal is to present a design approach for two-way MIMO array that achieves the required imaging performance with minimal number of antenna elements. This can be done by taking full advantage of the degrees of freedom from MIMO configuration, and tuning coherently between transmit and receive aperture functions. An equivalent two-way array can reduce the minimum number of array elements from  $N$  to  $2\sqrt{N}$ , which significantly decreases element density and mutual coupling within the physical aperture. It also helps to capitalize on the diversity of target illumination and scattering by viewing the target from multiple aspects. Before the design strategy can be discussed, we first derive the formulation of near-field point spread function (PSF) for wideband MIMO array with separate transmit/receive aperture functions.

### 3.2 Near-field wideband beam pattern formulation

For narrowband array, given the one-way patterns (the transmit array beam pattern and the receive array beam pattern), the complete two-way MIMO array beam pattern can be expressed by beam pattern multiplication. However, this simple multiplication does not hold for UWB MIMO arrays. In this section, theory and formulations are given for mathematically deriving the two-way pattern of an UWB array. The resulting theory covers beam pattern multiplication as a special case, and the conditions under which the beam pattern multiplication can hold are derived. For the far-field two-way array pattern, in the case of monochromatic condition, the formulation produces the Fraunhofer diffraction pattern.

We start with defining the elementary Green's function of a transmit/receive antenna pair within the imaging array. The free-space Green's function for the wave equation takes the form as

$$G_{fs} = (4\pi R)^{-1} \delta(t - R/c) \quad (3.1)$$

where  $R$  is the propagation distance,  $t$  is the time dimension and  $c$  is the speed of light. This is a Dirac delta distribution with the sphere  $t = R/c$  as its support. The basic geometry of the imaging system considered is illustrated in Figure 3.1. It consists of a transmit aperture with  $N_{Tx}$  antenna elements capable of emitting an EM impulse, and a receive aperture of  $N_{Rx}$  elements. The transmitter located at  $\mathbf{r}_{Tx}$  (a

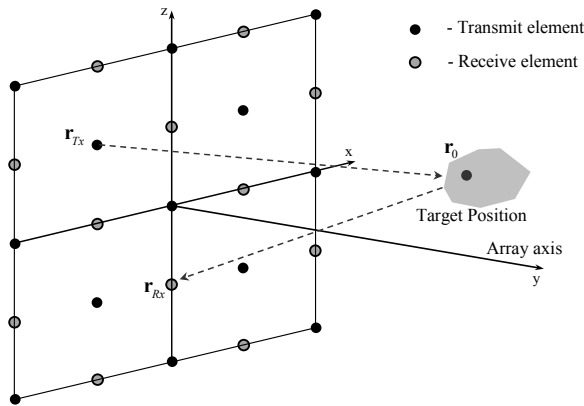


Figure 3.1 Geometry of multiple-input multiple-output array antenna composed of  $N_{Tx}$  impulse radiators  $\mathbf{r}_{Tx}$  and  $N_{Rx}$  receivers  $\mathbf{r}_{Rx}$  distributed in the transverse  $xz$ -plane with distribution function  $w_{Tx}(\mathbf{r}_{Tx})$  and  $w_{Rx}(\mathbf{r}_{Rx})$ , respectively.

vector in Euclidean space) transmits an impulse of the form  $\delta(t)$ . The wave arrives at the reflecting target located at  $\mathbf{r}_0$  at time  $|\mathbf{r}_0 - \mathbf{r}_{Tx}|/c$ . Then the target acts as a new source of the form  $(4\pi|\mathbf{r}_0 - \mathbf{r}_{Tx}|)^{-1}\delta(t - |\mathbf{r}_0 - \mathbf{r}_{Tx}|/c)$ . Finally, the scattered wave arrives at the receiver located at  $\mathbf{r}_{Rx}$  at time  $t = (|\mathbf{r}_0 - \mathbf{r}_{Tx}| + |\mathbf{r}_{Rx} - \mathbf{r}_0|)/c$ . Therefore, the time-domain waveform  $G_E(\mathbf{r}_0, \mathbf{r}_{Tx}, \mathbf{r}_{Rx}, t)$  at the receive antenna can be obtained by the convolution of the transmitted and scattered waves:

$$\begin{aligned} G_E(\mathbf{r}_0, \mathbf{r}_{Tx}, \mathbf{r}_{Rx}, t) &= (4\pi|\mathbf{r}_0 - \mathbf{r}_{Tx}|)^{-1}\delta(t - |\mathbf{r}_0 - \mathbf{r}_{Tx}|/c) * (4\pi|\mathbf{r}_{Rx} - \mathbf{r}_0|)^{-1}\delta(t - |\mathbf{r}_{Rx} - \mathbf{r}_0|/c) \\ &= (16\pi^2|\mathbf{r}_0 - \mathbf{r}_{Tx}||\mathbf{r}_{Rx} - \mathbf{r}_0|)^{-1}\delta(t - (|\mathbf{r}_0 - \mathbf{r}_{Tx}| + |\mathbf{r}_{Rx} - \mathbf{r}_0|)/c) \end{aligned} \quad (3.2)$$

We define  $G_E(\mathbf{r}_0, \mathbf{r}_{Tx}, \mathbf{r}_{Rx}, t)$  as the elementary Green's function of the two-way imaging array. The wave field  $u(\mathbf{r}_{Tx}, \mathbf{r}_{Rx}, t)$ , due to the responses within an distributed object can be expressed as the integration with the object space  $o(\mathbf{r}_0)$  by

$$\begin{aligned} u(\mathbf{r}_{Tx}, \mathbf{r}_{Rx}, t) &= \int_{\mathbf{r}_0} G_E(\mathbf{r}_0, \mathbf{r}_{Tx}, \mathbf{r}_{Rx}, t) \cdot o(\mathbf{r}_0) d\mathbf{r}_0 \\ &= \int (16\pi^2|\mathbf{r}_0 - \mathbf{r}_{Tx}||\mathbf{r}_{Rx} - \mathbf{r}_0|)^{-1}\delta(t - (|\mathbf{r}_0 - \mathbf{r}_{Tx}| + |\mathbf{r}_{Rx} - \mathbf{r}_0|)/c) \cdot o(\mathbf{r}_0) d\mathbf{r}_0 \end{aligned} \quad (3.3)$$

Equation (3.3) can be seen as the projection of the object space onto the ellipsoids that have major axis equal to  $|\mathbf{r}_0 - \mathbf{r}_{Tx}| + |\mathbf{r}_{Rx} - \mathbf{r}_0|$ , and foci at  $\mathbf{r}_{Tx}$  and  $\mathbf{r}_{Rx}$ .

Considering extend the formulation for a receiver aperture, each of the points within the aperture is associated with an elementary Green's function  $G_E(\mathbf{r}_0, \mathbf{r}_{Tx}, \mathbf{r}_{Rx}, t)$ . The receiver aperture time-domain output or image at focusing point  $\mathbf{r}$  due to a single impulse source at  $\mathbf{r}_{Tx}$  is formulated by combining the signals  $u(\mathbf{r}_{Tx}, \mathbf{r}_{Rx}, t)$  collected at each points within the receiver aperture  $\{\mathbf{r}_{Rx}\}$ , according to certain defined rule  $\Gamma$ :

$$I(\mathbf{r}, t) = \int_{\{\mathbf{r}_{Rx}\}} u(\mathbf{r}_{Tx}, \mathbf{r}_{Rx}, \Gamma(\mathbf{r}, \mathbf{r}_{Tx}, \mathbf{r}_{Rx}, t)) d\mathbf{r}_{Rx} \quad (3.4)$$

The image  $I(\mathbf{r})$  is actually the sum of ellipsoidal projections of the object. The rule  $\Gamma(\mathbf{r}, \mathbf{r}_{Tx}, \mathbf{r}_{Rx}, t)$  defines the ellipsoids' major axis by specifying the time at which the wave field associated with  $\mathbf{r}_{Tx}$  and  $\mathbf{r}_{Rx}$  is to be sampled for the summation.

$\Gamma$  is determined by specific imaging systems. For an beamforming system with dynamic focal points scanning through the space  $\mathbf{r}$ , the focusing time shall be

$$\Gamma(\mathbf{r}, \mathbf{r}_{Tx}, \mathbf{r}_{Rx}, t) = \Gamma(\mathbf{r}, \mathbf{r}_{Rx}) = (|\mathbf{r} - \mathbf{r}_{Tx\_fixed}| + |\mathbf{r}_{Rx} - \mathbf{r}|)/c \quad (3.5)$$

If the system is a fixed beam receiver, its output is

$$I(\mathbf{r}, t) = \int_{\{\mathbf{r}_{Rx}\}} u(\mathbf{r}_{Tx}, \mathbf{r}_{Rx}, t) d\mathbf{r}_{Rx}$$

with  $\Gamma(\mathbf{r}, \mathbf{r}_{Tx}, \mathbf{r}_{Rx}, t) = t$ , meaning that the aperture's rule is simultaneous summation.

Now we further include an extended transmitter aperture  $\{\mathbf{r}_{Tx}\}$  into the formula. Thus, the received signal at each receiver  $\mathbf{r}_{Rx}$  will consist of contributions from each of the transmitter  $\mathbf{r}_{Tx}$  within its aperture:

$$I(\mathbf{r}, t) = \int_{\{\mathbf{r}_{Rx}\}} \int_{\{\mathbf{r}_{Tx}\}} u(\mathbf{r}_{Tx}, \mathbf{r}_{Rx}, \Gamma(\mathbf{r}, \mathbf{r}_{Tx}, \mathbf{r}_{Rx}, t(\mathbf{r}_{Tx}))) d\mathbf{r}_{Tx} d\mathbf{r}_{Rx} \quad (3.6)$$

where  $t(\mathbf{r}_{Tx})$  is the time shifts relative to each transmitter  $\mathbf{r}_{Tx}$ , or can be seen as time adjusted to when each transmitter emits an impulse. Generally speaking, equation (3.6) indicates that the imaging array output is the linear superposition of the wave fields associated with each receiver and transmitter. And the integration is over both transmit and receive apertures. To steering the beam through the space, the  $\Gamma$  function shall be

$$\Gamma(\mathbf{r}, \mathbf{r}_{Tx}, \mathbf{r}_{Rx}, t(\mathbf{r}_{Tx})) = (|\mathbf{r} - \mathbf{r}_{Tx}| + |\mathbf{r}_{Rx} - \mathbf{r}|)/c \quad (3.7)$$

Substitute (3.3) into (3.6), we can further express the resulting image explicitly in terms of the target object:

## 56 Chapter 3. Multiple-input multiple-output arrays for real-aperture imaging

$$\begin{aligned} I(\mathbf{r}, t) &= \int_{\{\mathbf{r}_{Rx}\}} \int_{\{\mathbf{r}_{Tx}\}} \int_{\mathbf{r}_0} G_E(\mathbf{r}_0, \mathbf{r}_{Tx}, \mathbf{r}_{Rx}, \Gamma(\mathbf{r}, \mathbf{r}_{Tx}, \mathbf{r}_{Rx}, t(\mathbf{r}_{Tx}))) \cdot o(\mathbf{r}_0) d\mathbf{r}_0 d\mathbf{r}_{Tx} d\mathbf{r}_{Rx} \\ &= \int_{\mathbf{r}_0} PSF_{WB}(\mathbf{r}_0, \mathbf{r}, t) \cdot o(\mathbf{r}_0) d\mathbf{r}_0 \end{aligned} \quad (3.8)$$

where

$$PSF_{WB}(\mathbf{r}_0, \mathbf{r}, t) = \int_{\{\mathbf{r}_{Rx}\}} \int_{\{\mathbf{r}_{Tx}\}} G_E(\mathbf{r}_0, \mathbf{r}_{Tx}, \mathbf{r}_{Rx}, \Gamma(\mathbf{r}, \mathbf{r}_{Tx}, \mathbf{r}_{Rx}, t(\mathbf{r}_{Tx}))) d\mathbf{r}_{Tx} d\mathbf{r}_{Rx} \quad (3.9)$$

By rearranging the formulation, we see that  $PSF_{WB}$  represents the two-way array pattern or point spread function of the imaging array. Therefore, we define the formulation in (3.9) as the *array pattern of a general UWB MIMO array*. It is clear from this definition that the array pattern is a spatial variant function over both target location  $\mathbf{r}_0$  and scanning position  $\mathbf{r}$ . We can further foresee from the expression in (3.8) that  $PSF_{WB}$  alone does not determine the imaging quality. The object distribution  $o(\mathbf{r}_0)$  also has influences on the resulting image.

Since the formula is based on the Dirac delta function, the image for arbitrary transmitted waveform  $p(t)$  can be extended from (3.8) by convolution:

$$I(\mathbf{r}, t) = \int_{\mathbf{r}_0} PSF_{WB}(\mathbf{r}_0, \mathbf{r}, t) * p(t) \cdot o(\mathbf{r}_0) d\mathbf{r}_0 \quad (3.10)$$

What equation (3.10) indicates is that the waveform of the transmitted signal mainly influences in the temporal dimension or in the range direction of the image.

Assuming aperture functions  $w_{Tx}(\mathbf{r}_{Tx})$  and  $w_{Rx}(\mathbf{r}_{Rx})$  for the transmit and receive array, the expression of PSF is further completed with

$$\begin{aligned} PSF_{WB}(\mathbf{r}_0, \mathbf{r}, t) &= \int_{\{\mathbf{r}_{Rx}\}} \int_{\{\mathbf{r}_{Tx}\}} G_E(\mathbf{r}_0, \mathbf{r}_{Tx}, \mathbf{r}_{Rx}, \Gamma(\mathbf{r}, \mathbf{r}_{Tx}, \mathbf{r}_{Rx}, t(\mathbf{r}_{Tx}))) \cdot w_{Tx}(\mathbf{r}_{Tx}) \cdot w_{Rx}(\mathbf{r}_{Rx}) d\mathbf{r}_{Tx} d\mathbf{r}_{Rx} \\ &= \int_{\{\mathbf{r}_{Tx}\}} (4\pi |\mathbf{r}_0 - \mathbf{r}_{Tx}|)^{-1} \cdot w_{Tx}(\mathbf{r}_{Tx}) \cdot \delta(t - T_{Tx}(\mathbf{r}, \mathbf{r}_{Tx})) d\mathbf{r}_{Tx} \\ &\quad * \int_{\{\mathbf{r}_{Rx}\}} (4\pi |\mathbf{r}_{Rx} - \mathbf{r}_0|)^{-1} \cdot w_{Rx}(\mathbf{r}_{Rx}) \cdot \delta(t - T_{Rx}(\mathbf{r}, \mathbf{r}_{Rx})) d\mathbf{r}_{Rx} \end{aligned} \quad (3.11)$$

where

$$\begin{aligned} T_{Tx}(\mathbf{r}, \mathbf{r}_{Tx}) &= (|\mathbf{r}_0 - \mathbf{r}_{Tx}| - |\mathbf{r} - \mathbf{r}_{Tx}|) / c \\ T_{Rx}(\mathbf{r}, \mathbf{r}_{Rx}) &= (|\mathbf{r}_{Rx} - \mathbf{r}_0| - |\mathbf{r}_{Rx} - \mathbf{r}|) / c \end{aligned} \quad (3.12)$$

The aperture functions can be seen as array sampling function over the aperture, or aperture apodization as weighting of the elements. Equation (3.11) shows that the

near-field point spread function (PSF) of a wideband MIMO array can be represented by the convolution between the transmit array and receive array's space-time impulses responses. The radiation patterns of the transmit  $\text{Rad}_{Tx}(\mathbf{r}_{Tx}, \mathbf{r}_0)$  and receive  $\text{Rad}_{Rx}(\mathbf{r}_{Rx}, \mathbf{r}_0)$  antennas can also be included into the elementary Green's function of the two-way imaging array as

$$G_E(\mathbf{r}_0, \mathbf{r}_{Tx}, \mathbf{r}_{Rx}, t) = \text{Rad}_{Tx} \cdot \text{Rad}_{Rx} \cdot (16\pi^2 |\mathbf{r}_0 - \mathbf{r}_{Tx}| |\mathbf{r}_{Rx} - \mathbf{r}_0|)^{-1} \delta(t - (|\mathbf{r}_0 - \mathbf{r}_{Tx}| + |\mathbf{r}_{Rx} - \mathbf{r}_0|)/c)$$

As we can see, the characteristics of the antenna elements further make the PSF spatial variant.

### 3.3 Unified theory with narrowband far-field beam pattern

To illustrate the universality of the derived formulation, we derive the array pattern of a linear MIMO array when the transmitted waveform is a continuous monochromatic wave. As we can anticipate, for monochromatic transmission, the two-way beam pattern in the far-field should be similar to the Fraunhofer diffraction pattern  $(\sin \theta / \theta)^2$ .

For a linear array, we reduce the number of dimensions to  $(x, y)$ . A single point-like reflector is fixed at  $\mathbf{r}_0$ , therefore  $\delta(\mathbf{r}_0) = \delta(\mathbf{r} - \mathbf{r}_0)$ . The aperture function  $w_{Tx}(\mathbf{r}_{Tx})$  and  $w_{Rx}(\mathbf{r}_{Rx})$  represents uniform distribution over the x-axis. The propagation distance from the transmitter at  $\mathbf{r}_{Tx}$  to target at  $\mathbf{r}_0$  and back to the receiver at  $\mathbf{r}_{Rx}$  is  $d(\mathbf{r}_{Tx}, \mathbf{r}_0, \mathbf{r}_{Rx}) = |\mathbf{r}_0 - \mathbf{r}_{Tx}| + |\mathbf{r}_{Rx} - \mathbf{r}_0|$ . As the result, the elementary Green's function for the transmitter at  $d\mathbf{r}_{Tx}$  and receiver at  $d\mathbf{r}_{Rx}$  is expressed as

$$G_E(\mathbf{r}_0, \mathbf{r}_{Tx}, \mathbf{r}_{Rx}, t) = (16\pi^2 |\mathbf{r}_0 - \mathbf{r}_{Tx}| |\mathbf{r}_{Rx} - \mathbf{r}_0|)^{-1} \delta(t - d(\mathbf{r}_{Tx}, \mathbf{r}_0, \mathbf{r}_{Rx})/c)$$

Based on this, the array pattern for such scenario can be expressed as

$$\begin{aligned} PSF(\mathbf{r}_0, \mathbf{r}, t) &= \int_{\{\mathbf{r}_{Rx}\}} \int_{\{\mathbf{r}_{Tx}\}} G_E(\mathbf{r}_0, \mathbf{r}_{Tx}, \mathbf{r}_{Rx}, \Gamma(\mathbf{r}, \mathbf{r}_{Tx}, \mathbf{r}_{Rx}, t(\mathbf{r}_{Tx}))) \cdot w_{Tx}(\mathbf{r}_{Tx}) \cdot w_{Rx}(\mathbf{r}_{Rx}) d\mathbf{r}_{Tx} d\mathbf{r}_{Rx} \\ &= PSF(\mathbf{r}, t) \end{aligned} \quad (3.13)$$

The array pattern is only the function of the steering position and time. And the resulting image by integrating with the target function:

$$\begin{aligned}
 I(\mathbf{r}, t) &= \int_{\mathbf{r}_0} PSF(\mathbf{r}, t) \cdot o(\mathbf{r}_0) d\mathbf{r}_0 = PSF \cdot \int_{\mathbf{r}_0} \delta(\mathbf{r} - \mathbf{r}_0) d\mathbf{r}_0 = PSF(\mathbf{r}, t) \\
 &= \int_{\{\mathbf{r}_{Rx}\}} \int_{\{\mathbf{r}_{Tx}\}} w_{Tx}(\mathbf{r}_{Tx}) \cdot w_{Rx}(\mathbf{r}_{Rx}) \cdot (16\pi^2 |\mathbf{r}_0 - \mathbf{r}_{Tx}| |\mathbf{r}_{Rx} - \mathbf{r}_0|)^{-1} \\
 &\quad \cdot \delta(t - d(\mathbf{r}_{Tx}, \mathbf{r}_0, \mathbf{r}_{Rx})/c + \Gamma(\mathbf{r}, \mathbf{r}_{Tx}, \mathbf{r}_{Rx}, t(\mathbf{r}_{Tx}))) d\mathbf{r}_{Tx} d\mathbf{r}_{Rx}
 \end{aligned} \tag{3.14}$$

And  $\Gamma(\mathbf{r}, \mathbf{r}_{Tx}, \mathbf{r}_{Rx}, t(\mathbf{r}_{Tx})) = (|\mathbf{r} - \mathbf{r}_{Tx}| + |\mathbf{r}_{Rx} - \mathbf{r}|)/c$ , representing the steering of the beam. Here, the image is not a function of  $\mathbf{r}_0$  but  $\mathbf{r}$  representing the scenario with the target fixed and system focusing through the imaging space.

As stated by equation (3.10), the aperture response for a continuous wave transmission can be derived by convolving the spatial variant array pattern with the analytical signal  $p(t) = e^{i\omega t}$ . This convolution results in

$$\begin{aligned}
 I(\mathbf{r}, t) &= PSF(\mathbf{r}, t) * p(t) \\
 &= \int_{\{\mathbf{r}_{Rx}\}} \int_{\{\mathbf{r}_{Tx}\}} w_{Tx}(\mathbf{r}_{Tx}) \cdot w_{Rx}(\mathbf{r}_{Rx}) \cdot e^{i\omega(t - d(\mathbf{r}_{Tx}, \mathbf{r}_0, \mathbf{r}_{Rx})/c + \Gamma(\mathbf{r}, \mathbf{r}_{Tx}, \mathbf{r}_{Rx}, t(\mathbf{r}_{Tx})))} d\mathbf{r}_{Tx} d\mathbf{r}_{Rx} \\
 &= e^{i\omega t} \int_{\{\mathbf{r}_{Rx}\}} \int_{\{\mathbf{r}_{Tx}\}} w_{Tx}(\mathbf{r}_{Tx}) \cdot w_{Rx}(\mathbf{r}_{Rx}) \cdot e^{-i\omega(d(\mathbf{r}_{Tx}, \mathbf{r}_0, \mathbf{r}_{Rx})/c - \Gamma(\mathbf{r}, \mathbf{r}_{Tx}, \mathbf{r}_{Rx}, t(\mathbf{r}_{Tx})))} d\mathbf{r}_{Tx} d\mathbf{r}_{Rx}
 \end{aligned} \tag{3.15}$$

The spreading loss factor in (3.15) is ignored since we are considering far-field. Furthermore, because a narrowband array does not exhibit any down-range resolving capability and we are interested in the pattern over cross-range directions, the time harmonics outside the integrals can be neglected. Therefore,

$$\begin{aligned}
 I(\mathbf{r}) &= \int_{\{\mathbf{r}_{Rx}\}} \int_{\{\mathbf{r}_{Tx}\}} e^{-i\omega(d(\mathbf{r}_{Tx}, \mathbf{r}_0, \mathbf{r}_{Rx})/c - \Gamma(\mathbf{r}, \mathbf{r}_{Tx}, \mathbf{r}_{Rx}, t(\mathbf{r}_{Tx})))} d\mathbf{r}_{Tx} d\mathbf{r}_{Rx} \\
 &= \int_{\{\mathbf{r}_{Rx}\}} \int_{\{\mathbf{r}_{Tx}\}} w_{Tx}(\mathbf{r}_{Tx}) \cdot w_{Rx}(\mathbf{r}_{Rx}) \cdot e^{-ik(d_{Tx}(\mathbf{r}_{Tx}, \mathbf{r}) + d_{Rx}(\mathbf{r}_{Rx}, \mathbf{r}))} d\mathbf{r}_{Tx} d\mathbf{r}_{Rx} \\
 &= \int_{\{\mathbf{r}_{Tx}\}} e^{-ik \cdot d_{Tx}(\mathbf{r}_{Tx}, \mathbf{r})} \cdot w_{Tx}(\mathbf{r}_{Tx}) d\mathbf{r}_{Tx} \cdot \int_{\{\mathbf{r}_{Rx}\}} e^{-ik \cdot d_{Rx}(\mathbf{r}_{Rx}, \mathbf{r})} \cdot w_{Rx}(\mathbf{r}_{Rx}) d\mathbf{r}_{Rx}
 \end{aligned} \tag{3.16}$$

where  $k = 2\pi/\lambda$  represents the wavenumber, and

$$\begin{aligned}
 d_{Tx}(\mathbf{r}_{Tx}, \mathbf{r}) &= |\mathbf{r}_0 - \mathbf{r}_{Tx}| - |\mathbf{r} - \mathbf{r}_{Tx}| \\
 d_{Rx}(\mathbf{r}_{Rx}, \mathbf{r}) &= |\mathbf{r}_{Rx} - \mathbf{r}_0| - |\mathbf{r}_{Rx} - \mathbf{r}|
 \end{aligned} \tag{3.17}$$

By the expression in (3.16), we are able to separate the integrals between transmit and receive apertures and the array pattern becomes the multiplication between them.

Since the target's position is fixed at  $\mathbf{r}_0$  in our experiment, we can pull out the terms that is related to  $\mathbf{r}_0$  from the integral

$$I(\mathbf{r}) = A_{Tx0} \int_{\{\mathbf{r}_{Tx}\}} e^{ik|\mathbf{r}-\mathbf{r}_{Tx}|} \cdot w_{Tx}(\mathbf{r}_{Tx}) d\mathbf{r}_{Tx} \cdot A_{Rx0} \int_{\{\mathbf{r}_{Rx}\}} e^{ik|\mathbf{r}_{Rx}-\mathbf{r}|} \cdot w_{Rx}(\mathbf{r}_{Rx}) d\mathbf{r}_{Rx} \quad (3.18)$$

where

$$\begin{aligned} A_{Tx0} &= \int_{\{\mathbf{r}_{Tx}\}} e^{-ik|\mathbf{r}_0-\mathbf{r}_{Tx}|} \cdot w_{Tx}(\mathbf{r}_{Tx}) d\mathbf{r}_{Tx} \\ A_{Rx0} &= \int_{\{\mathbf{r}_{Rx}\}} e^{-ik|\mathbf{r}_{Rx}-\mathbf{r}_0|} \cdot w_{Rx}(\mathbf{r}_{Rx}) d\mathbf{r}_{Rx} \end{aligned} \quad (3.19)$$

Each integral of the equation (3.18) now is in the form used as the starting point to derive the theory that the beam pattern of a narrowband phased array at far-field is the Fourier transform of the aperture function. It is also traditionally used to explain the diffraction pattern that light makes passing through an aperture on the plate. We will make the assumption here, that the distance from the focal point  $\mathbf{r}$ , at which the beam is steered, to the transmit or receive aperture plane is much greater than the width of both transmit/receive apertures. This is commonly referred as the Fraunhofer approximation. As illustrated in Figure 3.2, if  $|\mathbf{r} - \mathbf{r}_{Aperture}| \gg L$  is valid, then we can arrived at the relation that  $|\mathbf{r} - \mathbf{r}_{Aperture}| \approx \mathbf{r} - \mathbf{r}_{Aperture} \sin \theta$ , where  $L$  represents the size of the aperture. Then the formulation becomes

$$\begin{aligned} I(\theta) &= A_{Tx0} \int_{\{\mathbf{r}_{Tx}\}} e^{ik \cdot (\mathbf{r} - \mathbf{r}_{Tx} \cdot \sin \theta)} \cdot w_{Tx}(\mathbf{r}_{Tx}) d\mathbf{r}_{Tx} \cdot A_{Rx0} \int_{\{\mathbf{r}_{Rx}\}} e^{ik \cdot (\mathbf{r} - \mathbf{r}_{Rx} \cdot \sin \theta)} \cdot w_{Rx}(\mathbf{r}_{Rx}) d\mathbf{r}_{Rx} \\ &= A_{Tx0} e^{ik\mathbf{r}} \int_{\{\mathbf{r}_{Tx}\}} e^{-ik \cdot \mathbf{r}_{Tx} \cdot \sin \theta} \cdot w_{Tx}(\mathbf{r}_{Tx}) d\mathbf{r}_{Tx} \cdot A_{Rx0} e^{ik\mathbf{r}} \int_{\{\mathbf{r}_{Rx}\}} e^{-ik \cdot \mathbf{r}_{Rx} \cdot \sin \theta} \cdot w_{Rx}(\mathbf{r}_{Rx}) d\mathbf{r}_{Rx} \end{aligned} \quad (3.20)$$

We further define  $\nu = \sin \theta$  in the expression, which leads to

$$I(\nu) = A_{Tx0} e^{ik\mathbf{r}} \int_{\{\mathbf{r}_{Tx}\}} w_{Tx}(\mathbf{r}_{Tx}) \cdot e^{-ik \cdot \mathbf{r}_{Tx} \cdot \nu} d\mathbf{r}_{Tx} \cdot A_{Rx0} e^{ik\mathbf{r}} \int_{\{\mathbf{r}_{Rx}\}} w_{Rx}(\mathbf{r}_{Rx}) \cdot e^{-ik \cdot \mathbf{r}_{Rx} \cdot \nu} d\mathbf{r}_{Rx} \quad (3.21)$$

This is mainly the Fourier transform of the transmit aperture function  $w_{Tx}(\mathbf{r}_{Tx})$  times the Fourier transform of the receive aperture function  $w_{Rx}(\mathbf{r}_{Rx})$ . If both apertures are the same rectangular functions as

$$\text{rect}\left(\frac{\mathbf{r}_{Aperture}}{L}\right) = h\left(\mathbf{r}_{Aperture} + \frac{L}{2}\right) - h\left(\mathbf{r}_{Aperture} - \frac{L}{2}\right) \quad (3.22)$$

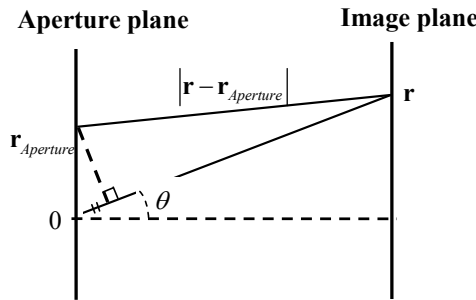


Figure 3.2 Illustration of the Fraunhofer approximation under the far-field condition.

where  $h(x)$  is the unit step function and  $L$  is the length of the aperture, the array pattern would become

$$I(v) = A_{Tx0} e^{ikr} \cdot \frac{\sin(kLv)}{kLv} \cdot A_{Rx0} e^{ikr} \cdot \frac{\sin(kLv)}{kLv} = A_{Tx0} A_{Rx0} \cdot e^{i2kr} \cdot \left(\frac{\sin(kLv)}{kLv}\right)^2 \quad (3.23)$$

which shows the form of the Fraunhofer diffraction pattern. The exponential in front can be omitted since its amplitude is a unit factor. Based on equation (3.21), if the transmit and receive apertures are shifted apart from each other while maintaining symmetry over the origin, the extra phase shift introduced by each of the Fourier transform will cancel each other leaving the beam pattern unchanged. This is completely valid only when the shifted offset by each aperture is much smaller than the apertures' distance to the imaging plane.

In order to derive the condition under which the beam pattern multiplication holds, we go back to (3.14) where we derived the beam pattern of an UWB MIMO array when the target is fixed and the beam is steered through the space. We further derived the two-way beam pattern for an arbitrary waveform via convolution with the wavelet  $p(t)$

$$I(\mathbf{r}, t) = \int_{\{\mathbf{r}_{Rx}\}} \int_{\{\mathbf{r}_{Tx}\}} w_{Tx}(\mathbf{r}_{Tx}) \cdot w_{Rx}(\mathbf{r}_{Rx}) \cdot (16\pi^2 |\mathbf{r}_0 - \mathbf{r}_{Tx}| |\mathbf{r}_{Rx} - \mathbf{r}_0|)^{-1} d\mathbf{r}_{Tx} d\mathbf{r}_{Rx} \cdot p(t - d_{Tx}(\mathbf{r}_{Tx}, \mathbf{r})/c - d_{Rx}(\mathbf{r}_{Rx}, \mathbf{r})/c) \quad (3.24)$$

Only when the applied waveform  $p(t)$  satisfies the relation that

$$p(t - \alpha - \beta) = p(t - \alpha) \cdot p(t - \beta) \quad (3.25)$$

then we can separate the two integrals by

$$I(\mathbf{r}, t) = \int_{\{\mathbf{r}_{Rx}\}} (4\pi |\mathbf{r}_0 - \mathbf{r}_{Tx}|)^{-1} \cdot w_{Tx}(\mathbf{r}_{Tx}) \cdot p(t - d_{Tx}(\mathbf{r}_{Tx}, \mathbf{r})/c) d\mathbf{r}_{Tx} \\ \cdot \int_{\{\mathbf{r}_{Rx}\}} (4\pi |\mathbf{r}_{Rx} - \mathbf{r}_0|)^{-1} \cdot w_{Rx}(\mathbf{r}_{Rx}) \cdot p(t - d_{Rx}(\mathbf{r}_{Rx}, \mathbf{r})/c) d\mathbf{r}_{Rx} \quad (3.26)$$

The resulting image is expressed as the product of the transmit and receive beam patterns. It is apparent that a narrowband signal  $p(t) = e^{i\omega t}$  satisfies such requirement. Otherwise, if the transmitted waveform does not satisfy this criterion in (3.25), the image shall be expressed as the convolution between the transmit array and receive array's space-time impulses responses, and further convolved with the transmitted waveform indicated in (3.11).

### 3.4 Effective aperture and synthetic aperture

For each transmit-receive array an equivalent array can be found whose one-way beam pattern is identical to a two-way pattern of the initial array. The aperture function of such an array is referred to as effective aperture. It can be treated as a receive aperture with object illuminated by a single transmitter or a transmit aperture with a single receiver. The effective aperture concept is a useful tool for array design as it helps to reduce the dimensions of the problem we are dealing with.

In the previous section, we have formulated the beam pattern of a narrowband array as the Fourier transform of the transmit aperture function  $w_{Tx}(\mathbf{r}_{Tx})$  multiplied with the Fourier transform of the receive aperture function  $w_{Rx}(\mathbf{r}_{Rx})$ .

$$I(\nu) = \int_{\{\mathbf{r}_{Tx}\}} w_{Tx}(\mathbf{r}_{Tx}) \cdot e^{-ik \cdot \mathbf{r}_{Tx} \cdot \nu} d\mathbf{r}_{Tx} \cdot \int_{\{\mathbf{r}_{Rx}\}} w_{Rx}(\mathbf{r}_{Rx}) \cdot e^{-ik \cdot \mathbf{r}_{Rx} \cdot \nu} d\mathbf{r}_{Rx} \\ = FT\{w_{Tx}(\mathbf{r}_{Tx})\} \cdot FT\{w_{Rx}(\mathbf{r}_{Rx})\} \\ = FT\{w_{Tx}(\mathbf{r}_{Tx}) * w_{Rx}(\mathbf{r}_{Rx})\} \quad (3.27)$$

As we can see, this is equivalent to convolving the transmit aperture function with the receive aperture function and taking the Fourier transform of the result. Hence, we can define the narrowband effective array as

$$E_{NB}(\mathbf{r}_{Array}) = w_{Tx}(\mathbf{r}) * w_{Rx}(\mathbf{r}) \quad (3.28)$$

This convolution of aperture functions has been also described by other researchers using the term 'co-array' [4].

The effective aperture of a wideband array can be derived by further separating equation (3.11) in terms of target location  $\mathbf{r}_0$  and imaging point  $\mathbf{r}$ . The part of PSF as the function of  $\mathbf{r}$  can be expressed as

$$PSF_{WB}(\mathbf{r}) = \int_{\{\mathbf{r}_{Tx}\}} w_{Tx}(\mathbf{r}_{Tx}) \cdot \delta(t + \frac{|\mathbf{r} - \mathbf{r}_{Tx}|}{c}) d\mathbf{r}_{Tx} * \int_{\{\mathbf{r}_{Rx}\}} w_{Rx}(\mathbf{r}_{Rx}) \cdot \delta(t + \frac{|\mathbf{r}_{Rx} - \mathbf{r}|}{c}) d\mathbf{r}_{Rx} \quad (3.29)$$

At the time zero along the array plane, the formulation is equivalent to the spatial convolution of the transmit and receive aperture functions, which serves as the definition of the effective aperture for a two-way wideband MIMO array.

$$\begin{aligned} E_{WB}(\mathbf{r}_{Array}) &= \int_{\{\mathbf{r}_{Tx}\}} w_{Tx}(\mathbf{r}_{Tx}) \cdot \delta(|\mathbf{r} - \mathbf{r}_{Tx}|) d\mathbf{r}_{Tx} * \int_{\{\mathbf{r}_{Rx}\}} w_{Rx}(\mathbf{r}_{Rx}) \cdot \delta(|\mathbf{r}_{Rx} - \mathbf{r}|) d\mathbf{r}_{Rx} \\ &= w_{Tx}(\mathbf{r}) * w_{Rx}(\mathbf{r}) \end{aligned} \quad (3.30)$$

Compare the definitions, it is clear that both narrowband and wideband effective arrays share the same form. This is not a surprise since the wideband response can be always seen as Fourier superposition of the monochromatic responses. Although the effective arrays for NB and WB cases have the similar functionality, the UWB effective array determines both space and temporal properties of the PSF while the NB array only affects the angular properties.

The effective aperture concept serves as a useful tool to reduce the complications for the MIMO array design. It offers a framework for selecting the aperture functions of the transmit and receive arrays. A design is valid if the effective array can be factorized into two arrays. However, an exact solution to this problem is still not straightforward due to a need of the deconvolution process.

We try to solve this problem from another angle by expressing the effective aperture function as a subset of the aperture space in terms of element position  $\mathbf{r}_{EAP}$  and its corresponding weight  $w(\mathbf{r}_{EAP})$

$$E_{AP} = \left\{ (\mathbf{r}_{EAP}, w(\mathbf{r}_{EAP})) \middle| \mathbf{r}_{EAP} = |\mathbf{r}_{Tx} + \mathbf{r}_{Rx}|, w(\mathbf{r}_{EAP}) = w_{Tx}(\mathbf{r}_{Tx}) \cdot w_{Rx}(\mathbf{r}_{Rx}) \right\} \quad (3.31)$$

Meanwhile, we define the synthetic aperture function of the two-way MIMO array as

$$S_{AP} = \left\{ (\mathbf{r}_{SAP}, w(\mathbf{r}_{SAP})) \middle| \mathbf{r}_{SAP} = \frac{|\mathbf{r}_{Tx} + \mathbf{r}_{Rx}|}{2}, w(\mathbf{r}_{SAP}) = \frac{w_{Tx}(\mathbf{r}_{Tx}) + w_{Rx}(\mathbf{r}_{Rx})}{2} \right\} \quad (3.32)$$

The elements within the synthetic aperture function are the midpoints of the lines connecting each transmit element and receive element. Unlike the one-way effective array with a single transmit or receive element, the synthetic aperture function assumes co-located transmit/receive transducers as its elements. Equation (3.31) and (3.32) are defined under the condition where no redundancy exists within the array. If different transmit/receive pairs within the array result in the same virtual element position, the corresponding weights at the same virtual element shall be summed.

Comparing the two definitions in (3.31) and (3.32), it's easy to see that the

synthetic aperture function is equivalent to the spatially half scaled version of the effective array aperture under the condition that the weightings of the original transmit and receive aperture functions are identical:

$$\mathbf{r}_{EAP} = 2 \cdot \mathbf{r}_{SAP}, \quad w(\mathbf{r}_{EAP}) = w(\mathbf{r}_{SAP}) \quad (3.33)$$

Such equivalency can be physically explained by the concept of exploding reflector model (ERM), under which the wave field is assumed to start expanding from the target at time zero with half of the actual propagation speed. Within ERM, the synthetic aperture with co-located transmit/receive transducers can be treated as one-way array with aperture size twice as large relative to the corresponding halved wavelength. Meanwhile, unit element weighting is a feasible strategy for sparse array design due to the fact that aperture weighting or apodization affects only the sidelobe but not grating lobes with the cost of reduced image resolution [17].

Thus, the spatial deconvolution procedure is simplified to a procedure of calculating geometries of transmit/receive pairs with a certain position of their middle point. The synthetic aperture function can be seen as repetitions of both transmit and receive array topologies and therefore, helping with generating direct strategies toward two-way MIMO array design.

### 3.5 Factorization approach

By designing the transmit and receive arrays in such a way that results in a uniform-weighted effective aperture function without redundancy, the wave interference of UWB signals is confined to a small spatial area around the mainlobe. The denser the spatial sampling in the effective aperture is, the further away from the mainlobe are the grating lobes pushed. Under the condition that the fractional bandwidth is much larger than 100%, the majority of the expected grating lobes will occur outside the IR thus drastically reducing their influence on the array patterns. The design approach based on the effective aperture has a principal advantage over conventional non-uniform (non-periodic) array design as it keeps under control both the width of the mainlobe and the grating lobe level. These two factors are crucial for distributed targets imaging with both high resolution and dynamic range.

The key step in the proposed design procedure is factorization of a desired uniform effective aperture into topologies of transmit and receive arrays. Assuming the element spacing within the receive array is  $\Delta_{Rx}$ , a uniform receive aperture function can be expressed as

$$w_{Rx} = \left\{ (\mathbf{r}_{Rx}, w(\mathbf{r}_{Rx})) \mid \mathbf{r}_{Rx} = [-m \cdot \Delta_{Rx} : \Delta_{Rx} : m \cdot \Delta_{Rx}], w(\mathbf{r}_{Rx}) = 1 \right\} \quad (3.34)$$

## 64 Chapter 3. Multiple-input multiple-output arrays for real-aperture imaging

where  $m = (N_{Rx} - 1)/2$  is a real number, and  $N_{Rx}$  represents the total number of elements within the receive aperture. Location of a single transmitter at the position  $n \cdot \Delta_{Rx}$  will result in the synthetic aperture as

$$S_{AP} = \left\{ (\mathbf{r}_{SAP}, w(\mathbf{r}_{SAP})) \middle| \mathbf{r}_{SAP} = \left[ \frac{-m+n}{2} \cdot \Delta_{Rx} : \frac{\Delta_{Rx}}{2} : \frac{m+n}{2} \cdot \Delta_{Rx} \right], w(\mathbf{r}_{SAP}) = 1 \right\} \quad (3.35)$$

So each of the transmit elements creates a spatially half scaled replication of the same receive aperture at the corresponding positions. In order to combine all these sub-synthetic apertures from each transmit element into a uniform aperture of the complete transmit-receive array, the distance between transmitters  $D_{Tx}$  needs to be

$$D_{Tx} = (2 \cdot m + 1) \Delta_{Rx} \quad (3.36)$$

The resulting effective aperture will have the same element spacing as the receive array. If one wants to create a denser effective aperture, sub-arrays within the transmit array can be introduced. By applying relation in (3.36) between the sub-array and receive aperture, the relation between the spacing within each sub-array  $\Delta_{Tx}$  and the one of the receive array can be derived

$$\Delta_{Tx} = \Delta_{Rx} / n_{subTx} \quad (3.37)$$

where  $n_{subTx}$  is the number of elements within each transmit sub-array. In this case, the element spacing in the effective aperture will be  $\Delta_{Rx} / n_{subTx}$ . The size of the resulting effective aperture  $L_{EAP}$  depends on the number of transmit sub-arrays  $N_{subTx}$  and can be evaluated as

$$L_{EAP} = \frac{\Delta_{Rx}}{n_{subTx}} \cdot [N_{Rx} \cdot n_{subTx} \cdot N_{subTx} - 1] \quad (3.38)$$

Equations (3.36) to (3.38) together describe the arrangement of the transmit array relative to the receive array and their element spacings for an arbitrary combination of the number of transmit and receive elements so that a uniform effective aperture can be achieved. The centers of transmit and receive arrays are commonly arranged at the same point in order to keep left/right symmetry of the complete beam pattern. The transmit aperture function can be explicitly expressed as

$$w_{Tx} = \left\{ (\mathbf{r}_{Tx}, w(\mathbf{r}_{Tx})) \middle| \begin{aligned} \mathbf{r}_{Tx} &= [\mathbf{r}_{subTx} - n \cdot D_{Tx} : D_{Tx} : \mathbf{r}_{subTx} + n \cdot D_{Tx}] \\ w(\mathbf{r}_{Tx}) &= 1 \end{aligned} \right\} \quad (3.39)$$

where  $\mathbf{r}_{subTx} = [-n' \cdot \Delta_{Tx} : \Delta_{Tx} : n' \cdot \Delta_{Tx}]$  is the element location within the transmit array sub-aperture, with  $n = (N_{subTx} - 1)/2$ , and  $n' = (n_{subTx} - 1)/2$ .

### 3.6 Design procedure

The design process starts from the required ISL defined in (2.30), which determines the minimal number of the virtual elements  $N_E$  within the effective aperture. After that the required cross-range resolution  $\delta_{cr}$  determines the effective aperture size relative to the wavelength at center frequency  $L_{EAP} = (R/\delta_{cr}) \cdot \lambda_c$ , where  $R$  represents the potential range of the target. In the next step, the number of transmit and receive elements can be chosen under the relation  $N_E = N_{Tx} \cdot N_{Rx}$  (the total number of antennas within the array is  $N = N_{Tx} + N_{Rx}$ ). The total number of antennas will be minimal by selecting equal or as close as possible number of elements in both transmit and receive arrays. After that, design of transmit and receive array topologies can be done based on equations (3.36) to (3.39). Because of different choices of sub-arrays, the described factorization procedure is not unique and allows for multiple solutions. To select the optimal among them, some practical issues, such as influences of the near-field spreading loss, mutual coupling, antenna element size, and costs of transmitter and receiver, shall be considered.

We consider a scenario of short-range imaging with a potential target at the range of 0.4 m, with a centimeter resolution and dynamic range of 30 dB. The number of virtual elements can be first determined as  $N_E = 10^{30/20} \doteq 32$ . The operational center frequency is selected as 11 GHz. To provide the cross-range resolution of about 1 cm at the range of 40 cm (which is equivalent to 1.4 degrees beamwidth) the effective aperture size should be approximately  $40\lambda_c$ . Among different combinations of transmit and receive element numbers ( $1 \times 32$ ,  $2 \times 16$ ,  $4 \times 8$ , etc), the one with minimal number of transceivers would be 4 transmit/8 receive or 8 transmit/4 receive. Under the same effective aperture size and resolution, different choices of sub-array arrangements within the transmit aperture are possible and are shown in Figure 3.3. By applying the equations (3.36) to (3.39) to the equivalent aperture, five different factorizations can be found. Their parameters are listed in Table 3.1. All the options result in the same uniform effective aperture with the same aperture size.

We consider several factors to compare among these different factorization options. The first is the differences of spreading loss associated with transmit/receive pairs within the array aperture. The spreading loss for a virtual element at  $\mathbf{r}_{EAP}$  is estimated as

$$W_{SP}(\mathbf{r}_{EAP}) = (|\mathbf{r}_{Tx} - \mathbf{r}_0| \cdot |\mathbf{r}_{Rx} - \mathbf{r}_0|)^{-1} \quad (3.40)$$

where  $\mathbf{r}_0$  is the position of the target. In the contrary to the far-field, variations of the bi-static angles of individual transceiver pair in the near-field of the array aperture cause essential differences in terms of weighting among virtual elements. Large

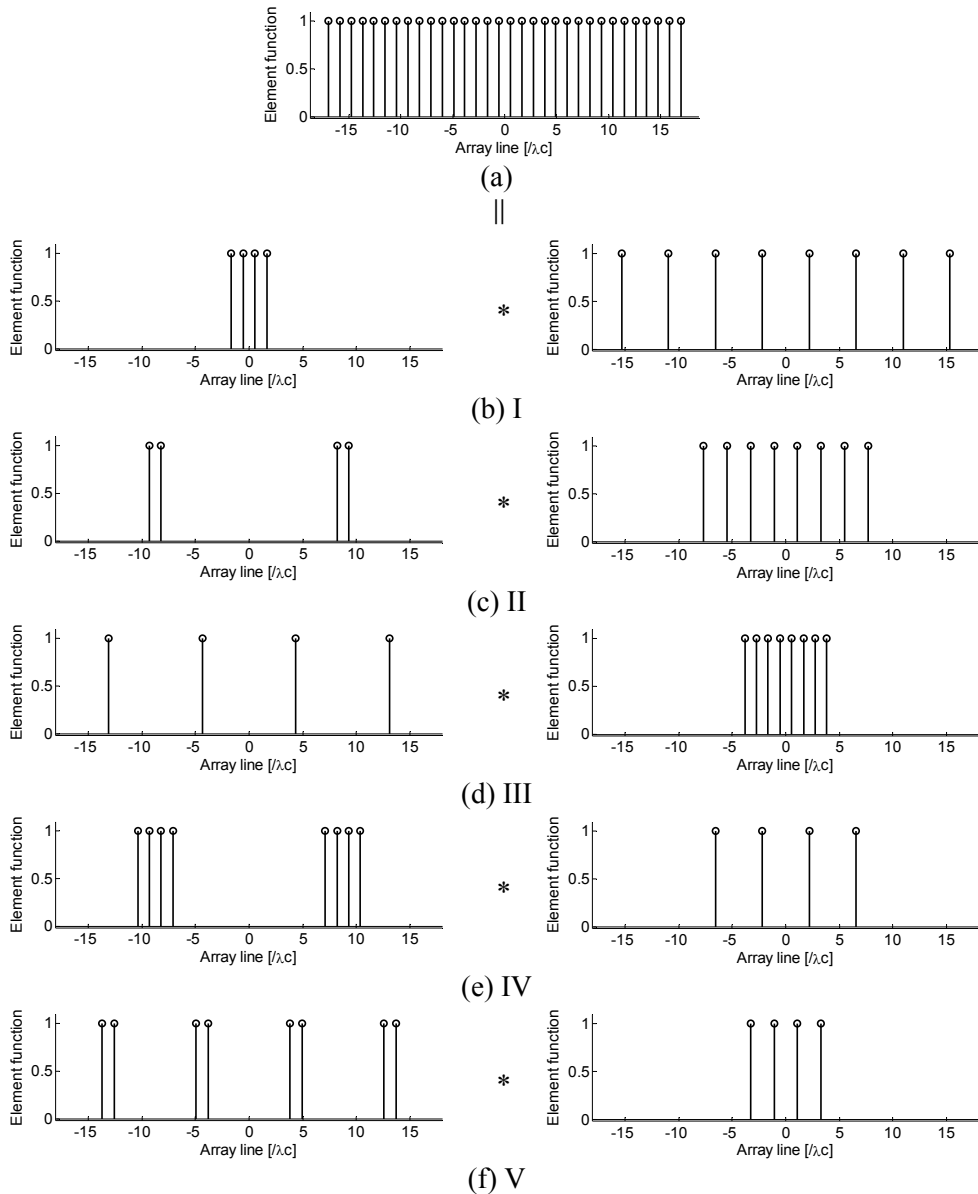


Figure 3.3 Factorization from a 32 element effective aperture to transmit and receive aperture functions. The receive array is kept uniform while different choices of transmit apertures are explored. (a) Effective aperture with 32 virtual elements, (b) factorization I with 1 transmit sub-array of 4 elements, (c) factorization II with 2 transmit sub-array of 2 elements, (d) factorization III with 4 transmit sub-array of 1 elements, (e) factorization IV with 2 transmit sub-array of 4 elements, (f) factorization V with 4 transmit sub-array of 2 elements.

TABLE 3.1

Comparison of maximum spreading loss ratio, and physical aperture size among 5 factorization options shown in Figure 3.3

Factorization No.		I	II	III	IV	V
Parameters	$N_{Tx}$	4	4	4	8	8
	$N_{subTx}$	1	2	4	2	4
	$n_{subTx}$	4	2	1	4	2
	$N_{Rx}$	8	8	8	4	4
Maximum Spreading loss ratio		0.70	0.87	0.76	0.84	0.75
Array size [ $/ \lambda_c$ ]		30.6	18.6	26.2	20.8	27.3

differences of spreading loss degrade the cross-range resolution of the array and reduce the signal to noise ratio (SNR) of the complete system. The maximum ratio of the spreading loss among the elements and physical aperture size of each MIMO array are compared in Table 1. The spreading loss there is estimated for the target location at  $15\lambda_c$  (0.4 m). Among all options, option II has the highest maximum spreading loss ratio, meaning that it exhibits the smallest differences of spreading loss among its transceiver pairs. Furthermore, option II uses the smallest space to achieve the same effective aperture size. In terms of mutual coupling, it also has the smallest number of elements that are closely located, therefore, resulting in the lowest coupling level between elements and the most relaxed requirement for the antenna element size. By considering these practical factors, the second option should be selected as the most feasible choice. In this case, due to the utilization of MIMO array topology, the total number of elements is reduced from 32 (the minimal number to achieve required sidelobe level) to 12.

Based on the second option we design a linear array topology and compare it with three other arrays designed using conventional methods. The array topologies and their effective aperture functions are illustrated in Figure 3.4. All four apertures have the same 50 cm width with 12 antenna elements. The first array represents a conventional one-way array with 1 transmit and 11 receive elements. The other three arrays are MIMO configurations, which consist of 4 transmit and 8 receive elements. The coordinates in the figure are given in terms of the wavelength at center frequency. Transmit and receive arrays are located at two different elevation levels to reduce direct coupling among the transmit and receiver elements. Theoretically, this does not influence the array performance in the aperture plane. The arrays are sparse arrays due to the fact that the average element spacing within their effective apertures

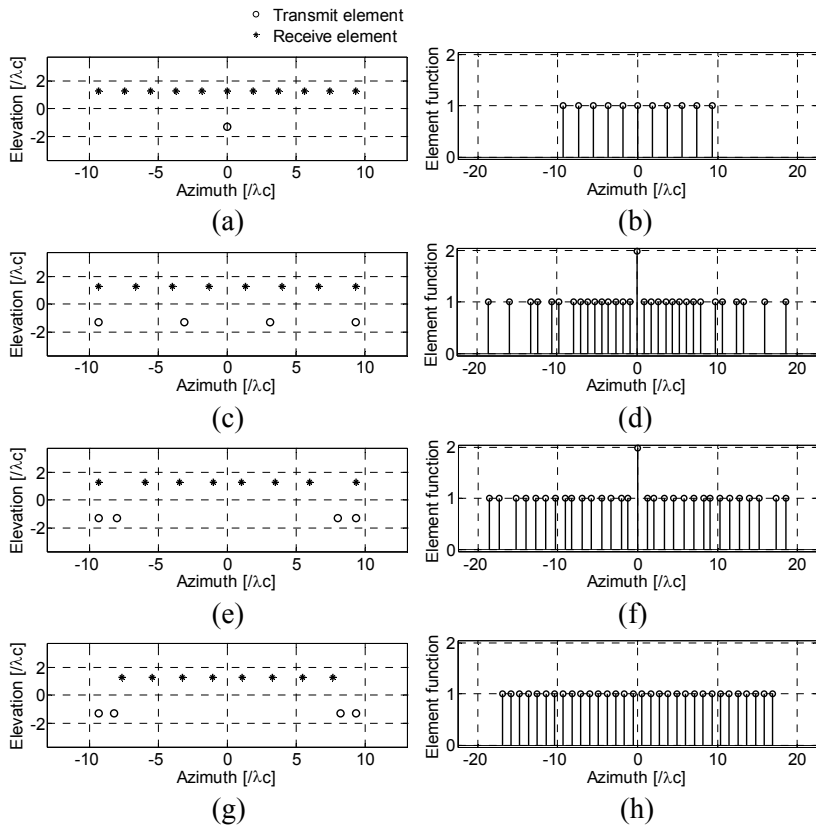


Figure 3.4 Topologies and corresponding effective aperture functions of four linear arrays. Topology (a) and effective aperture (b) of a uniform array with single transmitter, topology (c) and effective aperture (d) of a uniform MIMO array, topology (e) and effective aperture (f) of an optimized non-uniform MIMO array, topology (g) and effective aperture (h) of an array designed using the proposed strategy. All arrays consist of 12 antennas. The last three MIMO arrays have 4 transmit and 8 receive elements.

is larger than the wavelength at center frequency ( $\lambda_c$ ).

Because of the use of a single transmitter, the focusing capability of the first array purely depends on the receive aperture. The effective aperture and spatial sampling of such array is the same as the receive array. The second array uniformly distributes elements along both transmit and receive apertures. This intuitive choice leads to an undesirable effective aperture function. It is much denser at the center than its edge causing comparably worse cross-range resolution and a larger IR region that makes the reduction of grating/side lobe level less effective. The third array is designed

using a direct search optimization process. An ideal wideband beam pattern with a grating/side lobe level of ISL outside mainlobe is applied as an objective (or fitness) function. The optimization program operates iteratively in order to minimize the difference between the current beam pattern and the objective function. In order to fairly compare the arrays the number of transmit/receive elements ( $4 \times 8$ ) is implemented as a constraint during the optimization. As one can observe from its topology and effective aperture function, the irregular sampling shown in the uniform MIMO array is compensated during the optimization process by moving the transmit elements toward the edge while slightly adjusting the positions of receive elements. The second and third arrays both exhibit redundancy within their effective aperture functions.

The topology based on the option II from Figure 3.3 also contains 4 transmit elements, which are placed in two sub-arrays with two elements each. While the receive array is uniform, the two sub-transmit arrays are placed according to the element spacing of the receive aperture. In comparison with the topology shown in Figure 3.4a, the proposed design has a large effective aperture and thus should provide narrower beamwidth. In comparison with two other MIMO topologies, the proposed design avoids non-periodicity in its effective aperture and array redundancy, which results in more efficient use of the antenna elements.

The simulated beam patterns of the four arrays are compared in Figure 3.5. We investigate first the far-field monochromatic characteristics (at the center frequency of 11 GHz). The patterns are estimated at the center frequency by the Fourier transform of the corresponding aperture function [5]. The complete beam pattern of the MIMO array is computed by the product between transmit and receive array patterns [5]. For the proposed array design, grating lobes caused by sparsity of the array are located at the maximal distance from the mainlobe due to the proper correlation between transmit and receive aperture functions. By contrast, the other three arrays exhibit grating lobes closely located to the main beam. The grating lobes can not be efficiently eliminated by the wideband properties of the array. This is shown in Figure 3.5b where array wideband near-field beam patterns are computed. The wideband near-field beam pattern of the MIMO array is computed in the following way. Hertzian dipoles are used as transmit and receive antennas. A 1 cm diameter metal sphere is used as the point scatterer and located in front of the array center at the distance of  $15\lambda_c$ . The scattered electromagnetic field is computed by the applied electromagnetic simulation tool FEKO which utilizes the method of moment (MoM) to solve the integral equations. The simulated signal is obtained in frequency domain over the specified frequency band. It is further transferred into time domain by the fast Fourier transform (FFT). The data from all transceiver pairs are then focused within the near-field of the array aperture using the modified Kirchhoff migration [18]. Two-dimensional point spread function is generated over the cross-range and range. The maximum value along its range dimension is selected to

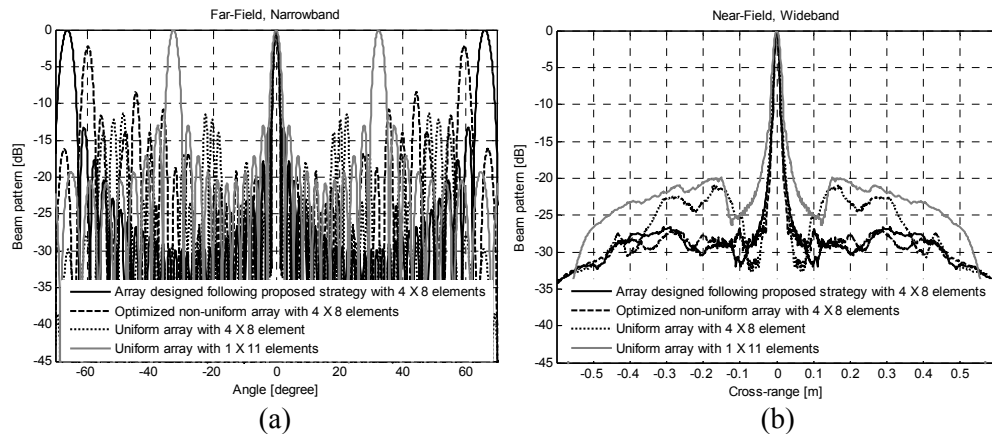


Figure 3.5 Beam patterns of the MIMO arrays (shown in Figure 3.4) under (a) far-field monochromatic, and (b) near-field ( $15 \lambda_c$ ) UWB (150%) conditions. Results are obtained by full-wave numerical simulation.

represent the beam pattern of the array in the near-field.

As one can see, the beam patterns of the proposed topology almost fully satisfy the design specifications: the sidelobe level for the near and far sidelobes is at the level of -30 dB and the beamwidth (at -3 dB level) equals 1.1 cm. The array overperforms the rest of the designs due to the highest resolution, the lowest sidelobe level, and better formed mainlobe focus, which can provide sharper image when facing distributed target in the near-field.

### 3.7 Near-field and bandwidth effects

In this section, we investigate the influence of target distance and bandwidth on the performance of MIMO array. The far-field monochromatic characteristics of the separate transmit and receive array as well as the resulting characteristics of the complete MIMO configuration, are shown in Figure 3.6 for the array designed following the proposed strategy. Due to the correct correlation between transmit and receive arrays, zeros of the transmit radiation pattern are placed at positions of closely located grating lobes resulting from the receive array. However, grating lobes located at higher angles are still prominent due to the overall sparsity of the complete effective aperture.

The narrowband array pattern degrades significantly when the focal point is moved

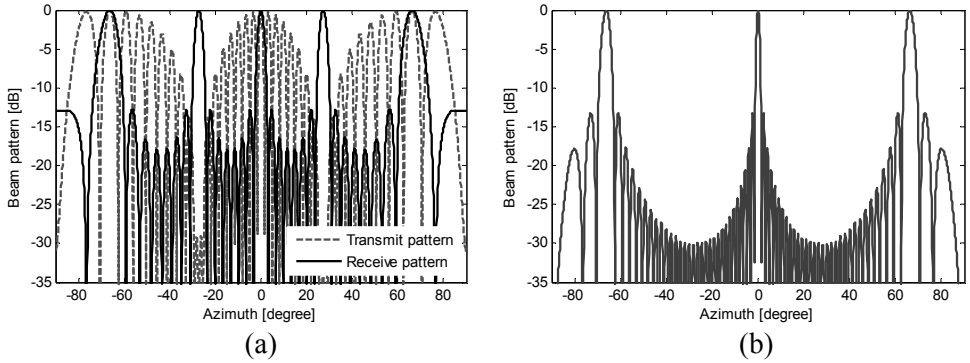


Figure 3.6 Far-field monochromatic characteristics of the MIMO array at 11 GHz. (a) One-way beam patterns of transmit and receive arrays, and (b) two-way beam pattern of the complete array.

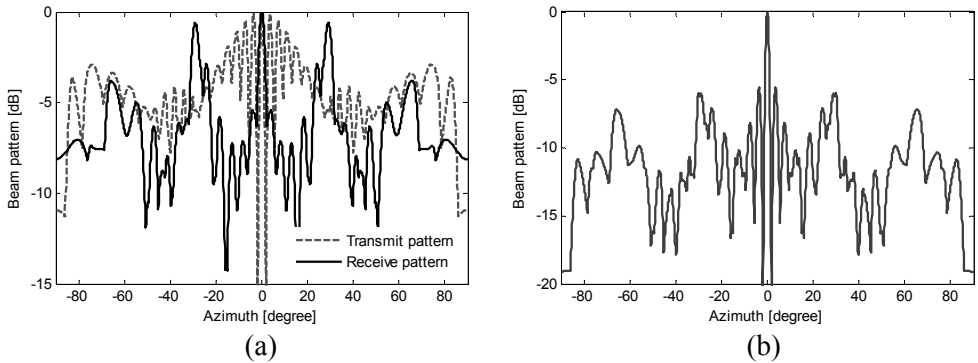


Figure 3.7 Near-field (at the distance of  $20\lambda_c$ ) monochromatic characteristics of the MIMO array at 11 GHz. (a) One-way beam patterns of transmit and receive arrays, and (b) two-way beam pattern of the complete array.

from far-field to the very near-field of the aperture at  $20\lambda_c$  range distance. The beam patterns of the MIMO array in near-field are illustrated in Figure 3.7. The near-field effect causes different changes to the transmit and receive array patterns, respectively. The grating lobes of the receive array are blurred while the zeros in the transmit beam pattern are not well formed. Therefore, closely located grating lobes are not cancelled and we lose further dynamic range for imaging.

Figure 3.8 illustrates the advantage of UWB MIMO array in the near-field of the aperture. The short impulse response of the system reduces in a large extent the appearance of grating lobes in the beam pattern of both transmit and receive arrays. After the convolution between the transmit and receive array's space-time impulse

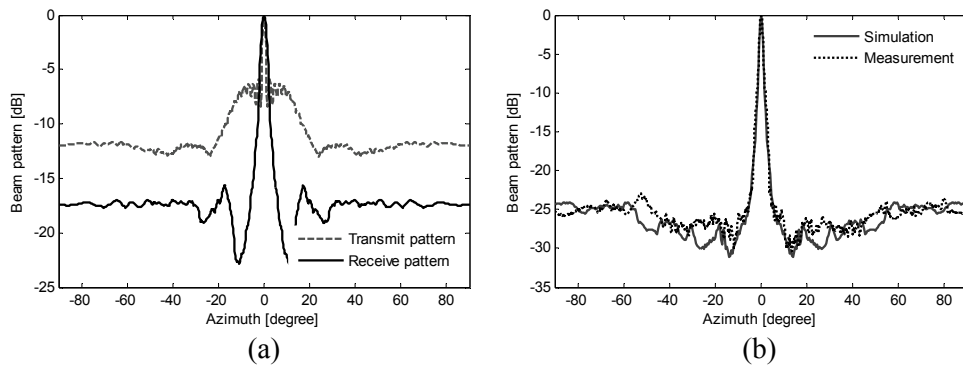


Figure 3.8 Near-field (at the distance of  $20\lambda_c$ ) UWB (150%) characteristics of the MIMO array at center frequency of 11 GHz. (a) One-way beam patterns of transmit and receive arrays, and (b) two-way beam pattern of the complete array obtained by both simulation and measurement.

responses, the complete multistatic array exhibits a rather flat beam pattern and is free of side/grating lobes. The MIMO array constructed with 12 of the designed UWB Vivaldi antennas is measured with network analyzer in anechoic chamber (Figure 3.9). The obtained beam pattern with 150% bandwidth matches with numerical simulation and shows a -25 dB sidelobe level approaching the ideal ISL level.

### 3.8 Experimental results

To test the proposed theory, near-field imaging measurements were performed. The measurement setup is shown in Figure 3.9. In order to avoid problems related to short-term instability (jitter) and limited dynamic range (both typical for time-domain measurements) actual data acquisition has been performed in frequency domain using a network analyzer. Three MIMO arrays based on topologies shown in Figure 3.4 are constructed using antipodal Vivaldi antennas. Vivaldi antenna arrays are popular UWB arrays and details on their design can be found in e.g. [19]-[22]. The chosen antenna element has an aperture size of 45 mm and exhibits consistent UWB characteristics over the frequency band from 2.7GHz to 26 GHz [23]. Array elements are connected to the network analyzer through a multi-port switch. The whole setup is mounted on a computer-controlled mechanical scanner, which allows further elevation scan for 3-D volumetric imaging. The data is collected in frequency-domain by switching through all transmit/receive pairs. It is then transformed to time-domain by inverse Fourier transform (IFFT) and focused using the modified

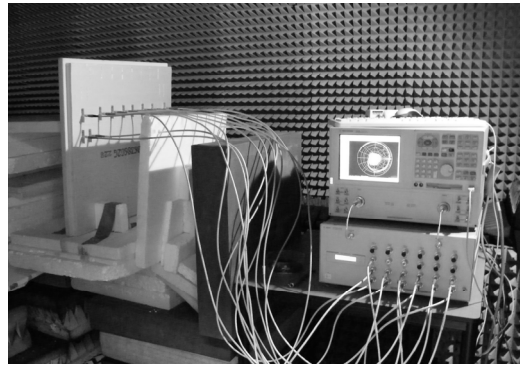


Figure 3.9 Measurement setup with MIMO linear array, multi-port switch and network analyzer in anechoic chamber.

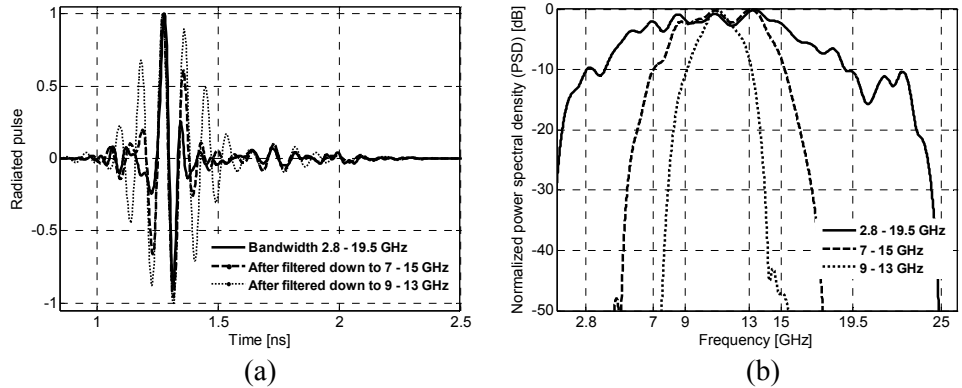


Figure 3.10 Bandwidth of the measurement setup before and after filtering. (a) Radiated impulse, and (b) spectrum after gating of reflections.

Kirchhoff migration [18].

An antenna face-to-face measurement is performed to define the operational bandwidth of the whole setup. The bandwidth of the complete system and its corresponding time-domain impulse after gating of reflections are shown by the solid lines in Figure 3.10. The operational bandwidth at -10 dB level ranges from 2.8 to 19.5 GHz with 16.7 GHz absolute bandwidth and center frequency at 11.15 GHz. The setup achieves 150% fractional bandwidth which fulfills the requirement for demonstrating the proposed UWB-MIMO array. To investigate the effect of bandwidth, band-pass filters are applied to reduce the fractional bandwidth to 72.7% and 36.4% with center frequency unchanged. These are indicated by the dash and dot lines in Figure 3.10. We can observe the increase of pulse duration after the filtering, which would result in an enlarged IR around the mainlobe after beamforming.

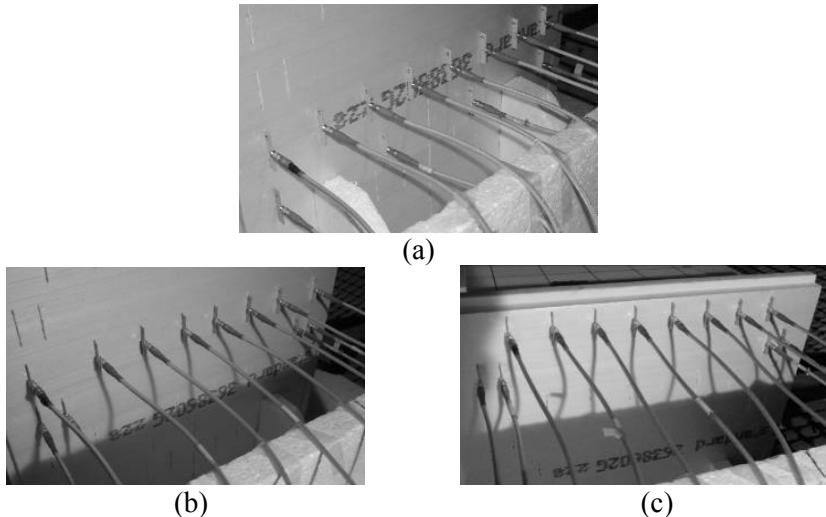


Figure 3.11 Pictures of the three tested MIMO arrays corresponding to the design examples shown in Figure 3.4. (a) uniform MIMO array, (b) optimized non-uniform MIMO array, and (c) array designed using the proposed strategy. All arrays consist of 12 antipodal Vivaldi antennas with 4 transmit and 8 receive elements.

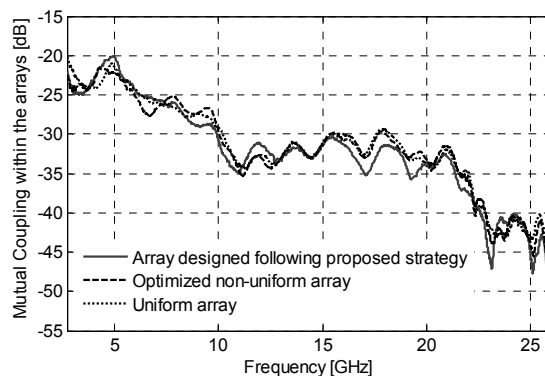


Figure 3.12 Measured mutual coupling within the tested MIMO arrays.

The physical structures of the three MIMO arrays are shown in Figure 3.11. All antenna elements are placed vertically producing vertical polarization (along the elevation plane). The array topologies exactly correspond with the ones shown in Figure 3.4. Mutual coupling of the closely spaced antennas could affect their performance within the array. Extensive measurements are carried out to evaluate its effects. The measured maximal coupling between elements within the three MIMO arrays is demonstrated in Figure 3.12. It is clear that the level of coupling is lower than -20 dB. Moreover, the radiation performance of a single element does not show

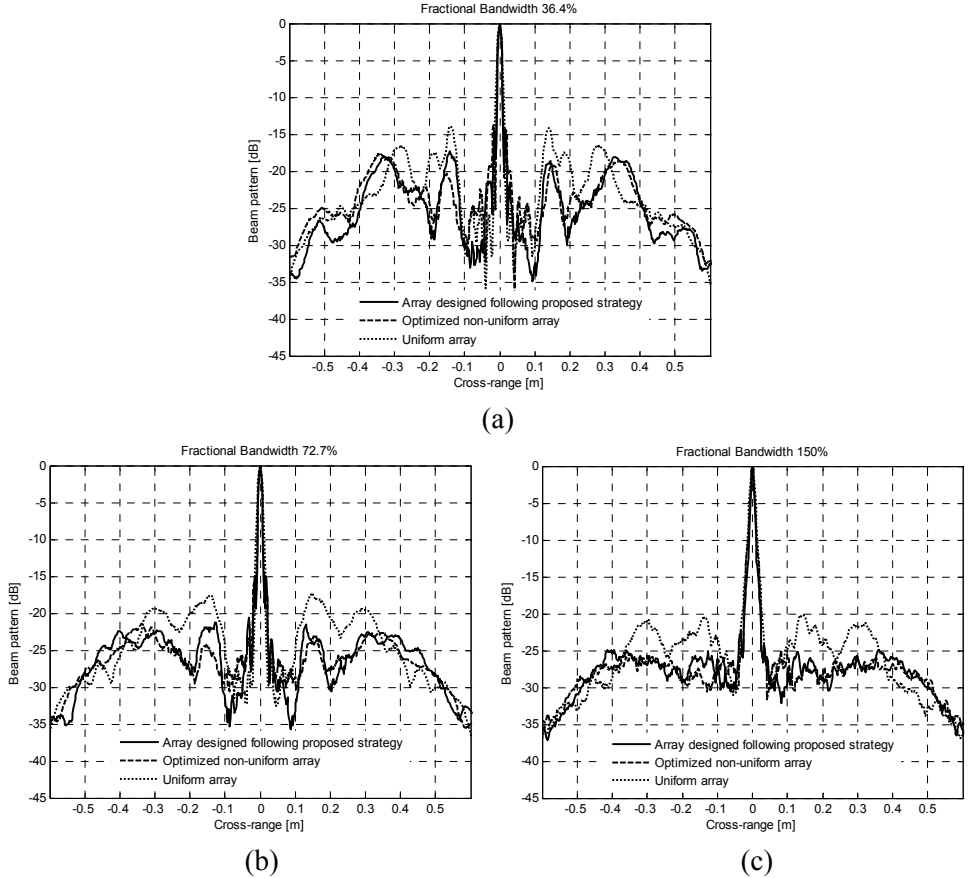


Figure 3.13 Beam pattern of three measured arrays in Figure 3.11 under different fractional bandwidth at (a) 36.4%, (b) 72.7%, and (c) 150%.

difference from that with neighboring elements at both sides. The direct coupling between transmit and receive elements exists only within a short duration after the excitation and can be effectively eliminated by subtraction of pre-recorded array coupling.

Figure 3.13 compares the beam pattern of the three arrays at different level of fractional bandwidth. Measurements are performed with a metal sphere placed at 40 cm range distance in front of the array center. The beam pattern is obtained by taking the maximum level along the range dimension of the focused two-dimensional image. The uniform array (array 1) is not satisfactory in terms of both narrowband and wideband properties and exhibits the highest grating/side lobe level of -20 dB at 150% fractional bandwidth. The performance of two other arrays (array 2 and 3) fit into our expectation. They both have comparable grating/side lobe level at -25 dB.

The array 2 pattern is relative flat due to the applied objective function during optimization which is fixed as constant ISL level over the azimuth outside the main beam. However, this also causes its mainlobe less ideal than the one from array 3. Both array 1 and array 2 exhibit approximately 5.4 dB grating/side lobe reduction when the fractional bandwidth increases from 36.4% to 150%. By contrast, the array 3 is able to take full advantage from the increasing bandwidth with 8.36 dB reduction under the same circumstances. The patterns obtained by measurement matches with our previous simulation shown in Figure 3.5(b). Among the three arrays, the array 3 provides the highest cross-range resolution of 1 cm (1.43 degree beamwidth). The array 1 has the least resolving capability of 1.4 cm due to its heavy weighting at the aperture center.

The differences between array patterns would have greater impact when the array faces targets with larger spatial dimensions. This is due to the fact that the resulting image represents the integration of the array PSF with the object space, which is indicated by equation (3.10). All three arrays are tested with a small distributed target as shown in Figure 3.14. A pair of scissors is placed horizontally at the same height in front of the array with 40 cm range distance from the antenna aperture. Under such imaging geometry, resolving capability in the cross-range direction is provided by the array aperture while the down-range is supported by the bandwidth of the transmitted signals. The results illustrate the importance of array design to the quality of the resulting image. The scissors can hardly be recognizable using array 1. The closely located grating/side lobes easily destroy the shape of the weak part of the target by interacting destructively or constructively with the real target responses. The arrays 2 and 3 both provide satisfactory reconstruction of the shape while the array 3 is exhibiting fewer artifacts. Comparing the three array designs, the proposed design strategy is clearly favorable in practice due to both simpler design procedure and superior array pattern / target reconstruction.

### **3.9 Summary**

In this chapter, we combined the advantages of a large operational bandwidth and MIMO technology to develop linear sparse arrays for short-range imaging. We showed that implementation of a multistatic approach in imaging instead of the classical monostatic one results in an additional reduction of amount of antenna elements while keeping similar beam patterns. The equivalence between MIMO array and classical arrays in terms of beam patterns and array topologies is demonstrated. The equivalence is exactly valid in the array far-field, however numerical simulations shows that the equivalence becomes quite accurate from the range of about half of the array aperture size. Furthermore, it is shown that by factorization of the equivalent array topology into topologies of the transmit and

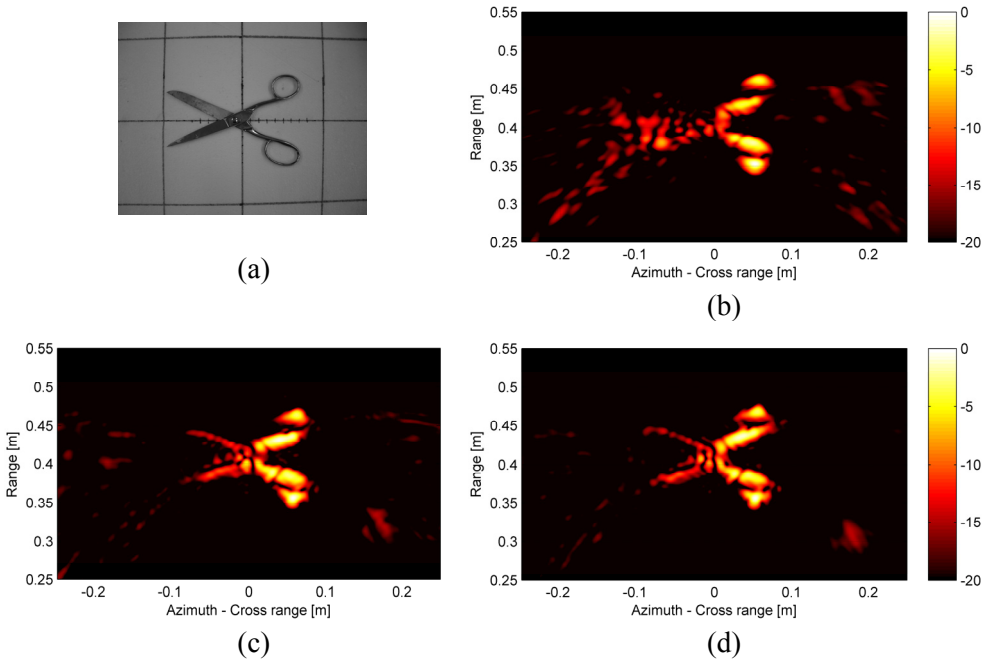


Figure 3.14 Two-dimensional image of a pair of scissors placed horizontally in front of the array aperture at 40 cm range. (a) Photo of the target, (b) image from the uniform array, (c) image from the non-uniform array, and (d) image from the array designed using the proposed strategy.

receive sub-arrays a classical array can be replaced with a MIMO one with similar beam patterns but with a smaller number of elements. The factorization procedure is not unique and allows for multiple solutions. The best solution is the one which has the smallest differences of spreading loss among its transceiver pairs and exhibits the least mutual coupling. Combination of both approaches allows for reaching the required sidelobe level with significantly fewer number of array elements in comparison with the classical (narrowband and monostatic) approach.

For demonstration of the theory, we implemented the proposed approach for a linear array design. The array is intended for the use within a concealed weapon detection system, in which a high-resolution imaging is performed as an intermediate step. The system should achieve sub-centimeter resolution using only 12 antennas. We experimentally compared the performances of three UWB MIMO arrays with different topologies: uniform topology, non-uniform topology numerically optimized to achieve the lowest sidelobe level and topology determined based on the approach described above. The array's beam patterns are investigated under different fractional bandwidth. The results confirm the decisive influence of the fractional bandwidth,

and show that the array designed following the proposed approach is superior to the uniform and numerically optimized non-uniform arrays (the antenna array with suggested topology achieves 1.4 degree beamwidth at -3 dB level and -25 dB grating/side lobe level with only 12 antenna elements). This conclusion is further supported by the analysis of 2-D images of distributed targets produced by the arrays.

## References

- [1] J. Li, P. Stoica, *MIMO Radar Signal Processing*, Wiley-IEEE Press, 2008.
- [2] O. T. Von Ramm, S. W. Smith, and F. L. Thurstone, “Grey scale imaging with complex TGC and transducer arrays,” in *Proc. Soc. Photo-Opt. Inst. Eng., Med. IV*, 1975, vol. 70, pp. 266-270.
- [3] C. R. Cooley, B. S. Robinson, , “Synthetic Focus Imaging Using Partial Datasets,” in *Proc. Ultrasonic Symposium*, 1994, vol. 3, pp. 1539-1542.
- [4] R. T. Hoctor and S. A. Kassam, “Synthetic aperture ultrasonic imaging system using a minimum redundancy phased array,” U.S. Patent 5 278 757, Jan. 11, 1994.
- [5] G. R. Lookwood, P.C. Li, M. O'Donnell, and F. S. Foster, “Optimizing the Radiation Pattern of Sparse Periodic Linear Arrays,” *IEEE Trans. Ultrason., Ferroelectr. Freq. Control*, vol. 43, pp. 7-14, Jan. 1996.
- [6] E. Fishler, A. Haimovich, R. Blum, D. Chizhik, L. Cimini, and R. Valenzuela, “MIMO radar: An idea whose time has come,” in *Proc. IEEE Radar Conf.*, Apr. 2004, pp. 71–78.
- [7] E. Fishler, A. Haimovich, R. Blum, L. Cimini, D. Chizhik, and R. Valenzuela, “Spatial diversity in radars — models and detection performance,” *IEEE Trans. Signal Process.*, vol. 54(3), pp. 823–838, Mar. 2006.
- [8] T. Aittomaki and V. Koivunen, “Low-complexity method for transmit beamforming in MIMO radars,” in *Proc. 2007 IEEE Int. Conf. Acoustics, Speech, and Signal Processing (ICASSP)*, Honolulu, USA, Apr. 2007, pp. II 305-308.
- [9] I. Bekkerman and J. Tabrikian, “Target detection and localization using MIMO radars and sonars,” *IEEE Trans. Signal Process.*, vol. 54, pp. 3873–3883, Oct. 2006.

- 
- [10] D. W. Bliss, and K. W. Forsythe, "Multiple-input multiple-output (MIMO) radar and imaging: Degrees of freedom and resolution," *IEEE Trans. Ultrason., Ferroelectr. Freq. Control*, vol. 43, pp. 7-14, Jan. 1996.
  - [11] K. W. Forsythe, D. W. Bliss, and G. S. Fawcett, "Multiple-input multiple-output (MIMO) radar: Performance issues," in *Proc. 38th Asilomar Conf. Signals, Systems and Computers*, Pacific Grove, CA, Nov. 2004, vol. 1, pp. 310–315.
  - [12] J. Li and P. Stoica, "MIMO radar with collocated antennas: Review of some recent work," *IEEE Signal Process. Mag.*, vol. 24(5), pp. 106–114, Sep. 2007.
  - [13] L. Xu and J. Li, "Iterative generalized likelihood ratio test for MIMO radar," *IEEE Trans. Signal Process.*, vol. 55(6), pp. 2375–2385, Jun. 2007.
  - [14] J. Li, P. Stoica, L. Xu, and W. Roberts, "On parameter identifiability of MIMO radar," *IEEE Signal Process. Lett.*, vol. 14(12), pp. 968–971, Dec. 2007.
  - [15] D. R. Fuhrmann and G. San Antonio, "Transmit beamforming for MIMO radar systems using partial signal correlations," in *Proc. 38th Asilomar Conf. Signals, Systems and Computers*, Pacific Grove, CA, Nov. 2004, vol. 1, pp. 295–299.
  - [16] P. Stoica, J. Li, and Y. Xie, "On probing signal design for MIMO radar," *IEEE Trans. Signal Process.*, vol. 55(8), pp. 4151–4161, Aug. 2007.
  - [17] D.H. Turnbull, F.S. Foster, "Beam Steering with Pulsed Two-Dimensional Transducer Arrays," *IEEE Trans. Ultrason., Ferroelectr. Freq. Control*, vol. 38, pp. 320-333, Jul. 1991.
  - [18] X. Zhuge, A. G. Yarovoy, T. G. Savel'yev, and L. P. Ligthart, "Modified Kirchhoff Migration for UWB MIMO Array-Based Radar Imaging," *IEEE Trans. Geosci. Remote Sens.*, vol. 48, pp. 2692-2703, Jun. 2010.
  - [19] J. D. S. Langley, P. S. Hall, and P. Newham, "Balanced antipodal Vivaldi antenna for wide bandwidth phased arrays," *IEE Proc. -Microw. Antennas Propag.*, vol. 143, pp. 97-102, Apr. 1996.
  - [20] T. L. Korzeniowski, "A 94 GHz Imaging Array Using Slot Line Radiators," *Electronic Doctorial Dissertations for UMass Amherst*, Jan. 1985.
  - [21] D. H. Schaubert, S. Kasturi, A. O. Boryssenko, and W. M. Elsallal, "Vivaldi antenna arrays for wide bandwidth and electronic scanning," in *Proc. EuCAP 2007*, Feb 2008, pp. 1-6.

- [22] M. Chiappe, and G. L. Gragnani, “Vivaldi Antennas for Microwave Imaging: Theoretical Analysis and Design Considerations,” *IEEE Trans. Instrum., Meas.*, vol. 55, pp. 1885-1891, Nov. 2006.
- [23] X. Zhuge, A. G. Yarovoy, L. P. Lighthart, “Circularly Tapered Antipodal Vivaldi Antenna for Array-Based Ultra-Wideband Near-Field Imaging,” in *Proc. European Radar Conference (EuRAD)*, Sep. 2009, pp. 250-253.

## CHAPTER 4

# TWO-DIMENSIONAL PLANAR MIMO ARRAYS

Two-dimensional (2-D) planar transducer arrays offer the potential for generating symmetrically focused electromagnetic beams that can be steered throughout a three-dimensional volume. Because a linear array is limited to focusing and steering only along the array direction, it has been long realized that the development of 2-D transducer arrays is the essential step to achieve instant resolving capabilities in both lateral directions. The major problem facing the development of 2-D arrays for imaging is the complexity arising from the large number of elements required in such systems. The cost of a fully populated high-resolution planar array which maintains half-wavelength element spacing in the two array directions is almost prohibitive for any commercial applications at this moment.

As we have demonstrated in the previous chapters, combination of MIMO and UWB offers a valid solution for reducing the number of elements needed to achieve the required resolution and dynamic range for imaging. Based on the hybrid approach, this chapter aims to further extend the MIMO-UWB array design approach to full 2-D dimensions. By exploiting the fundamental properties of planar arrays, we investigate several 2-D MIMO array methodologies which offer sound imaging capabilities over the complete three-dimensional space. Examples of proposed 2-D arrays are first analyzed in terms of resolution and side/grating lobe level by numerical simulation and verified by experimental measurements. Imaging of distributed targets further demonstrates the capabilities of the proposed UWB 2-D MIMO approach for real-time imaging applications.

The chapter is organized as follows. Reviews of existing theories regarding 2-D transducer arrays are presented in section 4.1. Influences of array redundancy and element shadowing are discussed in section 4.2. In section 4.3, three types of 2-D design strategies for two-way MIMO array design are introduced and analyzed. In section 4.4, experimental results of sparse 2-D arrays designed following the introduced approaches are presented and compared. The chapter is summarized in the last section.

## 4.1 Review of existing theories

For many who design microwave imaging systems, the ultimate goal is to obtain images that can closely resemble the pictures from an optical device. A real-time 3-D volumetric imaging system which provides image resolution analogous to that of the human eye remains the ideal device for microwave imaging. Under monochromatic condition, element spacing must be no further than one-half of a wavelength  $\lambda/2$ , (and in the near field even  $\lambda/4$ ) in order to prevent unwanted grating lobes. It is well known that high level grating lobes can severely reduce the contrast and dynamic range available for imaging, and in extreme cases produce overlapping multiple images of the same target. By satisfying the half (quarter)-wavelength criterion one must utilize an extremely dense array to achieve a moderate aperture size and resolution. For example, to achieve a centimeter resolution at 1 meter range, an array aperture needs to be at least a hundred times of a wavelength along both azimuth and elevation. In order to control its beam steering capability, this 2-D array will need to be filled with over  $201 \times 201$  (40401) elements. Unfortunately, fabrication of such a dense array and its associated beamforming electronics is still unrealistic using existing microwave technology.

To circumvent above-mentioned difficulties, significant efforts have been made to investigate the capabilities of sparse 2-D arrays. A typical approach to avoid appearance of grating lobes is through periodicity reduction by either randomly or non-uniformly arranging the array elements [1]-[4]. Although aperiodic array does not produce grating lobes, high level pedestal sidelobes are quite often found due to the drastic thinning process [5]. Besides an increase in the average sidelobe level, there is also an indicated loss in transducer gain associated with random sparse arrays [2].

Additional opportunity for array thinning lies in use of MIMO approach. Lockwood et al. proposed a framework for sparse 2-D array design by selecting different element spacing for transmit and receive elements [6]. Smith et al. investigated several representative 2-D array configurations under far-field condition using fast Fourier transform methods [7]. In [8], Schwartz further recommended curvilinear rather than rectilinear or random element distributions along with transmit and receive arrays for designing 2-D pulse-echo arrays. A few W-band multistatic 2-

D array topologies are proposed in [9], the performance of which has been demonstrated by bi-static SAR measurements.

Following the previous chapter, our goal is to introduce a design approach or strategy to obtain desired effective aperture functions for 2-D MIMO arrays, which can be a challenging task. Numerical methods could be applied to either directly optimize the beam pattern or minimize the difference between the effective aperture and a desired aperture function. Due to the high dimension nature of the 2-D array problem, optimization requires tremendous computation and time. Moreover, it quite often results in sparse arrays that are no better than arrays with randomly selected elements in practice [10]. Other existing planar array design methods are commonly based on rotational 1-D array analysis. According to the projection slice theory [11], the projection of array elements onto a rotated axis at certain angle within the array plane determines the pattern of the planar array at that particular angular cut. The traditional method first designs linear transmit/receive arrays whose effective array is able to fit into the design specification, then the designer tries to fill the fixed 1-D array into a two dimensional plane using different strategies.

Under the condition that the number of antennas within the array is highly limited, a compromised choice of design is to optimize the beam pattern only along two orthogonal planes. Therefore, the effective aperture function is arranged to assign all its available degrees of freedom to the two principle planes. As the result, the array performance other than these two optimized planes suffers significantly from beam pattern degradation. Although post-processing algorithm is able to improve the resulting image [12], it requires higher computational cost and complicated implementation which could limit its application in practice.

## 4.2 Array redundancy and element shadowing

In a multistatic array, each transmit/receive pair is associated with a synthetic virtual element located at the midpoint of the two corresponding transceivers. All the virtual elements together form the midpoint synthetic aperture. In the far-field, the virtual element has the exactly the same elementary Green's function as the associated transmit/receive pair. When it comes to the near-field of the array, such relation is approximate, with the phase front of the virtual element remains spherical while the real antenna pair turns to ellipsoidal. Although such approximation results in a moderate deviation of beam pattern in the near-field between the MIMO array and its synthetic aperture [13], the similarity between the two is still prominent allowing the synthetic aperture to be applied as a design tool [14].

The number of virtual elements within the MIMO array can be considered as a degree of freedom in terms of controlling the array pattern. The higher the control freedom, the better we are able to suppress the grating/side lobe level. For an array

with  $N_{Tx}$  transmit and  $N_{Rx}$  receive antennas, the maximum number of virtual elements is their multiplication  $N_{Tx} \cdot N_{Rx}$ . Array redundancy exists when two virtual elements overlap spatially within the two-dimensional synthetic aperture of the MIMO array, causing the total number of virtual elements to be less than  $N_{Tx} \cdot N_{Rx}$ . Such phenomenon causes the array to lose control freedom and thus reduce the dynamic range for imaging. During the beamforming process the overlapping elements' ellipsoidal projections not only collide within the focus region but also throughout the entire visible image space. Therefore, such overlapping elements make no contribution in terms of improving the mainlobe and sidelobe ratio.

While array redundancy can be easily eliminated by simply avoiding overlapping virtual elements, element shadowing is more difficult to control. Element shadowing can be seen as redundancy in certain direction. It appears when more than three elements overlap along one spatial dimension. In three-dimensional imaging, the interception of impulses will increase its dimension from points to arcs due to the fact that the projection is no longer ellipse but ellipsoid. And any two ellipsoid's interception in a 3-D space will be an arc through the half visible space. This arc will be located along the orthogonal plane to the line that connects the corresponding two virtual elements. Since any two virtual elements will be aligned along certain direction, it is the third possible colliding element that shall be carefully avoided. The preferred array shall distribute its control freedom uniformly over the entire rotational angles.

Figure 4.1 illustrates how element shadowing affects the array performances. By comparing the linear and rectangular array, we can see that element shadowing doesn't necessarily lead to an increased grating/side lobe level if all the elements are still weighted the same. However, with 21 times the total number of array elements in the rectangular array, the grating/side lobe level along the azimuth direction is still -25 dB which is much worse than its full potential ISL. Apparently plenty of control freedoms have been wasted along this direction. The cross array, also known as Mill's cross [15], represents the worst case scenario where one of the elements is over weighted in the azimuth plane causing severe performance degradation.

Different strategies of one-way phased array design have been proposed in order to reduce periodicity. This property coincides with the purpose to avoid element shadowing. Among the existing one-way array methods, the Fibonacci Spiral has shown consistent capability to avoid element shadowing due to its nature in terms of lack of transitional periodicity [16]. Meanwhile, such logarithmic spiral lattice is also able to maintain a substantial uniform cell size per element. The arrangement of the array elements is defined by the polar equation:

$$\begin{aligned} r &= \frac{d}{\sqrt{\pi}} \sqrt{n} & n = 1, \dots, N \\ \theta &= 2\pi \tau n \end{aligned} \quad (4.1)$$

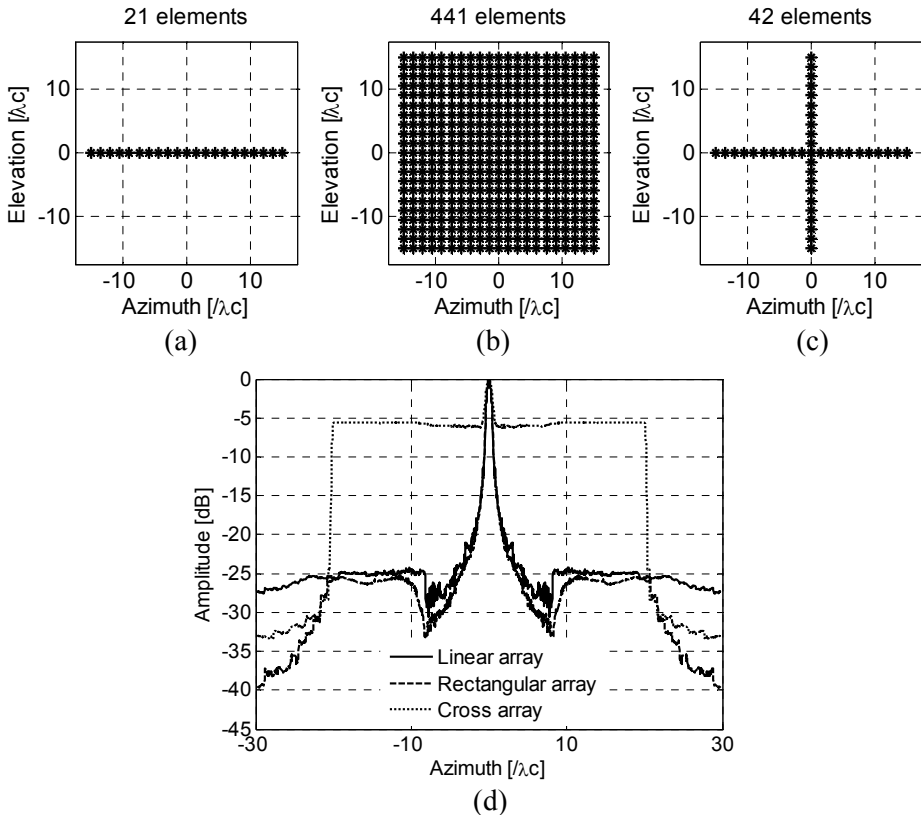


Figure 4.1 Effect of element shadowing. (a) Uniform linear array, (b) uniform rectangular array, (c) Mill's cross array, and (d) comparison among their beam pattern along the azimuth with focal point in the near-field at  $20\lambda_c$ , aperture size of  $30\lambda_c$ , and 150% fractional bandwidth.

where  $n$  is the number of elements, and  $d$  is the equivalent element spacing between adjacent elements.  $\tau$  is the golden ratio  $\frac{1+\sqrt{5}}{2} \approx 1.618$ , which prevents the repetition of rotation angles due to its properties of ‘continued fraction’.

Figure 4.2 demonstrates the improvement of near-field one-way array pattern when element shadowing can be carefully handled. With overall uniform control freedom over all the rotational angles, the array arranged according to the Fibonacci formula shows lower grating/side lobe level than the regular rectilinear array under the same aperture size and number of elements. Therefore, the design objective of two-way planar MIMO array is to select transmit and receive aperture functions that will together result in an effective aperture function which is able to mimic the properties of the logarithmic spiral lattice.

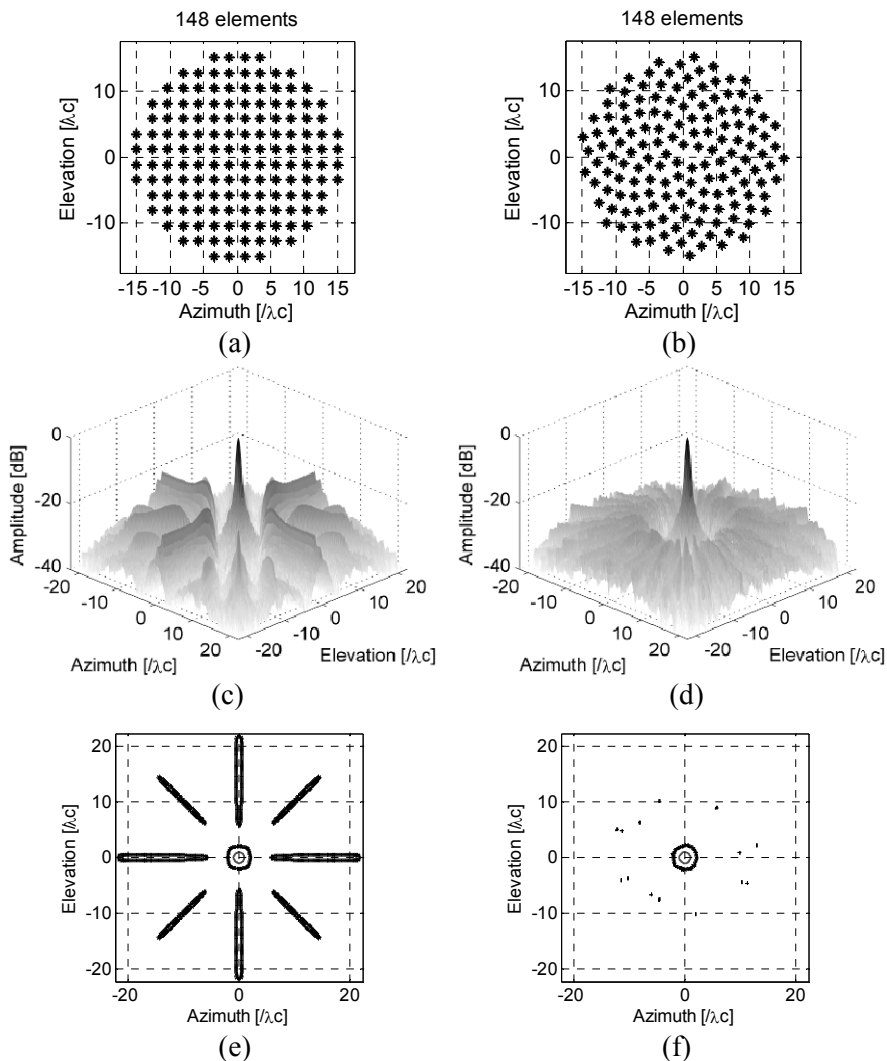


Figure 4.2 Comparison of one-way array pattern between periodic rectilinear array and spiral lattice array with the same number of array elements and aperture size. The focal point is placed in the array near-field at  $20 \lambda_c$  with 150% fractional bandwidth. (a) Element distribution within the rectilinear aperture, (b) element distribution within the spiral aperture, (c) beam pattern of rectilinear aperture including responses to -40 dB, (d) beam pattern of Spiral aperture including responses to -40 dB, (e) Contour plot of the rectilinear beam pattern to show -25 dB beam width, and (f) Contour plot of the Spiral beam pattern to show -25 dB beam width.

## 4.3 Two-dimensional design methodologies

In this section, three different 2-D design strategies are proposed and analyzed. Comparing with existing methods, the proposed design procedure begins directly from 2-D planar array using the synthetic aperture function. This brings us towards more efficient design methodologies by avoiding the 1-D to 2-D expansion procedure that often leads to either the compromise of performance or the increase of cost of the resulting array.

### 4.3.1 Equivalent uniform rectilinear array

In this section, we further extend the factorization approach introduced in Chapter 3 to two-dimensional array conditions. As we have demonstrated earlier, to avoid the appearance of closely located grating/side lobes, a uniformly distributed effective aperture function is preferred. The effective array can be seen as a mutual repetition between transmit and receive arrays. Therefore, our primary design objective is to build up a rectilinear synthetic aperture by properly assembling the transmit/receive apertures over the 2-D plane. The key step is to factorize a 2-D rectilinear uniform effective aperture function into the topologies of transmit and receive arrays.

Assuming the element spacing within the receive array along the two orthogonal directions are  $\Delta_x$  and  $\Delta_y$ , a uniform receive aperture function can be defined as

$$w_{Rx} = \left\{ (\mathbf{r}_{Rx}, w(\mathbf{r}_{Rx})) \middle| \begin{array}{l} \mathbf{r}_{Rx}[x] = [-m_x \cdot \Delta_x : \Delta_x : m_x \cdot \Delta_x] \\ \mathbf{r}_{Rx}[y] = [-m_y \cdot \Delta_y : \Delta_y : m_y \cdot \Delta_y] \end{array}, w(\mathbf{r}_{Rx}) = 1 \right\} \quad (4.2)$$

where  $m_x = (N_{Rx\_x} - 1)/2$  and  $m_y = (N_{Rx\_y} - 1)/2$  are real numbers, and  $N_{Rx\_x}$ ,  $N_{Rx\_y}$  represent the number of array elements along the two principle planes within the receive array. If a single transmitter is to be located at  $(n_x \cdot \Delta_x, n_y \cdot \Delta_y)$ , the resulting synthetic aperture function would become

$$S_{AP} = \left\{ (\mathbf{r}_{SAP}, w(\mathbf{r}_{SAP})) \middle| \begin{array}{l} \mathbf{r}_{SAP}[x] = \left[ \frac{-m_x + n_x}{2} \cdot \Delta_x : \frac{\Delta_x}{2} : \frac{m_x + n_x}{2} \cdot \Delta_x \right] \\ \mathbf{r}_{SAP}[y] = \left[ \frac{-m_y + n_y}{2} \cdot \Delta_y : \frac{\Delta_y}{2} : \frac{m_y + n_y}{2} \cdot \Delta_y \right] \end{array}, w(\mathbf{r}_{SAP}) = 1 \right\} \quad (4.3)$$

Each of the transmit elements creates a half scaled replication of the same receive aperture. In order to combine these sub-synthetic apertures from each transmit element to form a uniform aperture, the distances between transmitters along two planes,  $D_{Tx\_x}$  and  $D_{Tx\_y}$ , needs to be adjusted as

$$\begin{aligned} D_{Tx\_x} &= (2 \cdot m_x + 1) \Delta_x \\ D_{Tx\_y} &= (2 \cdot m_y + 1) \Delta_y \end{aligned} \quad (4.4)$$

The resulting effective aperture from such setting will be uniform along both principle directions, and has the same element spacing as the receive array. If one wants to create a denser effective aperture, sub-arrays within the transmit aperture can be introduced. By applying equation (4.4) for the two planes between the sub-array and receive array, the relation between the spacing within each sub-array  $\Delta'_x$ ,  $\Delta'_y$  and the ones of the receive array can be derived as

$$\begin{aligned} \Delta'_x &= \Delta_x / n_{subTx\_x} \\ \Delta'_y &= \Delta_y / n_{subTx\_y} \end{aligned} \quad (4.5)$$

where  $n_{subTx\_x}$  and  $n_{subTx\_y}$  are the number of elements within each transmit sub-array along the two planes. By introducing the sub-array, the element spacing would be reduced to  $\Delta_x / n_{subTx\_x}$  and  $\Delta_y / n_{subTx\_y}$  for the resulting effective aperture. The width of the effective aperture  $L_{EAP\_x}$  and  $L_{EAP\_y}$  along the two planes, depending on the number of transmit sub-arrays  $N_{subTx\_x}$  and  $N_{subTx\_y}$ , can be evaluated as

$$\begin{aligned} L_{EAP\_x} &= \frac{\Delta_x}{n_{subTx\_x}} \cdot [N_{Rx\_x} \cdot n_{subTx\_x} \cdot N_{subTx\_x} - 1] \\ L_{EAP\_y} &= \frac{\Delta_y}{n_{subTx\_y}} \cdot [N_{Rx\_y} \cdot n_{subTx\_y} \cdot N_{subTx\_y} - 1] \end{aligned} \quad (4.6)$$

The transmit aperture function can be explicitly expressed as

$$w_{Tx} = \left\{ \begin{array}{l} \left( \mathbf{r}_{Tx}, w(\mathbf{r}_{Tx}) \right) \left| \begin{array}{l} \mathbf{r}_{Tx}[x] = [\mathbf{r}_{subTx\_x} - n_x \cdot D_{Tx\_x} : D_{Tx\_x} : \mathbf{r}_{subTx\_x} + n_x \cdot D_{Tx\_x}] \\ \mathbf{r}_{Tx}[y] = [\mathbf{r}_{subTx\_y} - n_y \cdot D_{Tx\_y} : D_{Tx\_y} : \mathbf{r}_{subTx\_y} + n_y \cdot D_{Tx\_y}] \\ w(\mathbf{r}_{Tx}) = 1 \end{array} \right. \end{array} \right\} \quad (4.7)$$

where

$$\begin{aligned} \mathbf{r}_{subTx\_x} &= [-n'_x \cdot \Delta'_x : \Delta'_x : n'_x \cdot \Delta'_x] \\ \mathbf{r}_{subTx\_x}' &= [-n'_x \cdot \Delta'_x : \Delta'_x : n'_x \cdot \Delta'_x] \end{aligned} \quad (4.8)$$

represent the element positions within the transmit sub-array, with

$$\begin{aligned} n_x &= (N_{subTx\_x} - 1)/2, \quad n_y = (N_{subTx\_y} - 1)/2, \\ n'_x &= (n_{subTx\_x} - 1)/2, \quad n'_y = (n_{subTx\_y} - 1)/2. \end{aligned} \quad (4.9)$$

Equations in (4.4) to (4.7) describe the arrangement of transmit array relative to the receive array and their element spacings for arbitrary combination of the number of transmit and receive elements so that a uniform rectilinear synthetic aperture can be achieved. By going around the deconvolution process using the synthetic aperture concept, this strategy produces a uniformly distributed rectilinear effective aperture with no redundancy within the MIMO array. The arrangement proposed above effectively separates the aperture functions in terms of two major axes as

$$\begin{aligned} w_{Tx}(\mathbf{r}) &= w_{Tx}(x) \cdot w_{Tx}(y) \\ w_{Rx}(\mathbf{r}) &= w_{Rx}(x) \cdot w_{Rx}(y) \end{aligned} \quad (4.10)$$

Under such condition, the two-way wideband effective aperture will turn into separable function in its own by

$$\begin{aligned} E_{AP}(\mathbf{r}) &= \{w_{Tx}(x) \cdot w_{Tx}(y)\} * \{w_{Rx}(x) \cdot w_{Rx}(y)\} \\ &= \{w_{Tx}(x) * w_{Rx}(x)\} \cdot \{w_{Tx}(y) * w_{Rx}(y)\} \\ &= E_{AP}(x) \cdot E_{AP}(y) \end{aligned} \quad (4.11)$$

Therefore, the effective aperture can be separable in terms of two principle dimensions under the condition that the transmit and receive aperture functions are both separable. Such condition means that the array pattern outside the two major axes will not be worse than the two principle planes. The performance of the 2-D MIMO array over the complete 3-D image space can be ensured if the designs of both axes are properly specified.

A design example following this approach is illustrated in Figure 4.3. The complete MIMO array consists of 25 elements with 9 transmitters and 16 receivers. Note that the transmit array and the receive array are interchangeable without influencing the beam pattern due to the principle of reciprocity. The transmit array has 4 sub-arrays, each of which produces a quarter of the resulting effective aperture. As we can see, the synthetic aperture function is exactly a half scaled version of the effective aperture obtained by 2-D convolution. To access the uniformity of the resulting effective aperture, Voronoi diagram is used to define unit cells for each virtual element within the effective array. The Voronoi diagram divides the effective aperture into element cells within which all points are closer to the specific virtual element than any other element. It is important to maintain a uniform effective aperture in order to obtain smooth phase shifts among all adjacent transceiver pairs within the MIMO array, and avoid phase jumps so that grating lobes can be placed as far as possible from the mainlobe. As we can see from the figures, the effective aperture of the array following this strategy is completely uniform over the 2-D plane. Near-field beam pattern of the array under 150% fractional bandwidth for both center and edge scanning positions are further investigated. No grating plateau is visible despite the fact that the average element spacing along two principle direction is over  $2.7\lambda_c$ . However, due to the ignorance of element shadowing during the design process, element shadowing effect is prominent. The wide -22 dB beamwidth shown

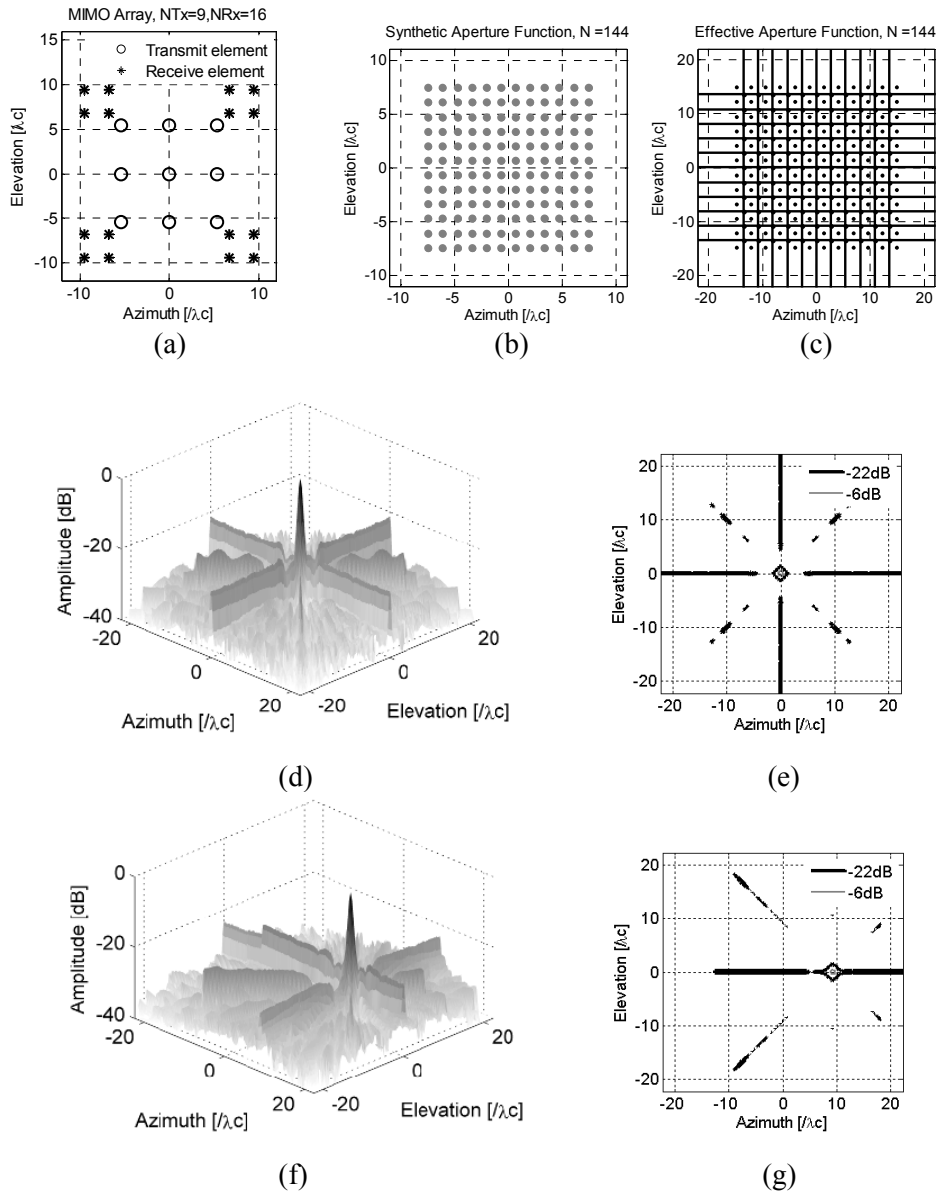


Figure 4.3 Equivalent uniform rectilinear array. (a) Array topology with 9 transmit and 16 receive elements. The transmit array includes 4 sub-arrays. (b) Synthetic aperture function, (c) effective aperture function by Voronoi diagram. (d) Beam pattern at center position  $(0, 20\lambda_c)$ , (e) contour plot of beam pattern at center position. (f) Beam pattern at edge position  $(9.5\lambda_c, 20\lambda_c)$ , (g) contour plot of beam pattern at edge position.

in Figure 4.3(e) and (g) indicates that control freedom of the entire two-way array is not fairly distributed over all angular cuts. Elements are shadowing each other along the two principle directions as well as at  $\pm 45$  degree angles. It causes a degraded control capability from the 2-D array along these lateral directions, and results in comparably higher sidelobe level and larger sidelobe size. Experience learned from one-way arrays (Figure 4.2) indicates that measures shall be taken in order to evenly distribute the control freedoms of the 2-D array over the complete angular plane.

### 4.3.2 Curvilinear composed array

Based on the performance of the rectilinear design, it is clear that element shadowing in a planar array configuration should be carefully handled in order to improve the array performance. To avoid certain geometric properties, we need to use designs which are uniform (no array redundancy) but less periodic in the two-dimensional space. Circle is an ideal geometry that can be consistent in terms of rotational properties. No matter which angle we look from, the circle will always have the same projection function. Of course, this is under the assumption that the sampling of the circle is dense enough, which is commonly not the case for sparse array. Moreover, the projection of a single circle tends to be over sampled at the edge of its projection than the center area, causing unwanted weighting function to the aperture. On the other hand, curvilinear geometries, such as the multiple ring and spiral, are able to maintain a uniform structure over the rotational angle and minimize element shadowing. Their geometric properties allow the array to maintain as much control freedom as possible in every projected axis over the 2-D space. Although the density function is similar between the multiple ring and spiral, the latter is superior in terms of its uniform distribution over the 2-D aperture plane and lack of transitional periodicity. This advantage would become apparent when the number of element decreases.

It is possible to form any form of effective array using transmit/receive apertures if the use of ‘dummy’ element is allowed. That means certain transmit/receive pairs will not be applied for data acquisition and focusing, which in turn leads to the lack of efficiency and extra unnecessary weight for the array. Therefore, it is not recommended unless certain properties of the array are restrictedly required. Without extra “dummy” elements, it is mathematically impossible to factorize the exact spiral or multiple ring structure into two valid array topologies. However, certain properties can be maintained if both transmit and receive aperture functions belong to certain type of curvilinear geometries.

Example of the design according to the curvilinear composed array strategy is shown in Figure 4.4. As the previous case, the MIMO array has the same number of transceivers within its aperture with 9 transmit and 16 receive elements. The transmit array is arranged on a ring structure while the receive array distributes on a spiral lattice. Due to the nature of ring and spiral structures, the effective aperture of the

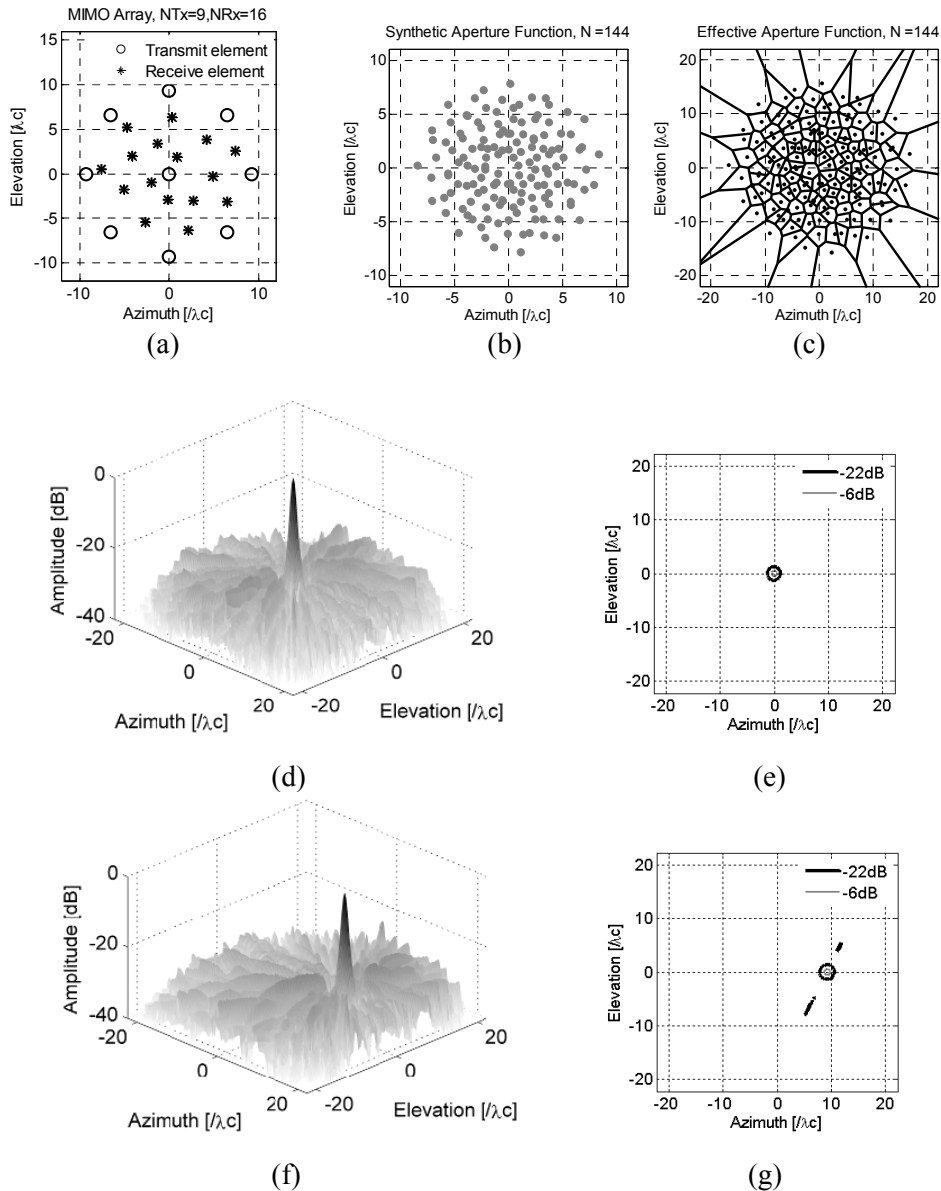


Figure 4.4 Curvilinear structure composed array. (a) Array topology with 9 transmit and 16 receive elements. (b) Synthetic Aperture Function,  $N=144$ . (c) effective aperture function by Voronoi diagram. (d) Beam pattern at center position  $(0, 20\lambda_c)$ , (e) contour plot of beam pattern at center position. (f) Beam pattern at edge position  $(9.5\lambda_c, 20\lambda_c)$ , (g) contour plot of beam pattern at edge position.

MIMO array behaves much less periodicity than the previous rectangular array. This drastically improves the array performance due to the reduction of element shadowing effect. On the other hand, as we compare the effective aperture functions, the distribution of elements in the effective array following such strategy is also less uniform over the planar surface. Some of the virtual elements within the effective aperture are very closely located to each other. When the element spacing is much smaller than the pulse length  $cT$ , the closely spaced elements can be regarded as array redundancy. Therefore, although such design approach reduces element shadowing through the nature of curvilinear structures, the MIMO array design under this strategy normally suffers from certain level of degradation in terms of mainlobe focus. The drawback in terms of array pattern is the presence of pedestal sidelobes appearing over the entire image space and close to the mainlobe. This is confirmed by the computed beam patterns. Comparing with the uniform rectilinear design in Figure 4.3, the grating/side lobe level improves with narrower beam width at -22 dB level. However, the sidelobe distribution is also less controllable and distributed into more lateral angles. The closely located sidelobes of the beam pattern would influence the image quality when imaging distributed targets in practice.

### 4.3.3 Mills Cross array

According to the beam pattern formulation introduced in Chapter 3, the point spread function (PSF) of an UWB MIMO array is equivalent to the convolution between the PSFs of both transmit and receive apertures

$$PSF_{WB} = PSF_{Tx}(\mathbf{r}, t) * PSF_{Rx}(\mathbf{r}, t) \quad (4.12)$$

This provides us a hint to look at the complete array pattern separately in terms of one-way transmit aperture and receive aperture. And as we can imagine, if the pattern of the transmit array is orthogonal to the one of the receive array, the two apertures will be able to complement each other making the pattern of the complete two-way array spatially balanced.

The most straightforward example following this philosophy is to utilize two uniform linear arrays forming the geometry of a cross. Such array geometry has been investigated in the field of ultrasound and acoustic imaging for pyramidal volumetric scanning [7] [17]. A linear array possesses all its control freedom along one direction and gradually degrades to none along the rotation toward its orthogonal. Each of the transmit/receive array has completely no resolving capability in the perpendicular direction. By combining transmit and receive arrays, the convolution of both PSF results in a pattern that is very similar to the diffraction pattern of a rectangular aperture. The cause of the sidelobes for the complete MIMO cross array along the directions of both transmit/receive arrays is due to the convolved response of the unresolved mainlobe of each one-way array with the sidelobe of the other one-way array. Meanwhile, the effective aperture of the cross array configuration indicates a

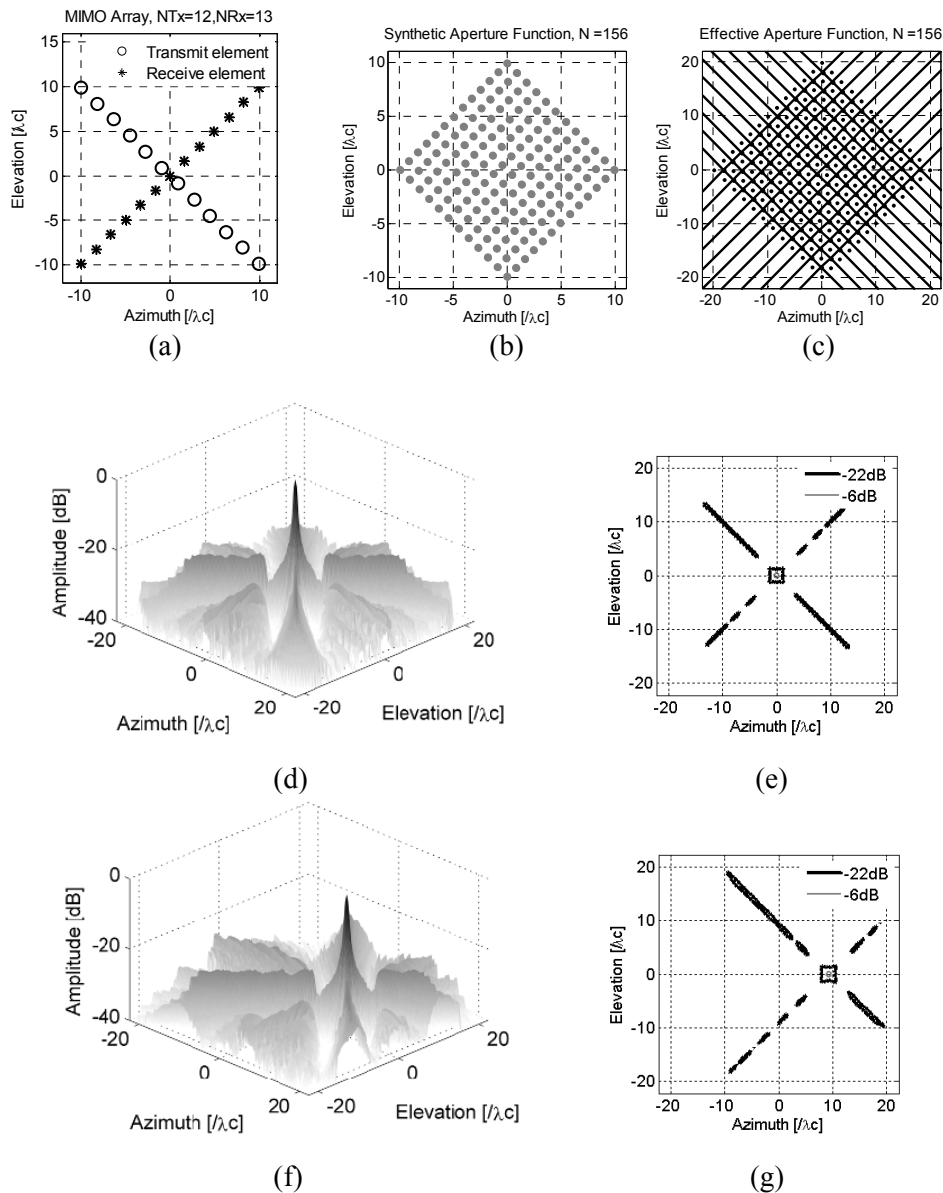


Figure 4.5 Mills Cross array. (a) Array topology with 12 transmit and 13 receive elements. (b) Synthetic aperture function, (c) effective aperture function by Voronoi diagram. (d) Beam pattern at center position ( $0, 20\lambda_c$ ), (e) contour plot of beam pattern at center position. (f) Beam pattern at edge position ( $9.5\lambda_c, 20\lambda_c$ ), (g) contour plot of beam pattern at edge position.

uniform square configuration which explains the similar array pattern to the diffraction of a square-like aperture. The shadowing of elements is prominent along the principle planes. This, in another angle, explains the appearance of sidelobes along the principle directions.

Example of the design according to the Mills Cross geometry is shown in Figure 4.5. Just as the previous case, the MIMO array has the same total number of transmit/receive elements ( $N = 25$ ) within its aperture. In order to have symmetrical beam pattern over the two principle planes, 12 of the elements are assigned within the transmit array and the rest 13 elements within the receive one. The near-field beam pattern of the array shows comparable sidelobe level but wider beamwidth than the rectilinear array shown in Figure 4.3. A larger separation between the mainlobe and sidelobes can be observed within the beam pattern.

## 4.4 Experimental verification

Near-field measurements are performed to test the proposed theory and array design strategies. The setup together with three constructed two-dimensional sparse MIMO arrays consisting of tapered slot antenna elements are illustrated in Figure 4.6. Although the proposed sparse array theory has greater potential in practice by combining with impulse systems, our experiment is conducted using network analyzer in order to precisely demonstrate the theoretical performance. Each one of the tested 2-D array represents one of the design strategies introduced in the previous section with exactly the same topology shown in Figure 4.3 to 4.5. Assuming to be utilized within a hand-held device, the aperture size of the 2-D array is fixed within a  $0.5 \times 0.5$  m planer area. The arrays are constructed using low profile antipodal Vivaldi antennas. This antenna element has an aperture size of 45 mm and exhibits consistent UWB characteristics in the frequency band from 2.7 to 26 GHz [18]. Array elements are connected to the network analyzer through a computer-controlled multi-port switch. The switch operates up to 20 GHz, which influences the higher frequency band of the setup. All the antenna elements within the planar array are placed in a vertical position producing vertical polarization along the elevation plane. Full-port calibration of the network analyzer, switch, and cables are performed before the measurement. The data is collected in frequency-domain by sweeping within the frequency band from 1 to 26 GHz, and switching through all transmit/receive pairs within the MIMO array. Each obtained frequency-domain signal is then windowed and transformed to time-domain by inverse Fourier transform (IFFT), and further focused using migration algorithms specially developed for MIMO array imaging [19]. Direct coupling between elements within each array is recorded in free-space and then be subtracted from all the measured data sets. This also serves as background subtraction which removes clutters from the raw data.

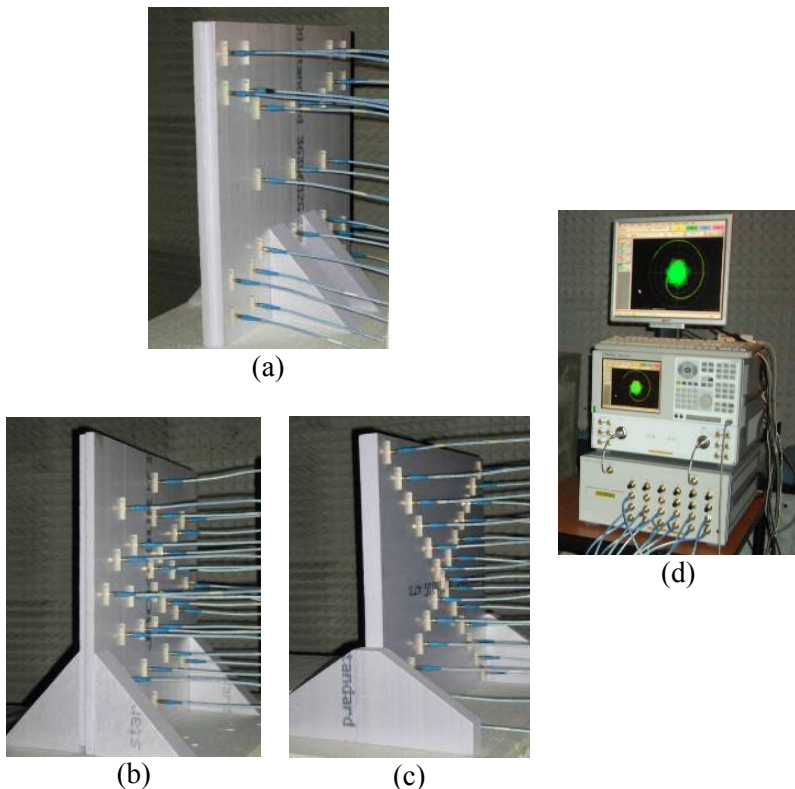


Figure 4.6 Measurement setup with 3 two-dimensional MIMO arrays connected to network analyzer through multi-port switch in anechoic chamber. (a) Equivalent uniform rectilinear array, (b) Curvilinear composed array, (c) Mills Cross array, and (d) network analyzer connected to array through multi-port test set. The topologies of the MIMO arrays correspond with the ones shown in Figure 4.3 to 4.5.

An antenna face-to-face measurement is performed to define the operational bandwidth of the whole setup. The bandwidth of the complete system and its corresponding time-domain impulse after gating of reflections are shown in Figure 4.7. The operational bandwidth at -10 dB level ranges from 2.8 to 19.5 GHz with 16.7 GHz absolute bandwidth and center frequency at 11.15 GHz. Under this frequency band, all four arrays are considered ultra-sparse arrays because their average element spacing within the effective apertures are more than 5 times of half-wavelength at center frequency  $\lambda_c / 2$ . The complete setup achieves 150% fractional bandwidth which is sufficient to reduce the grating lobes caused by array sparsity.

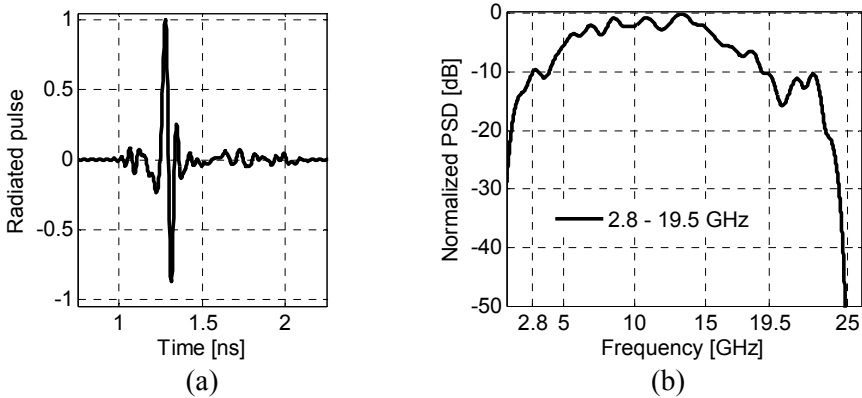


Figure 4.7 Operational frequency band of the complete measurement setup. (a) Radiated impulse, and (b) power spectrum density after time gating of multiple reflections.

#### 4.4.1 Tx/Rx coupling within 2-D MIMO array

It is widely recognized that mutual element coupling can be a potential problem in array systems. The influence of cross-coupling is prominent in narrowband phase array systems due to the fact that coupled signals among transducers are able to place its contribution throughout the entire image space during the beamforming process. By contrast, ultra-wideband array which radiates short pulses exhibits a high level mutual coupling in a relative short duration directly after transmission. The duration of this direct coupling is determined by both the type of antenna element and their arrangement. If the coupled signals can be separated from target responses in the range profiles of each transmit/receive pairs within the array, the mutual coupling would produce minimal influence on the resulting image of the target. On the other hand, an overlapped response of target from element coupling could significantly reduce the dynamic range of the imaging system. Subtraction of pre-recorded coupling is commonly not very effective in this situation due to the instability of the electronics which causes high amplitude residuals comparably stronger than the level of a small target in the array near-field.

Figure 4.8 shows the coupling level and maximum contaminated ranges of all transmit/receive pairs within each tested 2-D MIMO arrays. We define the maximum contaminated range as the distance in the range profile where amplitude of coupling drops 10 dB below the measured amplitude of a 1.5 cm diameter metal sphere at  $20\lambda_c$  range. The polystyrene foam used for the frame of the arrays has permittivity close to the air, therefore, placing minimum influence on the coupling among the antennas. Besides the differences in terms of coupling level due to array topology, all

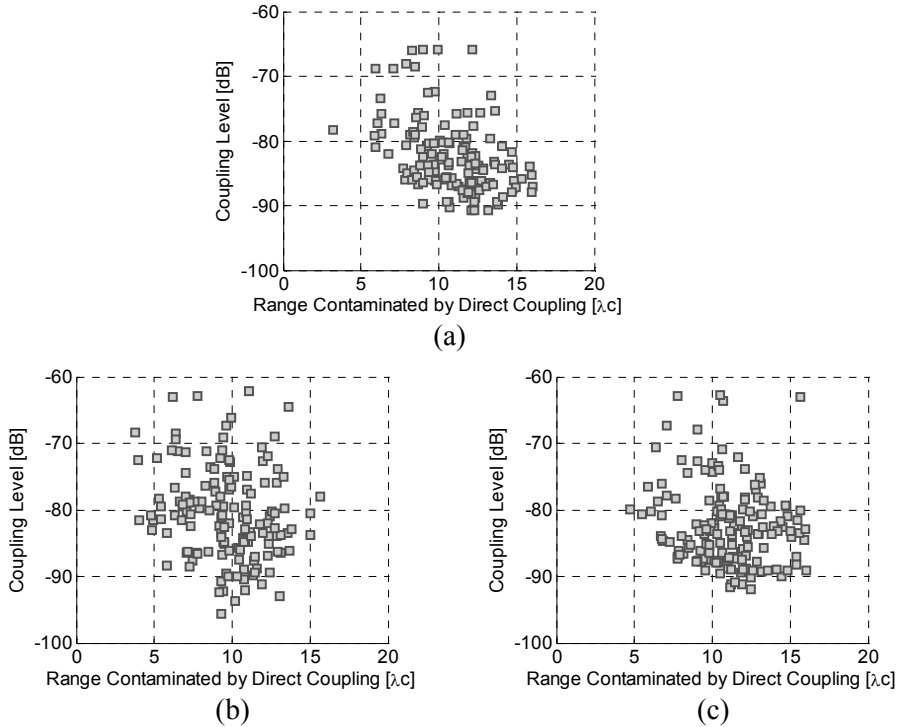


Figure 4.8 Coupling level and maximum contaminated range of all transmit/receive pairs within the measured (a) equivalent uniform rectilinear array, (b) curvilinear structure composed array, and (c) Mills Cross array. The maximum contaminated range is defined by the distance in the range profile where amplitude of direct coupling drops 10 dB below the response of a 1.5 cm metal sphere at  $20\lambda_c$  range distance.

of transmit/receive pairs within the three arrays are free of coupling's influence after  $16\lambda_c$ , which is fairly close to the aperture plane. The curvilinear array shows slight advantage over the other two in this aspect. The results indicate that imaging of the 2-D arrays will not be severely compromised by direct coupling if the target appears at further range distances than  $20\lambda_c$ .

#### 4.4.2 Beam pattern

Beam patterns of the all three 2-D arrays when focused at both center and edge positions are shown in Figure 4.9 and 4.10. The results are obtained from measurements with a 1.5 cm diameter metal sphere placed at 50 cm range distance in

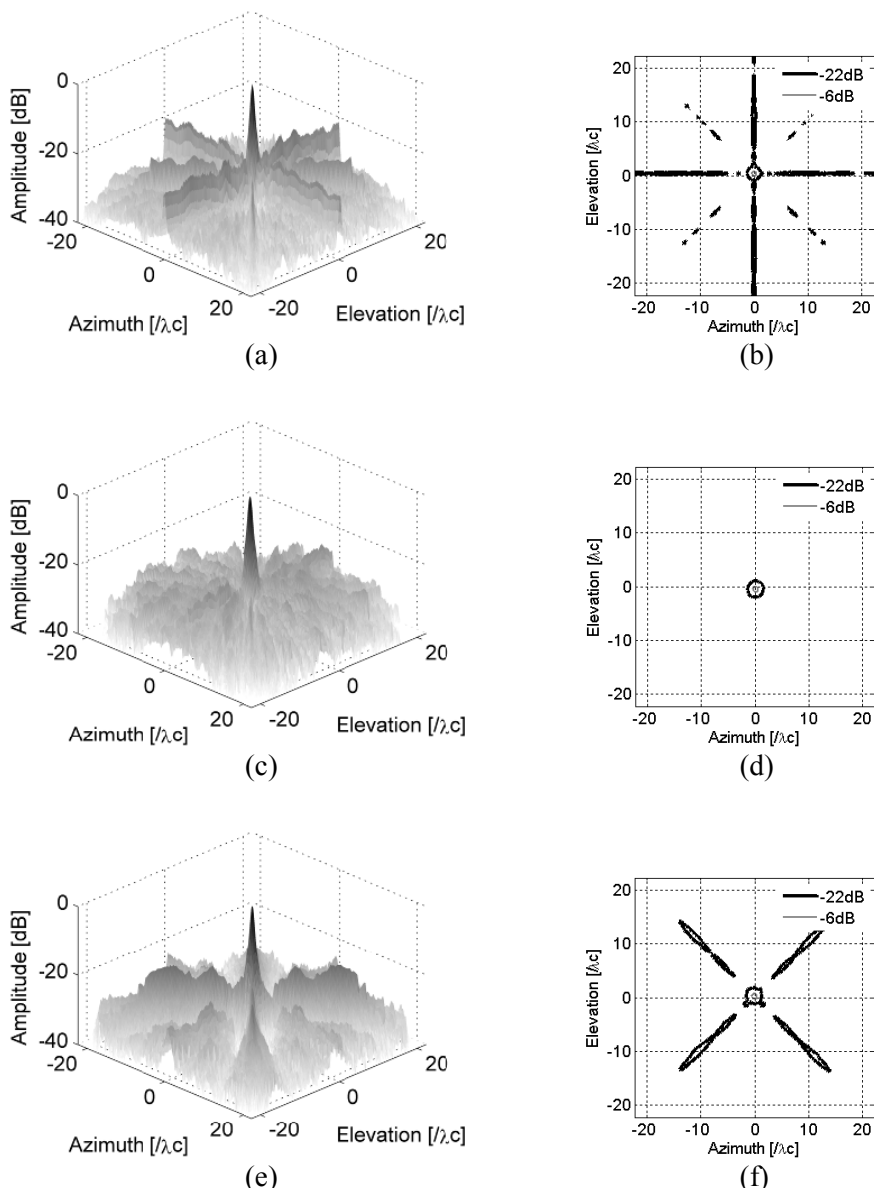


Figure 4.9 Beam pattern of three measured MIMO arrays with focal point at  $(0, 20\lambda_c)$ . (a) Beam pattern of equivalent uniform rectilinear array, (b) its contour plot. (c) Beam pattern of curvilinear structure composed array, (d) its contour plot. (e) Beam pattern of Mills Cross array, (f) its contour plot.

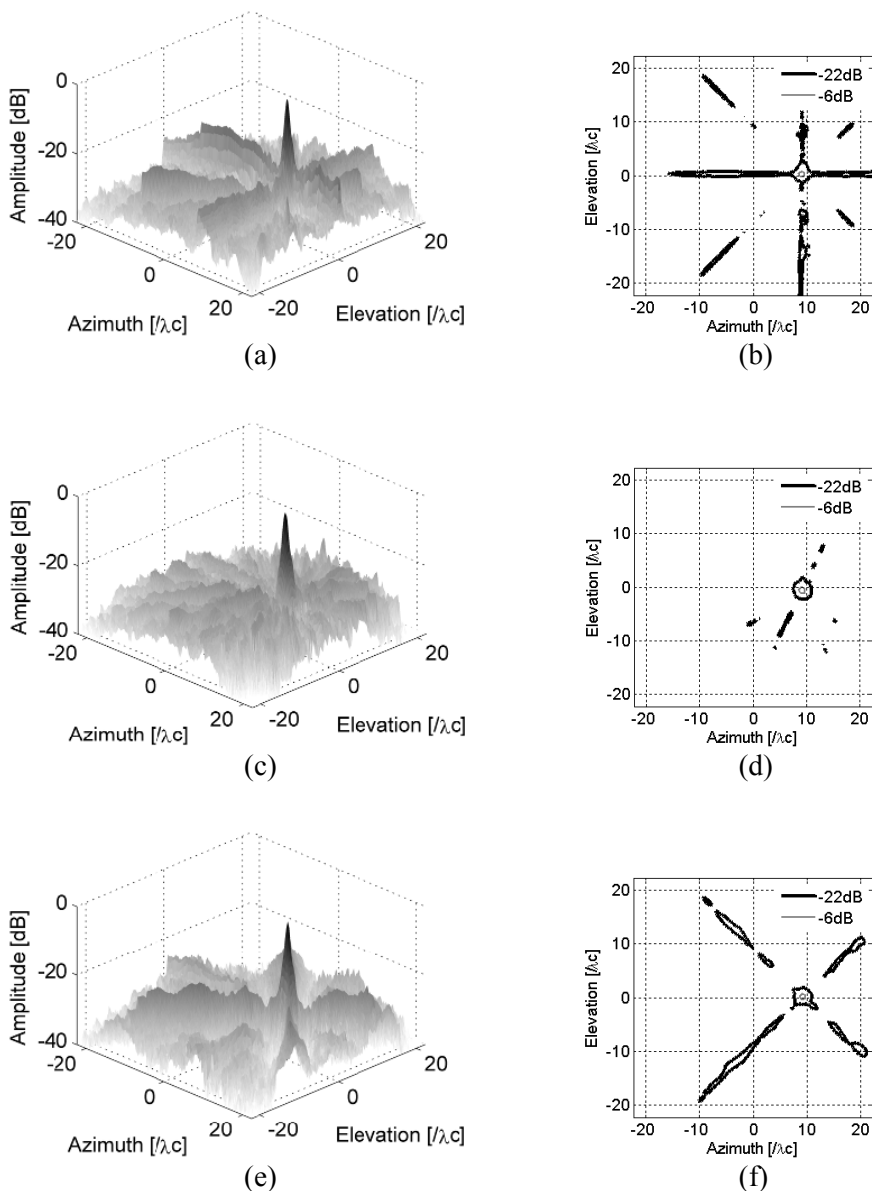


Figure 4.10 Beam pattern of three measured MIMO arrays with focal point at edge position  $(9.5\lambda_c, 20\lambda_c)$ . (a) Beam pattern of equivalent uniform rectilinear array, (b) its contour plot. (c) Beam pattern of curvilinear structure composed array, (d) its contour plot. (e) Beam pattern of Mills Cross array, (f) its contour plot.

TABLE 4.1  
SUMMARY OF BEAM PATTERN OF 2-D SPARSE MIMO UWB ARRAYS

MIMO Array (25 Elements)	-3 dB Angular Beam Width [degree]		Maximum grating/side lobe level [dB]	
	Simu	Meas	Simu	Meas
Equivalent uniform rectilinear array (9×16)	1.71	1.70	-20.1	-18.2
Curvilinear composed array (9×16)	2.11	2.01	-22.4	-22.1
Mills Cross array (12×13)	1.93	1.86	-20.1	-17.4

\*Simu stands for simulation result; Meas stands for measurement result.

front of both array center and edge, respectively. The 2-D beam pattern is computed by taking the maximum level along the range dimension of the focused three-dimensional images (PSF).

The measured beam pattern confirms the simulation (Figure 4.3 to 4.5) with great similarities. In terms of performances around mainlobe and within the interference region that is governed by narrowband properties, the rectilinear and cross arrays perform equally well due to their uniform effective aperture function. The curvilinear composed array falls slightly behind at this point due to the feature of its inherent design methodology, which makes it less controllable in terms of distribution in the effective aperture function. This array exhibits some closely distributed sidelobes to the mainlobe. This in turn could reduce its capability of reconstructing the continuous shape of a distributed target. From wideband properties point of view, the rectilinear and cross arrays represent the weak option due to their lack of consideration in terms of element shadowing. By contrast, the curvilinear array is well configured to avoid element shadowing effects, and shows lower level of sidelobes.

Both 3 dB beamwidth and maximum grating/sidelobe level of all three arrays are summarized in Table 4.1. Under the same physical size of the array, the equivalent uniform rectilinear array design results in the largest effective aperture, therefore, the highest angular resolution. The curvilinear composed array exhibits slightly less resolving capability due to its heavy weighting at the center of effective aperture. Among the proposed strategies, the curvilinear array provides the lowest grating/sidelobe level due to its well distributed control freedom over angular directions. The proposed 2-D MIMO array achieves experimentally 2 degree angular resolution and -22 dB grating/side lobe level with only 25 antenna elements within the array aperture. Such system has high potentials in applications such as surveillance, through-wall imaging and tracking.

#### 4.4.3 3-D volumetric imaging of distributed target

The potential of employing a 2-D sparse MIMO array lies in its capability of performing real-time 3-D volumetric imaging. Meanwhile, the differences of beam pattern would have greater impact when the array faces targets with higher spatial dimension. This is caused by the fact that the resulting image represents the integration between the array PSF and the object space, which is shown in Chapter 3. Therefore, the level of grating/side lobe varies depending on the dimension, shape and orientation of the possible target.

Two distributed targets are tested using three planar arrays as shown in Figure 4.11. We start with scissors, which is full of target features. The position of the scissors during test is shown. It is placed vertically at the same height in front of the array center with 50 cm range distance from the aperture plane. Under such imaging geometry, resolving capabilities in both cross-range directions are provided by the real-aperture array while the down-range is supported by the bandwidth of the transmitted signals. Besides its obvious cross figure, the scissors consist of two pieces of metal parts, which should be separable in the resulting image. The two circular rings (handles) at the end of each piece will give smaller reflections than the scissors' front joints, therefore, presenting a dynamic range test for the imaging array. Among the results of the three arrays, the cross array gives the highest sidelobe response distributed at  $\pm 45^\circ$  angles. Such pattern corresponds to its point spread function but appearing with higher amplitude due to the extension of the scissors in the  $\pm 45$  degree directions. The equivalent rectilinear array exhibits the second highest sidelobe level along the azimuth plane. It is not better than the cross array in the sense that the sidelobe passes directly through the center of the target. This leaves no separation between target response and energy leakage, which is definitely not wanted. The curvilinear composed array gives much lower sidelobe level and size. Close comparison indicates the advantages of the curvilinear array design. Due to the lower sidelobe level, the scissors are better reconstructed by the curvilinear array than the other two with much less artifacts in the 3-D image.

The picture of the revolver under test and the obtained images are shown in Figure 4.11. An important feature of the revolver is that it has a relative long extension in the elevation plane along its barrel. Therefore, any array that has sidelobe distributing long the elevation direction would result in untruthful image of the revolver. The interaction of side/grating lobes can be either constructive or destructive. Destructive interactions are visible in the images from the equivalent rectilinear array due to its energy leakage in the vertical direction. We can see the barrel is broken into two parts which is a clear sign of target break-up phenomenon. By contrast, the interactions of sidelobe and target responses from the curvilinear array result in constructive accumulation. This is why the jointing part of the revolver's barrel gives wider response than its real shape. Although the target does

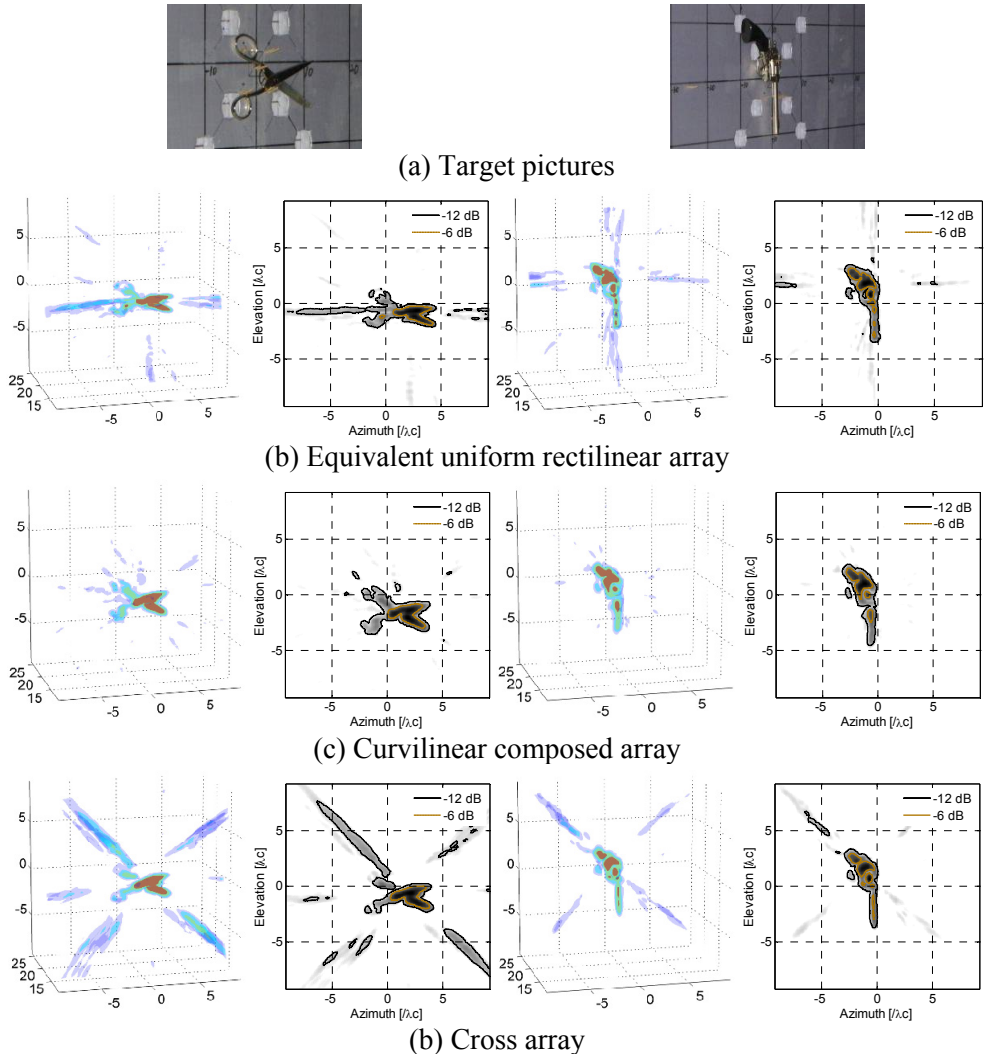


Figure 4.11 3-D volumetric imaging of scissors and revolver placed at  $20\lambda_c$  distance in front of three planar MIMO arrays. The 3-D plots are shown at -20 dB dynamic range. 2-D contours are plotted at -6 and -12 dB levels, respectively.

not have excessive extension along the diagonal directions, the sidelobe pattern of the cross array is still quite visible. The test results from distributed targets indicate an overall advantage of the curvilinear composed array in terms of producing 3-D images with lower and less artifacts. However, optimization of the array may be needed in order to reduce array redundancy and further improve its imaging capabilities.

## 4.5 Summary

In this Chapter, we investigated the capabilities of two-dimensional sparse multiple-input multiple-output (MIMO) ultra-wideband (UWB) arrays for near-field imaging. We have investigated and demonstrated the impact of shadowing and redundancy on the array performance. Based on the formulation of the two-way wideband beam pattern, the concept of synthetic aperture function is applied to factorize 2-D effective aperture into topologies of transmit and receive arrays. Such approach results in desired planar effective aperture functions without redundancy but with less control over element shadowing. By arranging element distributions of both transmit/receive arrays according to curvilinear geometries, element shadowing effect which is common over periodic arrays, can be reduced to further decrease the grating/side lobe level. Starting with the ISL for the requirements of specific application, different combination of the number of transmit and receive elements can be applied following the proposed strategies to obtain 2-D MIMO arrays with both high resolution and large dynamic range.

The theoretical results are verified by 2-D MIMO array measurements representing different approaches towards sparse array design. Their beam patterns at 150% fractional bandwidth and ability for shape reconstruction are investigated. The results confirm the simulation, and show that the array following curvilinear design is superior to both rectilinear and previous cross array design strategies. The realized 2-D MIMO array achieves 2 degree angular resolution and overall -22 dB grating/lobe level with only 25 antenna elements. The experimental results from 3-D volumetric imaging illustrate a strong potential of the proposed two-dimensional sparse MIMO array-based UWB imaging system in real-time short-range applications.

## References

- [1] R. E. Davidsen, J. A. Jensen, and S. W. Smith, "Two-dimensional random arrays for real time volumetric imaging," *Ultrason. Imaging*, vol. 16, pp. 143-163, 1994.
- [2] D.H. Turnbull, F.S. Foster, "Beam Steering with Pulsed Two-Dimensional Transducer Arrays," *IEEE Trans. Ultrason., Ferroelectr. Freq. Control*, vol. 38, pp. 320-333, Jul. 1991.
- [3] A. L. Moffett, "Array factors with non uniform spacing parameters," *IRE Trans. Antennas Propagat.*, vol. AP-10, pp. 131-146, 1962.

- [4] M. I. Skolnik, G. Newhauser, and J. W. Sherman, "Dynamic programming applied to unequally spaced array," *IEEE Trans. Antennas Propaga.*, vol. AP-12, pp. 35-43, 1964.
- [5] B. D. Steinberg, *Principles of Aperture and Array Systems Design*, New York: Wiley, 1976.
- [6] G.R. Lockwood and F.S. Foster, "Optimizing the Radiation Pattern of Sparse Periodic Two-Dimensional Arrays," *IEEE Trans. Ultrason., Ferroelectr. Freq. Control*, vol. 43, pp. 15-19, Jan. 1996.
- [7] S. W. Smith, H. G. Pavy, Jr., and O. T. von Ramm, "High-Speed Ultrasound Volumetric Imaging System – Part I: Transducer Design and Beam Steering," *IEEE Trans. Ultrason., Ferroelectr. Freq. Control*, vol. 38, pp. 100-108, Mar. 1991.
- [8] J.L. Schwartz, B.D. Steinberg, "Ultrasparse, Ultrawideband Arrays," *IEEE Trans. Ultrason., Ferroelectr. Freq. Control*, vol. 45, pp. 376-393, Mar. 1998.
- [9] S. S. Ahmed, A. Schiess, L.-P. Schmidt, "Near Field mm-Wave Imaging with Multistatic Sparse 2D-Arrays," in *Proc. EuRAD 2009*, pp. 180-183, 2009.
- [10] B. D. Steinberg, "Comparison between the Peak Sidelobe of the Random Array and Algorithmically Designed Aperiodic Arrays," *IEEE Trans. Antennas Propag.*, vol. AP-21, pp. 366-369, Jan. 1973.
- [11] B. D. Steinberg, H. M. Subbaram, *Microwave Imaging Techniques*, New York: Wiley, 1991.
- [12] X. Zhuge, A. G. Yarovoy, L. P. Ligthart, "A Sidelobe Reduction Technique for Enhancing Images of UWB Sparse MIMO Array," in *Proc. International Radar Conference – Surveillance for a Safer World*, Oct. 2009, pp. 1-6.
- [13] C. R. Cooley, B. S. Robinson, "Synthetic Focus Imaging Using Partial Datasets," *Ultrasonic Symposium*, vol. 3, pp. 1539-1542, 1994.
- [14] X. Zhuge, A. Yarovoy, "Near-field ultra-wideband imaging with two-dimensional sparse MIMO array," in *Proc. The Fourth European Conference on Antennas and Propagation (EuCAP)*, Barcelona, Spain, April 2010, pp. 1-4.
- [15] B. Y. Mills, and A. G. Little, "A high resolution aerial system of a new type", *Australian J. Phys.*, vol. 6, pp. 272-278, 1953.
- [16] D.W. Boeringer, "Phased Array Including A Logarithmic Spiral Lattice of Uniformly Spaced Radiating and Receiver Elements," U.S. Patent 6 433 754, May 2001.

- [17] P. Alais, P. Challande, and L. Eljaafari, “Development of an underwater frontal imaging system, concept of 3-D imaging system,” *Acoust. Imag.*, vol. 18, 1991.
- [18] X. Zhuge, A. G. Yarovoy, L. P. Lighthart, “Circularly Tapered Antipodal Vivaldi Antenna for Array-Based Ultra-Wideband Near-Field Imaging,” in *Proc. European Radar Conference (EuRAD)*, Sep. 2009, pp. 250-253.
- [19] X. Zhuge, A. G. Yarovoy, T. G. Savelyev, and L. P. Lighthart, “Modified Kirchhoff Migration for UWB MIMO Array-Based Radar Imaging,” *IEEE Trans. Geosci. Remote Sens.*, vol. 48, pp. 2692-2703, Jun. 2010.

## CHAPTER 5

# COMPARISON BETWEEN REAL-APERTURE ARRAY AND SYNTHETIC APERTURE

To better understand the properties of MIMO array, it is important to address the differences between a synthetic aperture and a real-aperture array. The technique of synthesizing a large antenna from a succession of spatial samples has its origin in radioastronomy. The idea of synthetic aperture radar (SAR) was conceived in the 1950s by Carl A. Wiley, a mathematician at Goodyear Aircraft Corporation in Litchfield Park, Arizona. In early 1952, Wiley, together with Fred Heisley and Bill Welty, constructed a concept validation system known as DOUSER. During the 1950s and 1960s numerous advancements were introduced in SAR technology [1] [2]. SAR is a form of radar in which multiple echoes are processed to yield higher-resolution images than those would be possible by conventional means. Either a single or multiple antennas are mounted on a moving platform (such as an airplane or spacecraft) which is used to scan a target scene. The echoes or waveforms received at the different antenna positions are post-processed to resolve the target. SAR can only be implemented by moving one or more antennas over relatively immobile targets. Replacing synthetic aperture with real-aperture array is the essential step toward demanding imaging applications where both high-resolution and real-time operations are required.

In the previous chapters we have demonstrated the imaging capabilities of UWB-MIMO arrays which are able to achieve high-resolution and high dynamic range with comparably small number of elements. This chapter aims to further compare the

designed real-aperture MIMO arrays against conventional SAR technique. The advantages and challenges faced by MIMO array comparing with SAR are firstly summarized. Then the near-field imaging performances of both methodologies are compared side by side with experimental results.

The chapter is organized as follows. The theoretical influence of replacing synthetic aperture with real-aperture array is discussed in section 5.1. The experimental comparison between MIMO-SAR and 2-D SAR are presented and discussed in section 5.2. The chapter is summarized in the last section.

## 5.1 Theoretical comparison

The notion of MIMO indicates that there are multiple radiating and receiving elements within the array aperture. In certain sense, MIMO array is a generalization of multistatic array concept. By the most general interpretation, SAR can be considered as a special case of MIMO. Although SAR traditionally employs a single transmit antenna and a single receive antenna, the positions of these two antennas are translated and all the information from the collected data over all scanned locations are processed coherently. The most significant difference between SAR and a typical MIMO array is that SAR does not have access to channel measurements for all transmit-receive combinations or pairs. For SAR, only the diagonal information of the scattering matrix is measured and becomes available for imaging. In this sense, MIMO can take full advantages of the degrees of freedom and diversity from the complete scattering matrix.

As we characterized the quality of imaging obtained within the near-field by the point spread function (PSF) [3], the PSFs of both SAR and MIMO array can be compared.

$$PSF_{SAR}(\mathbf{r}, \mathbf{r}_0) = \int_{\{\mathbf{r}_{An}\}} w(\mathbf{r}_{An}) \cdot (16\pi^2 |\mathbf{r}_{An} - \mathbf{r}_0|^2)^{-1} p(t - 2(|\mathbf{r}_0 - \mathbf{r}_{An}| - |\mathbf{r} - \mathbf{r}_{An}|)/c) d\mathbf{r}_{An} |_{t=t_{ref}} \quad (5.1)$$

$$\begin{aligned} PSF_{MIMO}(\mathbf{r}_0, \mathbf{r}) &= \int_{\{\mathbf{r}_{Tx}\}} (4\pi |\mathbf{r}_0 - \mathbf{r}_{Tx}|)^{-1} \cdot w_{Tx}(\mathbf{r}_{Tx}) \cdot p(t - T_{Tx}(\mathbf{r}, \mathbf{r}_{Tx})) d\mathbf{r}_{Tx} \\ &\quad * \int_{\{\mathbf{r}_{Rx}\}} (4\pi |\mathbf{r}_{Rx} - \mathbf{r}_0|)^{-1} \cdot w_{Rx}(\mathbf{r}_{Rx}) \cdot p(t - T_{Rx}(\mathbf{r}, \mathbf{r}_{Rx})) d\mathbf{r}_{Rx} |_{t=t_{ref}} \end{aligned} \quad (5.2)$$

where

$$\begin{aligned} T_{Tx}(\mathbf{r}, \mathbf{r}_{Tx}) &= (|\mathbf{r}_0 - \mathbf{r}_{Tx}| - |\mathbf{r} - \mathbf{r}_{Tx}|)/c \\ T_{Rx}(\mathbf{r}, \mathbf{r}_{Rx}) &= (|\mathbf{r}_{Rx} - \mathbf{r}_0| - |\mathbf{r}_{Rx} - \mathbf{r}|)/c \end{aligned}$$

Instead of formulating only one aperture function in the SAR mode, MIMO array exhibits the design freedom of adjusting both transmit and receive aperture functions. On the one hand, this poses a design challenge for engineers to properly formulae the array topologies, which have been addressed in Chapter 3 and 4. On the other hand, it offers the potential to reduce the number of elements within the aperture. The same level of PSF achievable by a SAR aperture with  $N$  elements or spatial sampling points can be obtained by a MIMO array of  $2\sqrt{N}$  elements (with  $\sqrt{N}$  transmit,  $\sqrt{N}$  receive antennas). Smaller number of elements means less demand for the front-end, shorter data acquisition time, and less mutual coupling. Because of the potential to simultaneously transmit and receive orthogonal signals, the coherence of target response can be maximally preserved and improving the ability to effectively combine the information from the antenna pairs over time-varying or frequency-selective target scattering.

Another major difference between MIMO array and SAR is the mutual coupling that exists among array antennas. It is intrinsic by the nature of antennas that when one is placed among the others in proximity and one is transmitting, the others will receive some of the transmitted energy. Furthermore, antennas rescatter a portion of any incident wave and act like small transmitters even when they are only receiving elements. The result is that energy interchange between a particular element within an MIMO array and a target occurs not only by the direct path, but also indirectly via scattering from the other antennas of the array.

It is evident that mutual coupling is an effect that complicates the design of array antennas. To qualitatively analysis the process of array coupling, we elaborate on the physical picture by examining the scenario of MIMO array consisting of both transmitting and receiving elements as illustrated in Figure 5.1. The generator attached to transmit antenna 1 excites a wave traveling from the generator toward the antenna indicated by the arrow. Majority of this energy is radiated directly into space toward the target while a part is coupled to the other antennas of the array. In a particular case, to the adjacent transmit antenna 2 and receive antenna 1. The field incident upon transmit antenna 2 causes current flow which re-radiates some of the energy and also launches a wave toward its generator. Out of the re-scattered energy, some is re-radiated into space toward the target and some in turn couples back to other elements, and so forth. If transmit antenna 2 is also being excited at the same time by its own source, the energy caused due to the source of transmit antenna 1 adds vectorially to the one from generator of antenna 2. This can alter the amplitude and phase of excitation of transmit antenna 2 depending on the output of transmit antenna 1. The total contribution to the incident field to the target from a particular transmit element in the array depends not only on the excitation by its own source, but also on the total parasitic excitations which depends on the couplings from the excitation of other transmitters. As for the receive array, the spherical wave scattered from the target arrives at the receive antenna 1 following the direct coupling from transmitter 1. The field incident on receiver 1 causes current flow that launches a

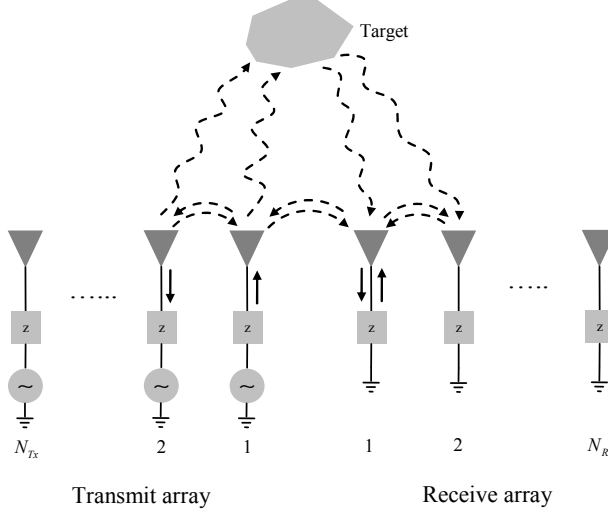


Figure 5.1 Effect of mutual coupling among transmit and receive antenna elements within a MIMO array.

wave into its feed and also re-scatters some of the energy into space and into adjacent antennas. The re-scattered wave from receive antenna 1 adds vectorially at receive antenna 2 with the wave scattered from the target. Thus the total input energy to each receive antenna from the incident wave is the vector sum of the waves coming directly from the target as well as those coupled parasitically from the other antennas. The exact extend and nature of the effects of coupling on MIMO array depend on several factors, including the type of antenna, the relative placement of the elements in the array, the type of excitation scheme used to excite the elements, and the potential position of the target to the array aperture. Under the condition that orthogonality among transmitters are achieved by time division multiplexing, meaning that the transmit antennas are sequentially excited, the active coupling within the transmit array does not exist. Since passive coupling is of minor practical importance, the main effect then comes to the direct coupling between transmit and receive antennas. Under UWB excitation, the received wave field from direct coupling can be separated from the reflections of the target by time gating at the receiver due to the fine time resolution provided by the short pulse duration.

The comparison between SAR and MIMO array is summarized in Table 5.1. There are inherent characteristics of each technology that might be advantages and disadvantages that are relevant for specific applications. For an application where high quality image of a stationary target is required, SAR can be a suitable choice due to its flexibility and possibility to provide higher dynamic range. On the other hand, MIMO is the clear favorable choice where real-time operation and imaging of

Table 5.1 List of advantages and disadvantages of SAR and MIMO arrays

	Advantages	Disadvantages
SAR	<ul style="list-style-type: none"> <li>- Simpler design process</li> <li>- Flexible to change the scanning scheme</li> <li>- Simpler processing scheme for focusing (higher computation efficiency)</li> </ul>	<ul style="list-style-type: none"> <li>- Limited data acquisition speed,</li> <li>- Require larger number of scan position or antenna pairs</li> <li>- Only suitable for stationary and slow moving target, less target coherence among collected signals</li> <li>- Collect only part of scattering matrix</li> </ul>
MIMO	<ul style="list-style-type: none"> <li>- Fast data acquisition (real-time)</li> <li>- Require less antenna elements comparing with SAR</li> <li>- Possible to image fast moving target Good coherence of target response among the signals</li> <li>- Complete scattering matrix for imaging</li> </ul>	<ul style="list-style-type: none"> <li>- More challenge for array topology design</li> <li>- More complicated processing scheme for focusing (comparing with SAR)</li> </ul>

moving targets are important to end-users of the application. By resolving the design challenges, it is evident that MIMO array based UWB imaging system can become an important technology step for microwave imaging.

In the following section, the performance of MIMO array and SAR are experimentally compared for near-field UWB imaging.

## 5.2 Experimental comparison

A laboratory 2-D near-field scanner coupled with wideband transceivers were used to gather 2-D SAR and MIMO-SAR data to compare their performances. The setup of both SAR and MIMO-SAR configurations are shown in Figure 5.2. In order to avoid problems related to short-term instability (jitter) and limited dynamic range (both typical for time-domain measurements), the actual data acquisition was performed in frequency-domain using a network analyzer. Single antenna was used to perform monostatic SAR measurements, while elements of the MIMO array were connected to the network analyzer through a multi-port switch. The array was mounted on a computer-controlled mechanical scanner, allowing both azimuth and elevation scan for 3-D volumetric imaging. The whole setup achieves 150% fractional bandwidth from 2.8 to 19.5 GHz.

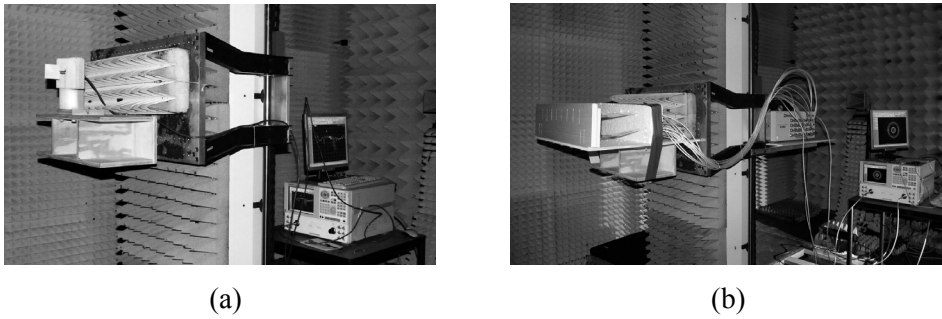


Figure 5.2 Measurement setup with network analyzer in anechoic chamber.

(a) 2-D SAR configuration, and (b) MIMO-SAR configuration with an additional multi-port switch.

Wideband aperture synthesis has to be performed in order to transform the wideband data gathered over a 2-D aperture into 3-D images of the target. The configuration of 2-D SAR measurement is shown in Figure 5.3, where the primed coordinates represent the position of the transceiver, and the unprimed coordinates represent a single point in the target space. Because of the monostatic configuration where transmit and receive antennas are collocated, the problem of the actual illumination and reflection model can be simplified to a single radiation model, referred to as the exploding reflector model (ERM), in which the wave field starts to expand from the target at time zero with half of the actual propagation speed. This makes the formulation of the reconstruction algorithm as the direct 3-D inverse Fourier transform (IFFT) of the measured data set,  $u(x', y', t)$ , after transformation into the frequency-wavenumber domain [4] [5]. The data after 3-D Fourier transform,  $u(k_x, k_y, \omega)$ , is equally spaced in frequency-domain. In order to prepare the data set for 3-D IFFT, it must be re-sampled along its frequency dimension. This is a one-dimensional interpolation from unevenly spaced grid to evenly spaced data following a specified dispersion relation. The reason of going back and forth between space-time domain and frequency-wavenumber domain is to take advantage of the high computational efficiency of the fast Fourier transform (FFT). However, this also requires a uniform spatial sampling. The ERM assumption further limits the use of the algorithm for near-field multistatic configurations.

For a UWB sparse aperture, the spatial dimension of the data set is drastically reduced while the frequency sampling is raised due to the large bandwidth. Larger frequency sampling also means more computation load for the interpolation procedure. Therefore, in certain extent, the frequency-wavenumber domain reconstruction would become equally or less efficient than direct time-domain migration algorithm, in which the reflectivity function can be calculated by

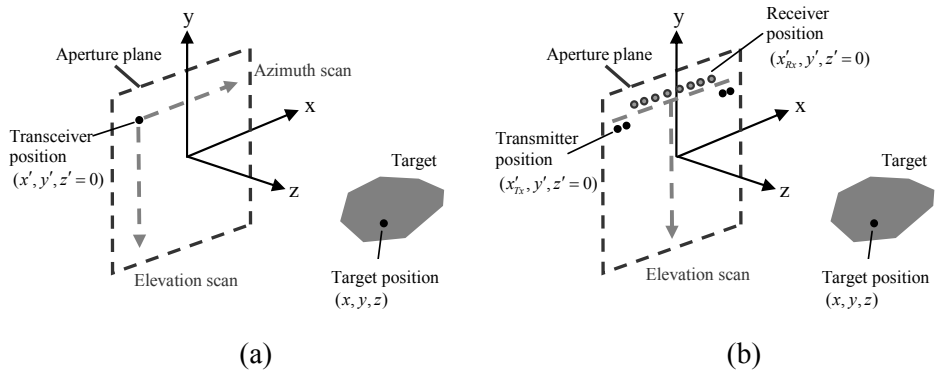


Figure 5.3 Wideband imaging configurations.

(a) 2-D SAR configuration, and (b) MIMO-SAR configuration.

integrating the backward propagated signals over the SAR aperture in order to move the observed events from the data acquisition position back to their true spatial location. Due to this straightforward implementation, the time-domain migration can be easily adapted to different types of data gathering including the MIMO-SAR configuration.

In comparison, the configuration of MIMO-SAR measurement is shown in Figure 5.3, where transmitter and receiver locations within the linear MIMO array are separately indicated. Due to both the multistatic configurations of the MIMO array and the demand for near-field operation, conventional algorithms which are based on virtual phase centers between transmit and receive antennas [6] are not accurate enough for the application. The time-domain algorithm can be easily adapted for MIMO configurations with arbitrary number of elements. A more efficient (fast convolution) algorithm, which applies separate imaging kernels for MIMO and SAR, is proposed in [7]. In terms of imaging algorithm, MIMO configuration requires more complicated processing scheme but can still be very efficiently implemented.

The point spread function (PSF) of both systems is firstly measured by placing a 2 cm diameter metal sphere in front of the center of the aperture at 50 cm range distance. The spatial sampling for SAR scan is 1 cm in both 2-D SAR and MIMO-SAR measurements. PSF of both cases are shown in Figure 5.4. No artifacts are visible in the images at -25 dB. The system achieves 1 cm resolution in all three dimensions. Comparing the two configurations, their quality of PSF is quite similar while MIMO-SAR scans the target with much faster speed by replacing the azimuth scan with real MIMO array aperture. Creeping wave causes a small response behind the mainlobe visible in the azimuth-range plot of the SAR image. It does not appear in the MIMO-SAR image due to the multistatic configuration which helps to mitigate

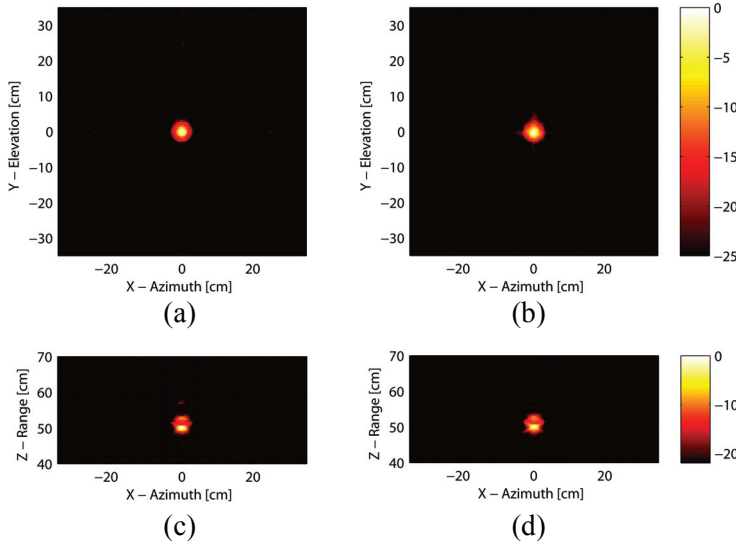


Figure 5.4 Point spread function of 2-D SAR and MIMO-SAR systems

(a) front view obtained by 2-D SAR, (b) front view obtained by MIMO-SAR, (c) top view obtained by 2-D SAR, and (d) top view obtained by MIMO-SAR. Spatial sampling of SAR is 1 cm in both cases.

the response of the creeping wave.

A distributed target is further used for testing the performance of the UWB imaging system. A pair of metallic scissors is placed at 50 cm range distance in front of center of aperture. The length of the synthetic aperture is 50cm in each scanning dimension, while the lengths of transmit and receive arrays are 50 cm and 41.2 cm respectively. 2-D and 3-D images of the target from both SAR and MIMO-SAR are presented in Figure 5.5. The dynamic ranges of the images are shown in 15 dB and 30 dB levels respectively. All reconstructed images provide a truthful reconstruction of the target. The two separate pieces of the scissors are well resolved.

Comparing the two configurations, MIMO-SAR system provides better results of handle reconstruction than SAR system. With MIMO-SAR system, the 3-D images at 30 dB dynamic range show higher level of artifacts, which corresponds with the beam pattern demonstrated in Figure 3.13. The dynamic range of the MIMO-SAR system is sufficient for the application at hand, but it could be lower than 2-D classical SAR system, depending on the total number of elements within the designed array as indicated by the ISL definition.

The proposed system is further tested in realistic scenarios for the concealed weapon detection. The target is a mannequin with attached weapons, as shown in Figure 5.6. The mannequin is 1.8 m in height and 0.5 m in width in a standing

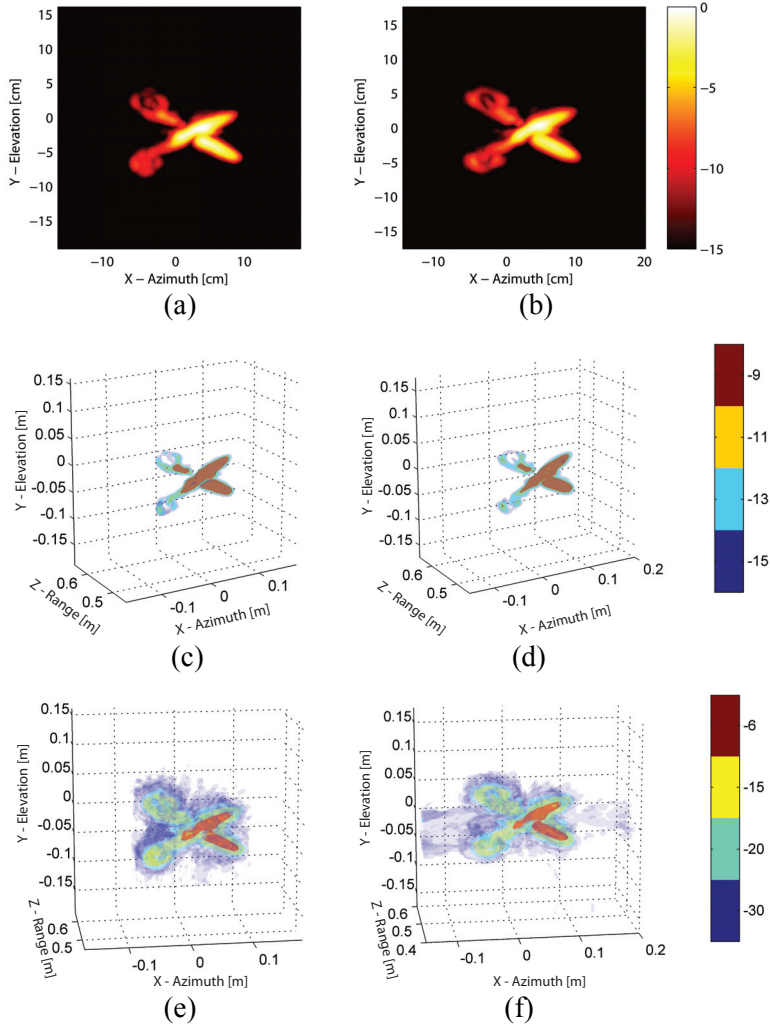


Figure 5.5 Reconstructed images of a pair of scissors.

(a) 2-D front view obtained by SAR, (b) 2-D front view obtained by MIMO-SAR, (c) 3-D view obtained by SAR with 15 dB dynamic range, (d) 3-D view obtained by MIMO-SAR with 15 dB dynamic range, (e) 3-D view obtained by SAR with 30 dB dynamic range, and (f) 3-D view obtained by MIMO-SAR with 30 dB dynamic range.

position facing the aperture plane. It is covered with aluminum foil in order obtain less contrast with the metallic weapon and achieve closer approximation of human body's reflectivity. The revolver and knife are attached to the waist and leg of the mannequin to mimic a typical situation during concealed weapon detection in

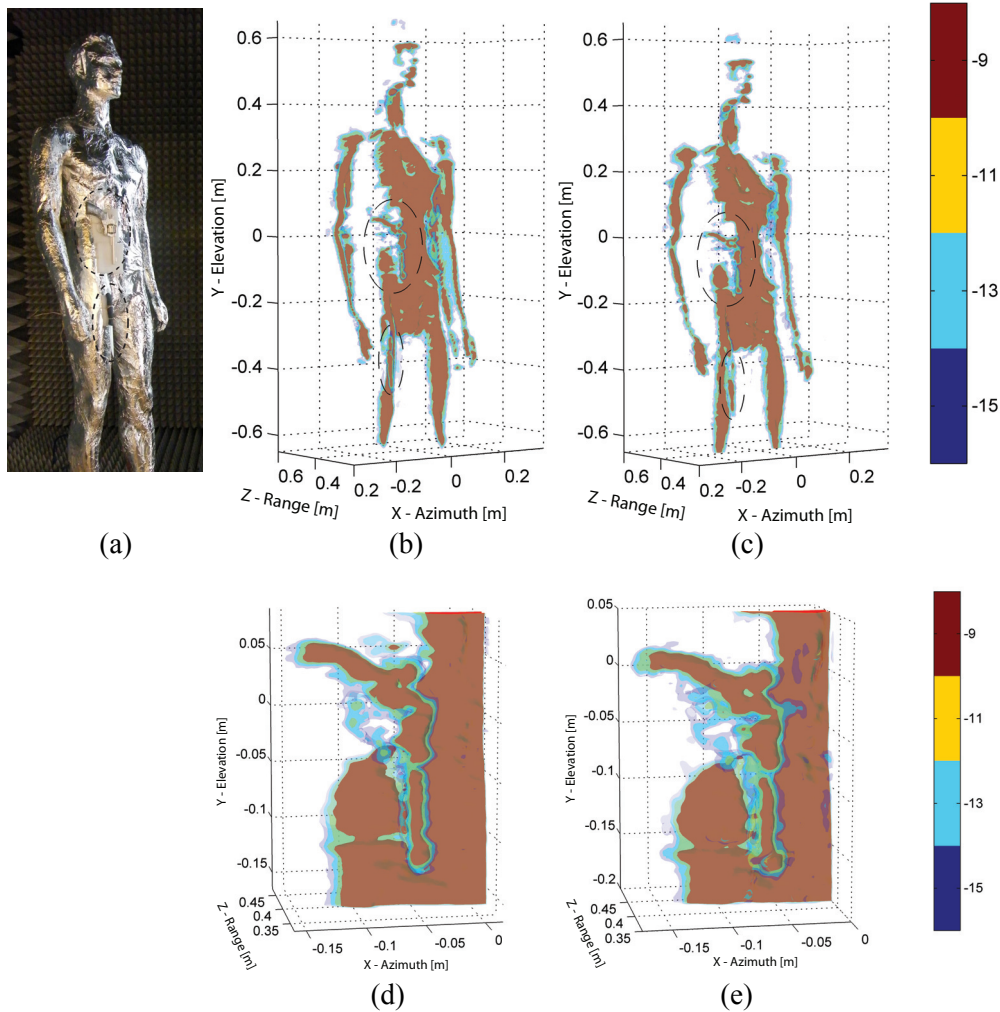


Figure 5.6 3-D volumetric imaging with SAR and MIMO-SAR systems.

(a) Mannequin under test with weapons (revolver and small knife) attached, (b) reconstruction by 2-D SAR, and (c) reconstruction by MIMO-SAR. Both weapons are encircled. Zoomed-in images of the revolver by (d) 2-D SAR, and by (e) MIMO-SAR.

practical conditions. The aperture dimensions of SAR are 50 cm wide and 130 cm high. The length of elevation SAR in the proposed system is the same 130 cm for comparison. Three-dimensional images of the mannequin and zoomed-in images of the revolver are shown and compared in Figure 5.6. In both approaches a truthful reconstruction of the body has been achieved. The shape of the mannequin is well imaged with adequate dynamic range to identify both weapons on the body. Extra

artifacts caused by creeping waves are observed in the SAR image. The MIMO-SAR configuration gives comparable results as 2-D SAR, which shows the capability of the designed MIMO array. Instead of 51 antenna pairs required for SAR data acquisition in azimuth plane, only 12 antennas are used in the “sparse MIMO” system. Thus, it clearly demonstrated the advantage of replacing SAR with real aperture MIMO array.

### 5.3 Summary

In this chapter, we compared the capabilities and potentials of MIMO array and SAR (or array with sequential operation of identical transmit/receive antenna pairs) for UWB near-field imaging. The theoretical characteristics of both approaches were discussed and analyzed. It is shown that advantages and disadvantages of the approaches are relative to specific applications at hand. It is also evident that MIMO array is advantageous over SAR for applications requiring both high-resolution and real-time operation.

Performance of the proposed MIMO imaging system has been experimentally verified by direct comparison with the near-field 2-D SAR. Imaging of objects with different level of complexity and required dynamic range has been performed. Comparable imaging capabilities of both approaches are demonstrated based on the point-spread function, small-sized targets and weapons within a typical CWD scenario. It is shown that both systems are capable of providing high-resolution three-dimensional images with low artifact level. In particular, we have demonstrated that using only 12 antenna elements and 1-D mechanical scanning satisfactory volumetric imaging performance for detecting weapons on human body can be achieved. The experimental results of the proposed imaging system illustrate the strong potential of the combined sparse UWB MIMO array imaging system in demanding applications.

## References

- [1] H. D. Griffiths, “Developments in Modern Synthetic Aperture Radar,” in *Proc. IEEE Radar Conference*, Apr. 2007, pp. 734-739.
- [2] C. A. Wiley, “Synthetic Aperture Radar – a paradigm for technology evolution,” *IEEE Trans. Aerospace & Electronic Systems*, vol. AES-21, pp. 440-443, 1985.
- [3] J. D. Taylor, *Introduction to Ultra-Wideband Radar Systems*, CRC Press, 1994.

- [4] R. H. Stolt, "Migration by Fourier Transform," *Geophys.*, vol. 43, pp. 23-48, 1978.
- [5] J. M. Lopez-Sanchez, J. Fortuny-Guasch, "3-D Radar Imaging Using Range Migration Techniques," *IEEE Trans. Antennas Propag.*, vol. 48, pp. 728-737, May 2000.
- [6] D. M. Sheen, D. L. McMakin, and T. E. Hall, "Three-Dimensional Millimeter-Wave Imaging for Concealed Weapon Detection," *IEEE Trans. Microw. Theory Tech.*, vol. 49, pp. 1581-1592, Sep. 2001.
- [7] F. Gumbmann, H.P. Tran, J. Weinzierl, L.-P. Schmidt, "Multistatic Short Range Ka-Band Imaging System," in *Proc. German Microwave Conference*, Mar. 2009, pp. 1-4.

## CHAPTER 6

# ADVANCED IMAGING ALGORITHMS FOR UWB MIMO ARRAY

An imaging system with three-dimensional (3-D) capability can be implemented by using wideband transceiver which synthesizes a two-dimensional (2-D) planar aperture. A 3-D image can be formed by coherently integrating the backscatter data over the measured time (or frequency band) and the two spatial coordinates of the 2-D aperture. In contrast to the synthetic aperture radar (SAR) technique, the aperture of our consideration consists of asymmetrical transmit and receive sub-arrays. Therefore, dedicated imaging algorithms have to be tailor-made to focus the collected wideband multistatic data sets, and to reconstruct the reflectivity map of the targets in near-field.

Based on the previously developed UWB MIMO array, two novel beamforming algorithms are to be introduced in the chapter, namely modified Kirchhoff migration and MIMO range migration algorithm. To put everything clear from the beginning, both the new algorithms, as all SAR algorithms, have been developed based on linearization of the electromagnetic wave scattering problem, or also known as Born approximation. This means that the interaction between the scatterers within the scene is neglected. This approximation is widely applied in the field of radar and ultrasonic imaging, since appropriate 3-D nonlinear imaging algorithms dealing with the inverse scattering problem have not yet been developed. The aim of this chapter

is to develop high-performance and efficient 3-D imaging technique for the identification and characterization of radar reflectivity components of complex objects appearing within the near-field of a 2-D MIMO array aperture.

The chapter is organized as follows. The extension of Kirchhoff migration for MIMO array imaging in both free-space and subsurface scenarios are presented in section 6.1. In section 6.2, the implementation of MIMO array imaging is further formulated in the frequency wavenumber domain in order to achieve higher computational efficiency. The chapter is summarized in the last section.

## **6.1 Modified Kirchhoff migration**

Two-dimensional synthetic aperture radar (SAR) processing is originally applied in space-born or air-born radar applications. It is further extended to 3-D in ground penetrating radar (GPR) systems in order to provide resolution in three dimensions. Such method is also known as diffraction stack migration or back projection algorithm. The first introduction of this type of algorithm can be traced back to the late 1960s [1]. By propagating each collected time-domain range profile backward in reverse time, the observed events are moved from the data acquisition position back to their true spatial location. Integrating the backward propagated signals over all the antennas within the radar aperture completes the calculation of diffraction stack for the migrated area. Due to its straightforward implementation, diffraction stack migration is quite flexible and can be easily applied to different type of data gathers, therefore gaining notable popularity among different systems. However, it also has some undesirable characteristics [2], which limit its use in high quality imaging applications. The reason for its shortcomings is rooted in the fact that while diffraction stack procedure is intuitively obvious, it is not based on a rigorous wave theory.

An alternative to the diffraction stack migration is Kirchhoff migration, which is based on wave equation. The firm wave equation basis for Kirchhoff integral migration was introduced in [3] and further refined in [4], [5]. Progress in the finite-difference calculation of travel times through the eikonal equation and Fermat's principle pushed the Kirchhoff method to be more accurate and applicable to prestack seismic imaging [6], [7]. Variations such as beam migration [8] and Kirchhoff-type inversion formulas [9], [10] further increase the diversity and practicability of the method. The Kirchhoff integral method represents a quantitative statement of Huygen's principle and delivers significantly higher-quality image and lower sidelobe level. Due to its potential to handle different irregular data gathers and computational efficiency, Kirchhoff migration method still remains the most practical approach for 3-D pre-stack seismic imaging. However, due to special requirements of application, adapting the integral method for MIMO array radar is not straight forward. The original Kirchhoff migration is formulated based on the

exploding reflector model (ERM) and is applicable for an array with a number of identical transmit and receive antenna pairs (common-offset data acquisition) or radar which is based on synthetic aperture (SAR). Kirchhoff method was applied to process GPR data in [11] and [12], in which the migration was carried out by an integral that represents a weighted summation over all the receivers. However, the synthesis over transmitters was not explicitly handled. In my research, a formulation for wave migration is derived that accounts for both the transmitter and receiver topologies by rigorous application of the Kirchhoff integral. This modified formulation adapts Kirchhoff migration to multi-static scenarios such as MIMO array-based radar with multiple spatially distributed transmit and receive antennas.

Another problem of applying the Kirchhoff theorem for array-based radar imaging is the forward Green's function that it uses to express the Helmholtz theorem. The Huygen's principle states that if the value of a wave field is known on a closed surface along with the normal and time derivative on that surface, the wave field at any point interior to the surface can be calculated by the integration over the surface. This theory is thoroughly valid only when we have an enclosed or infinite data acquisition surface that is able to intercept all the scattered wave fields from the target. This can hardly be realized, especially for a real-aperture array. Due to economic reasons and the limit of data acquisition time, the array is designed to cover only what is necessary. The limited aperture causes differentiation in array's responses to different target locations. Specifically, the same target located in the subsurface directly underneath the center of the array or closer to the aperture will have larger array response in the resulted images than those that are placed closer to the edge or further away from the aperture. The influence of a limited aperture is far more severe in near-field than in far-field. In order to minimize this effect, we suggest using a backward propagating expression of the Green's function in the modified Kirchhoff algorithm. Proper designs of transmitter and receiver topologies can also enhance edge targets while maintaining a low sidelobe level.

Finally, in a number of challenging applications of short-range imaging radar, such as GPR or through-wall radar, the array system is required to keep a standoff distance from the air-medium interface due to safety concerns, and to prevent medium's influence on antenna performance. In these cases, ignoring the refraction angle through the interface leads to time estimation error, which causes distortion and de-focusing of a subsurface image. Thus, when a medium interface appears between the array aperture and the imaging area, further re-formulation is needed in order to use the Kirchhoff migration to image the subsurface. For these reasons, the Kirchhoff integral is adapted to subsurface by including the Snell's law and Fresnel's equations into the expression of the Green's function.

### 6.1.1 Formulation

The principle of Kirchhoff migration is to back-propagate the scalar wave front,

measured in the data acquisition plane, to the object plane at time zero, using an integral solution to the scalar wave equation. The feasibility of applying Kirchhoff migration to electromagnetic waves lies on the fact that vector wave equations reduce to scalar wave equation in a homogeneous, isotropic medium. Given the time harmonic form of the vector wave equation in a source-free homogeneous medium  $\nabla \times \nabla \times \mathbf{E} - \omega^2 \mu \epsilon \mathbf{E} = 0$ , by using the vector identity that  $\nabla \times \nabla \times \mathbf{E} = \nabla(\nabla \cdot \mathbf{E}) - \nabla^2 \mathbf{E}$  and that the divergence of the E-field,  $\mathbf{E}$ , equals to zero in a source-free medium, it becomes  $\nabla^2 \mathbf{E} + k^2 \mathbf{E} = 0$ , where  $k^2 = \omega^2 \mu \epsilon$  with  $\omega$  the angular frequency,  $\epsilon$  and  $\mu$  the permittivity and permeability of the medium. In Cartesian coordinates, it consists of three scalar wave equations. Therefore, we are able to describe the inverse problem of the electromagnetic propagation as migration using the Helmholtz-Kirchhoff integral theorem. The Kirchhoff migration neglects all depolarization phenomena as it treats electromagnetic waves as scalar waves. In my research, the antenna is considered to be isotropic and constant velocity model is presumed in each subsurface of the media where the wave field propagates. Kirchhoff approximation is also regarded as one of the analytical approximate methods which can conveniently calculate scattering from a rough surface [13].

Mathematically the Kirchhoff integral is formulated in frequency-domain as

$$U(\mathbf{r}, \omega) = \frac{1}{8\pi^2} \int_{S_0} \frac{\partial R}{\partial n} \left[ \frac{i\omega}{vR} U(\mathbf{r}_0, \omega) e^{-i\omega\tau} + \frac{1}{R^2} U(\mathbf{r}_0, \omega) e^{-i\omega\tau} \right] dS_0 \quad (6.1)$$

and in time-domain as

$$U(\mathbf{r}, t) = \frac{1}{8\pi^2} \int_{S_0} \frac{\partial R}{\partial n} \left[ \frac{1}{vR} \frac{\partial}{\partial t} U(\mathbf{r}_0, t - \tau) + \frac{1}{R^2} U(\mathbf{r}_0, t - \tau) \right] dS_0 \quad (6.2)$$

where  $U$  represents the wave field within a source-free volume bounded by surface  $S_0$ ,  $\mathbf{n}$  is the unit normal to  $S_0$ ,  $\mathbf{r}$  is the vector from the origin to the point where the wave field is estimated,  $\mathbf{r}_0$  is the vector from the origin to the integration point,  $R = |\mathbf{r} - \mathbf{r}_0|$ , and  $\tau = R/v$  with  $v$  the propagation speed in the medium.

This formulation can not be applied directly to MIMO short-range imaging. Two issues have to be resolved beforehand. Firstly, the integrals in (6.1) and (6.2) are derived in one-way travel time. They can be applied for migration by assuming the exploding reflector model (ERM), under which the wave field starts to expand from the target at time zero with half the wave velocity in the medium. Such assumption is only feasible for collocated monostatic source and receiver. It is not applicable to use the conventional Kirchhoff integrals for MIMO array which consists of multistatic transceivers.

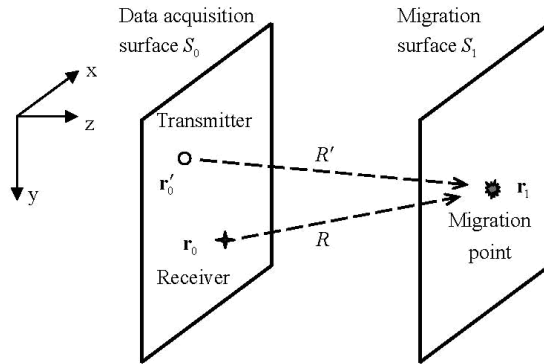


Figure 6.1 Geometry of migration for MIMO array. Wave fields measured with transmitters and receivers on surface  $S_0$  are used to evaluate the wave fields on the migration surface  $S_1$ .

Secondly, in the previous works of [3] and [14], a far-field approximation  $\omega/Rv \gg 1/R^2$  is applied, and the second term in the equations is dropped for higher computation efficiency. Since we are oriented in both near-field and UWB (including low frequencies), such assumption is inappropriate, thus both terms should be kept.

These shortcomings are to be resolved in the next section.

#### 6.1.1.1 Formulation for MIMO array

To apply the integral formulation for the migration of MIMO array, one must explicitly express the wave field on the migration surface  $S_1$  as an expression of wave fields from both transmitter and receiver apertures (Figure 6.1). We assume that the magnitudes of all radiating sources are identical and transform all the fields created by the sources and scattered from targets into wavenumber-frequency domain.

By using the extrapolation operator introduced in [3], we first extrapolate the received field  $\tilde{U}_{S_0}^r$  from the surface  $S_0$  to the migration surface  $S_1$  assuming that this migration plane is situated between the observation plane  $S_0$  and the volume occupied with scatterers. This results in the scattered field

$$\tilde{U}_{S_1}^{scattered}(k_x, k_y, z_1, \omega) = \tilde{U}_{S_0}^r(k_x, k_y, z_0, \omega) \cdot H(k_x, k_y, \Delta z, \omega) \quad (6.3)$$

where

$$H(k_x, k_y, \Delta z, \omega) = e^{i\Delta z \sqrt{(\frac{\omega}{v})^2 - k_x^2 - k_y^2}}$$

$$\Delta z = z_1 - z_0$$
(6.4)

The function  $H$  is the extrapolation operator embodying the exact dispersion relation for the scalar wave equation.

Now we further assume applicability of Born approximation for the scattered field, following which the scattered field  $\tilde{U}_{S_1}^{scattered}$  is proportional to the incident field  $\tilde{U}_{S_1}^{incident}$

$$\tilde{U}_{S_1}^{scattered} = f_r \cdot \tilde{U}_{S_1}^{incident}$$
(6.5)

where  $f_r$  stands for the reflectivity of the scatterer. The incident field can be further extrapolated using the same Kirchhoff integral from the source plane  $S_0$  to the migration plane  $S_1$

$$\tilde{U}_{S_1}^{incident}(k_x, k_y, z_1, \omega) = \tilde{U}_{S_0}^{source}(k_x, k_y, z'_0, \omega) \cdot H(k_x, k_y, -\Delta z', \omega)$$
(6.6)

where  $\Delta z' = z_1 - z'_0$ , and  $\tilde{U}_{S_0}^{source}$  represents the radiated field from the transmitting sources. The choice of sign of the extrapolation operator in equation (6.3) and (6.6) determines the direction of extrapolation.

By substituting both (6.3) and (6.6) into (6.5), one can derive expression for the target's reflectivity as

$$f_r = \frac{\tilde{U}_{S_0}^r(k_x, k_y, z_0, \omega) \cdot H(k_x, k_y, \Delta z, \omega)}{\tilde{U}_{S_0}^{source}(k_x, k_y, z'_0, \omega) \cdot H(k_x, k_y, -\Delta z', \omega)}$$
(6.7)

Taking into account that  $H(\Delta z') = 1/H(-\Delta z')$  and assuming  $\tilde{U}_{S_0}^{source}$  is a constant, one can obtain

$$f_r = \tilde{U}_{S_0}^r(k_x, k_y, z_0, \omega) \cdot H(k_x, k_y, \Delta z, \omega) \cdot H(k_x, k_y, \Delta z', \omega)$$
(6.8)

Transforming back to space-time domain

$$f_r = U_{S_0}^r(x, y, z_0, t) * H(x, y, \Delta z, t) * H(x', y', \Delta z', t)$$
(6.9)

where

$$\begin{aligned} H(x, y, \Delta z, t) &= \frac{1}{2\pi} \frac{\partial}{\partial z_0} \left[ \frac{\delta(t - r/v)}{r} \right] \\ H(x', y', \Delta z', t) &= \frac{1}{2\pi} \frac{\partial}{\partial z'_0} \left[ \frac{\delta(t - r'/v)}{r'} \right] \end{aligned} \quad (6.10)$$

and

$$\begin{aligned} r^2 &= \Delta z^2 + x^2 + y^2 \\ r'^2 &= \Delta z'^2 + x'^2 + y'^2 \end{aligned} \quad (6.11)$$

Equation (6.9) indicates that the complete MIMO integral can be recognized as consecutive three-dimensional convolutions of the observed wave field with the space-time operators related to the point source solutions of the transmit and receive apertures. After regaining the integral form of the convolutions and further performing the differentiation, we arrive at

$$\begin{aligned} f_r(\mathbf{r}_1) = & \int_{S_0} \int_{S'_0} \frac{\partial R}{\partial n} \frac{\partial R'}{\partial n} \frac{1}{RR'} \left[ \frac{1}{v^2} \frac{\partial^2}{\partial t^2} U(\mathbf{r}_0, \mathbf{r}'_0, t - \tau - \tau') \right. \\ & \left. + \frac{1}{v} \left( \frac{1}{R} + \frac{1}{R'} \right) \frac{\partial}{\partial t} U(\mathbf{r}_0, \mathbf{r}'_0, t - \tau - \tau') + \frac{1}{RR'} U(\mathbf{r}_0, \mathbf{r}'_0, t - \tau - \tau') \right] dS'_0 dS_0 \Big|_{t=0} \end{aligned} \quad (6.12)$$

where  $R = |\mathbf{r}_1 - \mathbf{r}_0|$  and  $R' = |\mathbf{r}_1 - \mathbf{r}'_0|$  as indicated in Figure 6.1;  $\tau = R/v$  and  $\tau' = R'/v$  are the time delays for corresponding transceivers; and  $S_0$  and  $S'_0$  represent the transmit and receive apertures respectively.

Equation (6.12) will be referred to forward MIMO Kirchhoff migration and will be used to perform imaging for array-based radar when radar aperture is able to intercept most of the scattered field from the target.

### 6.1.1.2 Compensation of limited aperture effects

If only a limited portion of the enclosing surface  $S_0$  is available for integration, the forward formulation does not provide shape images of reflectors. In practice, the forward Kirchhoff integral is applicable when the radar aperture is able to intercept most of the scattered field from targets that is aimed to be imaged. This is a problem not only in Kirchhoff migration but also for diffraction summation or synthetic aperture radar techniques. The limited aperture causes targets with same reflectivity to have undesired, different array responses due to their different positions. The target located at larger distance has weaker array response, because smaller parts of the scattered field are intercepted by the aperture. It is the same for targets close to the edge of the array comparing with central targets. On the other hand, a real

aperture array is designed to cover what is necessary and to probe an area that is as large as possible. In order to compensate the limited aperture effects, we experimentally replace the forward free-space Green's function with the backward expression as

$$G_{fs} = 4\pi R \cdot \delta(t + \frac{R}{v})$$

By using the backward formulation, the dependence of array response on aperture coverage can be reduced due to the fact that the backward elementary Green's function starts to compensate propagation loss at transceiver pair level. In this way, weak array responses caused by large range distance or limited aperture coverage are corrected before integration takes place. Therefore, the utilization of backward formulation offers a possibility to reduce the effects associated with limited aperture. Although we are aware of the fact that Huygen's principle is based on the assumption that no source exists inside the integration surface  $S_0$ , and the backward Green's function will not satisfy the scalar wave equations, our experiment results show that this method practically performs aperture equalization and gives complementary results to the forward formulation.

Based on the backward Green's function, the integral formulations are further derived, and we obtained

$$f_r(\mathbf{r}_l) = 2 \int_{S_0} \frac{\partial R}{\partial n} \frac{R}{v} \frac{\partial}{\partial t} [U(\mathbf{r}_0, t + \tau) + U(\mathbf{r}_0, t - \tau)] dS_0 \Big|_{t=0} \quad (6.13)$$

Corresponding with the forward expression in (6.2), equation (6.13) represents the formulation for backward migration of the wave field. And it makes sure that the target is imaged in accordance with its reflectivity under limited aperture conditions. The backward formulation should be applied when there is not enough aperture coverage for the probing area.

For array with multiple transmit and receive antennas, same procedure for the forward condition is followed. Then we obtained the backward MIMO Kirchhoff integral

$$\begin{aligned} f_r(\mathbf{r}_l) = & 4 \int_{S_0} \int_{S'_0} \frac{\partial R}{\partial n} \frac{\partial R'}{\partial n} \left[ \frac{RR'}{v^2} \frac{\partial^2}{\partial t^2} U(\mathbf{r}_0, \mathbf{r}'_0, t + \tau + \tau') \right. \\ & + \frac{1}{v} (R + R') \frac{\partial}{\partial t} U(\mathbf{r}_0, \mathbf{r}'_0, t + \tau + \tau') \\ & \left. + U(\mathbf{r}_0, \mathbf{r}'_0, t + \tau + \tau') \right] dS'_0 dS_0 \Big|_{t=0} \end{aligned} \quad (6.14)$$

Equation (6.14) produces migrated images that are further compensated for spreading loss and limited aperture effects.

As we can observe from both equation (6.12) and (6.14), a complete symmetry exists in terms of transmit and receive apertures. This symmetry complies with physical phenomenon according to the principle of reciprocity. In the past, Kirchhoff migration was commonly applied by using only the receiver integral at the time when the transmitted pulse reaches the reflector [11], [12]. The result from each source was then summed together to generate the migrated image. Without the source integral, the reciprocal symmetry between transmitter and receiver was not fully explored. And mathematically, the oblique angle and weighing factor related to transmitter's topologies were not included. In the situation when there is few sources' coverage, the one-way formulations will be sufficient. For an array with multiple transmitters and receivers, the complete MIMO Kirchhoff integral is crucial in order to obtain satisfactory results in difficult conditions where target response exhibits large dynamic range and is present together with high level clutters.

### 6.1.1.3 Extending Kirchhoff integral to subsurface

In this section, we further extend the Kirchhoff integral to subsurface scenarios. When a primary interface appears between the array and the target area, ground effects must be taken into consideration and be included in the Kirchhoff formula. Electromagnetic waves propagating in a planarly layered, isotropic medium can be reduced to two uncoupled scalar wave equations. And due to their double derivative terms, their solution follows the similar form of Green's function as in free-space. Here we specify the forward subsurface Green's function based on the approximation of both Snell's law and Fresnel's equations as

$$G_s = \frac{T}{4\pi(R_a + R_b)} \cdot \delta(t - \frac{\sqrt{\varepsilon_{r1}}R_a + \sqrt{\varepsilon_{r2}}R_b}{c})$$

where  $\varepsilon_{r1}$  and  $\varepsilon_{r2}$  are the dielectric permittivity in the two media as indicated in Figure 6.2. And  $R_a = |\mathbf{r}_{int} - \mathbf{r}_0|$  and  $R_b = |\mathbf{r}_l - \mathbf{r}_{int}|$  represent the wave propagation path in the two different media respectively.  $T$  is the transmission coefficient through the subsurface, which can be calculated using the Fresnel's equations.  $c$  is the speed of propagation in free-space.

Based on the subsurface Green's function, we first derive the formulation with transmitter remaining at its original position  $\mathbf{r}'_0$  as

$$\begin{aligned} U(\mathbf{r}_l, \mathbf{r}'_0, t) &= \frac{1}{8\pi^2} \int_{S_0} T \left[ \left( \sqrt{\varepsilon_{r1}} \frac{\partial R_a}{\partial n} + \sqrt{\varepsilon_{r2}} \frac{\partial R_b}{\partial n} \right) \frac{1}{cR} \frac{\partial}{\partial t} U(\mathbf{r}_0, \mathbf{r}'_0, t - \tau) \right. \\ &\quad \left. + \left( \frac{\partial R_a}{\partial n} + \frac{\partial R_b}{\partial n} \right) \frac{1}{R^2} U(\mathbf{r}_0, \mathbf{r}'_0, t - \tau) \right] dS \end{aligned} \quad (6.15)$$

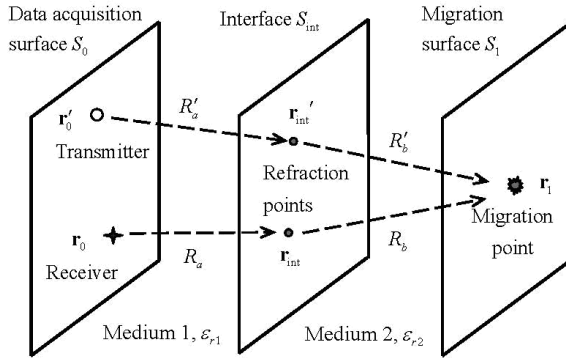


Figure 6.2 Geometry of migration for MIMO array in subsurface scenario. Wave fields measured on surface  $S_0$  are used to evaluate the wave fields on the migration surface  $S_1$  through the interface  $S_{\text{int}}$  between two media.

where  $\tau = (\sqrt{\epsilon_{r1}} R_a + \sqrt{\epsilon_{r2}} R_b) / c$ , and  $R = R_a + R_b$  as the path of propagation from the receiver  $\mathbf{r}_0$  through  $\mathbf{r}_{\text{int}}$  to the migration point  $\mathbf{r}_1$ .

Then the transmitter is further moved based on the reciprocal principle, and we arrive at the subsurface MIMO Kirchhoff integral

$$\begin{aligned} U(\mathbf{r}_1, t) = & \frac{1}{64\pi^4} \int_{S_0} \int_{S'_0} \frac{TT'}{RR'} \cdot \left[ \frac{AA'}{c^2} \frac{\partial^2}{\partial t^2} U(\mathbf{r}_0, \mathbf{r}'_0, t - \tau - \tau') \right. \\ & + \frac{1}{c} \left( \frac{A'B}{R} + \frac{AB'}{R'} \right) \frac{\partial}{\partial t} U(\mathbf{r}_0, \mathbf{r}'_0, t - \tau - \tau') \\ & \left. + \frac{BB'}{RR'} U(\mathbf{r}_0, \mathbf{r}'_0, t - \tau - \tau') \right] dS'_0 dS_0 \end{aligned} \quad (6.16)$$

$$\begin{aligned} \text{where } A &= \sqrt{\epsilon_{r1}} \frac{\partial R_a}{\partial n} + \sqrt{\epsilon_{r2}} \frac{\partial R_b}{\partial n}, \quad A' = \sqrt{\epsilon_{r1}} \frac{\partial R'_a}{\partial n} + \sqrt{\epsilon_{r2}} \frac{\partial R'_b}{\partial n} \\ B &= \frac{\partial R_a}{\partial n} + \frac{\partial R_b}{\partial n}, \quad B' = \frac{\partial R'_a}{\partial n} + \frac{\partial R'_b}{\partial n} \end{aligned}$$

and  $\tau = (\sqrt{\epsilon_{r1}} R'_a + \sqrt{\epsilon_{r2}} R'_b) / c$  with  $R' = R'_a + R'_b$  as the path from the transmitter  $\mathbf{r}'_0$  through  $\mathbf{r}_{\text{int}}$  to the migration point  $\mathbf{r}_1$ .

In the situation where the array aperture can not intercept most of the scattered fields from the targets, the backward Green's function should be applied

$$G_s = \frac{4\pi(R_a + R_b)}{T} \cdot \delta(t + \frac{\sqrt{\epsilon_{r1}} R_a + \sqrt{\epsilon_{r2}} R_b}{c})$$

This leads us to the backward subsurface SIMO and MIMO integral equations formulated as

$$\begin{aligned} U(\mathbf{r}_1, \mathbf{r}'_0, t) = & -2 \int_{S_0} \frac{1}{T} \left[ \left( \sqrt{\varepsilon_{r1}} \frac{\partial R_a}{\partial n} + \sqrt{\varepsilon_{r2}} \frac{\partial R_b}{\partial n} \right) \frac{R}{c} \frac{\partial}{\partial t} U(\mathbf{r}_0, \mathbf{r}'_0, t + \tau) \right. \\ & \left. + \left( \frac{\partial R_a}{\partial n} + \frac{\partial R_b}{\partial n} \right) U(\mathbf{r}_0, \mathbf{r}'_0, t + \tau) \right] dS_0 \end{aligned} \quad (6.17)$$

$$\begin{aligned} U(\mathbf{r}_1, t) = & 4 \int_{S_0} \int_{S'_0} \frac{1}{TT'} \cdot \left[ \frac{AA'RR'}{c^2} \frac{\partial^2}{\partial t^2} U(\mathbf{r}_0, \mathbf{r}'_0, t + \tau + \tau') \right. \\ & + \frac{1}{c} (AB'R + A'BR') \frac{\partial}{\partial t} U(\mathbf{r}_0, \mathbf{r}'_0, t + \tau + \tau') \\ & \left. + BB'U(\mathbf{r}_0, \mathbf{r}'_0, t + \tau + \tau') \right] dS'_0 dS_0 \end{aligned} \quad (6.18)$$

Equations (6.15) to (6.18) include refraction effect into the Kirchhoff formula and compensate both amplitude and time changes caused by the subsurface. These integrals can be applied as migration when being evaluated at the shot instant  $t = 0$ , where wave field  $U$  is replaced by target reflectivity  $f_r$ . When only one transmitter is used in the array for illumination, equation (6.15) and (6.17) should be applied evaluating the receiver's integral at the time when the transmitted pulse reaches the target. For a MIMO array, both transmit and receive integral are necessary by applying the formulas described in equation (6.16) and (6.18).

#### 6.1.1.4 Efficient calculation of travel time

The travel time for the wave field to propagate from the transmitter to the target and to scatter back to the receiver must be known in order to calculate the formulated Kirchhoff integrals. The calculation in free-space is straightforward and does not need further attention. In the subsurface, the wave refracts at the interface according to the Snell's law. An efficient time estimation method must be established in order to adjust the Kirchhoff formulas for practical applications.

Figure 6.3 illustrates the propagation paths associated with the incident and scattered wave fields from transmit and receive antennas to the location of the scatterer where radar reflectivity is to be estimated. A point scatterer is assumed to be buried in a lossless medium at a distance  $d$  from the interface. Its associated propagation time will be defined by the electrical length of the two-way paths travelled by a spherical wave from the antenna to the location of the point scatterer. Assuming that the spherical wave fields are locally planar, one can estimate the electrical path corresponding to the propagation path through Snell's law as follows.

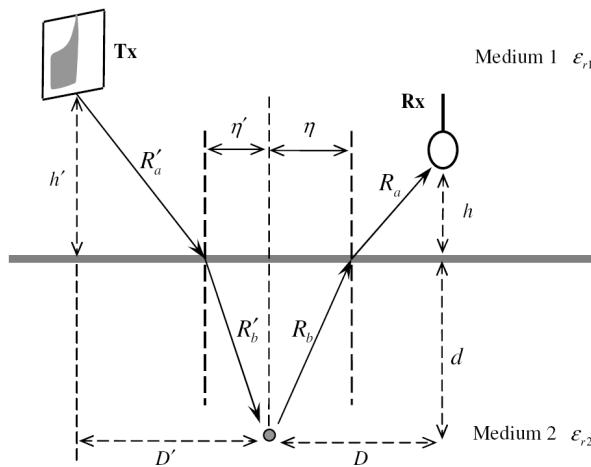


Figure 6.3 Geometry of propagation paths associated with the incident and refracted wave fields.

$$R = R_a + R_b = \sqrt{\varepsilon_{r1}} \sqrt{h^2 + (D - \eta)^2} + \sqrt{\varepsilon_{r2}} \sqrt{d^2 + \eta^2} \quad (6.19)$$

where  $h$  is the distance between the antenna and the interface, and  $\eta$  denotes the horizontal distance between the refraction point of the wave field and the target, which can be estimated by finding the truth zero of the function defined as

$$f(\eta) = \sqrt{\varepsilon_{r1}} \frac{D - \eta}{\sqrt{h^2 + (D - \eta)^2}} - \sqrt{\varepsilon_{r2}} \frac{\eta}{\sqrt{d^2 + \eta^2}} \quad (6.20)$$

A fast solution to find the root of this function is to apply the Newton-Raphson's method [15]. We start with an initial guess, which we choose  $\eta = 0$  for this problem to avoid possible convergence failures. Then the function is approximated by its tangent line. The interception of the tangent line crossing the x-axis provides the next estimate which typically leads to a closer approximation to the final solution. The algorithm iterates until the approximation is close enough to the solution. The Newton's method suits well for this problem and it converges remarkably fast with high accuracy in a minimal number of iterations.

In a three-dimensional space, the estimated travel time is a function of the horizontal distance between the antenna and the scatter  $D$  and the distances of both the antenna and the scatter to the interface ( $h$  and  $d$ ). Therefore, a two-dimensional map of travel time can be generated before migration for both transmitters and receivers, and it can be used iteratively by 1-D interpolation through 3-D migration process. This travel time mapping process is an efficient procedure, and it represents a practical way of implementation in GPR systems. Such method has been applied in

a multi-sensor vehicle-based suit for landmine detection [16], which demonstrated its ability to provide real-time images of the subsurface with 0.02 m scan step under 36 km/h scanning speed.

### 6.1.2 Results in free-space

Full-wave electromagnetic simulations are applied to demonstrate the performances of the developed Kirchhoff integral algorithms in free-space. The models are implemented by using the applied electromagnetic simulation tool, FEKO, which utilizes Method of Moment (MoM) to solve the integral equations. For the numerical model Hertzian dipoles are used as transmit and receive antennas. Due to the feature of the MoM solver, the modeled data are obtained in frequency-domain. It is firstly tapered using a high order Kaiser window to reduce sidelobes and then transformed to time-domain using inverse fast Fourier transform (IFFT).

A linear array with single transmit antenna and a receive array (SIMO) of 1 meter aperture size (range from -0.5 to 0.5 m) and 2 cm antenna spacing are modeled at first. Same received array is further combined with a transmit array with the same aperture size but 10 cm spacing to form a MIMO topology. The transmit antennas illuminate the scene sequentially one after another while each time all the receive antennas simultaneously record the scattered field from the targets. Both SIMO and MIMO arrays operate at the bandwidth from 3 to 10 GHz. Three metal spheres with 2 cm diameter are distributed on the same horizontal plane. The point spread functions (PSF) obtained by both diffraction stack and the modified Kirchhoff migration are shown in Figure 6.4 and 6.5.

It can be clearly observed that the forward Kirchhoff migration improves both cross-range (inline) resolution and sidelobe level comparing with the diffraction summation technique for both SIMO and MIMO arrays. Meanwhile, the influence of limited aperture appears for the targets that are located further and close to the edge of the aperture, when only small part of the scattered field can be intercepted by the antennas. The response of the forward Kirchhoff migration to the edge target is about 8.6 dB lower than its response to the central one. The diffraction stack algorithm is combined with range gain control to compensate the effect. However, as we can see from Figure 6.5, the results are not satisfactory since it significantly increases the sidelobe level and sidelobe size. On the other hand, the backward Kirchhoff migration not only enhances the targets but also exhibits high sidelobe rejection ratio. The response difference between central and edge target reduces to less than 3dB by applying the backward formulation.

In practice, both forward and backward Kirchhoff migration shall be combined to achieve the best performance. When the interested area is within the array coverage,

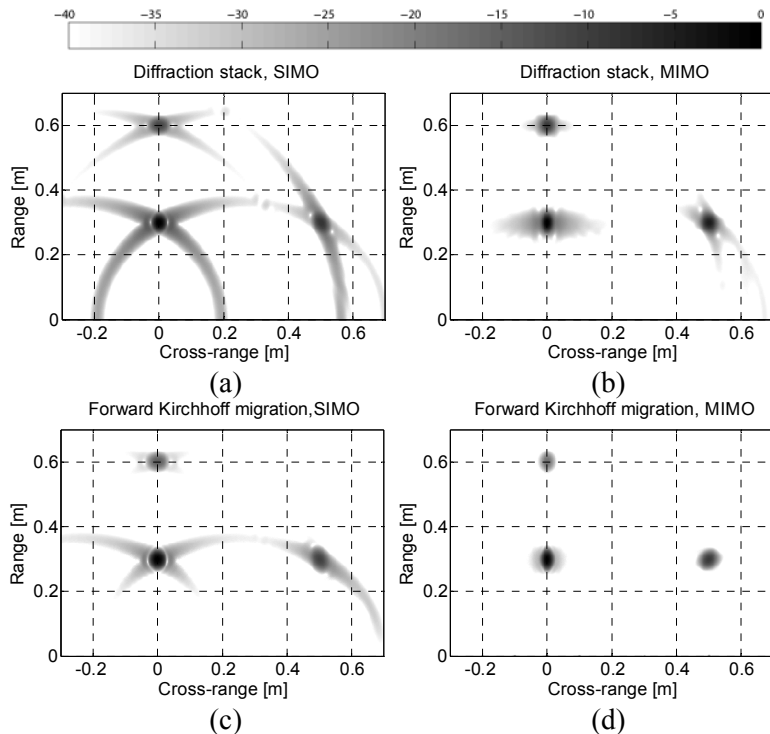


Figure 6.4 Comparison of point spread function between diffraction stack and the modified forward Kirchhoff migration for both SIMO and MIMO arrays. Images are shown in a 40 dB dynamic range: (a) Diffraction stack for SIMO and (b) MIMO array, (c) Forward Kirchhoff migration for SIMO and (d) MIMO array.

forward formulation shall be used since it provides lower sidelobe level and better array pattern. On the other hand, if the array has to cover an area comparable or much larger than its aperture, the backward formulation is more suitable to recover the whole area without missing edge targets. The PSF in free-space clearly demonstrates the advantage of combining MIMO array with the modified Kirchhoff migration over traditional one-way array and diffraction summation technique.

In the next step, an image of a more complicated target with a shape shown in Figure 6.6 has been computed. The target is modeled as perfect electric conducting (PEC) material. It has a width of 10 cm and a height of 20 cm. The first horizontal stroke and the main part of the vertical stroke of the target are in a rectangular shape. The second horizontal stroke takes the shape of a cylinder, while the end of the vertical stroke gradually reduces its width in both horizontal and depth dimensions. All these details are designed to test the imaging algorithms and how it can

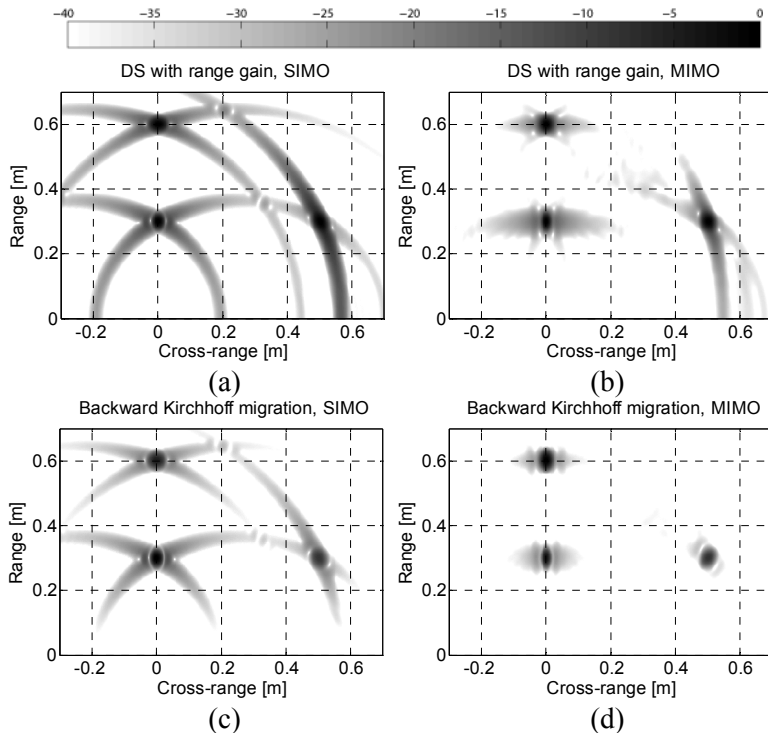


Figure 6.5 Comparison of point spread function between diffraction stack with range gain control and the modified backward Kirchhoff migration for both SIMO and MIMO array. Images are shown in a 40 dB dynamic range: (a) Diffraction stack for SIMO and (b) MIMO array, (c) Backward Kirchhoff migration for SIMO and (d) MIMO array.

reconstruct the contour of different target configurations. The specific antenna arrays used in the experiment are shown in (c) and (d) in Figure 6.6. The aperture extends 1 meter by 1 meter in both directions and consists of 81 antennas on the vertical plane. The difference between the SIMO and MIMO array is the number of antennas that are used as transmitters. The target is placed in front of the center of the array at the range of 0.5 meter. The near-field distribution on the array plane at central frequency (6.5 GHz) shows that the scattered fields are mostly received by the aperture (Figure 6.6 (b)). As we can see from the 3-D reconstructed images that the forward Kirchhoff migration is able to reduce the artifacts created by the interaction between the two horizontal strokes and reveals more details of the object, such as the flare of the vertical part and the horizontal connection between the second horizontal stroke and the vertical part. The results of both point spread functions and distributed target obtained in free-space by the modified Kirchhoff migration shows advantages over the diffraction summation algorithm in both SIMO and MIMO conditions.

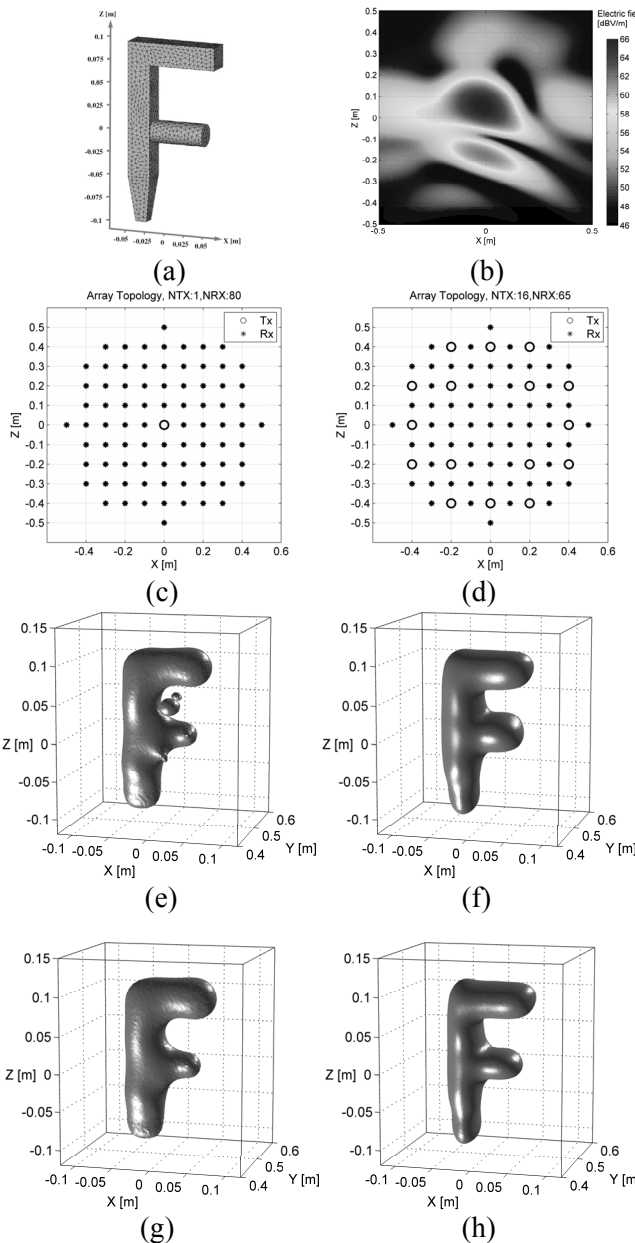


Figure 6.6 Comparison of algorithms for distributed target. (a) picture of the target modeled in MoM solver, (b) field distribution at central frequency 6.5 GHz on the data acquisition plane, (c) array topology with single transmit antenna (SIMO), (d) array topology with multiple transmit multiple receive antennas (MIMO), (e) 3-D image obtained by diffraction stack migration for SIMO array and (f) MIMO array, (g) 3-D image obtained by the forward Kirchhoff migration for SIMO array and (h) MIMO array. Images are shown in 15 dB dynamic range.

### 6.1.3 Results in subsurface

In this section, we evaluate the developed subsurface Kirchhoff integrals using measurement data from the ground penetrating radar developed at TUDelft. The array system of the GPR is shown in Figure 6.7. The transmit antenna was kindly provided by the University of Nice-Sophia Antipolis [32]. The GPR is designed to use all the 13 shielded loops within the receive array simultaneously to image the subsurface. Imaging capability of the radar is realized via the physical aperture of the receive array in the cross-scan direction and synthetic aperture in the along-scan direction. The operational band of the whole system (at the level of -10 dB) is from 0.3 GHz to 3.8 GHz. The detailed description of the system design can be found in [17].

We have demonstrated in [18] that the refraction of the wave front at the air ground interface virtually changes the free-space uniform array to an undesired spatial sampling, which causes degrade of image quality and PSF in the subsurface. Therefore, the receive array of the GPR has been changed to a non-uniform topology specially designed for subsurface.

During the measurement, the receive array is elevated approximately 20 cm above the ground, which is dry sand. The measured dielectric permittivity of the sand is 3.03. Prior to imaging, data pre-processing was performed, including the low-pass filtering of the raw data to suppress uncorrelated noise, the alignment of the direct coupling in every B-scan to compensate for time drift, and the background subtraction to remove direct coupling and ground surface reflection.

Figure 6.8 shows the results of scanning through the top of two metal discs buried under ground at the depth of 5 cm. The diameter of the discs is 5 cm and they are separated by 5 cm between the edges. Migration is performed using the forward subsurface Kirchhoff migration and, for comparison, diffraction stack algorithm. Images are formed within a 25 cm depth. The energy along the depth is projected into a horizontal plane. The dynamic range shown in the figures is 20 dB. As we can see from the images that both algorithms can detect the targets located at the center of the field. However, the subsurface Kirchhoff migration is able to clearly resolve the two discs. This proves the improvement in terms of cross-range (inline) resolution within the receive array.

Figure 6.9 shows the radar images of the scenario with a buried plastic box filled with paraffin and a metal barbed wire. The results are obtained in the same way and are shown in a 20 dB dynamic range. The diffraction stack algorithm gives quite strong response to the wire due to its metallic property comparing with its response to the dielectric target. However, it is impossible to identify the wire based on its cloud like response. In comparison, the modified Kirchhoff migration gives quite strong response to the rectangular plastic box and is able to partly recover the circular contour of the barbed wire. The missing central part of the wire on the image is

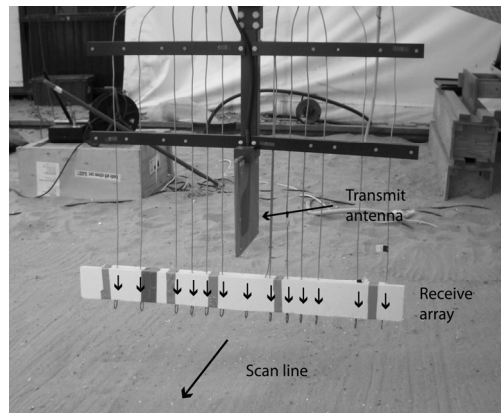


Figure 6.7 Antenna array of the GPR. The total aperture size of the array is 84 cm. Arrows indicate the position of transmit and receive antennas.

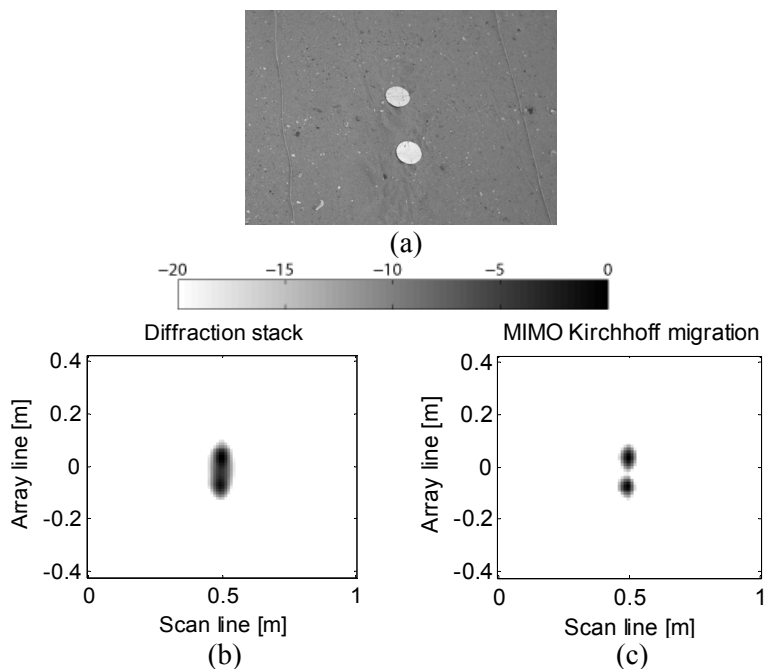


Figure 6.8 Focused images of two metal discs buried under ground at 5 cm depth, separation between the edge of two discs is 5 cm: (a) photo of targets before buried, (b) image processed by diffraction stack, (c) image processed by the forward Kirchhoff migration. Images are shown in a 20 dB dynamic range.

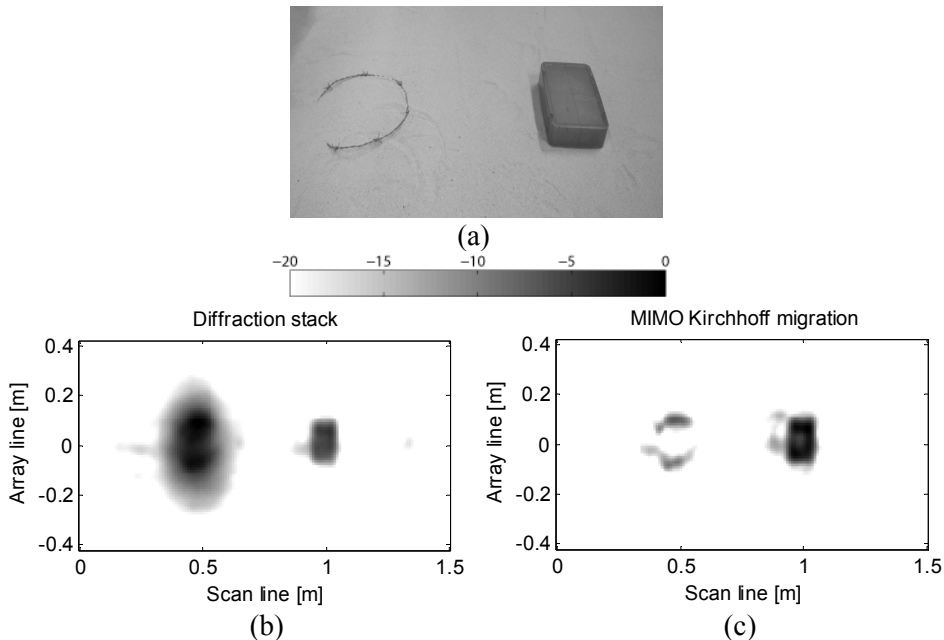


Figure 6.9 Focused images of a plastic box and a barbed wire buried under ground at 5 cm depth. (a) photo of targets before buried, (b) image processed by diffraction stack, (c) image processed by the forward Kirchhoff migration. Images are shown in a 20 dB dynamic range.

caused by the linear polarization property of the transmit Vivaldi antenna, which is orthogonal to the wire at its middle part. The interpretation of Kirchhoff migration is closer to the physical phenomenon due to its root from wave equation migration.

In order to demonstrate the performances of the proposed backward Kirchhoff technique for compensating the influence of limited aperture, a scenario with 6 anti-personnel mines buried at 5cm depth within a 1.5 m scan line is investigated (Figure 6.10a). Half of the mines are buried beneath the edge of the array while the others are directly under the array center. The first four mines from the left are NR22, which has a metal ring. This type of mine gives quite strong response due to its metal composition. The last two mines are PMN-2 mines, which have less metal components and thus produce smaller radar signature than NR22. As we can see from the focused results shown in Figure 6.10 at 20 dB dynamic range, the proposed backward technique has detected both central and edge located mines with equally strong response. Comparing with conventional diffraction stack method, the modified backward Kirchhoff migration provides equalization within the array aperture. It improves detection of targets located beneath the entire aperture coverage, which further leads to higher clutter rejection ratio and lower false alarm rate.

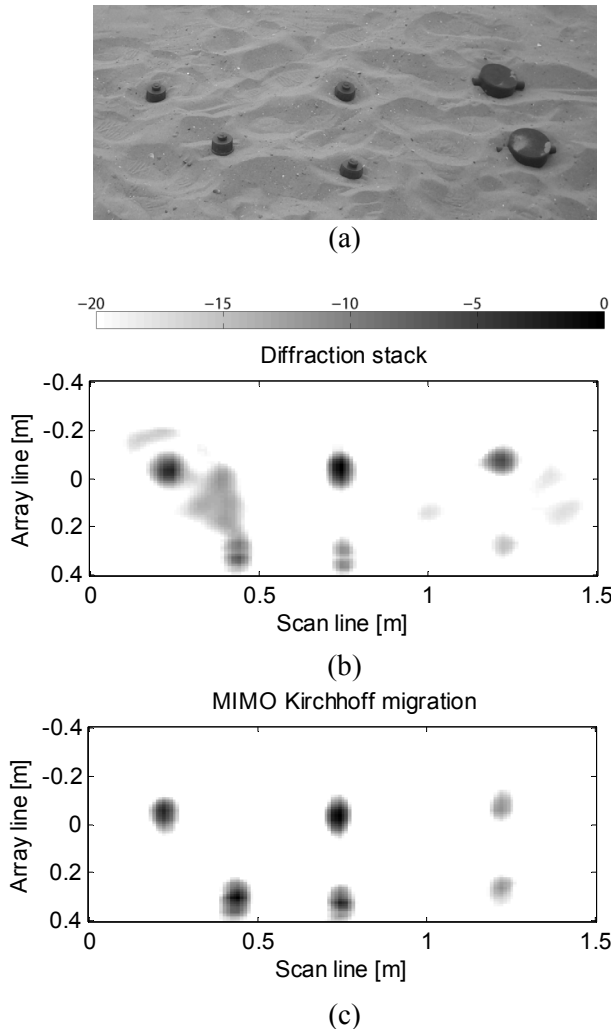


Figure 6.10 Images of 6 anti-personnel mines buried under ground at 5 cm depth. The targets include 4 NR22 and 2 PMN-2. (a) photo of targets before buried, (b) image processed by diffraction stack, (c) image processed by the backward Kirchhoff migration. Images are shown in a 20 dB dynamic range.

Further, a quasi-realistic test is performed with 5 anti-personnel landmines buried within a 2.5 meter scan line at different depths. The positions and depths of the mines are given in Table 1. Among the targets, the two M14 mines are difficult to detect due their small sizes and mainly plastic design. The ground surface was intentionally made rough to mimic a quasi-realistic condition. The obtained images after migration are shown in Figure 6.11. The modified Kirchhoff migration detects all the 5 mines including the two M14 that have much smaller radar signature. In contrast, the result

TABLE 6.1 TARGET MAP IN THE QUASI-REALISTIC TEST

No.	Type	Position	
		Scan line [cm]	Depth [cm]
1	PMN-2	25	20
2	M14	75	5
3	M14	125	5
4	PMN-2	175	5
5	PMN-2	225	10

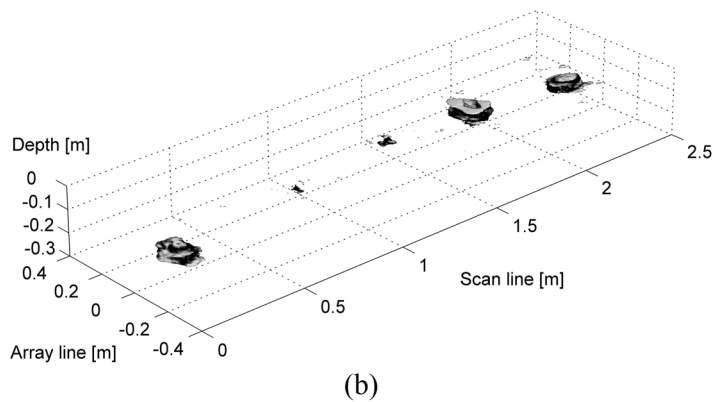
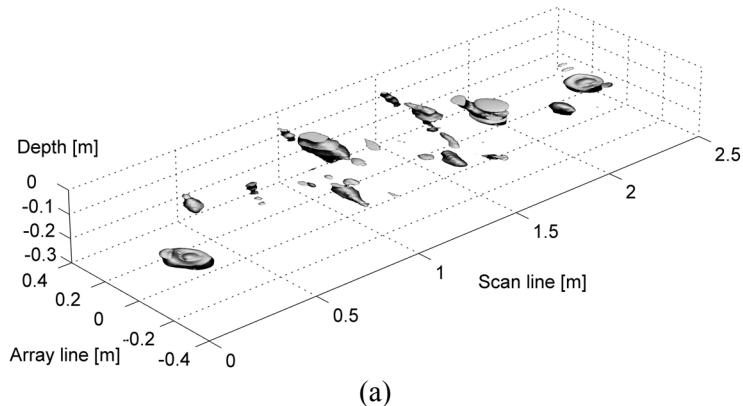


Figure 6.11 Images of a 2.5 m scan line with 5 anti-personnel landmines buried at different depth under a rough sandy surface. (a) 3-D image obtained by diffraction stack, (b) 3-D image obtained by the forward Kirchhoff migration. Images are shown in a 15 dB dynamic range.

from diffraction stack showed more clutters that would give much higher false alarm rate, especially in the weak targets' areas.

The result of the subsurface measurement verifies the practical improvement of the modified Kirchhoff migration in terms of cross-range (inline) resolution, sidelobe level, aperture equalization, clutter rejection ratio and its ability to reconstruct the shape of targets. The computational time needed to obtain the 3-D image shown in Figure 6.11 (  $251 \times 81 \times 31$  pixels) using MATLAB (R2007a) with a 2.66GHz workstation is 1.3 minutes by diffraction stack and 1.5 minutes by Kirchhoff migration. The modified Kirchhoff migration algorithm has been implemented in a multi-sensor vehicle-based suit for landmine detection [16], and demonstrated its ability to provide real-time confidence maps of the subsurface under 36 km/h scanning speed.

## 6.2 MIMO range migration

In this section, we explore the possibilities of performing image reconstruction for MIMO array in the spatial Fourier domain. For SAR data acquisition, this kind of approach is known as range migration, or Stolt ( $\omega - k$ ) migration, and is widely applied in synthetic aperture radar, computer tomography and magnetic resonance imaging. These methods have a common feature: they acquire uniformly sampled data which can be interpreted as the Fourier transform of a wanted image. Naturally, one wants to take full advantage of computing this transform by means of a fast Fourier transform (FFT). Thus, the implementation of the algorithm on a parallel computer becomes fairly straightforward [19]. This, on the other hand, requires a grid of evenly spaced data. Because of such properties, interpolation procedure may be needed and could increase the computation complexity of the imaging. A trade-off must be made to maintain the high computation efficiency nature of the algorithm with an acceptable accuracy level.

Similar to Kirchhoff migration, Stolt ( $\omega - k$ ) migration can be derived from scatter wave equation [20]. It is further extended to 3-D version in [21], named range migration algorithm (RMA). The algorithm requires a 1-D interpolation (Stolt interpolation [22]), and compensates completely the curvature of the wavefront. In the field of remote sensing, RMA was first introduced to focus SAR data acquired from a space-borne platform in the strip map mode. It was further adapted for spotlight mode in [23] [24]. An extended 3-D RMA for cylindrical and spherical geometries was presented in [25]. Other kinds of imaging algorithms include Range-Doppler (RD) algorithm [26] [27] and Chirp Scaling (CS) algorithm [28]. The performances between RD and CS, and between RD and wavenumber-domain algorithms are compared in [29] and [30] for SAR focusing. It was shown that wavenumber-domain approach is the most accurate, while RD and CS only partially

correct the range curvature and can provide defocused image under near-field conditions.

Because of its wave equation foundation, range migration has the potential to provide higher quality image than the standard diffraction stack method. On the other hand, it originates from exploding reflector model (ERM), which requires a monostatic (or SAR) data acquisition. In this section, we further develop the algorithm for MIMO array imaging, which requires a completely different dispersion relation.

### 6.2.1 Range migration for SAR configuration

We start with the inhomogeneous Helmholtz wave equation when the excitation is an impulse source

$$\left[ \frac{\partial^2}{\partial x^2} + \frac{\partial^2}{\partial y^2} + \frac{\partial^2}{\partial z^2} + k^2 \right] b(\mathbf{r}, \mathbf{r}', \omega) = -\delta(\mathbf{r} - \mathbf{r}') \quad (6.21)$$

Applying spatial Fourier transform (cross-range direction x, z) on both side of (6.21) gives

$$[-k_x^2 - k_z^2 + k^2 + \frac{\partial^2}{\partial y^2}] b(k_x, k_z, y, k) = 0 \quad (6.22)$$

Note that this process actually assumes that the propagation velocity does not vary in x and z directions. Based on ERM and consider only upcoming waves, the solution of equation (6.22) is

$$b(k_x, k_z, y, k) = b(k_x, k_z, y=0, k) e^{-ik_y y} \quad (6.23)$$

where  $k_y$  is defined as

$$k_y = \sqrt{\left(\frac{2\omega}{v}\right)^2 - k_x^2 - k_z^2} \quad (6.24)$$

Then the migrated image can be expressed as the inverse Fourier transform of equation (6.23) as

$$f(x, y, z, t=0) = \iiint b(k_x, k_z, y=0, \omega) e^{-i(k_x x + k_y y + k_z z)} dk_x dk_z d\omega \quad (6.25)$$

Expression in (6.25) is also known as Gazdag's Phase-shift Migration, and can handle variations of medium and propagation velocity in the depth (range) direction. When the environment is assumed to be uniform with constant propagation velocity, equation (6.25) can be developed by a change from  $\omega$  to spatial frequency  $k_y$ .

According to (6.24),  $d\omega$  can be written as

$$d\omega = \frac{k_y v^2}{\omega} dk_y \quad (6.26)$$

Note that, here the speed  $v$  is actually half of the propagation speed  $c/2$  in ERM model.

Replace  $d\omega$  in (6.25) by the equation (6.26), the migrated images becomes

$$f(x, y, z, t=0) = v^2 \iiint \frac{k_y}{\omega} b(k_x, k_z, z=0, \omega) e^{-i(k_x x + k_y y + k_z z)} dk_x dk_y dk_z \quad (6.27)$$

The advantage of (6.27) over (6.25) is that it can be calculated directly by a 3-D Fourier transform of the acquired data  $b(k_x, k_z, y=0, \omega)$ , scaled by  $\frac{k_y v^2}{\omega}$ , the Jacobian of the transformation from  $\omega$  to  $k_y$ . It can be seen that this scaling factor is equivalent to the obliquity factor  $\cos\phi$  utilized in the Kirchhoff migration.

Although the formulation of Stolt migration is rather simple, the procedure of the algorithm must be carefully implemented. After transformation, the wavenumber domain data continue being equally spaced in frequency and, therefore, in the  $k_y$  variable. In order to prepare the data for the final 3-D inverse fast Fourier transform (IFFT), the next step consists of a change of variables known as the Stolt interpolation, which is actually a 1-D interpolation from uneven spaced grid to evenly spaced data. This interpolation compensates the range curvature of all scatterers by an appropriate warping of the wavenumber domain backscatter data.

In summary, the Stolt migration consists of four sequential steps:

- The Fourier transformation of collected common-offset (SAR) data  $b(x, z, y=0, t)$  or  $b(x, z, y=0, \omega)$  to obtain  $b(k_x, k_z, y=0, \omega)$ ;
- The interpolation of evenly spaced  $k$  data into uniformly spaced data in  $k_y$  by using the dispersion relation defined in (6.24);
- and scaling of the Jacobian coefficients expressed in (6.26);
- The 3-D inverse FFT of the interpolated wavenumber domain data as expressed in (6.27).

### 6.2.2 Formulation for MIMO array

We have simplified the problem to two-dimension for better illustration. Consider a linear MIMO array placed along axis x (cross-range), and axis y is the range direction. Transmit antennas are located at  $(u, 0)$ , while receivers are placed at  $(v, 0)$ . The imaging geometry is illustrated by Figure 6.12.

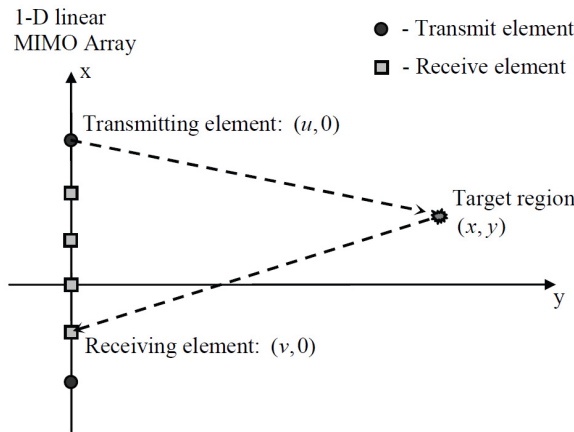


Figure 6.12 Imaging system geometry for MIMO array with asymmetrical transmit and receive elements.

The waveform of the transmitted signal is assumed to be  $p(t)$ . The time delay associated with propagation from each transmit antenna to a target position  $(x, y)$  is expressed as

$$\tau_u = \frac{\sqrt{(x-u)^2 + y^2}}{c}$$

And the time delay for the propagation from the target back to each receive antenna is estimated as

$$\tau_v = \frac{\sqrt{(x-v)^2 + y^2}}{c}$$

Therefore, the recorded wave field due to a point-like scatterer at  $(x, y)$  is formulated as

$$s(u, v, t) = p(t - \tau_u - \tau_v) = p\left(t - \frac{\sqrt{(x-u)^2 + y^2}}{c} - \frac{\sqrt{(x-v)^2 + y^2}}{c}\right) \quad (6.28)$$

Taking the Fourier transform on the temporal domain of the data set leads to

$$s(u, v, \omega) = p(\omega) \cdot e^{-ik\sqrt{(x-u)^2 + y^2}} \cdot e^{-ik\sqrt{(x-v)^2 + y^2}} \quad (6.29)$$

Then we apply two-dimensional spatial Fourier transform on both the transmitter  $u$  and receiver domain  $v$  of (6.29). The spreading loss of the propagation is ignored in order to obtain an analytical expression. The 2-D spatial Fourier transform can be

computed if the following spatial Fourier transform of the two exponentials in (6.29) were known:

$$\begin{aligned} E(k_u, k) &= \int e^{-ik\sqrt{(x-u)^2+y^2}} \cdot e^{-ik_u u} du \\ E(k_v, k) &= \int e^{-ik\sqrt{(x-v)^2+y^2}} \cdot e^{-ik_v v} dv \end{aligned} \quad (6.30)$$

These types of integrals, under certain conditions, can be evaluated analytically by using the method of stationary phase (MSP) [31]. The MSP states that the main contribution to the integral comes from points with stationary phase (nulls of the phase derivative) and gives an asymptotic expansion for the integral. The evaluation of the integrals in (6.30) by means of the MSP results in:

$$\begin{aligned} E(k_u, k) &\approx e^{-i\sqrt{k^2-k_u^2} \cdot y - ik_u x} \\ E(k_v, k) &\approx e^{-i\sqrt{k^2-k_v^2} \cdot y - ik_v x} \end{aligned} \quad (6.31)$$

By applying the expression in (6.31), the 2-D spatial Fourier transform of (6.29) can be expressed as

$$\begin{aligned} s(k_u, k_v, \omega) &= p(\omega) \cdot e^{-i\sqrt{k^2-k_u^2} \cdot y - ik_u x} \cdot e^{-i\sqrt{k^2-k_v^2} \cdot y - ik_v x} \\ &= p(\omega) \cdot e^{-i(k_u+k_v)x} \cdot e^{-i(\sqrt{k^2-k_u^2} + \sqrt{k^2-k_v^2})y} \end{aligned} \quad (6.32)$$

Therefore,

$$s(k_x, k_y, \omega) = p(\omega) \cdot e^{-ik_x x} \cdot e^{-ik_y y} \quad (6.33)$$

where the dispersion relations are formulated as

$$\begin{aligned} k_x &= k_u + k_v \\ k_y &= \sqrt{k^2 - k_u^2} + \sqrt{k^2 - k_v^2} \end{aligned} \quad (6.34)$$

Based on (6.33) and (6.34), the total received wave field of the MIMO array from the distributed target distributed over the space  $o(x, y)$  can be formulated as

$$\begin{aligned} b(k_u, k_v, \omega) &= p(\omega) \iint_{o(x,y)} f(x, y) \cdot e^{-ik_x x} \cdot e^{-ik_y y} dx dy \\ &= p(\omega) \cdot F(k_x, k_y) \end{aligned} \quad (6.35)$$

where  $f(x, y)$  represents the reflectivity map of the target scene. As we can see from (6.35), the final image or reflectivity of the target can be formulated as the 2-D inverse Fourier transform of the collected data set from the MIMO array under the modified dispersion relations defined in (6.34).

$$f(x, y) = \iint \bar{b}(k_u, k_v, \omega) \cdot e^{ik_x x} \cdot e^{ik_y y} dk_x dk_y \quad (6.36)$$

The wavenumber-domain backscatter data need to be resampled uniformly. According to (6.34),  $dk$  can be written as

$$dk = \frac{v}{\omega} \left( \frac{1}{k_{y\_u}} + \frac{1}{k_{y\_v}} \right)^{-1} \cdot dk_y \quad (6.37)$$

where  $k_{y\_u}$  and  $k_{y\_v}$  are

$$\begin{aligned} k_{y\_u} &= \sqrt{k^2 - k_u^2} \\ k_{y\_v} &= \sqrt{k^2 - k_v^2} \end{aligned} \quad (6.38)$$

After the interpolation, by substituting the frequency wavenumber variables, the reflectivity image takes the form

$$f(x, y) = \iiint \frac{v}{\omega} \left( \frac{1}{k_{y\_u}} + \frac{1}{k_{y\_v}} \right)^{-1} \cdot \bar{b}(k_x, k_y) \cdot e^{ik_x x} \cdot e^{ik_y y} dk_x dk_y \quad (6.39)$$

As we can see from (6.39), the expression of MIMO range migration requires a more complicated interpolation procedure than the SAR configuration. Specifically, the originally collected data over transmitter, receiver and frequency domain must be rearranged into a 2-D data format over  $k_x$  and  $k_y$ . The received 3-D data must be interpolated back to a 2-D matrix under the defined relations in (6.34). This process is more complicated and computational heavier than the 1-D interpolation required for SAR data processing.

Correspondingly, formulation for 2-D MIMO array requires multi-dimensional data interpolation procedure which is more complicated than the SAR configuration. The originally collected data over transmitter, receiver, and frequency domain needs to be rearranged into a 3-D data format. Although it is a quite complex processing procedure, the MIMO range migration is comparably efficient than the modified Kirchhoff migration under the condition that the dimension of the spatial domains of the MIMO array is large or the required image resolution is high. Range migration also provides a possibility to generate 3-D images in real-time, while Kirchhoff migration is more suitable for the kind of data acquisition where data over transceivers are collected sequentially over time.

### 6.2.3 Algorithm implementation

This section deals with the practical implementation of the proposed MIMO range migration algorithm. From the formulation in (6.39), the image reconstruction process can be separated into five sequential steps, namely: a cross-range FFT (additional FFT if original data is in time-domain), interpolation in the spatial

frequency domains, interpolation in the frequency domain, scaling with Jacobian and a 3-D IFFT.

The first and last steps are related to FFT operation on multi-dimensional matrix. The operation is obvious for dense spatial sampling, where Nyquist criteria are met for all four spatial frequencies. Under sparse spatial sampling, effects such as aliasing and folding can result in artifacts in the resulting image. This can be solved by proper re-sampling of the data set. It is important to note that direct interpolation of the original data will cause severe errors in the phase history across the aperture. Because the phase history associated with all scatterers is not adequately sampled, interpolation causes more ambiguities rather than reducing the aliasing effect. Test shows the image can be completely distorted under such operation. Instead of direct interpolation, we introduce a phase correction term over the entire data set in order to reduce phase ambiguities before re-sampling takes place. The phase correction terms which need to be applied before and after re-sampling are listed as follows

$$\begin{aligned} PH_{Before}(x_{Tx}, x_{Rx}, z_{Tx}, z_{Rx}, \omega) &= \exp \left[ ik \cdot (\sqrt{(x_{Tx} - x_0)^2 + y_0^2 + (z_{Tx} - z_0)^2} \right. \\ &\quad \left. + \sqrt{(x_{Rx} - x_0)^2 + y_0^2 + (z_{Rx} - z_0)^2}) \right] \\ PH_{After}(x'_{Tx}, x'_{Rx}, z'_{Tx}, z'_{Rx}, \omega) &= \exp \left[ ik \cdot (\sqrt{(x'_{Tx} - x_0)^2 + y_0^2 + (z'_{Tx} - z_0)^2} \right. \\ &\quad \left. + \sqrt{(x'_{Rx} - x_0)^2 + y_0^2 + (z'_{Rx} - z_0)^2}) \right] \end{aligned} \quad (6.40)$$

where  $(x_0, y_0, z_0)$  represent a reference target center, which is used as known knowledge to reduce aliasing within the original data set. After applying the correction term,  $PH_{Before}$ , the sampling rate can be increased in order to satisfy the Nyquist criteria. Then a second phase correction,  $PH_{After}$ , complex conjugate of the first one, is applied to restore the phase reference in the data. Note that the primed letter in (6.40) indicates that the sampling of both transmit and receive apertures is already increased. The flow chart of this pre-processing procedure is shown in Figure 6.13. The advantage of this approach is that the complete effect of aliasing can be eliminated and it is transparent for image reconstruction with no side effect. Note that such method only provides improvement when the target area is not significantly larger than the wavelength.

Among all the steps, the interpolation of the data set is of the most importance. This interpolation compensates the range curvature of all scatterers by appropriate warping of the wavenumber domain backscatter data. After the multi-dimensional FFT, the transformed data is still separately distributed over transmitters and receivers in the spatial frequency domain. It must first be re-arranged into common spatial frequencies according to the first two relations defined in (6.38). If two samples fall in to the same spatial frequency, the contributions need to be integrated so that no information is lost. After the first step of interpolation, the data continue to

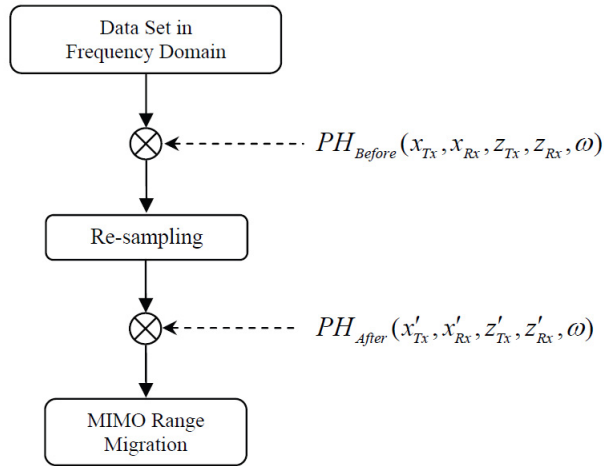


Figure 6.13 Pre-processing of data from sparse MIMO array before image reconstruction.

be spaced in frequency and, therefore, in the  $k$  variable. To prepare the data for the last 3-D IFFT, the next step is to change the variables, which can be implemented as a 1-D interpolation. As the result, the wavenumber domain backscatter data can be uniformly sampled in  $k_x$ ,  $k_y$ , and  $k_z$  domain.

After the two interpolation steps, the data has to be multiplied by an amplitude term derived in (6.37) due to the change of variables. Finally, the 3-D reflectivity image is obtained by simply applying the 3-D IFFT.

## 6.2.4 Sampling constraints

As we analyzed in Chapter 2, the performances of imaging depends largely on the spatial sampling of the aperture. This is especially true for MIMO array aperture. Because the more complicated dispersion relation for MIMO configuration, the effect of aliasing can be greatly magnified by the interpolation procedure in spatial frequency domains. To avoid aliasing effects, the phase shift from one spatial sampling point to the next must be less than  $\pi$  rad. For a closely located target, the maximum phase shift among the aperture sampling points occurs at the opposite edges between the target and aperture. Figure 6.14 illustrates the scenario for estimating the Nyquist criteria based on the configuration of MIMO array. Assuming the  $i^{th}$  transmitting element is located at  $(u_i, 0)$  while two receiving elements at the edge of the receive aperture are placed at  $(v_1, 0)$  and  $(v_2, 0)$ . The difference between

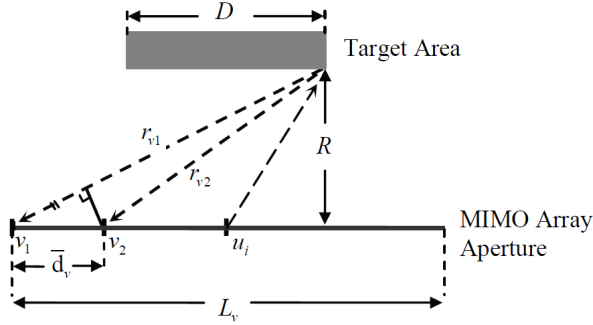


Figure 6.14 Illustration of Nyquist criteria for MIMO aperture spatial sampling

the propagation distances of the two receivers corresponding to the same transmitter is equal to the difference among them. Thus the relation has to be satisfied as

$$k|r_{v1} - r_{v2}| \leq \pi \quad (6.41)$$

where  $k = 2\pi/\lambda$  denotes the wavenumber in free-space, and the difference of propagation distance is approximated as

$$|r_{v1} - r_{v2}| \approx \bar{d}_v \cdot \frac{(L_v + D)/2}{\sqrt{(L_v + D)^2 / 4 + R^2}} \quad (6.42)$$

where  $L_v$  is the size of the receive aperture,  $D$  denotes the extent of the target, and  $R$  is the range distance of the target. Substituting (6.42) in (6.41), the spatial separation  $\bar{d}_v$  at the edge of aperture must satisfy

$$\bar{d}_v \leq \lambda \frac{\sqrt{(L_v + D)^2 / 4 + R^2}}{L_v + D} \quad (6.43)$$

Correspondingly, the sampling constraint for the transmit aperture is

$$\bar{d}_u \leq \lambda \frac{\sqrt{(L_u + D)^2 / 4 + R^2}}{L_u + D} \quad (6.44)$$

The sampling criteria in (6.43) and (6.44) are derived based on the model of MIMO array configuration. It must be reached for the smallest wavelength over the entire frequency band of the system. In chapter 2, we showed that the required sampling rate for SAR is twice the sampling rate of MIMO array derived above.

When the target is very close to the aperture, the propagation distance between the two spatial sampling points approaches the separation between them, which leads to the most restrictive requirement of  $\lambda/2$ . This is more restricted than usually required due to moderate target distance and limited antenna beamwidth. A practical imaging system can apply sampling intervals on the order of  $\lambda$  for both transmit and receive arrays respectively.

### 6.2.5 Imaging results

The performances of the proposed MIMO range migration algorithm in terms of accuracy of image reconstruction and computation efficiency are demonstrated with both full-wave numerical simulation and measurements using the developed 2-D MIMO array. The code of the algorithm has been implemented using MATLAB within a workstation with 64bit CPU (2.68 GHz) and 8 Gbit of RAM. The descriptions of the experiment setups and the results on simulated and measured data sets are presented in the following.

Figure 6.15 shows the topology of the tested MIMO array and its PSF obtained with numerical simulation. The topology of the MIMO array is the cross configuration with orthogonal transmit and receive linear arrays. Each transmit and receive array has an aperture size of 0.75 m and is sampled with 1 cm sampling step. The frequency band of simulation is from 3 to 20 GHz with 0.1 GHz frequency step and 171 frequency samples. The obtained PSF at 0.5 m range distance computed with MIMO range migration is shown in Figure 6.15 (b) and (c). The calculated image resolution is 2 mm in all three dimensions within  $0.75 \times 1.0 \times 0.75$  m area. Focusing of the tested array with such high resolution and within this large volume would require more than 10 hours, if using the time-domain imaging algorithms. In contrast, the computation time required by MIMO range migration is approximately 40 seconds. The computation efficiency of the proposed MIMO range migration algorithm is clearly demonstrated. The estimated PSF indicates a 1.5 cm cross-range resolution and 1 cm down-range resolution, and shows no artifacts at 40 dB dynamic range.

The same array is applied for imaging of distributed target. The Siemens star test pattern, which was originally used to test the resolution of optical instruments, is utilized as target. It consists of a pattern of slots on a circular patch, which radiate from a common centre and become wider as they get further from it. Theoretically, the spokes only meet at the exact centre of the star; the spokes and the gaps between them become narrower the closer to the centre one looks, but they never touch except at the centre. When being reconstructed by an imaging system with limited resolution, however, the spokes appear to touch at some distance from the centre. The smallest gap visible is limited by the resolving capability the system can produce, making the Siemens star a useful tool for comparing resolutions and imaging capabilities. Three Siemens stars with 6 cm radius are placed at 0.5 m range

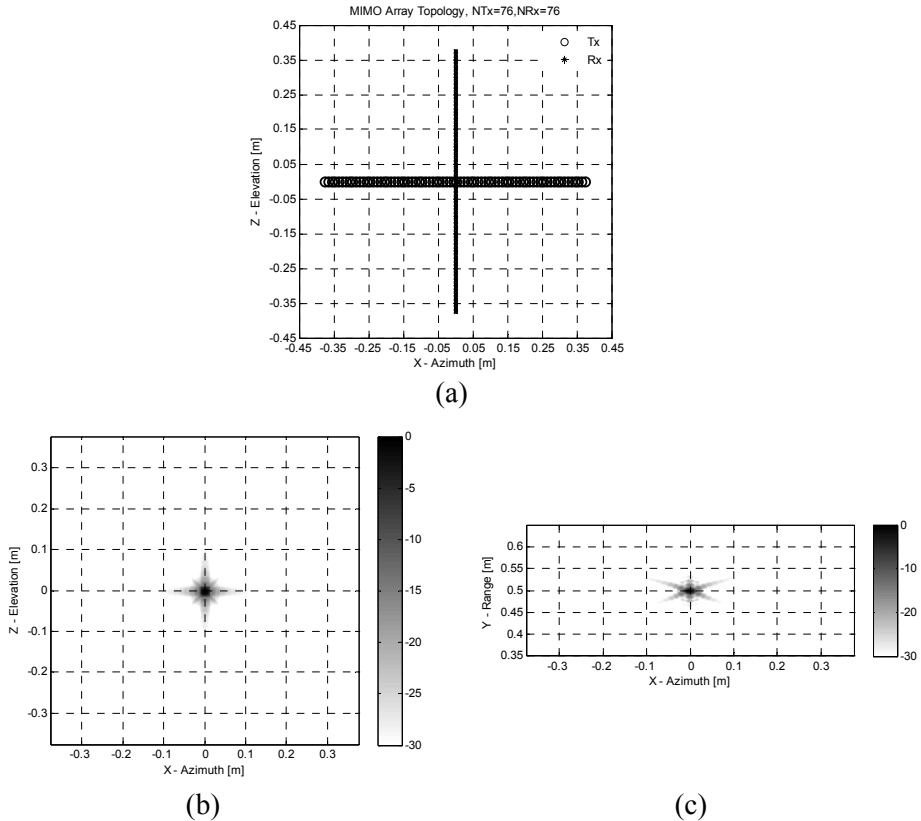


Figure 6.15 MIMO array applied for numerical simulation and its point spread function obtained with MIMO range migration. (a) Topology of the MIMO array, (b) front view of PSF, and (c) top view of PSF at 30 dB dynamic range.

distance. They are kept with 2 cm separation between edges in both down-range and cross-range directions. The target scenario and reconstructed 2-D and 3-D images by MIMO range migration are demonstrated in Figure 6.16. All surfaces of the Siemens stars are well resolved with no visible artifacts. The proposed algorithm is able to reconstruct the target reflectivity map with high imaging accuracy. Both angular and depth resolving capabilities are clearly demonstrated and confirms with theoretical performance of the test array.

The presented 3-D imaging algorithm has been validated experimentally by using a 2-D real-aperture MIMO array. The signals over all transceiver pairs are acquired with network analyzer through a multi-port switch. The 2-D array consists of 12 transmit and 13 receive elements arranged along two orthogonal directions. The array is 0.54 m wide along both azimuth and elevation axis. With the applied Vivaldi

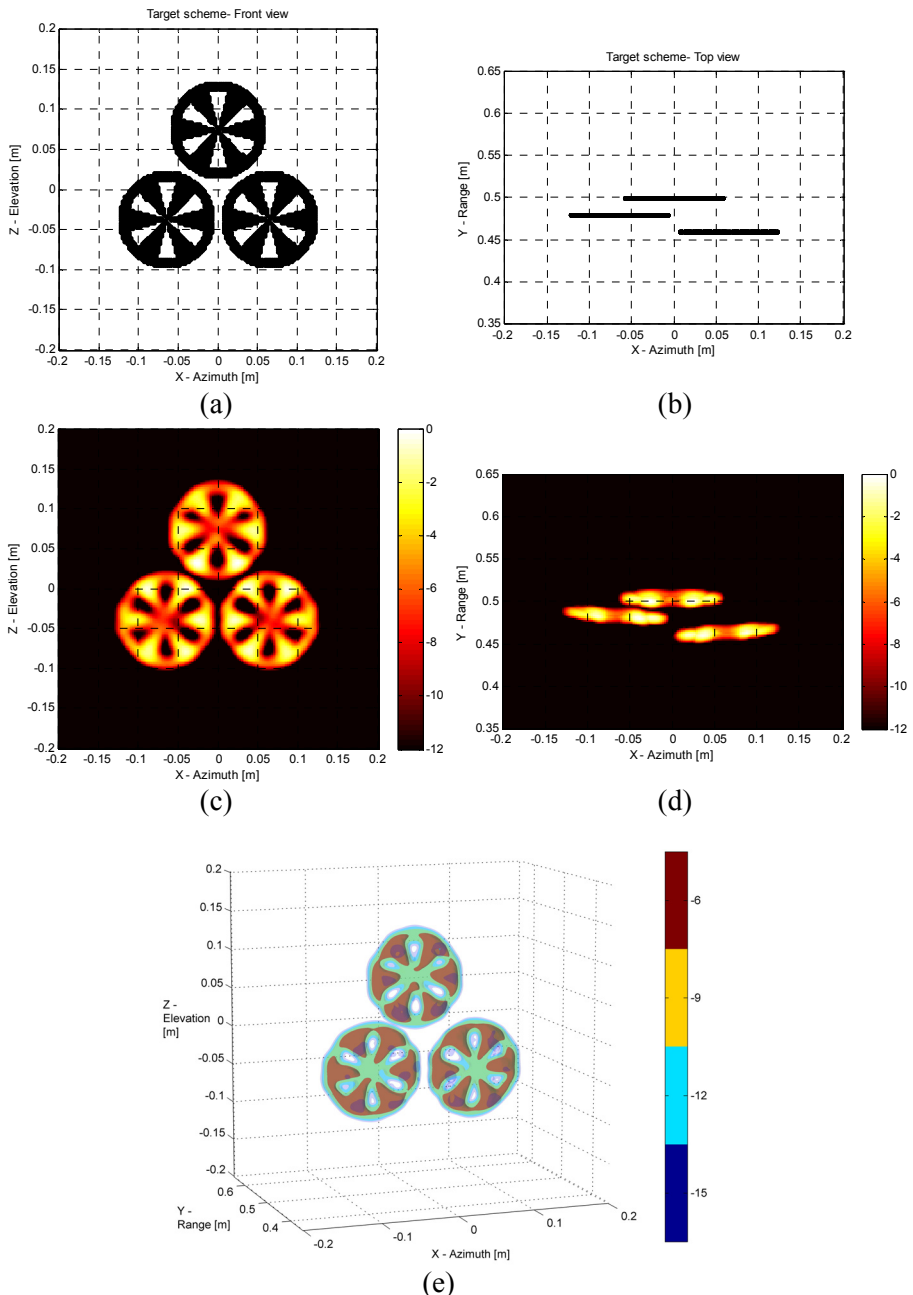


Figure 6.16 Test of MIMO range migration via numerical simulation. (a) Front view and (b) top view of target (Siemens star). Reconstructed target reflectivity in (c) front view, (d) top view, and (e) 3-D image.

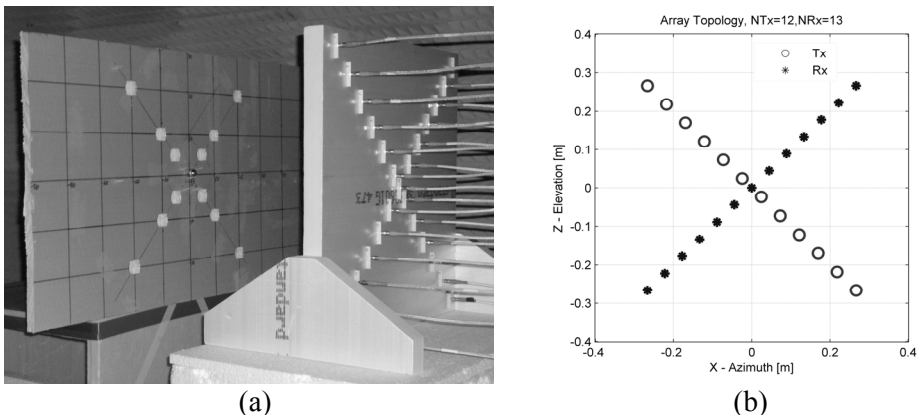


Figure 6.17 2-D array applied for measurement test of MIMO range migration algorithm. Targets are placed on the foam plate 0.5 m away from the array aperture. (a) Photo, and (b) topology of the 2-D MIMO array with 12 transmit and 13 receive elements placed in the cross configuration.

antenna, the complete system exhibits a bandwidth from 3 to 19.5 GHz. The sampling step along the transmit array is 6.86 cm and is 6.29 cm along the receive one. This means that we only fulfilled the Nyquist criteria derived in (6.53) and (6.54) within the spectrum below 4.4 and 4.8 GHz respectively. Figure 6.17 shows the array and measurement setup used in the experimental validation. A foam plate, which is placed at 0.5 m distance in front of the array, is used to support the test targets.

The measurement time required in the experiment was approximately 2.5 minutes under 251 frequency samples from 1 to 26 GHz. A 3-D reflectivity image confined in a volume of  $0.75 \times 1.0 \times 0.75$  with  $376 \times 501 \times 376$  voxels has been reconstructed. The processing time is 12 seconds with the current implementation. Figure 6.18 shows examples of some of the tested targets and slices of the reconstructed 3-D image. The targets include four metal spheres separated by 5 cm and a revolver which is approximately 10 cm wide and 20 cm long. Both front and side views of the targets show satisfactory performance from the proposed algorithm. The measured spatial resolutions are in agreement with the theoretical levels. Sidelobes appear along the  $\pm 45^\circ$  planes due to the low spatial sampling rate from both transmit and receive arrays. The level of artifacts would become much higher under low fractional bandwidth. To summarize, both simulated and measured imaging results confirm the imaging accuracy and high computation efficiency of the proposed MIMO range migration algorithm for near-field UWB imaging.

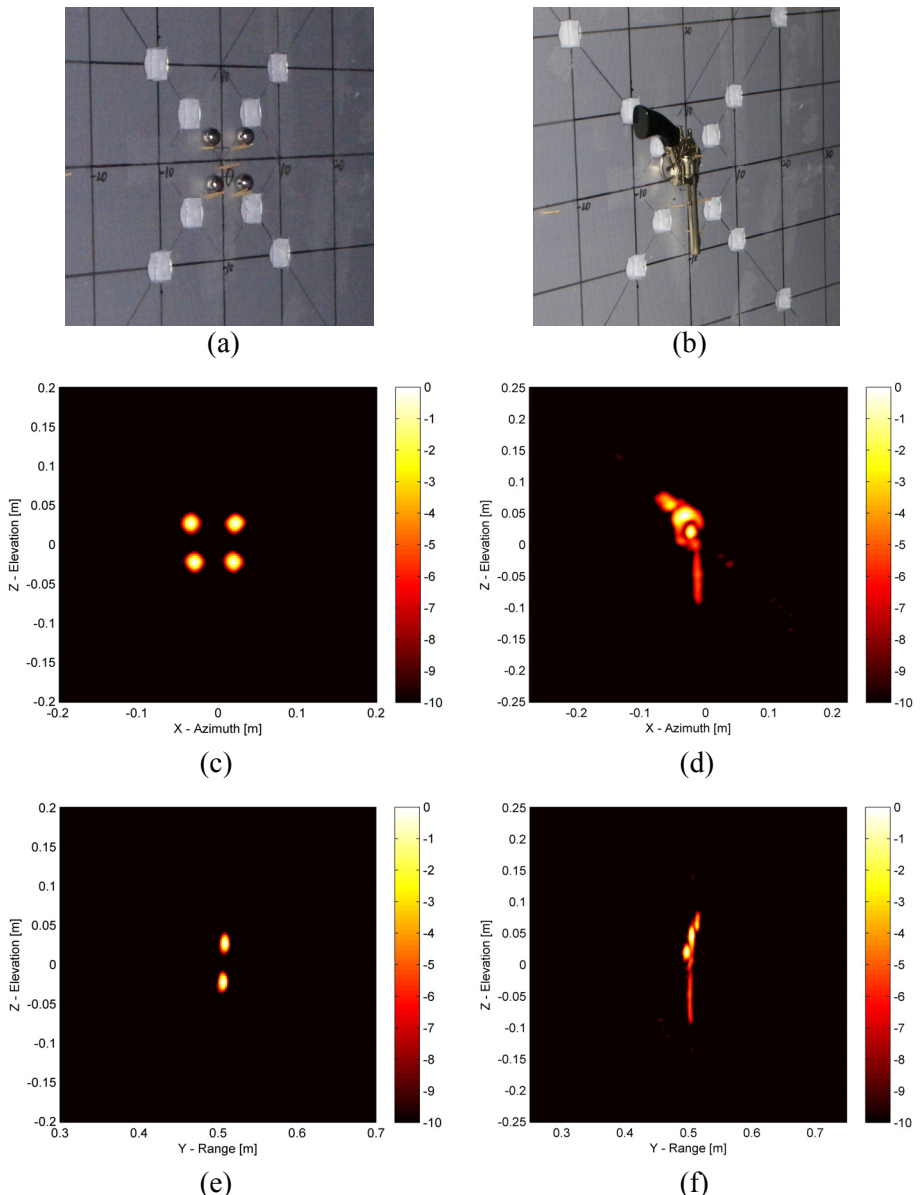


Figure 6.18 Reconstructed images of spheres and revolver measured by 2-D cross MIMO array. (a) Photo of 4 spheres separated by 5 cm placed at 0.5 m distance, (b) photo of revolver placed at 0.5 m distance. Front views of (c) spheres and (d) revolver. Side views of (e) spheres and (f) revolver.

### 6.3 Summary

In this chapter, we have proposed two high-performance beamforming algorithms for near-field 3-D MIMO array imaging.

The formulation of Kirchhoff migration is extended to cover MIMO array-based radar imaging in both free-space and subsurface scenarios. By applying the Kirchhoff integral to multi-static data acquisition, the integral expression for MIMO array imaging is derived. The near-field terms are left in the formulation in order to provide good imaging results at short ranges. A backward formulation is added to the original forward Kirchhoff integral in order to compensate the effect of commonly limited array aperture. Inclusion of the Snell's law and the Fresnel's equations to the integral formulation further extends the migration technique to subsurface. The developed migration technique is able to cope with arrays with arbitrary MIMO configurations, which frees the possibility to further explore the benefits of various array topologies.

Formulation of the range migration is further extended for MIMO array wideband imaging in the spatial wavenumber domain. The derivation has been justified by the application of the method of stationary phase. The implementation of MIMO range migration compensates completely the curvature of the wavefront in the near-field and provides high computational efficiency by the application of fast Fourier transform. As a result, it becomes fairly straightforward to develop real-time MIMO imaging system on powerful parallel computers. The performance of the algorithm has been demonstrated by both simulated and experimental data set showing satisfactory performance and significantly shorter processing time.

The developed imaging techniques can be widely applied in various applications, including through-dress, through-wall surveillance, subsurface survey and medical imaging.

## References

- [1] W.A. Schneider, "Developments in seismic data processing and analysis: 1968-1970," *Geophysics*, vol. 36, pp. 1043-1073, 1971.
- [2] J.D. Johnson and W.S. French, "Migration-The inverse method," *Concepts and Techniques in Oil and Gas Exploration.*, K.C. Jain and R.J.P. de Figueiredo, Eds. Soc. Exploration Geophysicists, 1982, pp. 115-157.
- [3] W.A. Schneider, "Integral formulation for migration in two and three dimensions," *Geophysics*, vol. 43, pp. 49-76, 1978.

- 
- [4] N. Bleistein, “On the imaging of reflectors in the earth,” *Geophysics*, vol. 52, pp. 7931-7942, 1987.
  - [5] D. Miller, M. Oristaglio, and G. Beylkin, “A new slant on seismic imaging: migration and integral geometry,” *Geophysics*, vol. 52, pp. 943-964, 1987.
  - [6] S. H. Gray, and W. P. May, “Kirchhoff migration using eikonal equation traveltimes,” *Geophysics*, vol. 59, pp. 810-817, 1994.
  - [7] H. Chang, J. P. VanDyke, M. Solano, G. A. McMechan, and D. Epili, “3-D prestack Kirchhoff depth migration: From prototype to production in a massively parallel processor environment,” *Geophysics*, vol. 63, pp. 546-556, 1998.
  - [8] Y. Sun, F. Qin, S. Checkles, and J. P. Leveille, “3-D prestack Kirchhoff beam migration for depth imaging,” *Geophysics*, vol. 65, pp. 1592-1603, 2000.
  - [9] P. Docherty, “A brief comparison of some Kirchhoff integral formulas for migration and inversion,” *Geophysics*, vol. 56, pp. 1164-1169, 1991.
  - [10] F. Soldovieri, A. Brancaccio, G. Prisco, G. Leone, and R. Pierri, “A Kirchhoff-Based Shape Reconstruction Algorithm for the Multimonostatic Configuration: The Realistic Case of Buried Pipes,” *IEEE Trans. Geosci. Remote Sens.*, vol. 46, pp. 3031-3038, Oct. 2008.
  - [11] D. Leparoux, D. Gibert, and P. Côte, “Adaptation of prestack migration to multi-offset ground-penetrating radar (GPR) data,” *Geophysical Prospecting*, vol. 49, pp. 374-386, 2001.
  - [12] M.L. Moran, R.J. Greenfield, S.A. Arcone, and A.J. Delaney, “Multidimensional GPR array processing using Kirchhoff migration,” *Journal of Applied Geophysics*, vol. 43, pp. 281-295, 2000.
  - [13] B. Guan, J. F. Zhang, X. Y. Zhou, and T. J. Cui, “Electromagnetic Scattering From Objects Above a Rough Surface Using the Method of Moments With Half-Space Green’s Function,” *IEEE Trans. Geosci. Remote Sens.*, vol. 47, pp. 3399-3405, Oct. 2009.
  - [14] J.W. Wiggins, “Kirchhoff integral extrapolation and migration of nonplanar data,” *Geophysics*, vol. 49, pp. 1239-1248, 1984.
  - [15] P. Deuflhard, *Newton Methods for Nonlinear Problems, Affine Invariance and Adaptive Algorithms*, Springer, 1994.
  - [16] A. G. Yarovoy, T. G. Savelyev, X. Zhuge, P. Aubry, L. P. Ligthart, J. Schavemaker, P. Tettelaar, E. den Breejen, “Performance of UWB array-based

- radar sensor in a multi-sensor vehicle-based suit for landmine detection," in *Proc. European Radar Conference (EuRAD)*, Oct. 2008, pp. 288-291.
- [17] A.G. Yarovoy, T.G. Savelyev, P.J. Aubry, P.E. Lys, and L.P. Lighthart, "UWB Array-Based Sensor for Near-Field Imaging," *IEEE Trans. Microw. Theory Tech.*, vol. 55, pp. 1288-1295, Jun. 2007.
  - [18] X. Zhuge, A. G. Yarovoy, T. G. Savelyev, P. J. Aubry, and L. P. Lighthart, "Optimization of Ultra-Wideband Linear Array for Subsurface Imaging," in *Proc. International Conference on Ground Penetrating Radar*, 2008, pp. 1-5.
  - [19] C. Yerkes and E. Webster, "Implementation of  $\omega$ - $k$  synthetic aperture radar imaging algorithm on a massively parallel supercomputer," in *Proc. SPIE*, Orlando, FL, 1994, vol. 2230, pp. 171-178.
  - [20] C. Cafforio, C. Prati, and E. Rocca, "SAR data focusing using seismic migration techniques," *IEEE Trans. Aerosp. Electron. Syst.*, vol. 27, pp. 194-207, Mar. 1991.
  - [21] J. M. Lopez-Sanchez, J. Fortuny-Guasch, "3-D radar imaging using range migration techniques," *IEEE Trans. Antennas Propag.*, vol. 48, no. 5, pp. 728-737, May 2000.
  - [22] R. Stolt, "Migration by Fourier transform techniques," *Geophys.*, no. 43, pp. 49-76, 1978.
  - [23] C. Prati, A. M. Guarnieri, and F. Rocca, "Spot mode SAR focusing with the  $\square k$  technique," in *Proc. IEEE Int. Geosci. Remote Sensing Symp. (IGARSS)*, Helsinki, Finland, June 1991, pp. 631-634.
  - [24] A. Golden Jr., S. C. Wei, K. K. Ellis, and S. Tummala, "Migration processing of spotlight SAR data," in *SPIE Algorithms for Synthetic Aperture Radar Imagery*, vol. 2230, Orlando, FL, 1994, pp. 25-35.
  - [25] J. Fortuny-Guasch, J. M. Lopez-Sanchez, "Extension of the 3-D range migration algorithm to cylindrical and spherical scanning geometries," *IEEE Trans. Antennas Propag.*, vol. 49, no. 10, pp. 1434-1444, Oct. 2001.
  - [26] J. R. Bennett and I. G. Cumming, "A digital processor for the production of Seasat synthetic aperture radar imagery," in *Proc. SURGE Workshop*, Frascati, Jun. 1979, ESA-SP-154.
  - [27] M. Y. Jin and C. Wu, "A SAR correlation algorithm which accommodates large range migration," *IEEE Trans. Geosci. Remote Sensing*, vol. GE-22, pp. 592-597, 1984.

- 
- [28] R. K. Raney, H. Runge, R. Bamler, I. G. Cumming, and F. H. Wong, “Precision SAR processing using chirp scaling,” *IEEE Trans. Geosci. Remote Sensing*, vol. 32, pp. 786–799, Jul. 1994.
  - [29] W. Hughes, K. Gault, G. J. Princez, “A comparison of the Range-Doppler and Chirp Scaling algorithms with reference to RADARSAT,” in *Proc. IEEE Int. Geosci. Remote Sensing Symp. (IGARSS)*, Nebraska, USA, May 1996, vol. 2, pp. 1221-1223.
  - [30] R. Bamler, “A comparison of range-Doppler and wavenumber domain SAR focusing algorithms,” *IEEE Trans. Geosci. Remote Sensing*, vol. 30, pp. 706–713, Jul. 1992.
  - [31] A. Papoulis, *Systems and Transforms with Applications in Optics*. New York: McGraw-Hill, 1968.
  - [32] E. Guillanton, J. Y. Dauvignac, C. Pichot, and J. Cashman, “A new design tapered slot antenna for ultra-wideband applications,” *Microw. Opt. Technol. Lett.*, vol. 19, no. 4, pp. 286–289, Nov. 1998.



## CHAPTER 7

# UTILIZATION IN DIFFERENT APPLICATIONS

The proposed theories of UWB focusing, MIMO array and imaging algorithms have been implemented in different applications for the development of high-performance short-range imaging systems. In the field of concealed weapon detection, array-based UWB imaging system provides an efficient tool to detect weapons hidden under clothes or within luggage. Features like low-cost and high integration potential of microwave technology enable the deployment of a large number of such systems to form sensor networks, which helps to achieve global monitoring of passengers. It makes such technology a potential solution for enhancing security at public settings such as subways, train stations, airports, stadiums and shopping malls.

By using the lower part of the microwave spectrum, UWB system provides strong imaging capabilities for subsurface applications. By combining with MIMO array, real-time observation of targets behind walls and detection of objects buried underground can be achieved. Demonstrators oriented for both through-wall and landmine detection are developed and validated by tests in realistic environment. The development and validation of the integrated set of new technologies permit future industrialization of powerful equipments for these demanding applications.

The chapter is organized as follows. The application of the developed technologies in the field of concealed weapon detection is presented in section 7.1. The development of through-wall imaging radar for security and rescue operations is described in section 7.2. The integration of array-based ground penetrating radar for

multi-sensor system dedicated to landmine detection is presented in section 7.3. The chapter is summarized in the last section.

## 7.1 Concealed weapon detection

The threat of terrorism has triggered researches on enhancing safety of using public transportation. In particular, deploying surveillance systems, which are capable of detecting concealed weapons and plastic explosives at major transportation hubs, is seriously considered. A distributed screening system with capabilities of weapons and explosive classification, which does not interfere with normal passenger flow, seems to be an ideal system for this purpose. A technology that exhibits both high screening performance and cost efficiency is desirable to realize such a system.

Several technologies which use different parts of the electromagnetic spectrum for screening can be considered. X-ray systems present an effective solution to detecting concealed weapons and are used by military. However, potential health risks due to exposure to ionizing radiation make it less acceptable for its usage in public safety. Terahertz technology has the capability of combined spectral identification with imaging due to the unique spectral signatures of many dangerous materials in the terahertz spectrum [1]. The high cost of such device at this moment makes it less likely to be widely deployed. The same cost issue holds for millimeter-wave imaging systems, which are capable of providing high-quality images by using a planar or cylindrical aperture [2, 3]. On the one hand, using electromagnetic waves with short wavelength (1-10 mm), millimeter-wave system allows for high-resolution (photo-like) 2-D images with concealed weapons that can be recognized with naked eyes. On the other hand, such high resolution has already raised privacy concerns from the public. Moreover, millimeter-wave imaging requires extremely dense spatial sampling of the scattered field within a relatively large imaging aperture. This leads to relatively long data acquisition time, a large number of antenna elements, and immense computational power for beamforming. These features limit the use of millimeter-wave system for non-stationary targets and scenarios that require real-time operation.

A planar or conformal UWB array with simultaneous signal reception is considered to be the best solution for the application. However, designing such system encounters a serious contradiction between the antenna size, spacing in the array and the level of sidelobes of the focused array, especially when high frequencies are used to achieve high resolution. A sparse array with multiple Tx and multiple Rx antennas (MIMO) can be the optimal solution regarding the above mentioned factors plus the complexity of the electronics. A planar array with four Tx and sixteen Rx antennas has been designed and evaluated [4]. The array aperture is about 50 cm by 50 cm. In spite of quasi real time data acquisition and imaging, the performance of the array was found to be insufficient due to the high level of

artifacts in the imagery. Point spread function (PSF) of the array revealed a level of sidelobes of -6 dB versus -30 dB for SAR, which is acceptable for small free-space targets but not for such extended targets as human body. One possible solution to decrease the sidelobe level is to increase the number of antennas in the array. However, this will make the entire system including the electronics much more complex and significantly increase the costs.

The combination of MIMO array focusing in the horizontal plane with SAR in the vertical plane represents a reasonable trade-off between the measurement speed and image quality. A linear MIMO array with four Tx and sixteen Rx antennas has been designed following the proposed theories. The array was installed on mechanical scanner to form a MIMO-SAR system. The operational frequency range was chosen to be 10-18 GHz at the time to achieve higher angular resolution. Despite security service already uses commercially available mm-wave imaging systems,; a microwave radar system can be significantly less expensive and, reduce ethical issues of imaging a person by not revealing private personal details.

The development of imaging radar prototype for concealed weapon detection was performed within the framework of EU granted project Radiotect.

### **7.1.1 Prototype of the system**

The development of cost-efficient imaging radar requires optimization with respect to system bandwidth, dimensions of antenna array, and the number of antenna elements, multi-channel electronics, and available components such as switches, cables and connectors. The latter limit the upper frequency to 18 GHz. The maximal available number of receiving channels was limited to sixteen. Meanwhile, a length of the antenna array of about 50 cm (width of a human body) along with sixteen Rx antennas leads to 3 cm as the maximal width of antenna element that gives 10 GHz as the lower frequency. Therefore, the antenna bandwidth was defined as 10-18 GHz. This system bandwidth can be implemented by using different UWB technologies. Here we considered the speed of data acquisition and the cost of the available solutions as the main factors. As a result, the video impulse technology with sequential sampling was selected for realization of the electronics consisting of pulse generator and multi-channel receiver.

A stacked patch antenna was used as antenna element for the array [5]. Such antenna is simple and has planar geometry. Return loss of the developed antenna determined by the measurement provides a -10 dB bandwidth from 10 to 18 GHz that satisfies the initial system requirements. Gain measured at the electrical boreside varies from 5 to 10 dBi in the specified frequency band. The MIMO array represents a specific topology, shown in Figure 7.1(a), which was designed based on the proposed design approach (Chapter 3). It consists of four Tx and sixteen Rx antennas with vertical polarization. The separation between the feeding points of the Rx

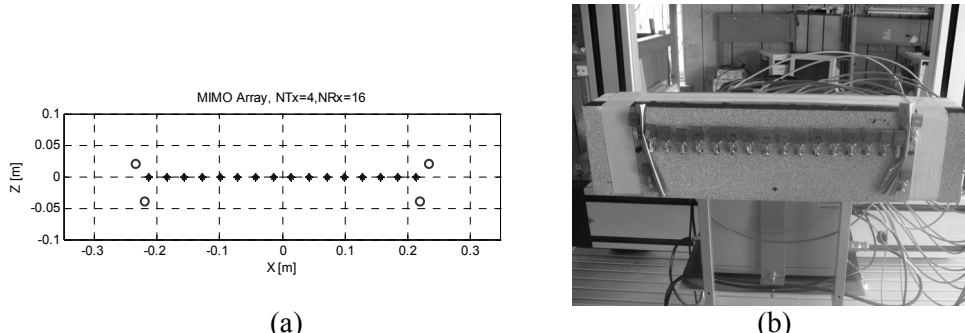


Figure 7.1 MIMO array integrated with mechanical scanner.

(a) Linear MIMO array topology, (b) MIMO-SAR system with array installed on scanner.

antennas is 2.5 cm that is less than the minimal operational wavelength of 3 cm. The array itself provides focusing only in the horizontal plane. For 3-D imaging the mechanical scanning in the vertical plane is used with a selected step of data acquisition. Both the antenna separation and the step of data acquisition influence the sidelobe level of PSF. Figure 7.1(b) presents a photo of the array installed on a high-precision scanner, which constitutes the MIMO-SAR system.

The electronics was built on a video impulse technology with sequential (stroboscopic) sampling by Geozondas Ltd. The electronics consists of transmitter, receiver (sampling converter) and computer with dedicated signal processing and visualization software. The transmitter is a pulse generator (Figure 7.2a) that fires a mono-pulse with 30 ps duration, while TTL triggering power and signal time delay are provided by the sampling converter. The latter represents an instrument with eight parallel channels, shown in Figure 7.2(b). In the MIMO-SAR case, the four transmit antennas are commuted to the pulse generator via a switch. Thus, one array data acquisition includes four transmission cycles and in each of them the sixteen Rx antennas receive simultaneously. Each receiving port of the sampling converter has two inputs, which allows for the connection of two receive antennas to one port. The data acquisition from the two Rx antennas is performed in the same time window, but the signal from the second antenna is delayed without overlap with the signal from the first antenna. A delay line was realized by means of a longer RF cable, i.e. eight Rx antennas were connected with shorter cables and the other eight with longer cables, while the respective acquired signals were separated by data processing later on.

Figure 7.3(a) shows a generated pulse which was measured by connecting the pulse generator with one of the receiving ports via a short cable and attenuator. The pulse duration at -6 dB level is 30 ps, yet the acquired signal includes a noticeable ringing that indicates non-ideality of the electronics and eventually brings artifacts to the image. The peak voltage of the pulse is -25 V that corresponds to 41 dBm peak power. Normalized spectra of the pulses acquired sequentially by all the receiving



Figure 7.2 Video impulse electronics with stroboscopic sampling by GeoZondas Ltd.  
(a) Pulse generator, (b) eight-channel sampling converter.

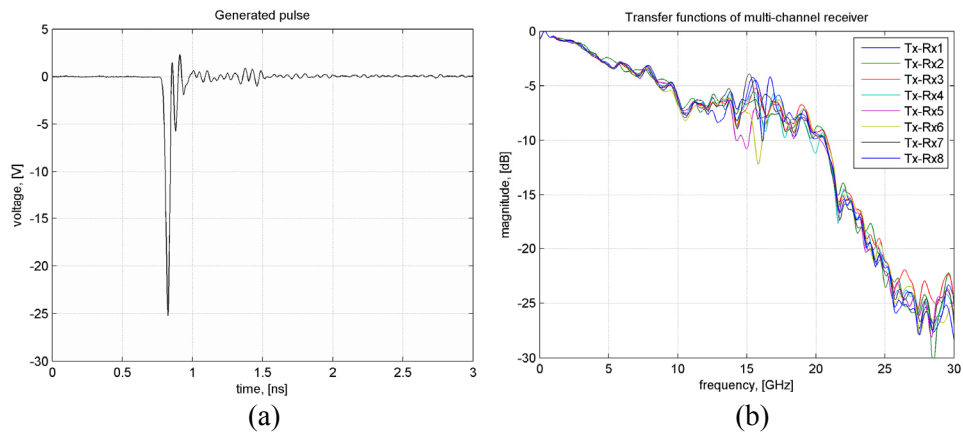


Figure 7.3 Characteristics of the impulse system.  
(a) Generated pulse, (b) transfer functions of the eight receiving channels.

channels are shown in Figure 7.3(b), and they can be treated as transfer functions of the electronics. We can see that the difference between the channels becomes 7 dB in the 10-18 GHz band which also deteriorates the image.

A quite important specification of the electronics is pulse repetition frequency (PRF) that defines the speed of data acquisition. Currently, it is 500 kHz. The time window of the measurement can be set up to 20 ns, while the maximal adjustable time delay is 100 ns, which allows for the measured range of 3 m at the maximal distance of 15 m. Stability of the electronics is characterized with a 2 ps jitter and a 15 ps/hour system time drift. The resolution of analogue to digital conversion is 12 bits. Dynamic range of the receiver was found to be 56 dB that can be increased by averaging of the acquired signal up to 86 dB. The maximal number of samples in a selected time window is 4096, and the maximal number of averages is 1024. Isolation between the channels, measured at 1 GHz, is 60 dB.

### 7.1.2 Test results

A series of measurements were performed with the MIMO-SAR prototypes in order to investigate their capability to image a hidden weapon carried on human body. The conducted experiments included measurements of PSF, cross-range capability, and imaging of weapons on human body.

The distance between antennas and the target was chosen to be 50 cm. The data were acquired within a 13 ns time window with 4096 points and 505 averages, and these settings resulted in 6 s per acquisition of the time window. For SAR, the maximal 2-D scanning was 50 by 100 cm with a step of 1 cm in both planes, which took about 8.3 hours per scan. For MIMO-SAR, the maximal scanning height was 170 cm with a step of 0.5 cm, which took about 2.3 hours. All the images were obtained by Kirchhoff migration for a 3-D grid with 0.5 x 0.5 x 0.5 cm voxel.

PSFs of the two prototypes were measured by using a metal sphere of 3 cm diameter and they are shown in Figure 7.4 as 2-D images obtained by energy projection of 3-D images along the range direction to the vertical plane. We can see that the MIMO-SAR PSF presents small artifacts. The diameter of the sphere's image corresponds to the actual 3 cm at -15 dB, which also indicates cross-range resolution of the imaging radar. We also estimated the cross-range resolution capability by imaging four spheres separated in the vertical plane by 3 cm between the edges. Figure 7.5 shows the successfully resolved spheres for both SAR and MIMO-SAR. The 3-D images are given in 6 dB dynamic range for the best visualization.

Various measurements of weapons attached to a person were tested. The scan of MIMO-SAR was 40 cm with the same 0.5 cm step. Meanwhile, the weapon was fixed on the leg of a person in a sitting position, which prevented minor movements (also due to breathing) which could consequently blur the image. The results are shown in Figure 7.6 and Figure 7.7. Both the gun and knife can be clearly seen at 20 dB dynamic range. The successful imaging results of weapons on body demonstrate the promising potential of the MIMO-SAR approach for concealed weapon detection.

For real time application, the demonstrated imaging potential should be evaluated in terms of the scanning speed. Therefore, we summarize the current data acquisition time and the scanning time, which are required to image an area of 50 x 50 cm with high resolution in Table 7.1. With off-the-shelf electronics, the MIMO-SAR approach is much faster than SAR. However, such data acquisition speed is still slower than realistic scenarios where the complete imaging should be formed within seconds.

However, we can significantly reduce the data acquisition time and the scanning time respectively by increasing PRF in the electronics. The current demonstrator works with a PRF of 500 kHz, while its developers declare 10 MHz for future

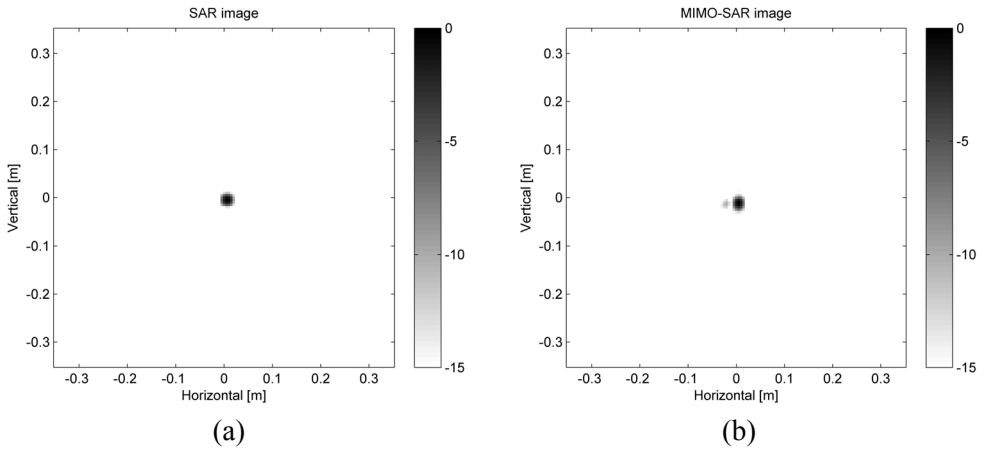


Figure 7.4 Point spread function (PSF) obtained with metal sphere of 3 cm diameter at 50 cm range distance. (a) SAR, (b) MIMO-SAR system.

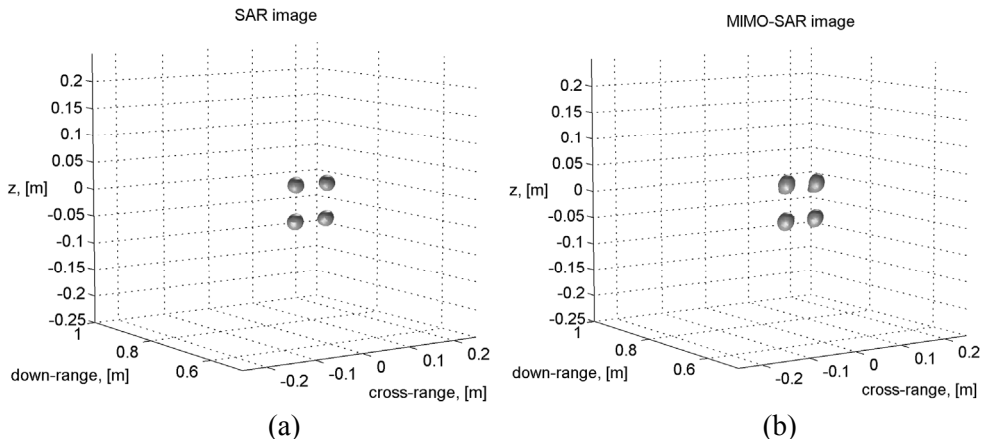
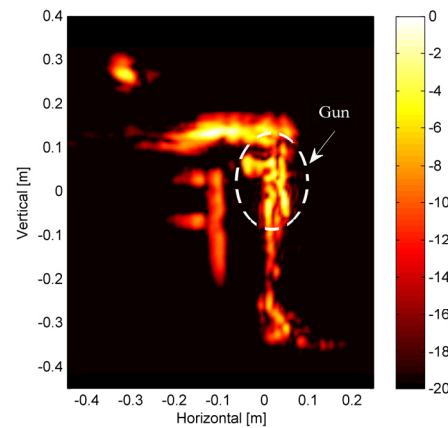


Figure 7.5 Images of four metal spheres separated by 3 cm at 50 cm range distance. (a) SAR, (b) MIMO-SAR system.

products. This would reduce the acquisition time by factor 20. Next to that, the currently used 4096 points and 505 averages to acquire one time window will be optimized, which will give at least another factor of 20. The use of better low-noise amplifiers in the receiver will improve its dynamic range and minimize the averaging. Thus, we can achieve a scanning time of a few seconds for MIMO-SAR with the selected video-impulse UWB technology.



(a)

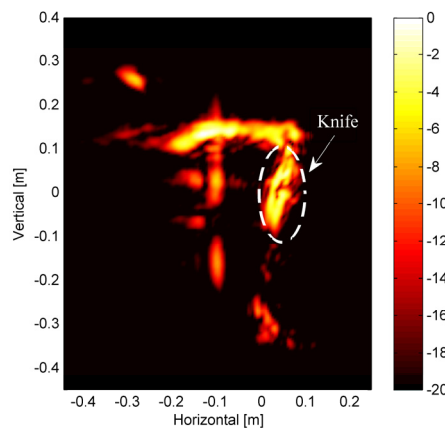


(b)

Figure 7.6 Imaging of gun attached to a person's leg. (a) Photo of test scenario, (b) imaging result.



(a)



(b)

Figure 7.7 Imaging of knife attached to a person's leg. (a) Photo of test scenario, (b) imaging result.

Table 7.1 Current imaging speed using off the shelf electronics

Time expenses	SAR	MIMO-SAR
Acquisition of one time window [s]	6	6
Scanning of human body [min]	250	40

## 7.2 Through-wall radar

In recent years, significant endeavors from the scientific and engineering communities have been addressed to the development of through-wall radar due to the increasing challenges and demands from public security, rescue and military applications. The purpose of through-wall radar is to detect, to locate and, possibly, to image the people inside the building structure, which could improve the operational efficiency and the safety of personnel.

Through-wall detection and imaging is a complex problem which needs cross-discipline researches in both electromagnetics and radar engineering. Conventional narrowband systems, such as Doppler radar and interferometric radar, are no longer applicable here due to their insufficient down-range resolution. By contrast, ultra-wideband (UWB) radar which has been investigated and applied in subsurface imaging applications is the most promising candidate due to its high resolution and capability of classification. However, a contradiction occurs between the need for penetrating walls by using lower frequencies and the requirement for fine resolution which implies higher frequencies and larger bandwidth. Therefore, the estimation of propagation loss, dynamic range, down-range and cross-range resolution of the radar system is needed in connection with the requirements for detection and imaging. The selection of different radar technologies, such as video impulse radar, stepped-frequency continuous wave (SFCW), frequency modulated continuous wave (FMCW) and noise radar, depends on the above mentioned physical implications derived from the end user requirements. Several UWB through-wall radars have been built and experimentally tested [6-9]. A review of existing through-wall radars is given in [10]. Most of them are video impulse systems, while there are also prototypes based on FMCW and quasi-random noise.

The development of through-wall imaging radar prototype was performed within the framework of EU granted project, PROBANT. The description of the project can be found in chapter 1. In the rest of this section, system design, trade-off, choice of UWB technology and development of the final demonstrator will be presented.

### 7.2.1 Propagation loss

There are four main contributors for the through-wall propagation loss, namely spreading loss, transmission loss through air-wall interface, material loss and target scattering loss. The estimation of the first three components is well known, so it will not be discussed here. However, the scattering from human body needs further investigation.

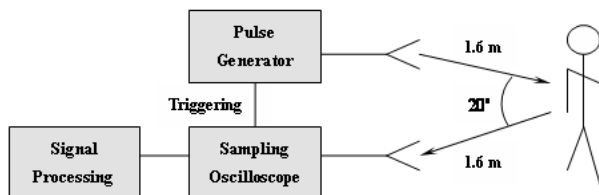


Figure 7.8 Illustration of UWB time-domain measurement scheme for human body detection.

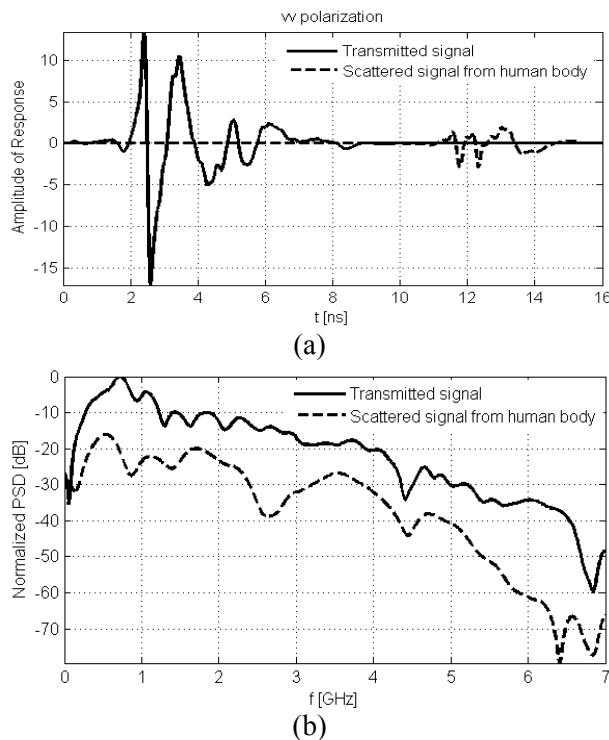


Figure 7.9 Transmitted signal and scattered signal from human body: (a) waveforms; (b) power spectral density.

In this research, the scattering from human body was studied by time-domain measurements. The experimental setup is illustrated in Figure 7.8. A video impulse with duration of 50 ps is generated by the pulse generator and applied to a vertically polarized transmit antenna. The scattered wave from human body is acquired with a co-polar receive antenna and sampling oscilloscope. The person under test was standing in front of the antennas at a distance of 1.6 m. The bistatic angle was 20 degree. To reduce the antenna coupling an absorber was placed between transmit and receive antennas.

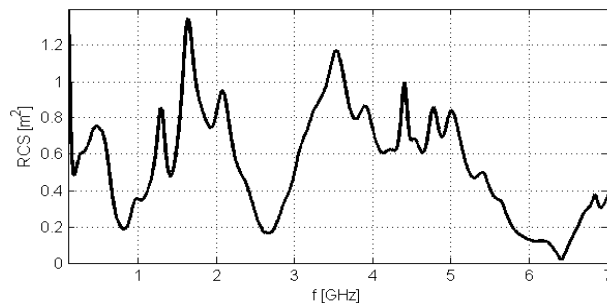


Figure 7.10 Measured Bistatic RCS of human body in the frequency band from 300 MHz to 7 GHz.

Table 7.2 Total propagation loss for different wall materials (the thickness of the wall is 0.2 m).

Material	Frequency (GHz)	Propagation Loss (dB)		
		Range: 0.5m	Range: 10 m	Range: 20 m
Concrete Block	1	-56.7	-108.7	-120.8
	3	-73.4	-125.4	-137.5
	5	-77.2	-129.2	-141.3
	7	-85.8	-137.8	-149.8
Brick	1	-50.6	-102.6	-114.6
	3	-67.5	-119.6	-131.6
	5	-78.9	-130.9	-143.0
	7	-95.1	-147.1	-159.2
Structure wood	1	-49.1	-101.1	-113.2
	3	-63.7	-115.7	-127.7
	5	-71.0	-123.0	-135.0
	7	-82.0	-134.0	-146.1

The antennas were also aligned in line-of-sight positions to acquire the transmitted signal. The transmitted signal and the received human scattering are illustrated in Figure 7.9. By compensating the spreading loss and using the radar range equation, the dependency of bistatic radar cross section (RCS) of human body on frequency is then obtained and shown in Figure 7.10. The applied antenna aperture of 20 cm forms the far field for the selected distance of 1.6 m at frequencies below 6 GHz. Therefore, the obtained RCS represents an approximate yet valid data for derivation of total propagation loss for through-wall radar.

The knowledge of the dielectric properties of different wall materials, given in [11], and the estimated human RCS allow us to compute the total propagation loss for the typical through-wall scenarios which are summarized in Table 7.2. The interference of waves reflected from both sides of the wall is neglected as only the first arrived signal is to be estimated. It comes to approximately 120 dB attenuation in L and S bands and to about 150 dB in C band for the targets at 20 m distance. Most of the existing through-wall imaging radars work in L and S band due to the significantly increasing loss of frequency [10].

## 7.2.2 Dynamic range

The required dynamic range of the radar system can be generally determined by the ratio between the strongest received signal and the minimal target response to be detected. The strongest signals for through-wall radar can be antenna coupling, narrow-band interference or reflection from the wall. Since the coupling and interference strongly depend on the antenna design and operational regulations, we assume here the wall reflection is the strongest signal.

During the operation, the wall will be most likely in the near-field of the antennas. Therefore, electromagnetic (EM) simulation is needed to estimate the wall reflection. A finite integration technique (FIT) model shown in Figure 7.11 was built using the commercial software CST. An elliptical-shaped dipole employed as transmit antenna is separated by 20 cm from a concrete wall. It is excited with a pulse which spectrum has a bandwidth at -10 dB from 0.1 to 7 GHz. Two shielded loops [12] are located at both sides of the wall at a 10cm distance from the wall. Their purpose is to estimate the electromagnetic waves reflected from the wall and penetrated through. The wall has a thickness of 20 cm, and its dielectric properties correspond to concrete [11]. Furthermore, the simulated wall includes a metal reinforcement grid inside with a 20 by 20 cm typical cell. The EM scenarios with and without the wall were simulated in order to obtain the wall reflection by subtraction. The obtained waveforms are shown in Figure 7.12.

To estimate the dynamic range over frequency, additional free space spreading loss, corresponding to 20 m range, along with the human RCS (Figure 7.10) were added to the power spectral density of the through-wall penetrated signal. As a result, Figure 7.13 illustrates the respective power spectra and dynamic range.

It can be seen that low frequencies (below 0.5 GHz) are blocked by the reinforcement that acts as a metal wall for wavelengths larger than the grid. The wall reflection is about -15dB below the transmitted signal due to the close antenna-wall spacing. The required dynamic range between the wall reflection and target response varies between 100 and 150 dB, and it increases with frequency. In practice, such a dynamic range of radar can be achieved by using a large number of averages of the received signal which implies longer data acquisition time.

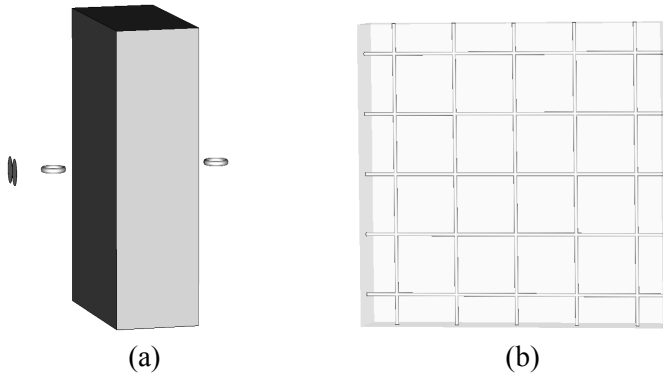


Figure 7.11 An electromagnetic model for power budget estimation. (a) EM model with elliptical-shaped dipole as transmit antenna, and two shield loops located at both sides of the 20 cm concrete wall as receiving antennas. The distance between each loop and the wall surface is 10 cm. (b) Illustration of the metal reinforcement grid inside the concrete wall with 20 by 20 cm typical cell dimensions.

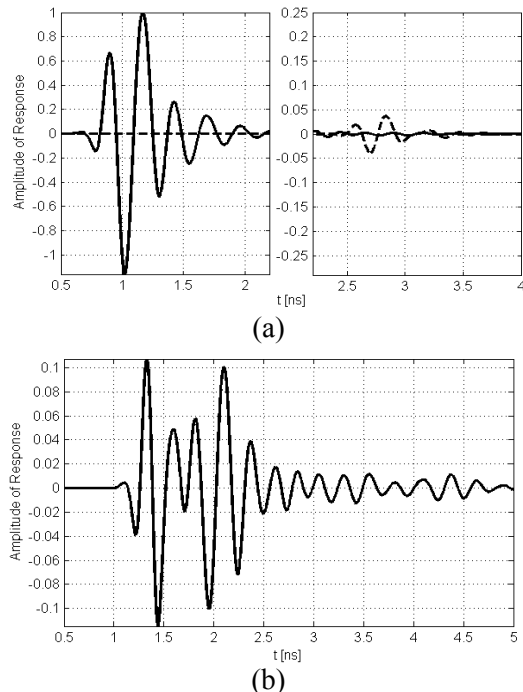


Figure 7.12 Waveforms obtained from the EM model. (a) Signals obtained at the loops at both sides of the wall, and (b) wall reflection obtained by subtraction.

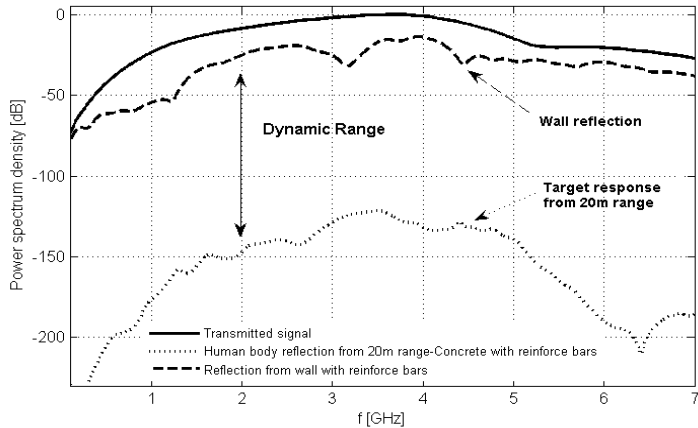


Figure 7.13 Dynamic range needed for through-wall radar to achieve 20 m detection of human body.

### 7.2.3 Choice of UWB technologies

The derived requirements have different implications in the different transmission schemes, namely video impulse, SFCW, FMCW and noise radars. Here we assume an operational band from 1 to 2 GHz, 20 m detection range and 1.5 m length array. This will result in a down-range resolution of 0.15 m and in a 2 m cross-range resolution at 20 m distance. This also means that the radar needs approximately 20 antennas, at least 133 ns time window, and it has to fulfill a dynamic range of about 120 dB.

For video impulse radar, a pulse of approximately 1.5 ns duration may be used, which requires a sampling step of 0.15 ns for accurate measurement. This gives 887 samples for each time window. Assuming a 20 m unambiguous range, the data acquisition time for a stroboscopic receiver will be  $118 \mu\text{s}$ . This speed is fast enough to detect motions of people and to perform averaging. The dynamic range can be fulfilled by time gating the antenna coupling and the wall reflection.

For SFCW radar, a 7.5 MHz maximal frequency step and 133 frequencies are derived from the unambiguous range and the 1 GHz bandwidth. Assuming a standard vector network analyzer is used, each frequency step will take approximately 1 ms. Then, we come to the data acquisition time of about 133 ms. Although it is much longer than that of the video impulse radar, it provides a higher energy and therefore, results in a larger dynamic range.

For FMCW radar, the data acquisition time is purely determined by the sweep time of voltage controlled oscillator, which is about 100~500  $\mu\text{s}$  depending on the

components. This scheme is faster than video impulse radar and it also provides a higher energy.

For noise radar, the data acquisition time can be derived from the pulse repetition frequency that is  $0.13 \mu\text{s}$  in our case. It is the fastest speed among all the options, and it allows large averaging to improve signal to noise ratio and the overall dynamic range. The time gating of antenna coupling and wall reflection can be used as well to improve the dynamic range further.

#### 7.2.4 Prototype of through-wall imaging radar

A through-wall imaging radar prototype was developed within PROBANT project based on FMCW technology. An ultra-wideband (UWB) imaging system with two-dimensional multiple-input multiple-output (MIMO) array and digital beamforming are designed to achieve both high resolution and low grating/side lobe level along two principle imaging planes. A photo of the system under test in front of a brick wall is shown in Figure 7.14. By using the MIMO array concept, the number of antenna elements is reduced in comparison with conventional array, which minimizes both weight and complexity of the imaging system.

Based on the theoretical analysis of the problem, we selected the operational frequency band to be 1-4 GHz and the frequency modulated continuous wave (FMCW) technology to provide a dynamic range of more than 100 dB for penetrating thick walls [13, 14]. Large duration of an FMCW signal ensures high energy even for low transmitted power, while demodulation of the signal gives high resolution and large dynamic range. The use of state of the art components allowed us to build a homodyne FMCW scheme with a high sweeping speed of 100  $\mu\text{s}/\text{GHz}$  and a 70 dB dynamic range. The latter can be increased significantly by longer data acquisition and inter-sweep averaging.

The key element of the scheme is voltage control oscillator (VCO) that determines frequency band, sweeping speed, harmonics level and, as such, it defines the rest of the scheme. We used a high linearity (0.25%), ultra-fast 1-4 GHz YIG-VCO manufactured specifically on our request. A relatively high level of harmonics required the sequential working in two parallel bands, more specifically 1.3-2.4 GHz and 2.4-4 GHz, with suppression of harmonics by low pass filters. VCO and power amplifier provide 27 dBm output power which is delivered to the four Tx antennas via switches that connect the Rx antennas to the receiver that consists of a low noise amplifier LNA, a mixer with in-phase and quadrature outputs (IQ) and anti-aliasing filters. The use of the IQ signals allows extracting more information about a target such as sign of a Doppler frequency or direction of arrival. The FPGA board drives VCO according to a flexible program, synchronizes the work of the whole scheme, acquiring the IQ data with a 12 Msample/s rate and performs signal processing. The frequency sweeping by VCO produces sequentially four ramps: rising and falling in



Figure 7.14 Prototype of the through-wall radar.

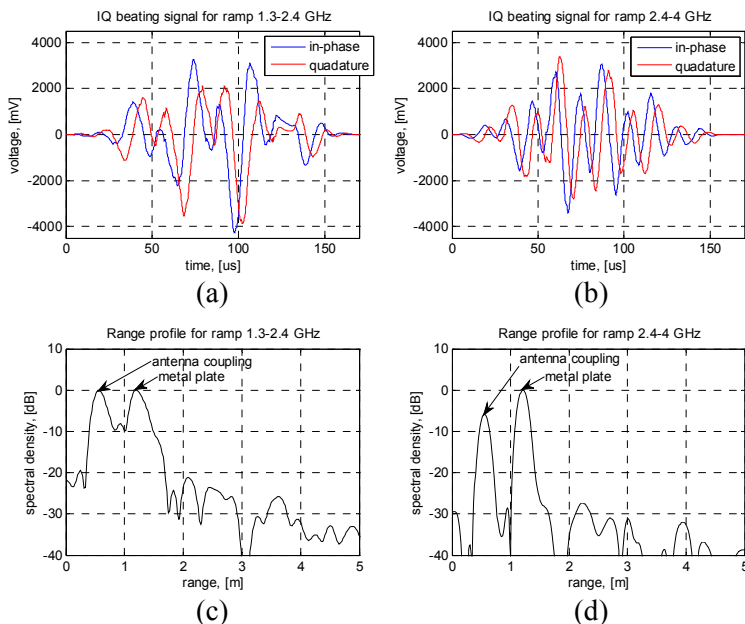


Figure 7.15 FMCW signals: (a)-(b) IQ signals for different ramps, (c)-(d) respective range profiles.

the 1.3-2.4 GHz (low) and 2.4-4 GHz (high) bands. As an example, Figure 7.15 shows IQ signals for different ramps reflected from a large metal plate. Note the sweeping period is 170  $\mu$ s. The range profiles are obtained from them by FFT and re-computing the beating frequency into range.

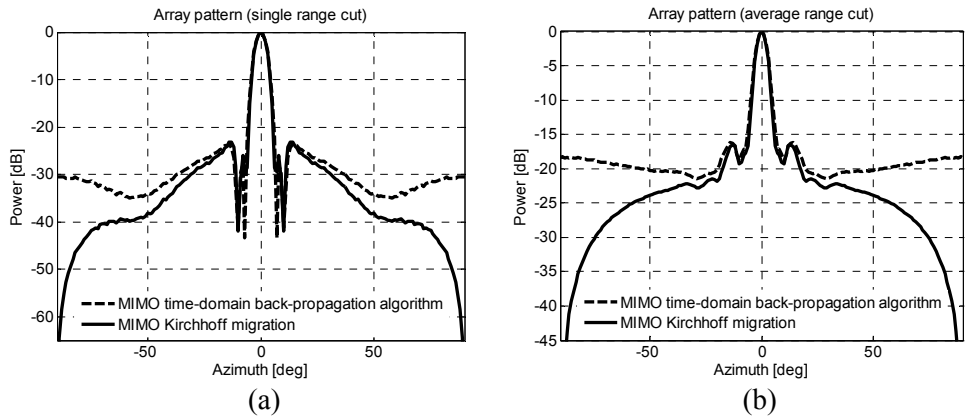


Figure 7.16 Near-field array patterns of MIMO arrays within the principle planes obtained with point-like target located at  $20\lambda_c$  range distance. (a) Single range cut, and (b) average range cut patterns of the array.

An antenna topology is carefully arranged to achieve optimal performance within two orthogonal planes (combination of the lowest level of sidelobes by a given width of the main lobe, which gives the sharpest image for the central positioned objects). The transducer array consists of four transmit and eight receive antennas, spatially distributed within a two-dimensional plane. Combining with digital beamforming, such device has the potential to achieve real-time imaging (display refresh rate of 10–12 radar images per second) with a single channel transmitter and receiver. The suggested 4 times 8 topology provides a compromise between system complexity and image quality.

The pattern of the MIMO array at near-field using both proposed time-domain imaging algorithms is shown in Figure 7.16. These patterns are obtained with 120% fractional bandwidth. The array together with MIMO Kirchhoff migration achieves 4.9 degree angular resolution, while maintaining an average sidelobe level of -16.5 dB. The 2-D array maintains the same performance along azimuth and elevation planes, which is important for 3-D imaging. To achieve the same performance using the uniform two-dimensional array with transmit/receive pairs, the number of antennas required would be much larger than the proposed two topologies.

## 7.2.5 Test results

Various free-space and through-wall scenarios were tested using the developed demonstrator. The formation of a radar image from the array data is to be done in FPGA with a high frame rate. Each data acquisition cycle gives 32 complex signals from the respective Tx-Rx channels and 1 complex signal from an internal reference

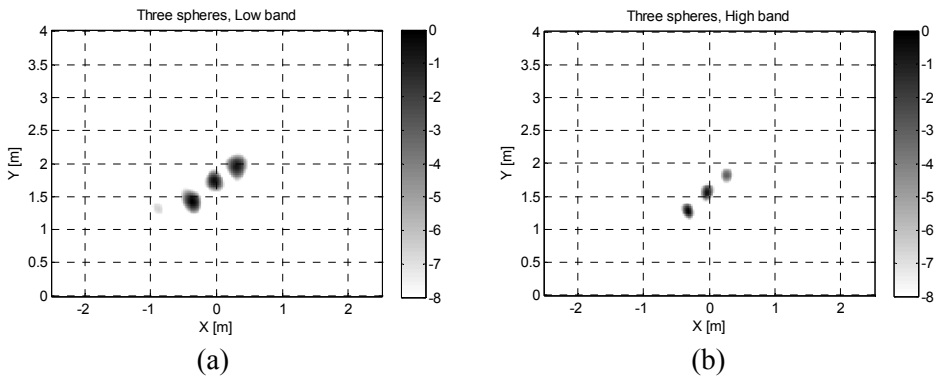


Figure 7.17 Imaging of three metal spheres in horizontal plane obtained in (a) 1.3-2.4 GHz band, (b) 2.4-4.0 GHz band.

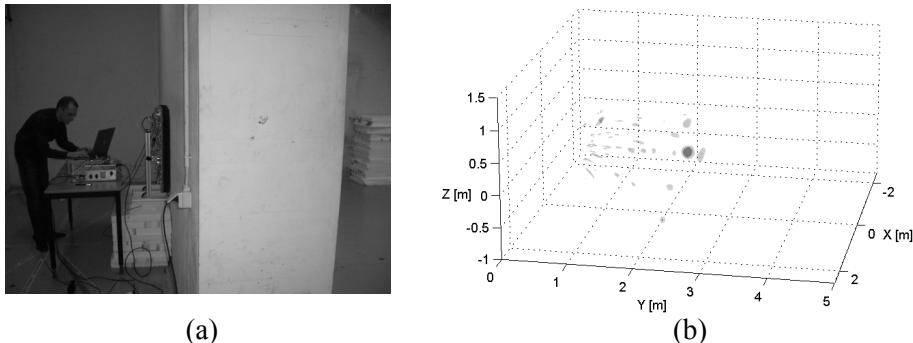


Figure 7.18 Imaging of a person through 60 cm thick reinforced concrete wall. (a) target scenario; (b) 3-D radar image of a standing person.

channel. The raw time-domain data are pre-processed by a Kaiser window, transformed into the range profiles by FFT. Then after subtraction of antenna crosstalk and, possibly background we calibrate the data by compensating for an internal electrical delay measured beforehand in each channel.

Figure 7.17 presents the results of a resolution measurement with three metal spheres of 3.5 cm diameter, separated from each other by 25 cm. As expected, the higher bandwidth and frequencies give a sharper image.

The imaging of a person through wall is illustrated in Figure 7.18. The wall is made of reinforced concrete with 60 cm thickness. Its dielectric constant, determined by measurement, equals to 6.4 at 3 GHz and the two-way propagation loss through it was found to be 60 dB at 3 GHz. A person was standing still behind the wall at a 2.3 m distance from the radar. His radar image shown in Figure 7.18(b) was obtained for the 2.4-4 GHz band.

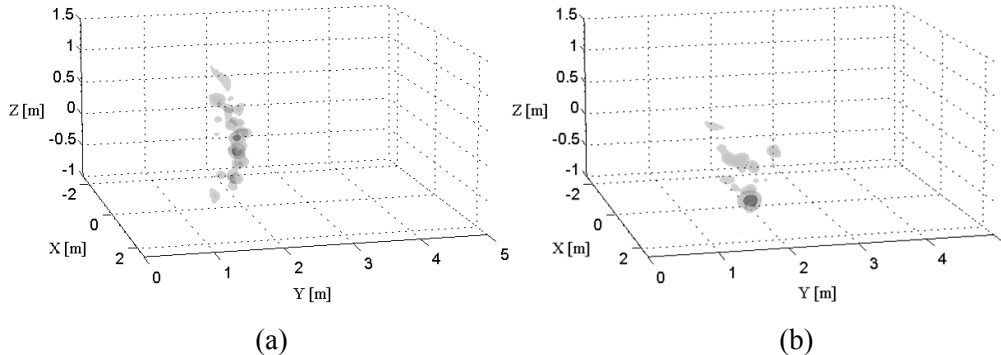


Figure 7.19 Imaging of a person in (a) standing position, and (b) laying position.

Furthermore, our experiments in free space and through thinner walls demonstrated a capability to discriminate between standing and laying persons (Figure 7.19). As we can see, the conducted tests have demonstrated a capability of the UWB-MIMO radar to image a person through wall and to discriminate between people in different positions. Further research should cover discrimination between armed and unarmed people, breathing detection, and tracking of moving people.

### 7.3 Ground penetrating radar in a multi-sensor fusion system

It has been demonstrated that GPR is a useful sensor for multi-sensor system dedicated to landmine detection, especially for humanitarian demining [15]. Numerous field trials of different GPR sensors have proven that while for most ground types, GPR sensor can achieve desirable detectability level; the reduction of the false alarm rate remains as the most important task for GPR developers. This can be achieved by the combination with other sensors like metal detector and visual or infra-red camera. GPR should be a leading sensor for buried objects, while infra-red (visual) camera should lead for surface-laid objects. Metal detector should verify if there is any metal content in the objects detected by camera or GPR. Performance of the whole multi-sensor suit depends very much on the way how information from different sensors is fused.

For a number of years TNO Defence, Security and Safety has been investigating the capabilities of sensor fusion for landmine detection [16]. TNO has developed a multi-sensor test platform to demonstrate the capabilities of sensors in real-time operation on a multi-sensor system (Figure 7.20). The system has to scan ground with a speed of at least 2km/h. Such operational speed is too high for conventional GPR based on sequential data acquisition. Thus, it was decided to use the multi-



Figure 7.20 TNO multi-sensor test trolley for landmine detection research.

channel UWB sensor with digital beamforming, which is newly developed in IRCTR [17]. This radar can support the scanning speed up to 148km/h due to its innovative system design. However, realization of real-time data processing for this system remains as a challenge. In this section, we will describe the developments of such real-time processing scheme and experimental verification of its performance.

### 7.3.1 Array-based UWB GPR Sensor

IRCTR mini-array GPR comprises a pulse generator, an antenna array system, a seven-channel signal conditioner and an eight-channel sampling converter. A block scheme of the mini-radar is shown in Figure 7.21.

The generator fires a step pulse with a rise time of about 90 ps. Such a waveform improves radar power budget at low frequencies, which are not efficiently radiated by the transmit antenna due to the relatively small size of its physical aperture. The receiver chain consists of a seven-channel signal conditioner and an eight-channel sampling converter (built by GeoZondas Ltd., Lithuania). The receiver chain has an analog bandwidth from 200 MHz up to 6 GHz and the linear dynamic range of 69 dB (with averaging over 128 samples). The sampling converter operates with the sampling rate of 500 kHz per channel. Observation time window can be varied from 32 ps till 20 ns with a number of acquisition points available from 16 till 4096. Large flexibility in duration of the observation time window and the sampling time allows us to adjust the system to different ground types and data acquisition scenarios. A very important feature of the sampling converter is its high measurement accuracy. The maximal error in the amplitude scale and the time scale linearity of the sampling converter is about 1%.

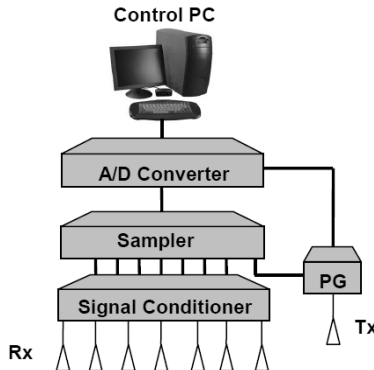


Figure 7.21 Block scheme of GPR developed at IRCTR.

An important part of the receiver chain is the signal conditioner. The signal conditioner improves the signal to noise ratio and allows the use of the whole dynamic range of the ADC. The equivalent noise floor (which includes the quantization noise of ADC) of the receiver is less than 1.5 mV RMS without averaging. The spectrum of the noise corresponds to the almost white noise so it can be efficiently suppressed by averaging. The signal conditioner decreases the noise floor and improves the signal-to-noise ratio by almost 30 dB.

The long-term stability of the radar is characterized by the time-delay drift of about 12 ps/hour. To improve the long term stability of the system the eighth channel of the sampling scope is used. This channel acquires one of two signals. For the time axis calibration a 4GHz harmonic signal from the internal generator of the sampling scope is acquired. For the delay drift compensation the reference signals from the generator is acquired. The data post-processing is used for compensation of the time drift based on the reference signals acquired in the eighth channel. As a result of this compensation, the time drift less than 1ps/hour has been achieved.

The radar antenna system consists of a single transmit antenna elevated 60cm above the ground and a linear array of the receive antennas (loops) elevated 20cm above the ground. The whole antenna system is mounted on the TNO test platform and covered with a protective shield (Figure 7.22).

### 7.3.2 GRP embedding in multi-sensor suit

The scheme of the multi-sensor system is given in Figure 7.23. The data acquisition and transfer is synchronized by means of a tick wheel mounted on a vehicle. The wheel sends a TTL pulse via RS232 to the sensor units and fusion processor at given intervals (2.5 cm). The GPR sensor unit acquires and processes a B-scan when



Figure 7.22 Antenna system of the GPR mounted on the test platform.

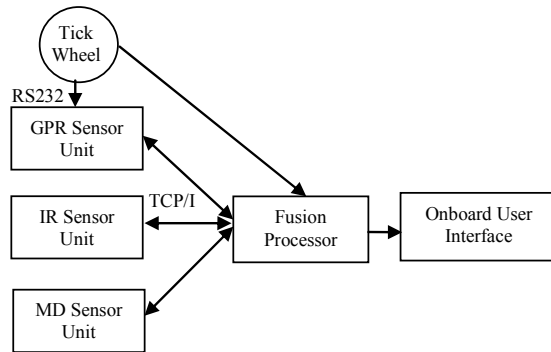


Figure 7.23 the scheme of the multi-sensor system.

triggered by the tick wheel. It stores the raw and/or pre-processed data and transfers it through TCP/IP to the fusion processor on request.

Standard processing scheme includes background subtraction, subsurface imaging and confidence map computation. Second step is the most time consuming one and typically is realized only in off-line processing. However, both the detecting and the correct positioning of subsurface targets can be essentially improved by adding subsurface imaging into the real-time processing chain. Thus, a dedicated real-time imaging scheme has been developed and implemented in the system.

Background subtraction is done in two major steps: subtraction of the antenna coupling and moving average subtraction. Size and shape of the moving window has been optimized to fit the geometry of the antenna system and scanning speed. Band pass filter is applied in each A-scan signal in order to suppress uncorrelated noise outside the operational bandwidth.

Imaging scheme is based on the modification of Kirchhoff migration algorithm introduced in chapter 6. Under near-field conditions, this technique is able to

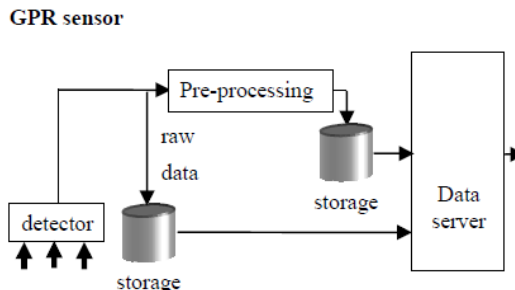


Figure 7.24 Data flow in the real-time processing chain of the GPR sensor unit.

improve both spatial resolution and signal to clutter noise ratio (SCNR) of the survey comparing with conventional synthetic aperture radar (SAR) imaging techniques, such as diffraction stack algorithm. The idea of Kirchhoff migration is to back-propagate the scalar wave front, measured in the data acquisition plane, to the object plane at time zero, using an integral solution to the scalar wave equation.

The feasibility of applying this algorithm to electromagnetic problems lies on the fact that vector wave equations reduce to scalar wave equation in a homogeneous, isotropic medium. The algorithm is based on complete linear operations and therefore can be efficiently implemented. The focusing is performed in both cross-track and along-track directions to provide instant 3D resolution. The obtained images are updated iteratively as the scanning continues. In this way, the computation load can be further spread over the sequential data acquisition time. The refraction effect of air-ground interface is also compensated for better focusing of buried targets. The time delay due to propagating underground is calculated according to Snell's law of refraction using a Newton-Raphson method, which converges fast within minimum number of iteration.

Confidence maps are computed in the following way. The resulting 3-D image is continuously translated into two-dimensional matrixes by using a windowed energy projection as the area under scanning moves outside the footprint of the transmit antenna. Then, it is scaled by a background model which is trained as the array response to the minimum detectable target. The resulting confidence map is expressed in logarithmic scale for larger dynamic range and transferred to the fusion computer sequentially within a short latency. The computed confidence map is aligned to the total detection grid of the whole multi-sensor system which has a size of 2.5 cm.

The processing scheme is implemented in the data flow shown in Figure 7.24. Here the pre-processed data stored and transferred by the GPR sensor unit are the confidence maps.

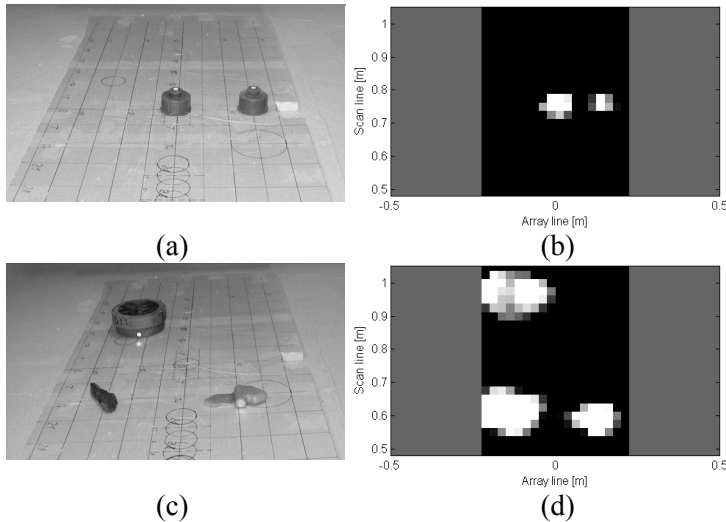


Figure 7.25 Laboratory tests with surface laid mines. (a) Two identical small plastic mines with 10 cm separation, and (b) corresponding confidence maps. (c) Two mines and a metal debris, and (d) corresponding confidence map generated by the GPR unit.

### 7.3.3 Test results

The performance of the developed data processing scheme has been evaluated in laboratory conditions. The radar has scanned over a number surface-laid mines (which is the most difficult for GPR type of targets due to masking of target return by ground bounce). Typical scenarios and the produced confidence maps are shown in Figure 7.25. It can be seen that the radar efficiently detects and localizes plastic mines. Furthermore, the processing scheme allows separate detection of small targets laid close to large ones. The computational time needed to provide the confidence map of one meter scan line is less than 2 seconds. This processing speed fulfills the requirement for real-time operation.

After the laboratory test, the complete system has been tested in quasi-real conditions at premises of TNO. A number of anti-tank and anti-personnel mines as well as typical false alarms have been buried in a grass field. The vehicle was moving with a speed of about 36 km/h. The test run shows no problems with the real-time operation of the GPR. The radar was capable to detect all surface-laid and buried mines. The test fields as well as an example of a section of the test results are demonstrated in Figure 7.26.

In the section of the test filed, variety of mines were placed including 3 metal anti-tank mines buried at different depths from 10 cm to 20 cm, and 6 metal anti-

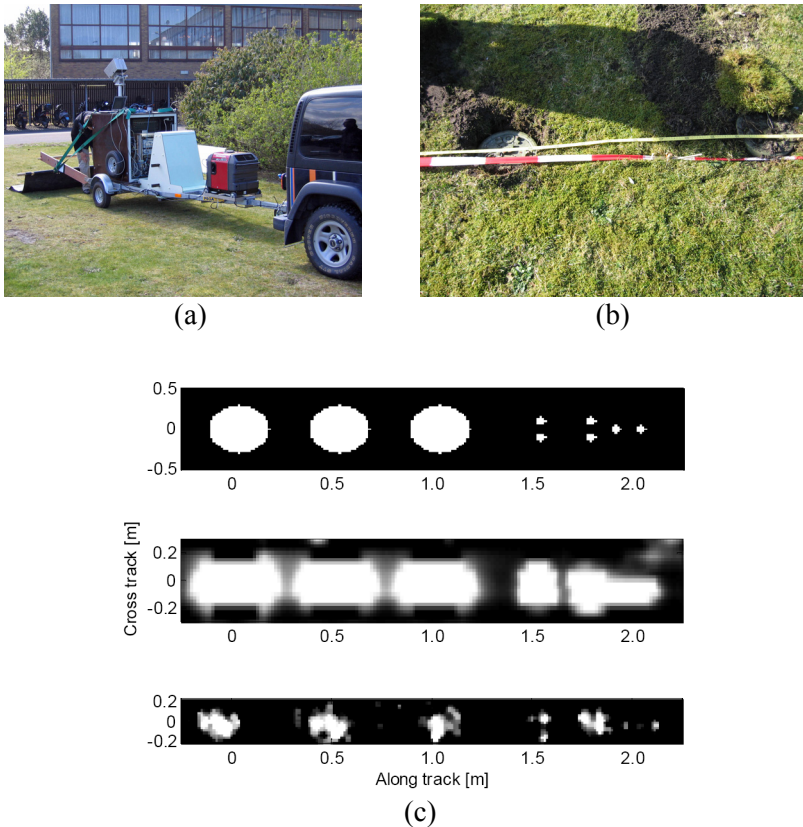


Figure 7.26 Quasi-real test performed at TNO. (a) Photo of the multi-sensor system including GPR, electro optic camera, and array metal detector. (b) Photo of the test soil and buried mines. (c) Scenario with buried anti-tank and anti-personnel mines (top), confidence map of the metal detector array (middle), and GPR confidence map (bottom).

personnel mines (some were flash-buried, some were buried at a depth of 5 cm below ground surface). The result shows that the GPR unit was able to detect all mines as separate targets in proper positions, while metal detector can not resolve separate anti-personnel mines. A single false alarm has been produced due to a surface-laid scatterer.

The developed UWB array-based time-domain GPR has been successfully integrated in a vehicle-mounted multi-sensor system for landmine detection. The dedicated processing scheme is able to provide real-time confidence maps of both surface laid and buried mines with high resolving capabilities. The test run further demonstrated a reliable detection under the vehicle speed of 36 km/h.

## 7.4 Summary

In this chapter, we have demonstrated the application of various developed theories and designs in several projects, related to applications including concealed weapon detection for public security, through wall or rubble imaging for rescue operation, and subsurface imaging for landmine detection. Satisfactory results from laboratory experiments and quasi-realistic tests by developed prototypes confirm the validation of the theoretical study, and further demonstrate the possibility of achieving full functional real-time imaging systems. The development and validation of the developed new technologies in this thesis provide clear indications and directions for future industrialization, and development of powerful imaging equipments for surveillance, crisis intervention, and medical diagnosis in the future.

## References

- [1] A. Luukanen, L. Grönberg, T. Haarnoja, P. Helistö, K. Kataja, M. Leivo, A. Rautiainen, J. Penttilä, J. E. Bjarnason, C. R. Dietlein, M. D. Ramirez, and E. N. Grossman , “Passive THz imaging system for stand-off identification of concealed objects: results from a turn-key 16 pixel imager,” in *Proc. SPIE*, 6948, 69480O (2008), doi:10.1117/12.784922.
- [2] D. M. Sheen, D. L. McMakin, and Th. E. Hall, “Near Field Imaging at Microwave and Millimeter Wave Frequencies,” in *Proc. IEEE int. Microwave Symp. 2007*, Jun. 2007, pp. 1693-1696.
- [3] D. M. Sheen, D. L. McMakin, J. Barber, T. E. Hall, and R. H. Severtsen, “Active imaging at 350 GHz for security applications,” in *Proc. SPIE* 6948, 69480M (2008), doi:10.1117/12.778011.
- [4] T. G. Savelyev, X. Zhuge, A. G. Yarovoy, L. P. Ligthart, B. Levitas, “Comparison of UWB SAR and MIMO-Based Short-Range Imaging Radars,” in *Proc. European Radar Conference (EuRAD)*, Sep. 2009, pp. 109-112.
- [5] B. Yang, A.G. Yarovoy, and L. P. Ligthart, "UWB Stacked Patch Antenna Design for Near-Field Imaging Radar Antenna Array", in *Proc. EuCAP 2009*, Berlin, Mar. 2009, pp. 817-821.
- [6] Y. Yang, A.E. Fathy, “See-through-wall imaging using ultra wideband short-pulse radar system”, in *Proc. Antenna Propag. International Symposium*, Jul. 2005, vol. 3B, pp. 334 - 337.
- [7] A. Beeri, R. Daisy, “High-Resolution Through-Wall Imaging”, in *Proc. SPIE*, vol. 6201, 62010J (2006).

- 
- [8] A. R. Hunt, "Image Formation Through Walls Using a Distributed Radar Sensor Array", *Applied Imagery Pattern Recognition Workshop 2003*, Oct. 2003, pp. 232 - 237.
  - [9] R. Zetik, S. Crabbe, J. Krajnak, P. Peyerl, J. Sachs, R. Thoma, "Detection and localization of persons behind obstacles using M-sequence through-the-wall radar", in *Proc. SPIE*, vol. 6201, 62010I (2006).
  - [10] S. E. Borek, "An overview of through the wall surveillance for homeland security", *Applied Imagery and Pattern Recognition Workshop*, Oct. 2005, pp. 6pp.-47.
  - [11] A. Muqabe, A. Safaai-Jazi, A. Bayram, A.M. Attiya, and S.M. Riad, "Ultra-wideband through-the-wall propagation", *IEE Proc. Microw. Antennas Propag.*, vol. 152, no. 6, pp. 581-588, Dec. 2005.
  - [12] A. G. Yarovoy, R. V. de Jongh, and L. P. Lighthart, "Ultra-wideband sensor for electromagnetic field measurements in time domain," *Electronics Letters*, vol. 36, pp. 1670-1680, 2000.
  - [13] A. G. Yarovoy, X. Zhuge, T. G. Savelyev, L. P. Lighthart, "Comparison of UWB Technologies for Human Being Detection with Radar," in *Proc. European Microwave Conference (EuMC)*, Oct. 2007, pp. 1574-1577.
  - [14] X. Zhuge, T. G. Savelyev, A .G. Yarovoy, "Assessment of Electromagnetic Requirements for UWB Through-Wall Radar," in *Proc. International Conference on Electromagnetics in Advanced Applications (ICEAA)*, Sep. 2007, pp. 923-926.
  - [15] McDonald, J., et al., *Alternatives for landmine detection*, Rand Corporation (2003).
  - [16] J. G. M. Schavermaker, E. Den Breejen, K. W. Benoist, K. Schutte, P. Tettelaar, M. de Bijl, P. J. Fritz, L. H. Cohen, W. van der Mark, R. J. Chignell, "LOTUS field demonstration of integrated multisensor mine detection system in Bosnia," *Detection and Remediation Technologies for Mines and Minelike Targets VIII*, in *Proc. SPIE*, 2003, vol. 5089, pp.1324-1335.
  - [17] A. G. Yarovoy, T. G. Savelyev, P. J. Aubry, P. E. Lys, and L. P. Lighthart, "UWB array-based sensor for near-field imaging," *IEEE Trans. Microw. Theory Tech.*, vol. 55, no. 6, pp. 1288-1295, Jun. 2007.



# CHAPTER 8

## CONCLUSIONS

Array-based ultra-wideband microwave imaging system exhibits strong potential in many short-range applications. Existing systems based on synthetic aperture radar technology or array with sequential operation of identical transceiver pairs are costly and commercially difficult to be widely deployed. Moreover, their utilization is problematic in many demanding scenarios where compact and lightweight high-resolution imaging systems are required, which can provide real-time perception of the target.

The combination of UWB technology and real-aperture MIMO array offers a sound solution to the increasing demand for safe, reliable and cost-effective imaging sensors with high resolution capability. UWB impulse with high fractional bandwidth controls the appearance of grating lobes caused by the sparsity of the array, while asymmetric transmit and receive arrays further reduce the required number of antenna elements within the array aperture. The combined advantages of UWB technology and MIMO technique allow drastic reduction of element density, data-acquisition time, computational costs for imaging, and costs of the system as compared to conventional SAR systems.

With the works described in the thesis, the practical feasibility of an array-based ultra-wideband imaging system for several demanding applications has been demonstrated. The developed theory of ultra-wideband focusing, 1-D and 2-D MIMO array, and imaging algorithms for near-field wideband focusing allow the use of sparse aperture array, simple and cheap technologies to achieve high resolution, high quality imaging. The contents of this thesis represent an important step forward and contribution to the development of high-performance, low-cost UWB imaging systems with high resolution. Through the chapters, the author aimed to provide the scientific society with a fundamental theory and detailed experimental study of

MIMO UWB array's capabilities, as well as the proper concept to design a sound imaging system.

## 8.1 Results and novelties of this research

Within the framework of this thesis, the following novel results have been achieved and presented in this thesis:

1. *Properties of ultra-wideband focusing.* A novel concept and theory regarding ultra-wideband focusing, which corrects the previous misunderstanding regarding the impact of bandwidth on imaging, has been proposed. It was widely accepted that grating lobes are not encountered under sparse aperture/array condition. The proposed theory in this thesis shows that sparsity only ensures the existence of a grating lobe free region within the image space rather than the absence of grating lobes. Instead, the bandwidth relative to the center frequency, or fractional bandwidth, has the deterministic impact on the formation of grating lobes. Specifically, the bandwidth of an imaging system must exceed its central frequency in order to benefit from the merit of wideband impulse properties, allowing high-resolution imaging with significantly reduced number of antenna elements. The proposed theory helps to resolve the dilemma between angular resolution and grating lobe level for a sparse aperture/array.
2. *MIMO Array Topology design.* Novel design concept and strategies for one-dimensional and two-dimensional multiple-input multiple-output arrays have been proposed. The proposed approach allows straightforward formation of array topologies without the need of numerical optimization. The designed arrays following the proposed strategies are able to provide three-dimensional imaging capabilities and low grating/side lobe level with large element spacing and minimum number of antenna elements needed.
3. *Combination of ultra-wideband technology and MIMO array technique.* It is demonstrated that the combination of ultra-wideband and MIMO array is a beneficial concept for microwave imaging systems. The MIMO array-based UWB imaging system is able to provide high down- and cross- range resolution, low side/grating lobe level, simplified RF scheme and significantly increased data acquisition speed. A deterministic procedure for designing UWB MIMO array for short-range imaging has been formulated. The process adapts requirements from the application into specific array specifications, such as operational frequency band, the number of elements needed, aperture dimension, and array topology, etc.
4. *Comparison between SAR and MIMO array.* A comprehensive experimental comparison between synthetic aperture radar (SAR) and real-aperture MIMO

array has been performed. Clear advantage of the real-aperture system in terms of reduced number of required measurements is observed which pushes the MIMO system concept further into practical design and application.

5. *Modified Kirchhoff migration for MIMO configuration.* Modified Kirchhoff migration has been developed for both free-space and subsurface UWB imaging. The applied modifications allow for the extension of the classical Kirchhoff algorithm, which is based on the exploding reflector concept and is applicable to co-located transmit-receive antennas, to multistatic imaging with arbitrary positions of the transmit and receive antennas. The algorithm combines the high quality imaging performance with acceptable computational costs and can be applied to demanding applications in practice.
6. *Range migration algorithm for MIMO configuration.* Range migration algorithm is reformulated for multistatic array configuration in the frequency-wavenumber domain. By taking advantage of the computation efficiency of the fast Fourier transform (FFT), imaging speed of MIMO array-based system is significantly increased while maintaining high-quality imaging capabilities.
7. *Demonstration of UWB MIMO system in different applications.* Within the framework of several European projects, prototypes of MIMO array-based UWB imaging systems were designed and implemented for through-wall imaging (PROBANT), ground penetrating radar (Cadmium), and concealed weapon detection (RADIOTECT, ATOM). The feasibility of operational MIMO UWB systems under various practical circumstances has been demonstrated. Thanks to the combination of UWB, MIMO array, and advanced digital beamforming algorithms, high-resolution 3-D images were obtained using sparse aperture array with simplified front-end and low-cost equipments.

## 8.2 Recommendations

In this section, several recommendations for future research as a continuation of the work presented in this thesis are given. During the research, a number of new problems and topics, which require further study and investigation, have been identified. A list of new directions to be investigated includes:

- The development of full-wave imaging algorithms. Full-inversion algorithms are commonly applied for narrowband 2-D electromagnetic problems. The ill-posed and non-linear nature of the inverse problem and the huge amounts of data to be processed make such solution quite challenging in practice. How to add more theoretical concept into the image reconstruction process with less computation complexity and instability is still a topic for future research.

- By combining images obtained from different parts of the MIMO array, it is theoretically possible to generate elevation maps by interferometry technique with unprecedented precision and resolution. Investigation of interferometry using ultra-wideband signal and multistatic array configuration is needed to determine the potential of such technique for short-range applications.
- Research of active sparse UWB array using full-wave numerical analysis. This is challenging due to the large dimension of the electromagnetic problem. It is an important step for applications where real high-gain array antenna or focusing is needed for energy transfer or information transfer purposes.
- Investigate the capabilities and design of three-dimensional wideband aperture/array. Although stand-off systems are quite often preferred in practice, 3-D aperture can provide another dimension and design freedom for high-resolution imaging, particularly in short-range applications.
- Automatic target recognition is a necessary step toward practice. Having obtained a high-resolution image, the task is to identify whether it contains important information so that action can be taken. As the output of an UWB imaging system, images are provided in three-dimensions, and features may also hide in the way in which are changing with time. Such large data sets in four dimensions of space and time are not easy for human brain to interpret. Computer software can help by searching large amount of data rapidly using agreed rules, which can emulate an initial examination by a professional with all the experiences needed. The human factor is the slowest link in the processing chain and needs all the help that can be given.
- Waveform diversity can provide another dimension to explore the benefit of MIMO array. By utilizing variant waveforms for different elements within the array, the cancellation of grating/side lobes may be possible, which can further improve the dynamic range of the complete imaging system.
- Microwave systems for cancer detection and hyperthermia treatment are of interest for decades. The social implications of improved technology for detection and treating cancer are profound and enormous. The research work is inherently multidisciplinary and requires diverse areas of expertise in electromagnetics, signal processing, microwave imaging and biomedical engineering. At present, a large amount of research and engineering work has to be completed before this optimistic vision becomes reality.

## APPENDIX

# DESIGN OF LOW PROFILE UWB ANTENNA FOR NEAR-FIELD IMAGING

This appendix presents the design of a low profile circularly tapered antipodal Vivaldi antenna for ultra-wideband near-field imaging. The proposed circular termination at the end of radiating flare and optimization of the feeding transition result in extension of the operational bandwidth and improvement of antenna impulse response. The antenna design with dimensions of 45×48.5 mm achieves satisfactory impedance matching and radiation across the frequency band from 2.7 to 26 GHz with more than 160% fractional bandwidth. Both SMA and 2.4 mm connectors are tested with the manufactured antenna in order to confirm its UWB performances.

### A.1 Introduction

One of the challenges for the development of array-based ultra-wideband microwave imaging system is to design satisfactory antenna element with both small dimension and large fractional bandwidth. High resolution, high dynamic range radar imaging requires a large number of elements within the array system. Element dimension has to be small enough in order to place necessary amount of elements within an imaging device. Meanwhile, large bandwidth (at least 100%) is needed for both high down-range resolution and well-controlled beam steering capabilities. In our case, a small antenna with less than 5 cm aperture size, more than 150% fractional bandwidth, and

satisfactory impulse response is required in order to verify the proposed theories of UWB focusing.

In the past, different types of small UWB antennas have been investigated, including resistively loaded pyramidal horn antenna [1], stacked patch antenna [2], leaky lens antenna [3], and tapered slot antennas [4][5]. Among the existing designs, the antipodal tapered slot antenna provides approximately the required operational bandwidth while maintains sufficient radiation efficiency, simple design structure and low fabrication cost. Therefore, the antipodal Vivaldi antenna is chosen as a basis for developing antenna elements for the UWB imaging array.

Vivaldi antenna is widely investigated and applied in various applications due to its broad bandwidth, low cross-polarization, and high directivity [6]. The dual exponentially tapered antipodal slot antenna (DETASA) is a modified form from the traditional Vivaldi antenna by exponentially tapering both the inner and outer edges of the radiating flare and placing the mirrored flares on both side of the substrate. It is a slow leaky end-fire travelling wave antenna. The electromagnetic wave travels down the gradually curved path of the flares. As the separation between the flares increases, the bond of the wave becomes progressively weaker and radiates away. A wideband performance can be achieved using DETASA with its inherently simple wideband transition from microstrip line to tapered slot flare through parallel strips. In order to further extend the operational bandwidth and its radiation performance, a modification of DETASA is introduced by merging the exponential flare with a circular tapering termination. It creates a longer path for the current flow, making the antenna bandwidth wider and smoother.

The transition of the antenna from the feeding source to the radiation flares are designed based on high frequency transmission-line theory. In order to reduce reflections through the microstrip line to twin line transition, the thickness and dielectric properties of the substrate are chosen in such a way that the width of the microstrip line and twin line remains the same while both possessing a characteristic impedance close to  $50\ \Omega$ . In order to verify and further optimize the antenna design, numerical model has been developed using commercial software CST Microwave Studio, which is a time-domain solver based on finite integration technique (FIT). The end-launch connector that connects the feeding line to the Vivaldi antenna is included in the numerical model, which helps to accurately estimate the overall performance of the antenna. The final design has been manufactured using the *Taconic TRF-45* substrate, which exhibits stable dielectric constant and low dissipation factor.

The remaining of the appendix is organized in three sections. The design and optimization of the antenna are described in section A.2 Section A.3 presents both the theoretical and experimental performances of the antenna including its UWB characteristics. Finally, conclusions are stated in section A.4.

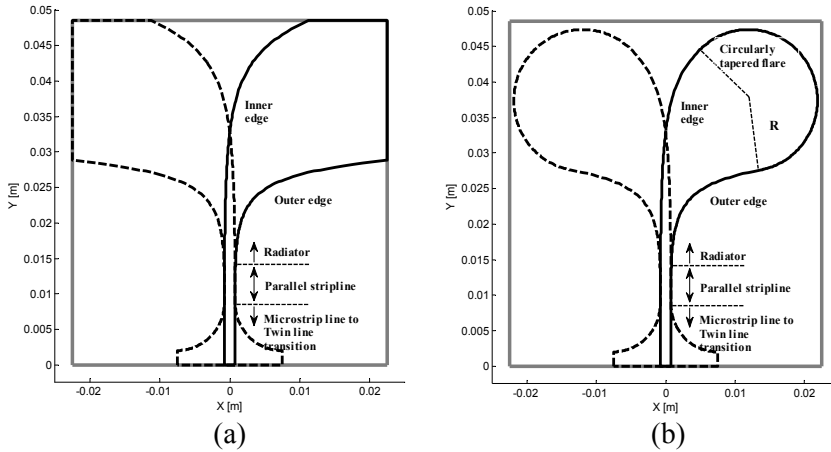


Figure A.1 Geometry of (a) DETASA, and (b) the design with circular tapering at the end of the radiation flare.

## A.2 Antenna element design

The geometries of both DETASA and the proposed design are shown in Figure A.1. The antenna flare mainly consists of three parts. The first section is the circularly tapered transition from microstrip line to the double-sided parallel stripline. The second part is the parallel stripline, which is a balanced structure providing wideband transitions. The last part is the radiation flare. It is further constructed by three curves, including the inner and outer edges that are defined by exponentials and a termination of the flares. With the proposed design, a circularly tapered end is merged with each flare before it reaches the end of the substrate. This extra geometry provides better and smoother termination for the antenna.

The connection between microstrip line and the radiation flares can be seen as a transition from an unbalanced structure to a balanced structure. The shape of the tapering along the microstrip line is designed mainly based on empirical method. Due to the fact that the ground width is changing along with the transition, the characteristic impedance of such structure can not be kept constant with length. In order to reduce reflections through the transition, the width of both microstrip line and twin line are specified based on transmission-line theory. Given the dimensions of the microstrip line, the characteristic impedance can be calculated as [7]

$$Z_0 = \begin{cases} \frac{60}{\sqrt{\epsilon_e}} \ln\left(\frac{8d}{W} + \frac{W}{4d}\right) & \text{for } W/d \leq 1 \\ \frac{120\pi}{\sqrt{\epsilon_e} [W/d + 1.393 + 0.667 \ln(W/d + 1.444)]} & \text{for } W/d \geq 1 \end{cases} \quad (\text{A.1})$$

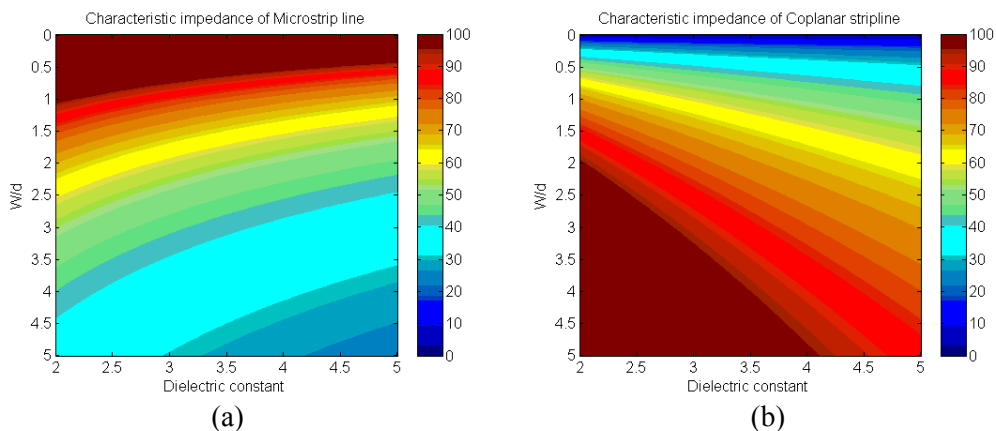


Figure A.2 Characteristic impedance of (a) microstrip line, and (b) coplanar stripline for different  $W/d$  ratio and substrate dielectric properties.

where  $W$  is the width of the upper microstrip line,  $d$  is the thickness of the substrate and  $\epsilon_r$  is the effective dielectric constant of the microstrip line.

According to the theory presented in [8], the approximate formula for calculating the characteristic impedance of the twin line is given by

$$Z_0 = \frac{\eta}{d/W + \left\{ 1 + \ln[(\pi d/W) + 1 + \ln(\pi d/W + 1)] \right\}} \quad (\text{A.2})$$

where  $\eta$  is the intrinsic wave impedance of the filled dielectric material between the parallel striplines.

Based on the approximations given in (A.1) and (A.2), we try to find the common  $W/d$  ratio under which both the microstrip line and the CPS can have the same characteristic impedance close to the matched  $50 \Omega$ . Figure A.2 illustrates the change of characteristic impedance of both microstrip line and CPS for different  $W/d$  ratio and dielectric properties. We can observe an intrinsic contradiction between the two different structures. Generally speaking, the characteristic impedance of the microstrip line decreases with increasing  $W/d$  ratio while it is the exactly the opposite situation for the twin line. In order to find the intersection between the two surfaces, we need to use the substrate with higher dielectric permittivity. On the other hand, high dielectric constant substrate will limit the performance of the radiating part of the antenna as it constrains the field within the substrate reducing radiation from the antenna. Therefore, trade-off has to be made to compromise between both sides of the performances. In the end, we decide to print the antenna on the *Taconic TRF-45* substrate, which has a dielectric constant of 4.5 (with dissipation factor 0.0035) and thickness of 1.02 mm. In this case, both

TABLE A.1  
DIMENSIONS AND PARAMETERS OF THE ANTENNA DESIGN

Variable	Value
Width, $W$	45 mm
Height, $H$	48.5 mm
Width of the microstrip line	1.5 mm
$k_s$	700
$k_w$	$4 \times 10^5$
$sf_i$	1.5
$sf_o$	3
Radius of the circular tapering, $R$	10 mm

microstrip line and CPS will have the same width (1.5mm) while maintaining the same characteristic impedance of about  $57\Omega$ .

The inner and outer edge of the radiation flare are defined by exponential functions that can be expressed as

$$\begin{aligned} x_{inner} &= \pm[-(c_s + c_w)/2 + c_s \cdot \exp(k_s y_{inner}^{sf_i})] \\ x_{outer} &= \pm[-(c_s + c_w)/2 + c_w \cdot \exp(k_w y_{outer}^{sf_o})] \end{aligned} \quad (\text{A.3})$$

where  $x_{inner}$  and  $x_{outer}$  are the horizontal distances from the inner and outer exponential edges to the center line of the antenna.  $y_{inner}$  and  $y_{outer}$  are the vertical distances from the edges to the bottom line of the antenna. The other parameters are obtained by the trial-and-error optimization procedure using full-wave electromagnetic simulation.

In order to smooth the sharp edges of the traditional DETASA, circular tapering is used before the edges reach the end of the substrate. In order to avoid sudden gradient change between the exponential edges and the circular tapering, optimization is performed to search for appropriate tapering parameters along the pre-fixed inner and outer exponential edges and provide defining parameters for the antenna configuration. Extra spacing is kept between the flares and the edge of the substrate. This additional space helps to reduce ringing of the time-domain impulse response. Table A.1 shows the variables and dimensions of the designed antenna. The final design is realized within a substrate dimension of  $45 \times 48.5\text{ mm}$ .

### A.3 Performances of the antenna

In order to investigate and optimize the antenna performance, full-wave electromagnetic models are developed using CST Microwave Studio 2009. End-launch connector is used as the feeding structure in the numerical model in order to accurately estimate the overall performance of the antenna. The connector is modeled as the same dimensions of the chosen SMA connector for the manufactured antenna. The numerical model of the antenna together with connector is shown in Figure A.3. The designed antenna has been manufactured as shown in Figure A.4. Both SMA and 2.4 mm connectors have been tested in order to confirm the antenna performances. The simulated and measurement results are presented in the following.

Numerical models with and without the circular termination are simulated. The numerical comparison helps to verify the theoretical influence of such geometry. Figure A.5 shows the differences in terms of return loss and antenna impulse response. As we can see, the lower part of the spectrum is extended for the proposed antenna geometry. The return loss becomes smooth showing less reflection from the antenna aperture. Meanwhile, the radiated pulse becomes sharper and exhibits less ringing after the main pulse. Both results show that the extra circular tapering helps improve both matching and radiation of the UWB antenna.

The return loss of the antenna obtained by simulation and measurement with SMA and 2.4 mm connectors are shown in Figure A.6. For this design,  $S_{11}$  is below -10 dB above 2.7 GHz. No upper limit has been found up to 26 GHz. Simulation was only performed up to 15 GHz due to computation limit. Discrepancies between the two measured connectors are caused by the differences of connector structures. Specifically, the 2.4 mm connector requires two extra screws through the antenna substrate in order to clamp the antenna into place. At lower part of the spectrum, the measured results match perfectly with our numerical simulation. This place extra emphasize on the importance of connectors on the accuracy of EM simulation.

Figure A.7 shows the measured gain of the antenna with SMA connector in both E- and H-planes. The antenna behaves as a dipole at low frequencies, which is visible in its H-plane radiation patterns below 6 GHz. The H-plane patterns become narrower towards higher frequencies. Meanwhile, the E-plane patterns become even wider towards higher frequencies due to the circular tapering of the radiating flare. This tapering results in a wider radiation in E-plane than that in H-plane distinguishing this antenna from traditional DETASA designs.

The radiated pulses in both E and H planes are shown in Figure A.8. The antenna maintains sharp and straight impulse response over a wide looking angle (-45 to 45 degree) with less than 100 ps pulse duration. This is an important characteristic for near-field imaging in order to form a large synthetic aperture, which in turn results in high cross-range resolution.

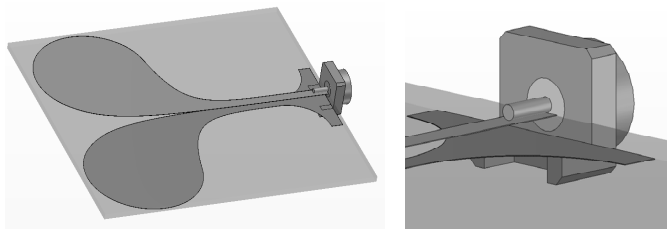


Figure A.3 Numerical model of the designed antenna element and its feeding structure realized in CST Microwave Studio.

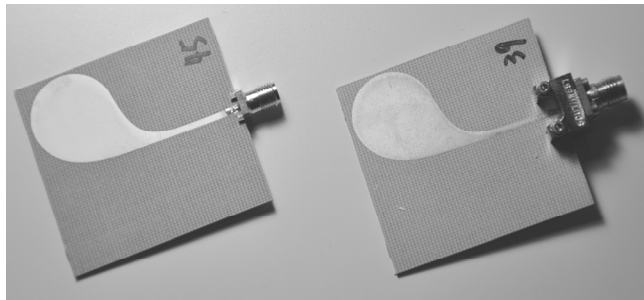


Figure A.4 Photo of the manufactured antenna ( $45 \times 48.5 \text{ mm}$ ) with SMA connector (left) and 2.4 mm connector (right).

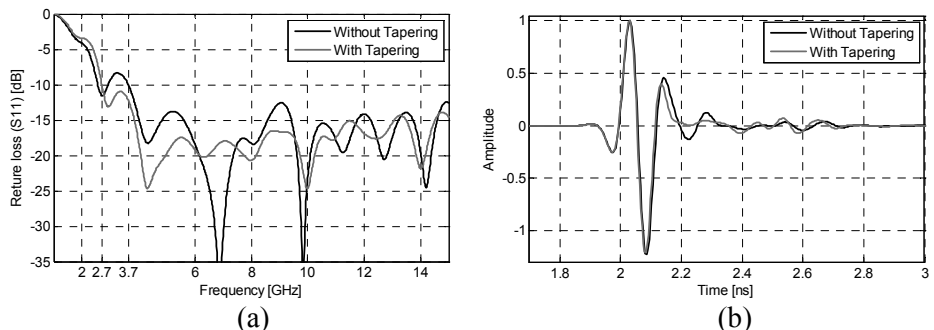


Figure A.5 Comparison of simulated (a) return loss and (b) impulse response at boreside between conventional DETASA and the proposed design with circular termination.

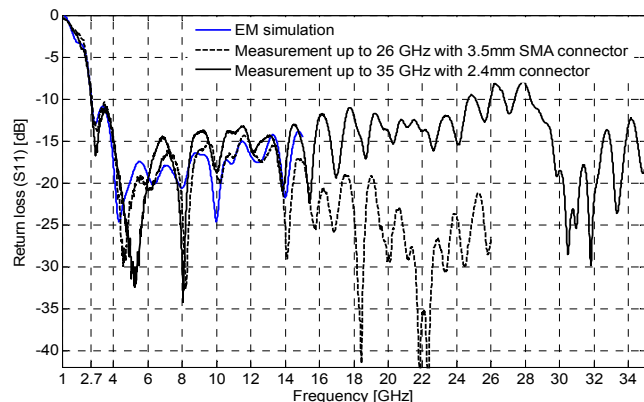


Figure A.6 Return loss of the designed antenna obtained by EM simulation and measurements of the manufactured antenna with SMA and 2.4 mm connectors.

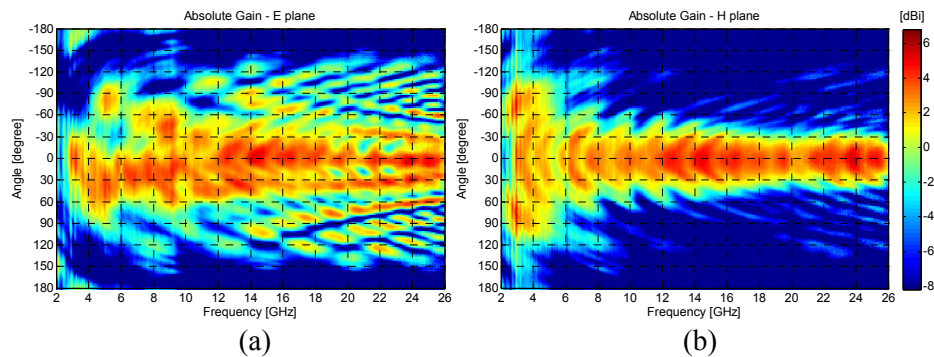


Figure A.7 Measured gain of the antenna in (a) E-plane and (b) H-plane.

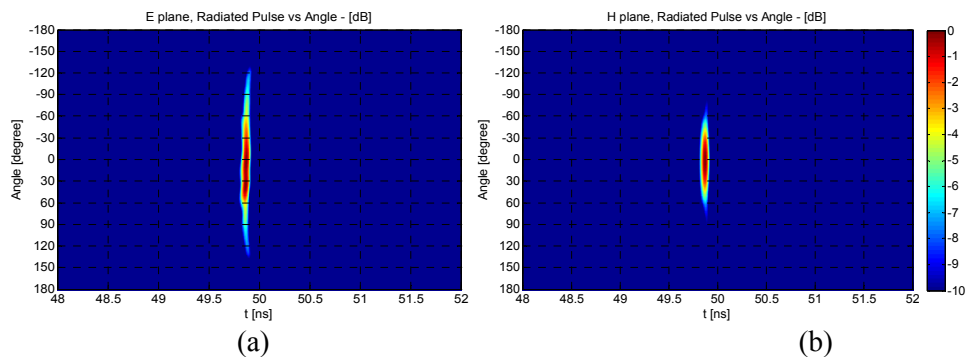


Figure A.8 Radiated pulse of the manufactured antenna in (a) E-plane and (b) H-plane.

## A.4 Summary

This appendix has presented the design of a low profile circularly tapered antipodal Vivaldi antenna for UWB near-field imaging. Proposed circular termination at the end of the radiating flare and optimization of the feeding transition result in extension of the operational bandwidth and improvement of antenna impulse response. The final design is realized within dimensions of  $45 \times 48.5$  mm and achieves satisfactory impedance matching and radiation performance over the bandwidth from 2.7 GHz to 26 GHz with more than 160% fractional bandwidth. Measurement results illustrate the consistent UWB characteristics of the proposed antenna, which is ideal for near-field imaging applications. Array imaging experiments using the designed antenna can be found in Chapter 3, 4, and 5.

## References

- [1] X. Li, S.C. Hagness, M.K. Choi and D.W. van der Weide, "Numerical and Experimental Investigation of an Ultrawideband Ridged Pyramidal Horn Antenna With Curved Launching Plane for Pulse Radiation," *IEEE Antennas and Wireless Propag. Letters.*, vol. 2 , pp. 259-262, 2003.
- [2] R. Nilavalan, I. J. Craddock, A. Preece, J. Leendertz and R. Benjamin, "Wideband Microstrip Patch Antenna Design for Breast Cancer Tumour Detection," *IET Microw. Antennas Propag.*, vol. 1, no. 2, pp. 277-281, 2007.
- [3] S. Bruni, A. Neto, F. Marliani "The Ultrawideband Leaky Lens Antenna" *IEEE Trans. Antennas Propag.*, vol.55, no.10, pp. 2642-2653, Oct. 2007.
- [4] W.C. Khor, M.E. Bialkowski, A. Abbosh, N. Seman and S. Crozier, "An ultra wideband microwave imaging system for breast cancer tumour detection," *IET Microw. Antennas Propag.*, vol. 1, no. 2, pp. 277-281, 2007.
- [5] J. Bourqui, M. Okoniewski, E.C. Fear, "Balanced Antipodal Vivaldi Antenna for Breast Cancer Detection," in *Proc. EuCAP*, Nov. 2007, pp. 1-5.
- [6] R. Janaswamy, D.H. Schaubert, "Analysis of tapered slot antenna," *IEEE Trans. Antennas Propag.*, vol. 33, pp. 1058-1065, Sep. 1987.
- [7] D.M. Pozar, *Microwave engineering*, 2<sup>nd</sup> ed., Wiley, New York, 1998.
- [8] P. Grivet, P.W. Hawkes, *The physics of transmission lines at high and very high frequencies*, vol. 1, Academic Press, London and New York, 1970.



## LIST OF ACRONYMS

ADC	Analog-to-digital converter
CT	Computed tomography
CWD	Concealed weapon detection
CAT	Computer-assisted tomography
CS	Chirp Scaling
DETASA	Dual exponentially tapered antipodal slot antenna
EM	Electromagnetic
ERM	Exploding reflector model
FIT	Finite integration technique
FFT	Fast Fourier transform
FMCW	Frequency modulated continuous wave
GPR	Ground penetrating radar
GGP	Generalized Gaussian pulse
ISL	Ideal sidelobe level
INSL	Ideal near-field sidelobe level
IR	Interference region
IFFT	Inverse fast Fourier transform
LNA	Low noise amplifier
MoM	Method of moment
MRI	Magnetic resonance imaging
MMW	Millimeter-wave
MMIC	Monolithic microwave integrated circuit
MIMO	Multiple-input multiple-output
MSP	Method of stationary phase
NIR	Non-interference region

---

NDT	Non-destructive testing
PSF	Point spread function
PEC	Perfect electric conducting
PRF	Pulse repetition frequency
RD	Range Doppler
RCS	Radar cross section
RF	Radio Frequency
RMA	Range migration algorithm
SAR	Synthetic aperture radar
SNR	Signal to noise ratio
SIMO	Single-input multiple-output
SCNR	Signal to clutter noise ratio
SFCW	Stepped-frequency continuous wave
TWI	Through-wall imaging
UV	Ultraviolet
UWB	Ultra-wideband
VCO	Voltage control oscillator

## SUMMARY

Compact, cost-efficient and high-resolution imaging sensors are especially desirable in the field of short-range observation and surveillance. Such sensors are of great value in fields of security, rescue and medical applications. Systems can be formed for various practical purposes, such as detecting concealed weapons in public places, locating people inside buildings or beneath rubbles during emergency rescue, detecting landmine with small vehicle-based systems, and finding early-stage lesions inside human bodies. The advantage of such systems is that imaging can be achieved in real-time, which allows for safer and more effective operation as well as intelligence gathering.

In order to observe moving targets, the system must operate quickly enough to generate a focused real-time 3-D image. Cost efficiency is another factor to consider for market reasons. Existing systems based on synthetic aperture radar (SAR) technology or array with sequential operation of identical transceiver pairs are costly, thus commercially difficult to be widely deployed. Their drawbacks are obvious when compared with compact, lightweight and high-resolution imaging systems which can provide real-time perception of the target.

The combination of ultra-wideband (UWB) technology and real-aperture multiple-input multiple-output (MIMO) array offers a novel and practical solution for safe, reliable and cost-efficient imaging sensors with high resolution capability. UWB impulse with high fractional bandwidth controls the appearance of grating lobes caused by the sparsity of the array; while asymmetric transmit and receive arrays further reduce the number of required antenna elements within the array aperture. Compared to the conventional SAR systems, the combined advantages of UWB technology and MIMO technique can drastically reduce element density, data-acquisition time and the system costs.

The development of UWB-MIMO array and related imaging algorithms is an important and novel research subject. The International Research Centre for Telecommunications and Radar (IRCTR) of Delft University of Technology has initiated several projects with the purpose to develop high performance array-based UWB imaging systems for different short-range applications. Under this framework,

my research has achieved the following novelties and main results which are elaborated in the thesis:

*Properties of UWB focusing.* A novel theory of ultra-wideband focusing is proposed, which has corrected the previous misunderstanding of the impact of bandwidth on imaging. The proposed theory shows that sparsity only ensures the existence of a grating lobe free region within the image space rather than the complete absence of grating lobes. Instead, the bandwidth relative to the center frequency, or fractional bandwidth, has deterministic impact on the formation of grating lobes. Specifically, the bandwidth of an imaging system must exceed its central frequency in order to benefit from the merit of wideband impulse properties, allowing high-resolution imaging with significantly reduced number of antenna elements. The proposed theory helps to resolve the dilemma between angular resolution and grating lobe level for a sparse aperture/array.

*MIMO array topology design.* Novel design approaches for one-dimensional and two-dimensional MIMO arrays have been proposed. They allow direct formation of array topologies without the need of numerical optimization. The designed arrays following the proposed strategies are able to provide three-dimensional imaging capabilities and low grating/side lobe level with large element spacing and minimum number of antenna elements.

*Combination of UWB technology and MIMO array technique.* It is demonstrated that the combination of UWB and MIMO array is a beneficial concept for microwave imaging systems. The MIMO array-based UWB imaging system is able to provide high down- and cross-range resolution, low side/grating lobe level, simplified RF scheme and significantly increased data acquisition speed. A procedure for designing UWB-MIMO array for short-range imaging has been formulated. The process translates requirements from the application into specific array specifications, such as operational frequency band, number of elements needed, aperture dimension, and array topology.

*Modified Kirchhoff migration for MIMO configuration.* Modified Kirchhoff migration has been developed for both free-space and subsurface imaging. The modifications allow for extension of the classical Kirchhoff algorithm, which is based on the exploding reflector concept and is formulated for co-located transmit-receive antennas, to multistatic imaging with arbitrary positions of transmit and receive antennas. The algorithm combines the high quality imaging performance with acceptable computational costs, thus can be applied to demanding applications in practice.

*Range migration algorithm for MIMO configuration.* Range migration algorithm is formulated for multistatic array configuration in the frequency-wavenumber domain for near-field imaging. By taking advantage of the computation efficiency of the fast Fourier transform (FFT), imaging speed of MIMO array-based system are significantly increased while maintaining high-quality imaging capabilities.

*Demonstration of UWB-MIMO system in different applications.* Within the framework of several European projects, prototypes of MIMO array-based UWB imaging systems were designed and implemented for through-wall imaging (PROBANT), ground penetrating radar (Cadmium), and concealed weapon detection (RADIOTECT, ATOM). The feasibility of operational systems under various practical circumstances has been demonstrated. Thanks to the combination of UWB focusing, MIMO array and advanced digital beamforming algorithms, high resolution 3-D images were obtained using sparse aperture array with simplified front-end and low-cost equipments.



# SAMENVATTING

Compacte, kostenefficiënte, hoge-resolutie beeldvormende sensors zijn vooral gewild bij observatie en bewaking op korte afstand. Dergelijke sensors zijn van grote waarde op het gebied van beveiliging, bij reddingsoperaties en medische toepassingen. Er kunnen voor diverse praktische toepassingen systemen worden opgezet, zoals voor het opsporen van verborgen wapens op openbare plaatsen, het lokaliseren van mensen in gebouwen of onder puin tijdens reddingsoperaties, het opsporen van landmijnen met kleine voertuigsystemen en het opsporen van verwondingen binnenin het menselijk lichaam. Het voordeel van dergelijke systemen is dat beelden direct kunnen worden verkregen, zodat er op veiligere en effectievere manier informatie kan worden verkregen en kan worden gehandeld.

Om bewegende doelen te kunnen observeren, moet het systeem snel genoeg kunnen opereren om direct een scherp 3D-beeld te kunnen genereren. Kostenefficiëntie is vanwege de huidige markt een andere belangrijke factor in de overwegingen. Bestaande systemen op basis van synthetische aperture radar (SAR)-technologie of array met sequentiële werking van identieke transceiverparen zijn duur, en dus commercieel gezien moeilijk op grote schaal inzetbaar. In vergelijking met compacte, lichtgewicht, hoge-resolutie beeldvormende systemen die in real-time beelden van het doel kunnen leveren, zijn hun nadelen voor de hand liggend.

De combinatie van ultrabreedband (UWB)-technologie en real-aperture multiple-input multiple-output (MIMO)-array biedt een nieuwe en praktische oplossing voor veilige, betrouwbare en kostenefficiënte, hoge-resolutie beeldvormende sensors. UWB-pulsen met hoge fractionele bandbreedte beperken het optreden van grating lobes veroorzaakt door de onvolledige bezetting van de array; terwijl asymmetrische zend- en ontvangst-arrays het aantal vereiste antenne-elementen binnen de array-apertuur nog verder terugbrengen. De gecombineerde voordelen van de UWB-technologie en MIMO-techniek kunnen de elementdichtheid, de systeemkosten en de tijd waarbinnen gegevens worden verzameld sterk reduceren in vergelijking met conventionele SAR-systemen.

De ontwikkeling van een UWB-MIMO-array en daaraan gerelateerde beeldvormende algoritmes is een belangrijk en nieuw onderzoeksonderwerp. Het International Research Centre for Telecommunications and Radar (IRCTR) van de

TU Delft heeft diverse projecten gestart met als doel krachtige array-beeldvormende systemen met UWB-technologie voor verschillende korteafstandstoepassingen te ontwikkelen. Mijn onderzoek heeft in deze context de volgende nieuwe inzichten en resultaten opgeleverd die verder worden toegelicht in mijn proefschrift:

*Kenmerken van UWB-focusering.* Er wordt een nieuwe theorie over ultrabreedband-focusering voorgesteld, waarmee het eerdere misverstand over de impact van bandbreedte op het beeld wordt gecorrigeerd. De voorgestelde theorie toont aan dat onvolledige bezetting van het array slechts het optreden van grating lobes binnen een bepaald gebied van het beeldbereik voorkomt, maar grating lobes niet in zijn geheel kan voorkomen. De bandbreedte gerelateerd aan de centrale frequentie, of fractionele bandbreedte, heeft een deterministische invloed op de vorming van grating lobes. Concreet gezegd, de bandbreedte van een beeldvormend systeem moet groter zijn dan de centrale frequentie om te kunnen profiteren van de voordelen van breedbandpulsen, waardoor hoge-resolutie beelden mogelijk zijn met aanzienlijk minder antenne-elementen. De voorgestelde theorie helpt het dilemma op te lossen tussen hoekresolutie en grating lobe-niveau voor een apertuur/array met onvolledige bezetting.

*Ontwerp van MIMO-array-topologie.* Er zijn nieuwe benaderingen voorgesteld voor het ontwerp van eendimensionale en tweedimensionale MIMO-arrays. Hiermee kunnen direct array-topologieën worden gevormd, zonder dat numerieke optimalisatie is vereist. De ontworpen arrays die de voorgestelde strategieën volgen, leveren driedimensionale beelden en een laag grating/side lobe-niveau bij een grote afstand tussen de elementen en een minimum aantal antenne-elementen.

*Combinatie van UWB-technologie en MIMO-array-techniek.* Aangetoond is dat de combinatie van UWB en MIMO-array een goed concept is voor microgolf-beeldvormende systemen. Het op MIMO-array gebaseerde UWB-beeldvormende systeem biedt hoge down- en cross-range resolutie, lage side/grating lobe-niveaus, een vereenvoudigd RF-schema en aanzienlijk grotere snelheden bij het verkrijgen van gegevens. Er is een procedure voor het ontwerp van UWB-MIMO-arrays voor beeldvorming op korte afstand geformuleerd. Het proces past de eisen aan voor de array-specificaties die uit de toepassing voortkomen zoals operationele frequentieband, aantal benodigde elementen, apertuurdimensie en array-topologie.

*Aangepaste Kirchhoff-migratie voor MIMO-configuratie.* Een aangepaste Kirchhoff-migratie is ontwikkeld voor zowel beeldvorming in de vrije ruimte als ondergronds. De aanpassingen maken een uitbreiding van het klassieke Kirchhoff-algoritme naar multistatische beeldvorming met willekeurig gepositioneerde zend-en ontvangst-antennes mogelijk, die gebaseerd is op het 'exploding reflector'-concept en geformuleerd is voor samengeplaatste zend-ontvangstantennes. Het algoritme combineert hoge kwaliteit van beeldvorming met acceptabele rekenkosten, en kan zo bij veeleisende praktijktoepassingen worden gebruikt.

*Algoritme voor afstandsmigratie voor MIMO-configuratie.* Het algoritme voor afstandsmigratie (*range migration*) is geformuleerd voor een multistatische arrayconfiguratie in het frequentie-golfgetaldomein voor beeldvorming in het nabije veld. Door gebruik te maken van de rekenefficiëntie van de snelle Fourier-transformatie, kan de snelheid van beeldvorming van MIMO-array-systemen aanzienlijk worden vergroot terwijl de hoge kwaliteit van de beeldvorming behouden blijft.

*Demonstratie van UWB-MIMO-systemen in verschillende toepassingen.* Binnen diverse Europese projecten zijn prototypen van op MIMO-array gebaseerde UWB-beeldvormende systemen ontworpen en geïmplementeerd voor 'door de muur'-beeldvormingstechniek (through-wall imaging; PROBANT), grondradar (ground penetrating radar; Cadmium) en detectie van verborgen wapens (RADIOTECT, ATOM). De haalbaarheid van operationele systemen onder verschillende praktische omstandigheden is inmiddels aangetoond. Dankzij de combinatie van UWB-focusering, MIMO-array en geavanceerde digitale bundelvormende algoritmen, zijn hoge-resolutie 3D-beelden bereikt met gebruikmaking van een aperture-array met onvolledige bezetting in vereenvoudigde, goedkope apparatuur.



---

# AUTHOR'S PUBLICATIONS

## Patent

- [1] X. Zhuge, A. Yarovoy, J. Fortuny-Guasch, A. Martinez, J. M. Lerat, L. Duchesne, "An ultra-wideband radar imaging system using a two-dimensional multiple-input multiple-output (MIMO) transducer array," European Patent Application no. 09173986.2-2220, Dec. 2009.

## Journals

- [2] X. Zhuge, A. G. Yarovoy, T. G. Savylyev, and L. P. Lighthart, "Modified Kirchhoff Migration for UWB MIMO Array-Based Radar Imaging," *IEEE Trans. Geosci. Remote Sens.*, vol. 48, pp. 2692-2703, Jun. 2010.
- [3] X. Zhuge, A. G. Yarovoy, "A Sparse Aperture MIMO-SAR-Based UWB Imaging System for Concealed Weapon Detection," *IEEE Trans. Geosci. Remote Sens.*, accepted for publication in vol. 48, Issue 12, Dec. 2010.
- [4] X. Zhuge, A. G. Yarovoy, "Ultra-Wideband Sparse MIMO Arrays for High-Resolution Near-Field Imaging," *IEEE Trans. Antennas Propag.*, submitted.
- [5] X. Zhuge, A. G. Yarovoy, "Investigation of 2-D Sparse MIMO UWB Arrays for High Resolution Near-Field Imaging," *IEEE Trans. Antennas Propag.*, submitted.
- [6] A. G. Yarovoy, X. Zhuge, "A High-Resolution UWB Imaging System Based on Two-Dimensional Sparse MIMO Array," *IEEE Trans. Microw. Theory Tech.*, submitted.
- [7] T. Savylyev, X. Zhuge, B. Yang, P. Aubry, A. Yarovoy, L. Lighthart, and B. Levitas, "Comparison of 10–18 GHz SAR and MIMO-Based Short-Range Imaging Radars," *International Journal of Microwave and Wireless Technologies*, Available on CJO 08 Jun. 2010, doi:10.1017/S1759078710000383

## Conferences

- [8] X. Zhuge, A. Yarovoy, "Near-Field Ultra-Wideband Imaging with Two-Dimensional Sparse MIMO Array," in *Proc. the Fourth European Conference on Antennas and Propagation (EuCAP)*, April 2010, pp. 1-4.
- [9] X. Zhuge, A. Yarovoy, "Design of Low Profile Antipodal Vivaldi Antenna for Ultra-Wideband Near-Field Imaging," in *Proc. the Fourth European Conference on Antennas and Propagation (EuCAP)*, Apr. 2010, pp. 1-5.
- [10] X. Zhuge, A. Yarovoy, "Comparison between Wavefront-Based Shape Reconstruction and Beamforming for UWB Near-Field Imaging Radar," in *Proc. European Radar Conference (EuRAD)*, Sep. 2010, accepted for publication.
- [11] X. Zhuge, A. Yarovoy, "MIMO-SAR Based UWB Imaging for Concealed Weapon Detection," in *Proc. European Conference on Synthetic Aperture Radar (EUSAR)*, Jun. 2010, pp. 194-197.
- [12] X. Zhuge, A. Yarovoy, "Design of Ultra-Wideband Non-uniform Linear Array for Subsurface Imaging," in *Proc. European Conference on Synthetic Aperture Radar (EUSAR)*, Jun. 2010, pp. 63-66.
- [13] T. Savelyev, X. Zhuge, B. Yang, A. Yarovoy, L. Ligthart, "Development of UWB Microwave Array Radar for Concealed Weapon Detection," in *Proc. 11th International Radar Symposium (IRS-2010)*, Jun. 2010, pp. 1-4.
- [14] A. Yarovoy, X. Zhuge, "SIMO-Based Approach for Subsurface Sensing," in *Proc. 20<sup>th</sup> International Symposium on Electromagnetic Theory (EMTS)*, Aug. 2010, pp. 274-277.
- [15] A. Yarovoy, X. Zhuge, T. Savelyev, J. Matuzas, B. Levitas, "Human Being Imaging with Low-Frequency UWB Radar," in *Ultra-Wideband Short-Pulse Electromagnetics 9*, ed. Frank Sabath, Springer, 2009.
- [16] X. Zhuge, A. G. Yarovoy, L. P. Ligthart, "Circularly Tapered Antipodal Vivaldi Antenna for Array-Based Ultra-Wideband Near-Field Imaging," in *Proc. European Radar Conference (EuRAD)*, Sep. 2009, pp. 250-253.
- [17] X. Zhuge, T. G. Savelyev, A. G. Yarovoy, L. P. Ligthart, B. Levitas, "Comparison of Different Migration Techniques for UWB Short-Range Imaging," in *Proc. European Radar Conference (EuRAD)*, Sep. 2009, pp. 184-187.

- 
- [18] T. G. Savelyev, X. Zhuge, A. G. Yarovoy, L. P. Ligthart, B. Levitas, "Comparison of UWB SAR and MIMO-Based Short-Range Imaging Radars," in *Proc. European Radar Conference (EuRAD)*, Sep. 2009, pp. 109-112.
  - [19] B. Yang, A. Yarovoy, P. Aubry, X. Zhuge, "Experimental Verification of 2D UWB MIMO Antenna Array for Near-Field Imaging Radar," in *Proc. European Microwave Conference (EuMC)*, Sep. 2009, pp. 97-100.
  - [20] X. Zhuge, A. G. Yarovoy, L. P. Ligthart, "A Sidelobe Reduction Technique for Enhancing Images of UWB Sparse MIMO Array," in *Proc. International Radar Conference – Surveillance for a Safer World*, Oct. 2009, pp. 1-6.
  - [21] X. Zhuge, A. G. Yarovoy, L. P. Ligthart, "Design of Circularly Tapered Antipodal Vivaldi Antenna for Near-Field Imaging Array," in *Proc. URSI Benelus forum*, 2009, pp. 1-3.
  - [22] T. G. Savelyev, X. Zhuge, A. G. Yarovoy, L. P. Ligthart, "Advanced Real-Time techniques for GPR Imaging of Landmines," in *Proc. IEICE Tech. Rep.*, vol. 109, no. 219, SANE2009-68, Oct. 2009, pp. 19-24.
  - [23] X. Zhuge, T. G. Savelyev, A .G. Yarovoy, L. P. Ligthart, "UWB Array-Based Radar Imaging Using Modified Kirchhoff Migration," in *Proc. IEEE International Conference on Ultra-Wideband (ICUWB)*, Sep. 2008, pp. 175-178.
  - [24] X. Zhuge, T. G. Savelyev, A .G. Yarovoy, L. P. Ligthart, J. Matuzas, B. Levitas, "Human Body Imaging by Microwave UWB Radar," in *Proc. European Radar Conference (EuRAD)*, Oct. 2008, pp. 148-151.
  - [25] A. G. Yarovoy, T. G. Savelyev, X. Zhuge, P. Aubry, L. P. Ligthart, J. Schavemaker, P. Teltelaar, E. den Breejen, "Performance of UWB array-based radar sensor in a multi-sensor vehicle-based suit for landmine detection," in *Proc. European Radar Conference (EuRAD)*, Oct. 2008, pp. 288-291.
  - [26] N. T. Thanh, L. van Kempen, T. G. Savelyev, X. Zhuge, M. Aftanas, E. Zaikov, M. Drutarovsky, H. Sahli, "Comparison of Basic Inversion Techniques for Through-Wall Imaging Using UWB Radar," in *Proc. European Radar Conference (EuRAD)*, Oct. 2008, pp. 140-143.
  - [27] X. Zhuge, A. G. Yarovoy, T. G. Savelyev, P. J. Aubry, and L. P. Ligthart, "Optimization of Ultra-Wideband Linear Array for Subsurface Imaging," in *Proc. International Conference on Ground Penetrating Radar*, 2008, pp. 1-5.
  - [28] B. Yang, X. Zhuge, A. G. Yarovoy, L. P. Ligthart, "UWB MIMO Antenna Array Topology Design Using PSO for Through Dress Near-Field Imaging," in *Proc. European Microwave Conference (EuMC)*, Oct. 2008, pp. 1620-1623.

- 
- [29] X. Zhuge, M. Hajian, A. G. Yarovoy, L. P. Lighthart, "Ultra-wideband Imaging for Detection of Early-Stage Breast Cancer," in *Proc. European Radar Conference (EuRAD)*, Oct. 2007, pp. 38-42.
  - [30] X. Zhuge, T. G. Savylyev, A .G. Yarovoy, L. P. Lighthart, "Subsurface Imaging with UWB Linear Array: Evaluation of Antenna Step and Array Aperture," in *Proc. IEEE International Conference on Ultra-Wideband (ICUWB)*, Sep. 2007, pp. 66-70.
  - [31] X. Zhuge, T. G. Savylyev, A .G. Yarovoy, "Assessment of Electromagnetic Requirements for UWB Through-Wall Radar," in *Proc. International Conference on Electromagnetics in Advanced Applications (ICEAA)*, Sep. 2007, pp. 923-926.
  - [32] A. G. Yarovoy, X. Zhuge, T. G. Savylyev, L. P. Lighthart, "Comparison of UWB Technologies for Human Being Detection with Radar," in *Proc. European Microwave Conference (EuMC)*, Oct. 2007, pp. 1574-1577.

## ACKNOWLEDGEMENTS

I would like to express my gratitude to those who have given their support to me during the process of my Ph.D. study and thesis writing.

First of all, I would like to thank my promoter Prof. Alexander Yarovoy for being a great mentor to me in the last four years. He is an inspiration and paradigm to me as an excellent scientist in his field of expertise. He has generously shared his knowledge and vision with me. He is always kind and warm as a friend and family in his way of guiding and teaching. It has been a great pleasure working with him.

I am also very grateful to Prof. Leo Ligthart who opened the gate of research group of IRCTR to me, when I came to him as a master graduate. Thanks for that, I not only had the opportunity to pursue my academic ambition, but also to experience the professionalism and hospitality of the group.

I am lucky to have many good colleagues. Thank Dr. Timofey Savelyev for sharing his experiences in different institutes, which was especially constructive for the beginning of my research. Many thanks to Pascal Aubry who is always happy to help and spent so many hours with me doing measurements in anechoic chamber and TNO DSS facilities, as well as the technical supports from Johan Zijderveld and Paul Hakkaart. Thank Bill Yang for his companion as a peer researcher and a friend, with whom I shared the office for four years. We spent lots of time bouncing ideas and support each other's research. Thanks to Prof. Piet van Genderen for his valuable comments to the translation of my summary and propositions. Thank Yann Dufournet for kindly sharing his experience of thesis editing and the detailed matters of the defense in the final busy moment.

I appreciate all the assistance from our secretaries: Dominique Meijer, Mia van der Voort, Marjon Verkaik-Vonk, Stefanie van Gentevoort, and financial managers: Ad de Ridder and Jeffrey Ransun. They have been always kind and helpful.

I would like to thank all my colleagues at IRCTR. I enjoyed working in this friendly and international atmosphere where everybody is dedicated to research and science.

Finally, I'm in indebted to my parents and Jing for their unconditional support and understanding during all the years when I'm far away from home. They have

helped me with my life and career and given me all of the things that have gotten me here. They are the source of power for me to face all the challenges that life has to offer.

*Zhuge Xiaodong*

*Delft, 12 August 2010*

## ABOUT THE AUTHOR

Xiaodong Zhuge was born in Beijing, China, in 1982. He received the B.S. degree in Telecommunication Engineering from Beijing University of Posts and Telecommunications, Beijing, China in 2004, and the MSc. degree with Cum Laude from Delft University of Technology (TUDelft), Delft, the Netherlands in 2006.

He joined the International Research Center for Telecommunications and Radar (IRCTR), TUDelft in 2006 where he started working towards his Ph.D. degree. During the four years' period, he has been involved in several national and European projects in the effort to develop array-based UWB imaging systems. Some of the relevant results of these studies are presented in this Ph.D. dissertation. His main research interests include UWB imaging, signal processing, and antenna array design.

Xiaodong Zhuge has published more than 30 papers on UWB imaging in different applications. He was the recipient of the 2007 European Radar Conference (EuRAD) Young Engineers Prize for the paper that best advanced the state-of-the-art in radar at the 10th European Microwave Week, Munich, Germany. A patent application is pending on the two-dimensional MIMO transducer array he developed within a European project.

### **Award**

EuRAD Young Engineers Prize, European Radar Conference 2007, Munich, Germany, October 10-12, 2007.

Award for the article entitled: "Ultra-Wideband Imaging for Detection of Early-Stage Breast Cancer".